INTERNATIONAL SYMPOSIUM ON GEOMECHANICS

ISRM Specialized Conference
Conference Proceedings
Volume 2021

ISSN: 2805-6426 (Online)

Editor: Guillermo Alzate Espinosa

GIGA
GRUPO DE INVESTIGACIÓN EN GEOMECÁNICA APLICADA

UNIVERSIDAD NACIONAL DE COLOMBIA

INTERNATIONAL SYMPOSIUM ON GEOMECHANICS

Conference Proceedings of the 9th International Symposium on Geomechanics – ISRM Specialized Conference: *"Applied Geomechanics in Proactive Designs: Opportunities, Challenges and Security",* May 5 – 6 2021, Virtual.

ISSN: 2805-6426 (Online)
Periodicity: Biennial

ACKNOWLEDGMENTS

The organization of the event thanks the members of the scientific committee, the Universidad Nacional de Colombia for its support through the Research System - SIUN, the ANH and MINCIENCIAS for their support through research project 801-2019 and all the organizations that linked to the symposium

Medellin – May, 2021

Table of Contents

© 2021 Universidad Nacional de Colombia – ISRM, ISSN 2805-6426 Guillermo Alzate Espinosa (Ed.)

Seismically inverted geomechanic properties as key rock typing enablers in the Barnett shale play

John H. Alzate[a], Deepak Devegowda[a]

[a,] *University of Oklahoma, Norman, United States*

ABSTRACT

Previous studies show that Lambda-rho/Mu-rho cross plots from seismic data can be used to quantitatively grade unconventional plays. In this work which condenses the results of first author's M.Sc. thesis, we examine the utility of these cross plots with actual field data acquired from the Lower Barnett play. We use seismically inverted Poisson's ratio as a fracability discriminator and Young's modulus as an indicator of Total Organic Carbon (TOC) richness and porosity. We classify the Lower Barnett shale in the study area into four rock groups: Brittle-Rich, Rich-Ductile, Brittle-Poor, and Ductile-Poor. We validate these results using production logs and microseismic data acquired on four wells. Production logs directly measure the rates coming from each perforation cluster while microseismic events directly measure locations where the rock breaks which is a good proxy to the stimulated rock volume, SRV. Integration of seismic data, production logs and microseismic data indicates that Brittle-Rich zones are the most suitable locations to drill wells in this particular play because they exhibit two components: significant hydrocarbon in place and sufficient strength to sustain effective fractures. On the other hand, rock zones characterized as Ductile-Poor should be avoided during drilling and fracturing since once the fracturing pressure is released, the rock will close back against the proppant resulting in ineffective completions. Brittle-poor zones adjacent to zones with high TOC (rich zones) can also be target drilling locations since the brittle/competent rock can sustain long-lasting hydraulic fracture treatments bridging the gap between the hydrocarbon rich zone and the wellbore.

KEYWORDS

Reservoir characterization; Seismic inversion; Hydraulic fracturing; Microseismic.

1. INTRODUCTION

One of the key developments critical to making shale wells economically productive over extended periods of time is the use of hydraulic fracture treatments. In combination with horizontal well technology, shale gas wells are now orders of magnitude more productive than wells completed in similar settings in the 1990s to the early 2000s (Agrawal et al., 2012). Shale wells are now routinely completed with a suite of hydraulic fracture treatments in several stages (Bennett et al., 2006; Bruner and Smosna, 2011). The stages are designed to contact as much of the reservoir rock as possible, thereby creating highly conductive oil and gas migration pathways between the reservoir rock and the wellbore (Daniels et al., 2007; Cipolla et al., 2008; Mayerhofer et al., 2010; Cipolla et al., 2012; Yu and Aguilera, 2012).

Additionally, as our knowledge of shales has expanded from the classical homogeneous seal rock model to that of a reservoir rock characterized by considerable lateral and vertical variability, there is an increasing need to exploit this knowledge for optimal well and fracture placement. The work presented in this paper is organized around this main theme: to identify optimal locations for infill drilling and for hydraulic fracture treatments by mapping these heterogeneities and identifying the location and distribution of significant hydrocarbon accumulations to extract shale oil and gas resources more efficiently and economically.

To identify sweet spots in unconventional organic-rich shale reservoirs, it is generally recognized that the optimal placement of wells and hydraulic fracture treatments are controlled by reservoir quality, that

is a function of porosity and total organic carbon (TOC) as well as completion effectiveness defined by the potential for fracture initiation and the ability for the fractures to remain open for extended periods of time (Cipolla et al., 2011). Cipolla et al. (2011) provide a comprehensive analysis of the factors affecting the reservoir quality and the completion effectiveness based on an analysis derived from the use of several field measurements such as sonic well logs, microseismic analysis, and seismic data. Maity and Amizadeh (2012) also present a similar approach for multiscale data integration for reservoir characterization using seismically inverted rock properties to extend well log data to interwell reservoir volumes to characterize shales. Refunjol et al. (2012), using a Barnett Shale case study, present a methodology to correlate hydraulic fracture-induced microseismic events with seismic attributes such as curvature and also explore the utility of $\lambda\rho$ / $\mu\rho$ crossplots, but did not link the microseismic event distribution to rock brittleness.

Although these studies have expanded our understanding of shale reservoirs and the types of analyses necessary to quantify reservoir quality, the aforementioned workflows are somewhat limited because of the lack of validation with field production data. The work presented in this paper therefore is unique because, first, we derive a template based on seismic-derived attributes to quantify reservoir quality for regional and field-scale shale characterization. Second, we validate the template against production logs acquired in four horizontal wells completed with multiple-stage hydraulic fracture treatments. These production logs quantify gas production rates across each of the fracture stages and provide a means to validate the rock classification template. We then explore the relationship between the location of microseismic events and the $\lambda\rho$ / $\mu\rho$ crossplots to characterize fracture propagation and profiles.

We also validate observations of brittleness in shales exhibiting low values of Poisson's ratios. Consequently, with the rock quality template generated from seismic-derived attributes of $\lambda\rho$ and $\mu\rho$, we are then able to provide reliable estimates of variations in rock quality laterally and vertically across shales, thereby enabling the successful placement of productive wells and hydraulic fracture treatments.

2. SEISMIC DATA AND INVERSION FUNDAMENTALS

The original seismic data was acquired by Devon in April 2009, about three months after the wells A, B, C, and D were hydraulically fractured. Overall, the seismic data are high quality, with frequencies approaching 100 Hz (Thompson 2010). Table 1 summarizes the acquisition parameters.

Since the Barnett shale, shows up in the 1100 to 1400 ms time window, the frequency content is restricted to the 10-100 Hz band due to the filters applied.

Table 1. Acquisition parameters used to allow subsequent azimuthal processing. From Thompson (2010).

Number of live lines	30
Number of stations per line	120
Receiver line interval	660 ft
Receiver group spacing	220 ft
Shot line interval	880 ft
Vibrator array interval	220 ft
Patch size	26,180 ft by 25,520 ft
Nominal bin size	110 ft by 110 ft
Number of vibrator sweeps	8
Number of vibrators per array	3
Sweep range	10-110 Hz, 10 s duration, 3 db/octave
Number of geophones per group	6 in a 6 ft circle around station.

The seismic survey consists of 365 in-lines, 269 cross-lines with a bin size of 110 x 110 feet, covering around 20 square miles in a region where 308 vertical and 127 horizontal wells were drilled before the seismic data were acquired

For this study we were provided (Perez 2010) with pre-stack depth migrated volumes of P and S-impedance, lambda-rho and mu-rho, Young modulus and Poisson's among others. These products resulted from seismic inversion processes applied on the near and mid-offset components (3°-43°) of the original pre-stack unmigrated survey.

Properly tied or calibrated to well measurents, seismic inversion is a powerful tool that allow us to characterize the interwell regions. Seismic inversion is based on the convolution of the seismic wavelet and the Earth's reflectivity through a forward model.

The seismic data was inverted using a commercial inversion algorith (Hampson-Rusell^{TM}) that requires angle dependent wavelets and angle stacks and results in estimates of P-impedance, S-impedance and density (Hampson and Rusell 2005).

Once the P and S impedance volumes have been generated they can be used to calculate the Lame parameters of imcompressibility, λ, and rigidity, μ as well as the Young's modulus, E, and Poisson's ratio, ν. Incompressibility is more sensitive to the pore fluids than to the matrix, and for elastic materials rigidity is only influenced by the matrix connectivity (Dufor et al. 2002, Goodway et al. 1997).

For homogeneous isotropic linear elastic materials,

$$V_P^2 = \frac{(\lambda+2\mu)}{\rho} \tag{1}$$

Vp: Compressional wave velocity;

ρ: Density;

$$V_S^2 = \frac{\mu}{\rho} \tag{2}$$

Vs: Shear wave velocity;

$$Z_P = \rho V_P \tag{3}$$

Zp: P-wave impedance.

$$Z_S = \rho V_S \tag{4}$$

Zs: S-wave impedance.

The Lame parameters can be related to the impedances in the following manner;

$$\lambda\rho = Z_P^2 - 2Z_S^2 \tag{5}$$

$$\mu\rho = Z_S^2 \tag{6}$$

The Young's modulus and Poisson's ratio can then be calculated from;

$$E = \frac{\mu(3\lambda+2\mu)}{\lambda+\mu} \tag{7}$$

$$\nu = \frac{\lambda}{2(\lambda+\mu)} \tag{8}$$

2.1. Microseismic data: monitoring the hydraulic fracturing process

The microseismic mapping technique is a passive seismic imaging technique and records microseisms generated as a consequence of some processes within the reservoir such as fluid flow, hydraulic fracturing, enhanced oil recovery processes, etc (McGillivray 2005, Daugherty et al. 2009, Noe 2011). These microseisms are characterized by a very small energy radiated in the form of seismic waves with frequencies in the range of 50 to 500 Hz (Hanks and Kanamori 1979 Baig and Urbancic 2010, Goodway 2012;). These seismic waves comprise of shear and compressional waves with their associated velocities. For hydraulic fracturing processes, microseisms are generated when the rock fails in the shear mode (Cipolla et al. 2011, Cipolla et al. 2012). The shear failure may be a slip or tear failure and may be attributed to changes in the effective stress state (Cipolla et al 2011). The stress state disturbance is generally caused by pore pressure changes due to any of the processes listed above.

The microseisms generated emit shear and compressional waves. By processing the data collected in the monitoring array, the location and magnitude of the generated microseismis can be determined (Bennett et al. 2006). The monitoring arrays comprises of sensitive, multicomponent geophones. Figure 1 sketches a typical configuration of treatment and monitoring wells during a hydraulic fracture mapping process.

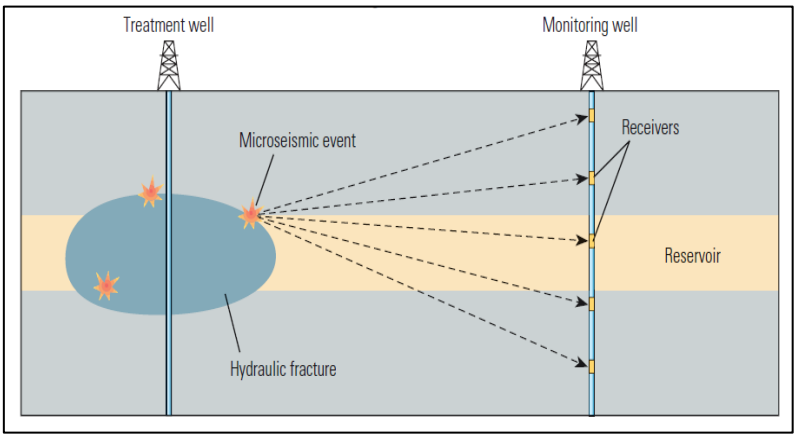

Figure 1. Sketch of a typical configuration of treatment and monitoring wells during a hydraulic fracture monitoring process. (Bennett et al. 2006).

Although microseismic monitoring holds immense value to the petroleum industry, its application and interpretation is associated with several challenges. The most important aspect of quality control for acquiring microseismic data is related to the location of the monitoring array or monitoring well. The recorded data tends to be biased as smaller magnitude events are recorded near the monitoring array. On the other hand, at large distances from the monitoring well, only larger magnitude events tend to be recorded. (Baig and Urbancic 2010; Cipolla et al. 2011; Cipolla et al. 2012; Shemeta and Anderson 2010; Warpinski 2009).

Additionally, in order to ensure that the analysis is meaningful, microseismic data needs to be filtered by the signal to noise ratio, SNR. When the SNR is very low, identifying the locations of the microseisms may be inaccurate and are often associated large error ellipsoids which can render fracture mapping challenging. (Cipolla et al. 2011; Kidney et al. 2010).

3. METHODOLOGY

In Perez et al. (2011), a workflow based on “heuristic” rock physics templates (Figure 2) was developed to guide the interpretation of seismically inverted properties in unconventional reservoirs. The shale reported in their study varies in composition from 60/40% quartz/clay to 100% quartz and porosity ranges from 0% to 20%, but the underlying principles can easily be extended to interpretation in other

shales with differing compositions. We provide a brief overview of their approach that we have adopted in this work.

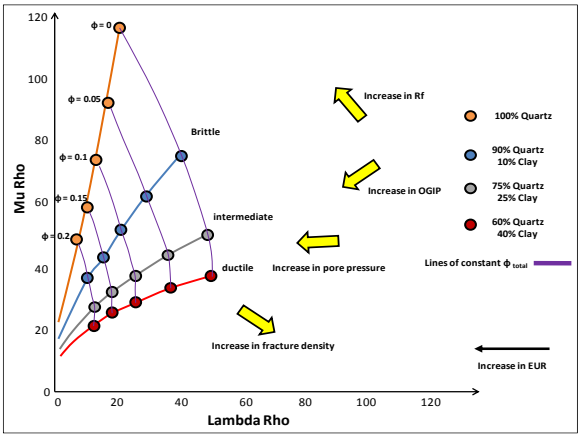

Figure 2. Heuristic template to interpret seismic, well log, or laboratory rock properties in terms of EUR, Original gas in place (OGIP), recovery factor (RF), pore pressure, and fracture density (Perez et al., 2011).

Because the local gas-in-place estimates are linked to porosity, on the $\lambda\rho$ / $\mu\rho$ crossplot (Figure 2), the gas-in-place or the richness of the rock is likely to track the porosity increase. Additionally, changes in rock composition are also directly related to the brittleness of the rock with quartz-rich rocks being brittle and clay-rich rocks ductile. In shales, the efficacy of the hydraulic fracture stimulation is linked to the extent of the stimulated reservoir volume and this is controlled by the brittleness of the rock. Moreover, brittle rocks can sustain propped fractures effectively while ductile rocks tend to heal themselves against the proppant. The recovery factor (RF) or fraction of hydrocarbons in place that can be produced is a function of these two properties: the richness of the rock, dictated by porosity, and the amenability to hydraulic fracturing, controlled by mineralogy and brittleness. Consequently, a rock quality template based on $\lambda\rho$ / $\mu\rho$ crossplots is likely to be very informative for effective well and hydraulic fracture placement and forms the basis of this work.

The relationship between elastic properties such as the Young's modulus and reservoir quality properties such as porosity and TOC in shales has been well documented. Takahashi and Tanaka (2010) show that static as well as dynamic Young's modulus exhibit an inverse relationship to porosity in soft sedimentary rocks. Kumar et al. (2012) also document the inverse relationship between Young's modulus and porosity, TOC, and clay content based on nano-indentation tests on samples from the Woodford, Haynesville, Eagle Ford, and the Barnett Shale, finding similar trends for all plays. These studies demonstrate the usefulness of Young's modulus as an indicator of porosity and therefore gas-in-place and rock richness. Figure 3 (left side) shows the seismic-derived Young's modulus on a $\lambda\rho$ / $\mu\rho$ crossplot and following the arguments provided by previous studies, the variation in the Young's modulus is a consequence of TOC and porosity differences.
Figure 3 (right side) shows the corresponding values of Poisson's ratios across the seismic volume on a $\lambda\rho$ / $\mu\rho$ crossplot. Figure 3 (right side) displays well-defined color bands representing portions of the data having similar Poisson's ratio and demarcates brittle zones that are associated with higher completion efficiency and that exhibit low values of Poisson's ratio. The higher values of Poisson's ratio associated with more ductile rocks are distinctly separated from the more brittle regions of this crossplot.

We then propose the following reservoir quality classification template as shown in Figure 4 obtained by combining Figures 6 and 7 that highlights Poisson's ratio and Young's modulus variations in the 3D seismic volume. These are: Group 0 or "Brittle and Rich" (red points) are those portions of the Barnett Shale having low values of Poisson's ratio and low values of Young's modulus; Group 1 or "Rich and Ductile" (yellow points) are those regions of the shale play characterized by high values of Poisson's ratio and low values of Young's modulus; in Group 2 or "Brittle and Poor" (green points) fall all portions of the shale play exhibiting low values of Poisson's ratio and high values of Young's modulus; and

Group 3 or "Ductile and Poor" (blue points) are those parts of the shale play with high Poisson's ratio and high Young's modulus.

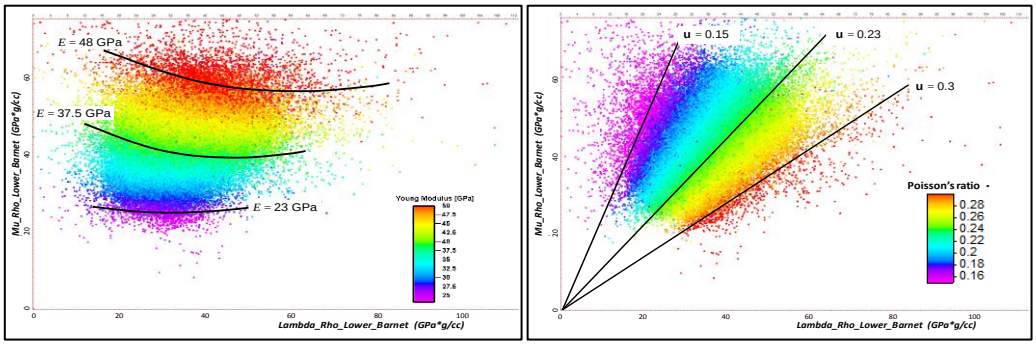

Figure 3. Seismic $\lambda\rho$ / $\mu\rho$ crossplot for the Lower Barnett Shale. Left. Color indicates the Young's modulus, E, decreasing toward the origin. Right. Color indicates the Poisson's ratio versus lines of fixed Poisson's ratio converge at the origin

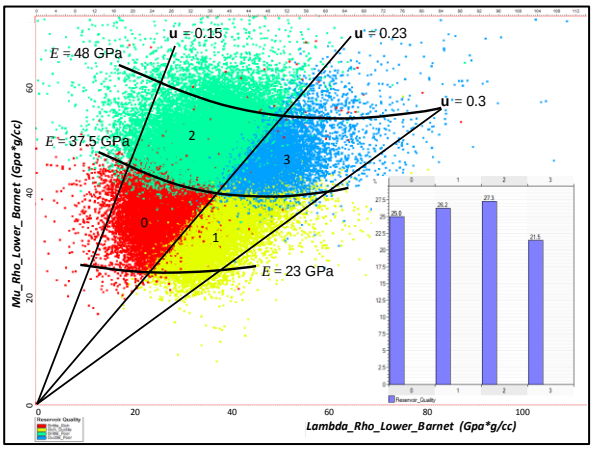

Figure 4. Lower Barnett reservoir quality classification based on seismically inverted rock properties. Four groups are defined: Group 0 or "Brittle and Rich," Group 1 or "Rich and Ductile," Group 2 or "Brittle and Poor," and Group 3 or "Ductile and Poor.

4. RESULTS AND ANALYSIS

To assess the validity of the classification scheme described above, we then explore the relationship between individual fracture stage gas production rates and the $\lambda\rho$ and $\mu\rho$ parameters in the immediate vicinity of each perforation cluster or fracture stage. The gas production rates for each stage along each of the four laterals were acquired from production logs.

The production rates recorded at each stage for each of the wells is provided in Table 2. Well B is the best-performing well, followed by Well D, Well C, and Well A.

In Figure 5, we overlay these gas production rates on the rock classification template previously defined.

The grouping of the most prolific and least productive fracture stages in Figure 5 clearly indicates a strong relationship between the fracture productivity and the properties of the rock surrounding the perforation clusters.

The most prolific zones tend to be associated with the previously defined Group 0, while points located within Group 3 are relatively less productive. Consequently, Figure 5 provides strong evidence that supports the motivating factors for this work: (1) that the productivity of shale well fractures is determined by the mechanical properties and richness of the rock in the vicinity of the completion and (2) that seismic-derived properties enable classification of rock types on a regional scale.

Figures 6 and 7 examine the performance of each fracture stage on a well-by-well basis with the same conclusions.

Table 2. Gas production rates per stage for each of the four production wells along with the classification of the rock volumes surrounding each fracture stage.

Well name	Gas rate per stage (MSCFD)	Well gas rate (MSCFD)	Rank	Reservoir quality	Gas rate per stage (MSCFD)
Well A	650	1260	4	Brittle-Poor	650
	450			Brittle-Poor	450
	80			Ductile-Poor	80
	80			Ductile-Poor	80
Well B	650	40000	1	Brittle-Rich	650
	1250			Brittle-Rich	1250
	700			Brittle-Rich	700
	800			Brittle-Rich	800
	400			Brittle-Rich	400
	200			Brittle-Rich	200
Well C	250	1600	3	Brittle-Poor	250
	650			Rich-Ductile	650
	350			Ductile-Poor	350
	100			Ductile-Poor	100
	250			Ductile-Poor	250
Well D	850	2400	2	Brittle-Poor	850
	100			Ductile-Poor	100
	150			Ductile-Poor	150
	400			Rich-Ductile	400
	250			Brittle-Poor	250
	150			Ductile-Poor	150
	100			Ductile-Poor	100
	400			Ductile-Poor	400

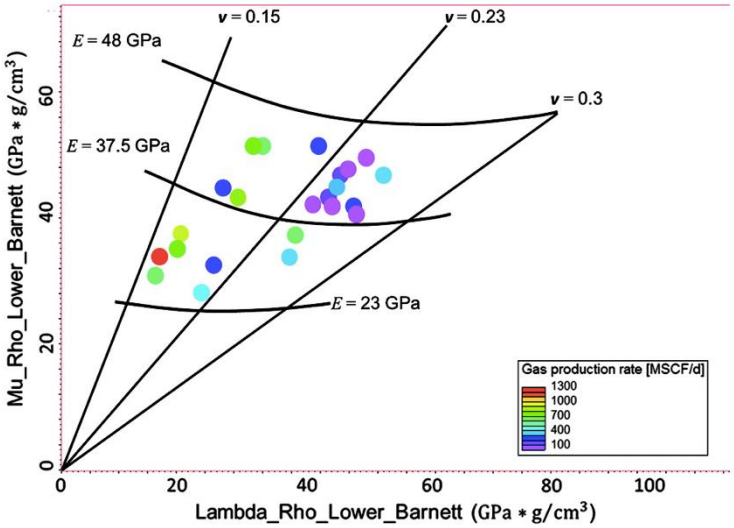

Figure 5. Seismic $\lambda\rho$ / $\mu\rho$ extracted along the wellbores with production logs. The color indicates the gas rate at each individual perforation.

Because we now have a rock classification template, we can also analyze the distribution of the rock types in relation to the location of the horizontal laterals of each of the wells. Figure 8 shows a vertical slice across a 390-ft section of the lower Barnett and the corresponding well locations. The figure reinforces our earlier observations supporting the substantially higher productivity of Well B, completed in the brittle-rich zone, in comparison to the other wells completed in less attractive target layers.

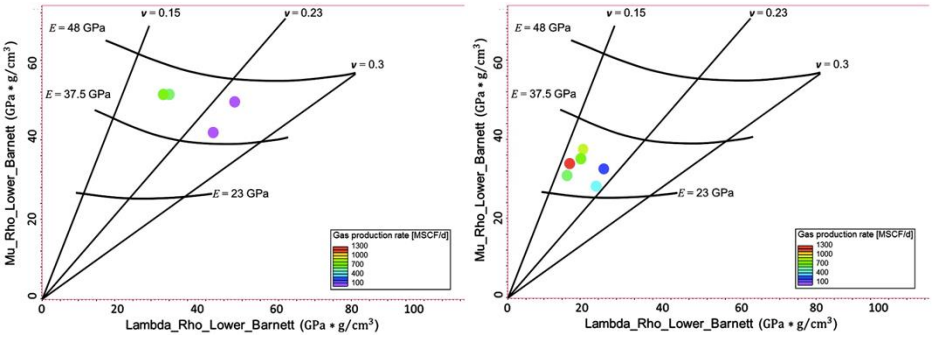

Figure 6. Seismic $\lambda\rho$ / $\mu\rho$ extracted along the wellbores with production logs. The color indicates the gas rate at each individual perforation in Well A (Left) and Well B (Right).

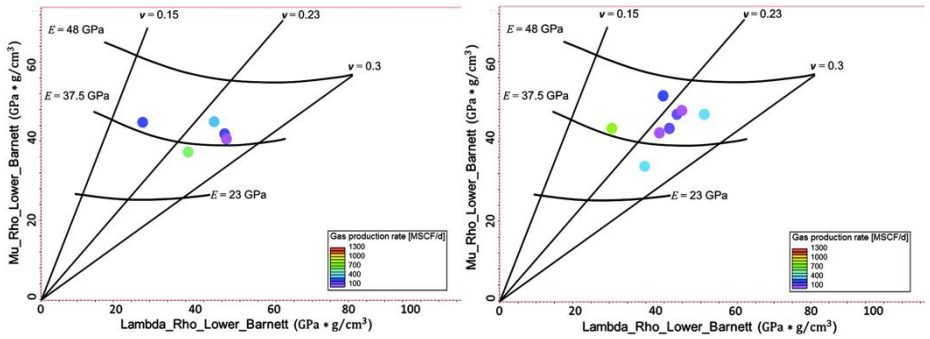

Figure 7. Seismic $\lambda\rho$ / $\mu\rho$ extracted along the wellbores with production logs. The color indicates the gas rate at each individual perforation in Well C (Left) and Well D (Right).

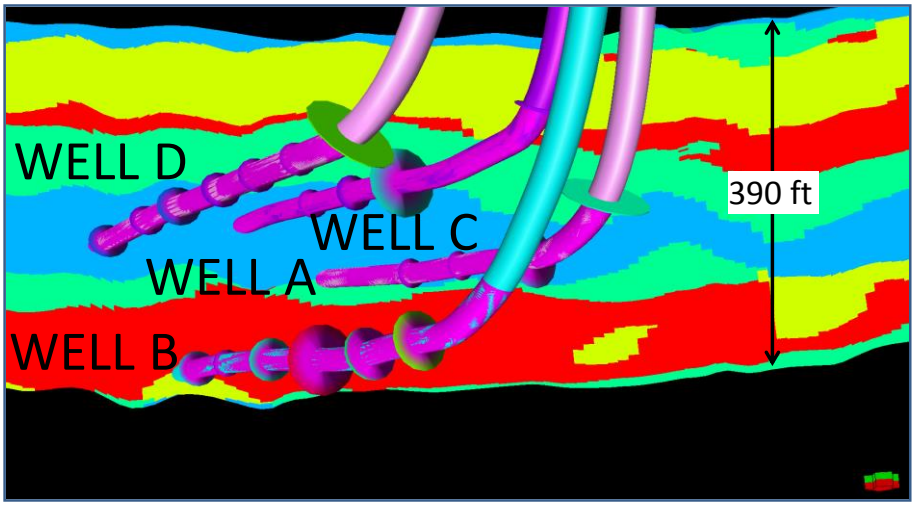

Figure 8. East–west vertical slice through the reservoir quality volume showing the location of the wells having production logs. The color in the layers is following the rock classification proposed. Well B is entirely completed in a Brittle-Rich (red) layer, while most of Well A, Well C, and Well D rest in a Ductile-Poor (blue) layer.

We then also employed the microseismic data recorded while fracturing these wells to map the stimulated volume of rock. Our goal was to analyze the patterns of fracture growth and their relation to the rock classification template described earlier. In Figures 9 and 10, we plot the $\lambda\rho$ / $\mu\rho$ values corresponding to the microseismic events measured for Wells A, B, and C, D, respectively. Additionally, in these figures, we also indicate by means of a histogram the percentage of all recorded events located within the different rock classes.

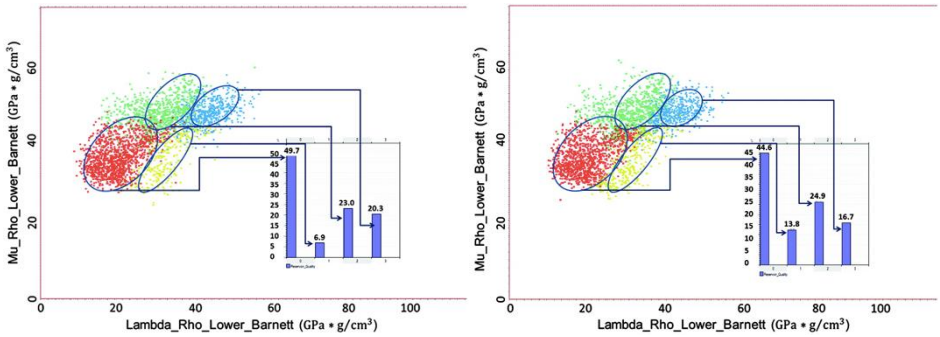

Figure 9. $\lambda\rho$ / $\mu\rho$ crossplots showing the microseismic events recorded while hydraulically fracturing Well A (Left) and Well B (Right). About 73% of the microseismic events recorded while stimulating Well A and 65% of the microseismic events recorded while stimulating Well B fall in portions of the rock classified as Brittle according to this reservoir quality classification.

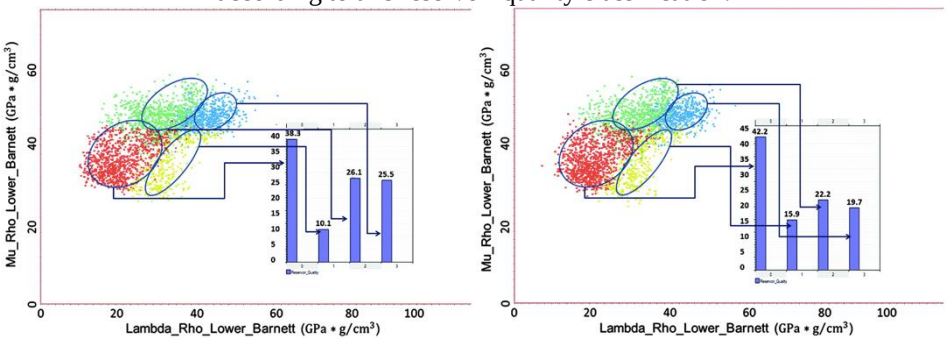

Figure 10. $\lambda\rho$ / $\mu\rho$ crossplots showing the microseismic events recorded while hydraulically fracturing Well C (Left) and Well D (Right). About 64% of the microseismic events recorded while stimulating Well C and 65% of the microseismic events recorded while stimulating Well D fall in portions of the rock classified as Brittle according to this reservoir quality classification.

An interesting observation is that, irrespective of the location of the lateral, fracture events are preferentially clustered in the brittle rock types with roughly 65%–70% of all events for all wells recorded in the brittle red and green clusters. Remarkably, across the four laterals studied, the Brittle-Rich rock contains more than 40% of the microseismic events generated. This indicates that: a) The fractures tend to grow towards portions of the rock characterized by low Young's moduli and low Poisson's ratios irrespective of the fracture starting point and; b) In addition to having a big stimulated rock volume, the competence of the rock along the wellbore is critical to achieve effective hydraulic fracture treatments.

To summarize, we provide the flow rates and rock classes associated with each stage of each well in Table 2. The data also provides the total production per well and a well ranking based on these numbers. The rock classes recorded in Column 5 of Table 2 show excellent correlation with the individual fracture stage productivity with high accuracy, although there are a few stages, one each in Wells B, C, and D that do not conform to this classification. However, in general, the classification correlates with productivity very satisfactorily and Well B, the most productive well, is entirely completed in a Brittle and Rich zone. For the other three wells, the perforations completed in zones with good fracability (green) are distinct from most of the other stages completed in Poor and Ductile regions (blue) in terms of productivity."

5. CONCLUSIONS AND RECOMMENDATIONS

The work presented in this paper demonstrates a promising approach to use 3D surface seismic data, microseismic, and production logs for regional-scale reservoir characterization. The 3D seismic data set was inverted for attributes such as the $\lambda\rho$ / $\mu\rho$ parameters which were then used to classify reservoir sweet spots on the basis of rock properties such as the Young's Moduli and Poisson's ratios. The proposed classification template was validated against a data set acquired in the Lower Barnett shale

play where we demonstrate the link between reservoir quality and amenability to hydraulic fracturing in four horizontal wells with multiple stage completions.

The 3D seismic data used in this study were calibrated to measurements on over 400 wells in the area of interest, which ensures a satisfactory reliability of the inversion results and increases the confidence of the model predictions in the interwell volumes (regional scale). It is recommended that for future studies, elastic properties such as Young moduli and Poisson's ratio from static measurements (i.e., from preserved cores and from drilling cuttings) be used to calibrate the dynamic measurements from sonic logs and from seismic inversion (local scale).

ACKNOWLEDGEMENTS

The authors especially want to thank the people at DEVON Energy for releasing this unique data set that led to an exciting research study. We also want to thank Roderick Perez of the University of Oklahoma for doing the time-depth conversion and the seismic inversion and Kurt J. Marfurt for his invaluable feedback.

REFERENCES

Alzate J. H. 2012. *Integration of Surface Seismic, Microseismic, and Production Logs for Shale Gas Characterization: Methodology and Field Application.* MS thesis, The University of Oklahoma, Norman, Oklahoma, USA.

Agrawal, A., Y. Wei, and S. A. Holditch, 2012, A technical and economic study of completion techniques in five emerging US gas shales: A Woodford Shale example. SPE 135396. *SPE Drill & Compl*, 27, 39–49.

Baig, A. and Urbancic, T. 2010. Magnitude Determination, Event Detectability, and Assessing the Effectiveness of Microseismic Monitoring Programs in Petroleum Applications. *CSEG Recorder*, (February), 22-26.

Bennett, L., J. LeCalvez, D. R. Sarver, K. Tanner, W. S. Birk, G. Waters, J. Drew, G. Michaud, P. Primiero, L. Eisner, R. Jones, D. Leslie, M. J. Williams, J. Govenlock, R. C. Klem, and K. Tezuka, 2006, The source for hydraulic fracture characterization. *Oilfield review/Schlumberger*, 42–57.

Bruner, K. R., and R. Smosna, 2011, A comparative study of the Mississippian Barnett Shale, Fort Worth Basin, and Devonian Marcellus Shale, Appalachian Basin. *Technical Report DOE/NETL-2011/1478, National Energy Technology Laboratory (NETL) for The United States Department of Energy*.

Cipolla, C., Warpinski, N.R.., Mayerhofer, M.J., et al., 2008. The Relationship Between Fracture Complexity, Reservoir Properties, and Fracture Treatment Design. *The 2008 SPE Annual Technical Conference and Exhibition, Denver, Colorado, 21-24 Sept 2008*.

Cipolla, C., R. Lewis, S. Maxwell, and M. Mack, 2011. Appraising unconventional resource plays: Separating reservoir quality from completion effectiveness. *International Petroleum Technology Conference*, IPTC 14677.

Cipolla, C., S. Maxwell, and M. Mack, 2012, Engineering guide to the application of microseismic interpretations. *Hydraulic Fracturing Conference, SPE, Paper* SPE 152165.

Daniels, J., G. Waters, J. LeCalvez, J. Lassek, and D. Bentley, 2007, Contacting more of the Barnett Shale through an integration of real-time microseismic monitoring, petrophysics and hydraulic fracture design. *Annual Technical Conference and Exhibition, SPE, Paper* SPE 110562.

Daugherty, J. and Urbancic, T. 2009. Microseismic Monitoring of a Carbon Sequestration Field Test. In *Frontiers + Innovation. Proceedings of the 2009 CSPG CSEG CWLS Convention, Calgary, Alberta*.

Dufor, J., J. Squires, W. N. Goodway, A. Edmunds, and I. Shook, 2002, Integrated geological and geophysical interpretation case study and Lame rock parameter extractions using AVO analysis on the Blacfoot 3C-3D seismic data, South Alberta, Canada. *Geophysics*, 67, 27–37.

Goodway, B., Chen, T., and Downton, J. 1997. Improved AVO fluid detection and lithology discrimination using Lame petrophysical parameters; "λρ', "μρ", & "λ/μ" fluid stack, from P and S inversions. *Expanded abstract presented at the 67th SEG Annual International Meeting, Dallas, Texas, 2-7 Nov 1997.*

Goodway, B. 2012. Microseismic: Monitoring induced seismicity. *Oral presentation given at the Microseismic User Group (MUG), Inaugural meeting, Canadian Society of Exploration Geophysicists. 28 Feb 2012.*

Hampson, D. P., and T. E. Rusell, 2005, Simultaneous inversion of pre-stack seismic data. *75th Annual International Meeting, SEG, Expanded Abstracts*, 1633–1637.

Hanks, T.C. and Kanamori, H. 1979. A Moment Magnitude Scale. *Journal of Geophysical Research* 84 (B5), 2348-2350.

Kidney, R.L., Zimmer, U., and Boroundmand, N. 2010. Impact of distance-dependent location dispersion error on the interpretation of microseismic event distributions. *The Leading Edge* (March), 284-289.

Kumar, V., C. H. Sondergeld, and C. S. Rai, 2012, Nano to macro mechanical characterization of shale. *Annual Technical Conference and Exhibition, SPE, Paper* SPE 159808-PP.

Maity, D., and F. Aminzadeh, 2012, Reservoir characterization of an unconventional reservoir by integrating microseismic, seismic, and well log data. *SPE Western Regional Meeting, Paper* SPE 154339.

Mayerhofer, M. J., E. P. Lolon, N. R. Warpinski, C. L. Cipolla, D. Waiser, and C. M. Rightmire, 2010, What is stimulated reservoir volume?. *SPE Production and Operations*, 89–98.

McGillivray, P. 2005. Microseismic and Time-lapse Seismic Monitoring of a Heavy Oil Extraction Process at Peace River, Canada. *CSEG Recorder*, 5, 5-9.

Noe, J. Microseismic Frac Mapping: Moving Beyond the Dots from an Engineering Perspective. 2011. *Oral presentation given at The OGS Shales Moving Forward Workshop, Norman, Oklahoma, 21 July* 2011.

Perez, M., D. Close, B. Goodway, and G. Purdue, 2011, Developing templates for integrating quantitative geophysics and hydraulic fracture completions data: Part I — Principles and theory. *81st Annual International Meeting, SEG, Expanded Abstracts*, 1794–1798.

Perez, R. 2010. Application of LMR inversion and clustering analysis in the Barnett Shale. *SEG Expanded abstract presented at the 80th SEG Annual Meeting, Denver, Colorado, 18-22 Oct 2010.*

Refunjol, X. E., K. M. Keranen, J. H. LeCalvez, and K. J. Marfurt, 2012, Integration of hydraulically induced microseismic events location with active seismic attributes: A North Texas Barnett Shale case study. *Geophysics*, 77, No. 3, KS1–KS12.

Shemeta, J. and Anderson, P. It's a matter of size: Magnitude and moment estimates for microseismic data. *The Leading Edge* (March), 296-302.

Takahashi, T., and S. Tanaka, 2010, Rock physics model for interpreting dynamic and static Young's moduli of soft sedimentary rocks, *IRSM International Symposium and 6th Asian Mechanics Symposium on Advances in Rock Engineering, New Delhi, India, 23-27 Oct 2010.*

Thompson A. M. 2010. *Induced Fracture Detection in the Barnett Shale, FT. Worth Basin, Texas*. MS thesis, The University of Oklahoma, Norman, Oklahoma, USA.

Warpinski, N. 2009. Microseismic Monitoring: Inside and Out. *J. Pet Tech* (November), 80-85. SPE-118537.

Yu, G., and R. Aguilera, 2012, 3D analytical modeling of hydraulic fracturing stimulated reservoir volume. *Latin American and Caribbean Petroleum Engineering Conference, SPE, Paper* SPE 153486.

© 2021 Universidad Nacional de Colombia – ISRM, ISSN 2805-6426 *Guillermo Alzate Espinosa (Ed.)*

Geomechanical Behaviour of Loro-Acaé Block in Putumayo Basin

Henry Arias[a]*, Oscar Bravo[b], Hernán Mantilla[a], Jefferson Mateus[a], Leonardo Alippio[a], Paula Silva[a], Alexander López[a], Juan Puerta[a], Néstor Saavedra[a].

[a]Ecopetrol S.A, Bogotá, Colombia
[b]Ecopetrol Contractor, Bogotá, Colombia
**Henry.Arias@ecopetrol.com.co*

ABSTRACT

In Putumayo basin at south of Colombia is located Loro-Acaé Block in an anticlinal structure lightly folded. Several vertical wells were drilled from 60's, achieved more than 10 thousand feet; currently, in the new campaign, wells are planned and drilled with high deviation angles (>30°) being a challenge related to wellbore stability in shale rocks of Orteguaza and Villeta formations and wellbore geometry issues in interbedded rocks of Pepino and Rumiyaco formations. Also, gas overpressures are detected in shales and limestones of Villeta formation can overcome 15 ppg increasing the challenge to drill these wells minimizing the risks associates to well kicks, mud cuts, pack offs, stuck pipe and losses. T Sandstone, member of Villeta formation, has the lowest fracture gradient in this formation. Using MW over 14 ppg to control gas and shales stability, a lot of times there were induced fractures in T Sandstone with mud losses and disequilibrium of hydrostatic column become mud cut and gas influx, and then, well control operations. A 3D pore pressure model was developed in Loro-Acaé Block in order to stablish lateral and depth variations in Rumiyaco and Villeta formations. This model is currently being used during well planning to determine risks associated with gas influx, and therefore, establish better well trajectories and adequate mud weight to avoid issues related with gas presence. An attack angle analysis in the well trajectories planning with critical displacements is done as well with the aim of improving the stability of fissile rocks (especially shales). A geomechanics real time monitoring has been done which has allowed avoid and/or mitigate drilling risks related to rock mechanical behaviour: wellbore stability across cavings morphology, rate and size analysis, minimum horizontal stress and fracture initiation gradient as limits of ECD, calculate or change the BHA trip speed, suggested circulation points to well cleaning while tripping, suggested changes in MW according to wellbore stability observed and controlling of casing setting points to isolate formations of different behaviours. The geomechanical analysis plays a fundamental role in this challenge since it allows solving the stress-strain problem in laminated rocks to determine their stability as well as the pore pressure behaviour of the fluids: water, gas and oil. This analysis helps establish the drilling phases, the mud densities to be used and the best well orientation to reach drilling success.

KEYWORDS

Rock behaviour, overpressure, attack angle, fracture gradient, gas influx, Putumayo basin

1. INTRODUCTION

In Loro-Acaé Block there are 39 drilled wells: 17 in Loro field, 15 in Acaé field and 7 in San Miguel field. Production of Vicepresidencia Andina y Occidente – Putumayo (including Área Sur and Área Occidente) is about 6.500 BOPD. Primary target is Caballos formation with a crude oil of 26 to 32° API, porosity between 3% to 10%, permeability 1.5 – 180 mD and a mechanism of rock-fluid and aquifer expansion. Secondary targets: Pepino conglomerates, Villeta N Sandstone, Villeta A Limestone and Villeta T Sandstone.

Eight deviated wells were drilled by Ecopetrol from 2018 to 2020. The principal challenge was Loro-16 well with over 7.000 ft of vertical section, almost 13.000 ft MD, with the highest overpressure in Villeta formation (MW used 16.3 ppg). This well had one side-track caused by stuck pipe, MPD system

to drill production section and 121 days of drilling operations. Several lessons learned were given by this well and applied in planning and execution of new wells with success.

Abnormal pore pressure distribution and borehole instabilities contribute to the majority of the loss times and well complexities. A sufficient mud overbalance with respect to the pore pressure avoids the influx possibilities but cannot ensure a stable wellbore. Therefore, collapse pressure estimation is important to understand the minimum downhole fluid pressure gradient to prevent compressive wellbore failures (Agbasi et al., 2021). Wellbore collapse frequently occurs during oil and gas drilling, and therefore it is treated as the most important problem for the drilling safety. The pressure difference between the formation pore pressure (or collapse pressure) and the fracture pressure (or leakage pressure) is called the safety pressure window (Xie et al., 2021). Pore pressure and wellbore failures are considered the most critical drilling challenges. If uncontrolled, it can lead to well abandonment. Significant non-productive times (NPT) are usually associated with these issues. Various geological processes (such as sedimentation, compaction, tectonic processes, erosion), rock mechanical strength and petrophysical properties (porosity, permeability, density) control the pore pressure distribution and in turn impacts on the stability of borehole walls (Baouche et al., 2020). Incorrect prediction or the absence of pore pressure evaluation can lead to severe damage of the rig, loss of personnel, waste of resources and environmental pollution. Predicting pore pressure in 3D reveals lateral variations in subsurface pressure which normally, are caused by structural, stratigraphic and or other depositional tendencies in basin development (Abbey et al., 2020).

Layered rocks such as shales often exhibit different properties along or across bedding planes. Elastic properties like bulk modulus, Young's modulus and Poisson's ratio, show directional properties. The same can be concluded for compressive and tensile rock strength (Aadnoy et al., 2009). Shale formations, due to the presence of laminations and weak planes, exhibit directional strength characteristics. In most conventional wellbore stability analyses, rock formations are typically assumed to have isotropic strength (Lee et al., 2012). In this paper, the attack angle of the formations drilled was taken into account in a qualitative point of view. The well inclination and azimuth were compared to dip and dip azimuth of the formations. According to the attack angle and relative orientation of the well, the trajectory of the well is classified as updip, downdip or crossdip. The mechanical behaviour of Cretaceous formations like Villeta in Putumayo basin are controlled by bedding planes. Cuantitative evaluations made in closed areas have shown very high mud weight to control the bedding failure. Both field experience and laboratory evidence from cylinder collapse tests, indicate that hole instability is not a problem when drilling normal to bedding but becomes very serious when the hole is parallel or very nearly parallel to bedding (Okland & Cook, 1998).

Loro field has been drilled from the 60´s in different campaigns. The times employed to drill the wells varies from 30 to 220 days with an average of 70 days. The well that took more time to be completed presented issues associated to mud losses and influx simultaneously. During the drilling of this well mud cuts were presented in the intermediate section and it was necessary to control the well with a mud density of 15.2 ppg. Differential sticking is also a common issue in sandstones due to high mud density used to control the formation pressures. Stuck pipe is also a big problem in Villeta formation due to instability associated to overpressures. Often, the remedial action is to increase mud density but this caused severe mud losses and the stability problems became bigger. In the last wells some problems were overcome by implementing drilling technologies. Modern analysis like 3D pore pressure in the planning phase and real time wellbore stability analysis while drilling were implemented to enhance the quality of the information to detect variables deviations from the normal parameters. The target of the implementation of modern analysis is to answer questions not answered up to date. This article presents how those analysis has been addressed and the obtained results.

2. LITHOLOGY AND GEOLOGICAL STRUCTURE

Putumayo basin is located at the south of Colombia (Figure 1). This basin corresponds to a sedimentary sequence with a high lithological heterogeneity. Rock formations include ages from Cretaceous to Neogene, and even Quaternary deposits. Jurassic igneous is reached at the end of the well. Wells drilled

in the Loro-Acaé Block (Figure 1) show initially surface deposits of boulders and pebbles of igneous and metamorphic rocks (coming from Macizo Colombiano). Then, Orito-Belén formation with a a monotonous sequence of siltstones, claystones, some sandstones, and some anhydrites interbeddings. Claystones of this formation could be chemically unstable. Next, Orteguaza formation composed by shales and several sandstone and coal interbeddings, and Pepino formation with two conglomeratic bodies (Upper and Lower) separated by claystones.

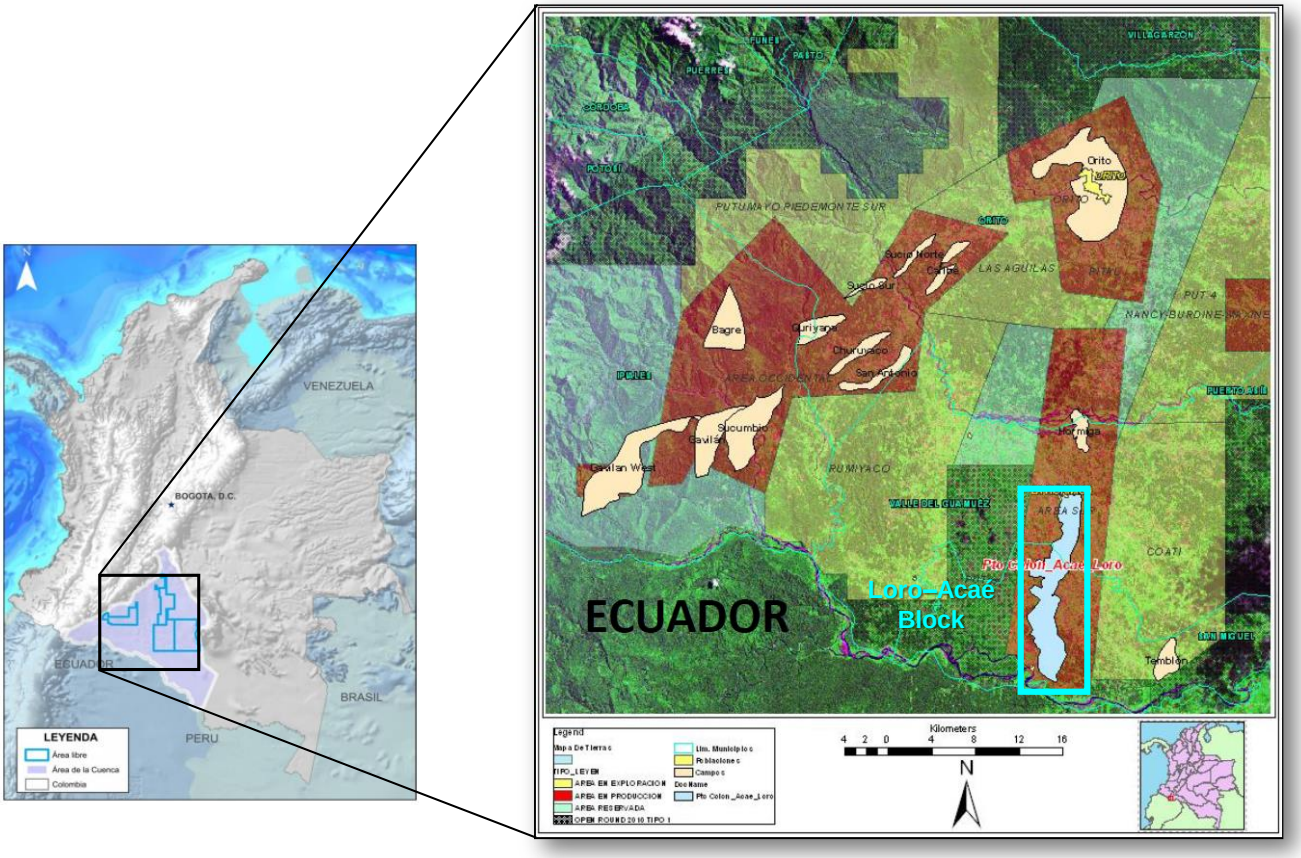

Figure 1. Putumayo basin (left) and Loro-Acaé block (right) location.

Continues the Rumiyaco formation composed by a sequence of claystones and siltstones, and then, Villeta formation (Cretaceous) made by shales with interbeddings of limestones and some sandstones with hydrocarbons. It is common to find high overpressure of gas in Villeta formation that can sometimes exceed 14 ppg, controlled using MW over 15 ppg. Target zone is Caballos formation composed by sandstones with hydrocarbons at normal pressure (8.3 ppg) with several shales interbedded. Figure 2 shows the stratigraphic sequence of Putumayo basin.

The geological structure of the Loro-Acaé Block is an anticlinal slightly folded whit dips no higher than 10°. Structure is elongated at North, limited at East by a reverse fault which affects the Jurassic rocks and the Cretaceous rocks of Caballos and Villeta. Figure 3 shows the structural map at Caballos formation top.

3. DRILLING EVENTS RELATED TO DRILLED WELLS

Drilling events are frequently related to heterogeneity of lithology (See Title 2). Deviated wells over 30° generate important events of packoff / stuck pipe with lost in hole and side-tracks. Several tight spots are presented while tripping forcing reaming and backreaming practices. Sometimes, tight spots lead to packoff attempts, rotary strikes, erratic/high torque and difficult hole cleaning conditions.

Tabular/blocks cavings are common because of laminated rocks instability (shales of Orteguaza and Villeta formations). Also, it is very common to observe reworked cavings,

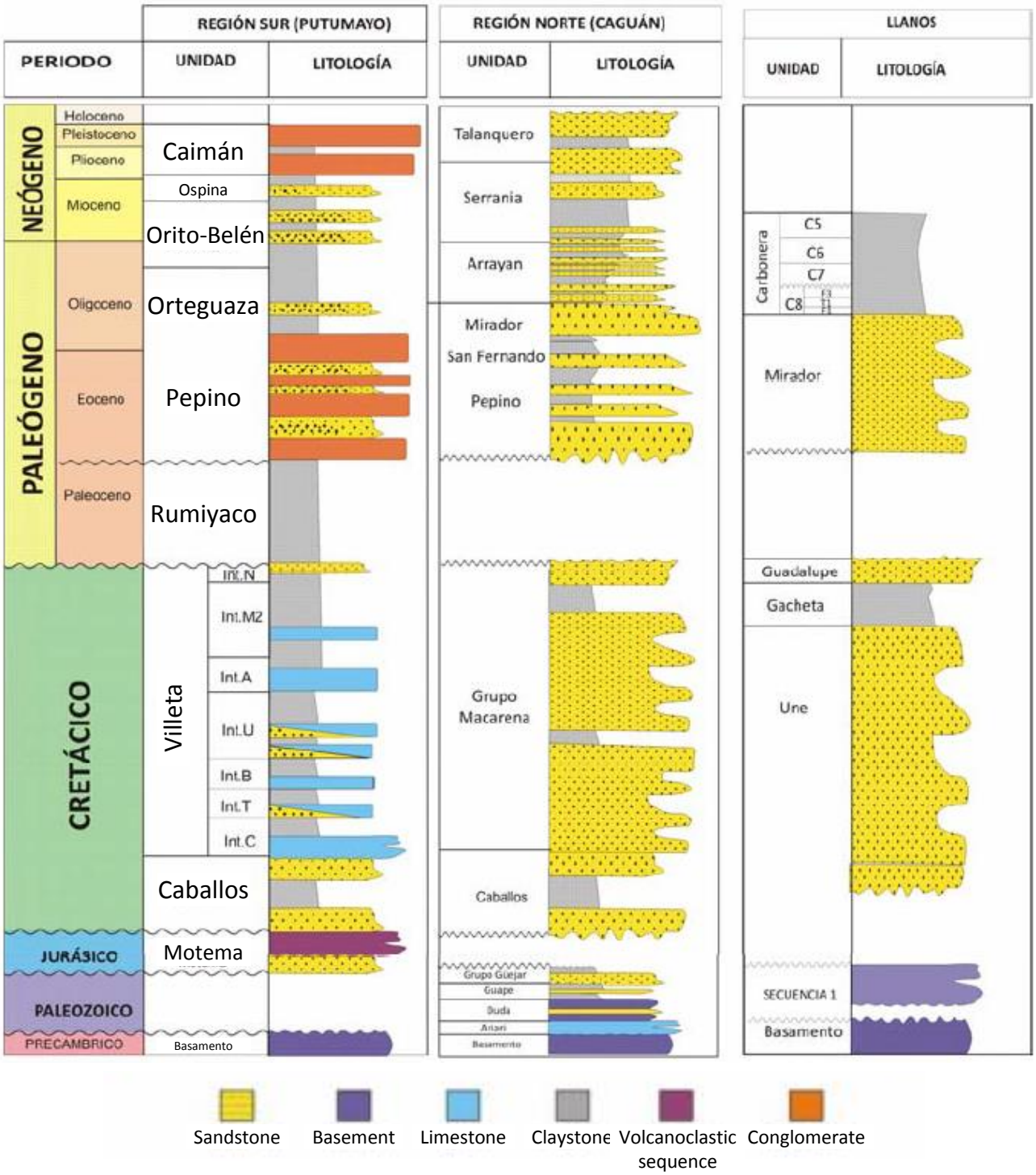

Figure 2. Chronostratigraphic column of Putumayo basin zones. Left: Putumayo; Middle: Caguán; Right: Llanos. Modified from Gems, 2008.

Gas cut mud and gas influx were presented while drilling and/or tripping in Villeta formation when the mud weight was not high enough. Most of times well control operations were done increasing MW up to 15 ppg or more to kill the well.

Some mud losses occurred near to surface (unconsolidated deposits), in Pepino´s conglomerates and/or in Caballos formation sandstones (reservoir zones) due to seepage into high porosity/permeability

rocks/deposits. Also, in T Sandstone of Villeta formation is common generate drilling induced tensile fractures while drilling, usually when MW is over 14 ppg. An underbalanced in the hydrostatic column due to mud losses in T Sandstone while drilling or running casing generated mud cut, leading to well control operations. When drilling Loro-16 ST well at Villeta formation, it was necessary to use a mud density of 16.3 ppg to control gas presence/influx, and the casing was set at T Sandstone to avoid induced fractures and mud losses. After that, Villeta T and C were drilled in the same section with Caballos formation (target) using MPD system with maximum MW of 11 ppg.

Another common event related to Villeta overpressure is the gas influx from Villeta C (base of Villeta formation). MW is decreased to drill production section (Caballos formation) after casing cementing and drillout. A gas influx could lead to well control operations if Villeta C unit is not covered completely by an intermediate casing.

Finally, Caballos and Motema (Jurassic igneous) formations can be drilled with MW close to 9 ppg. No big issues are presented in this section. In San Miguel-11 well, a water influx was coming in Upper Caballos formation due to water injection operation done in San Miguel-5 well, located about 650 ft (at Caballos deep). MW for kill the well was 11.0 ppg.

Figure 3 shows the mud weight used in Villeta formation to control gas influx in Loro-Acaé Block. In the south zone of Loro field (e.g., location of Loro-16 well) is the biggest overpressure observed in Villeta formation (about 14.3 ppg) using MW of 16.3 ppg to gas control. San Miguel field and the northern part of Acaé field has the lowest pressure observed to date in the field with pore pressure gradient close to 11.3 ppg.

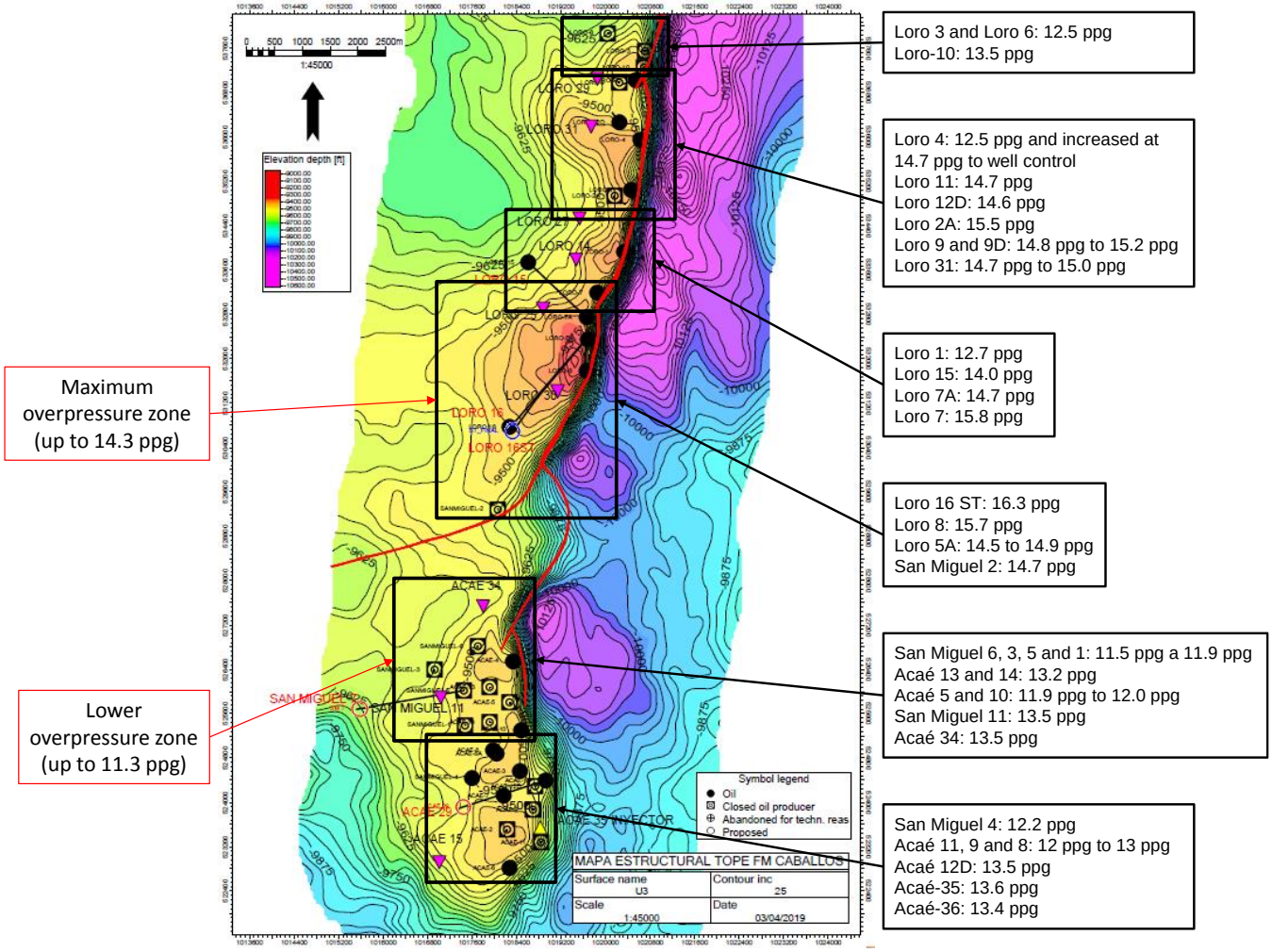

Figure 3. MW used in Villeta Formation along Loro-Acaé Block to control gas influx and wellbore stability.

Figure 4 contains drilling events of Loro 12D well as an example of Loro-Acaé block. Most of tight spots were presented in Orito-Belén formation. Stuck pipe occurred in this formation may be a pack off due to unstable and reactive claystones. Tight spots and stuck pipe in Pepino formation were caused by stepping between claystones and conglomerates. Some tight spots were presented in Rumiyaco formation due to well deviation higher than 30° (note the caliper enlargement in this formation).

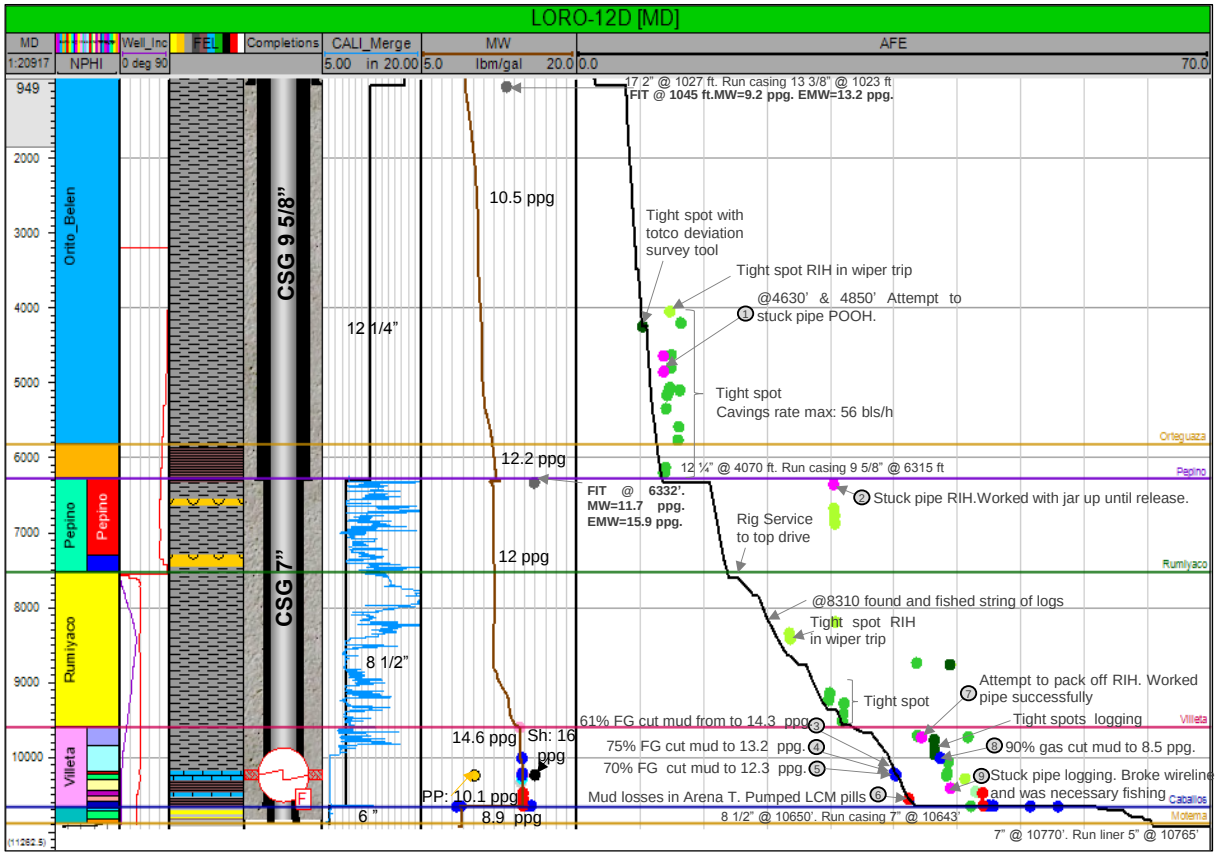

Figure 4. Drilling events presented in Loro-12D well

Figure 5 indicates drilling events occurred in Villeta formation at Loro-12D well. Some gases were presented in Villeta M2 and Villeta A Limestones with mud cut. Mud losses were presented in T Sandstone of Villeta formation while drilling and running casing with MW 14.7 ppg (MiniFRAC in T Sandstone Loro-11: closure pressure gradient 14.4 ppg). Mud cut in T Sandstone can be by an underbalanced in the hydrostatic column due to mud loss. Restrictions were presented running electrical logs in 8 ½" section.

Figure 6 shows the events related to drillout. Mud cut after mud losses while running the casing can be related by an underbalanced in the hydrostatic column. Gas influx presented in Villeta C unit occurred because casing did not cover completely this unit and MW was decreased till 8.8 ppg (casing settlement point). Finally, Figure 7 presents an overview of drilling events occurred in Loro-Acaé block.

4. MUD WEIGHT WINDOW

The mud weight window was built from sonic, density and porosity logs run in different wells drilled in Loro-Acaé block. This information allowed to represent the main drilling events that occurred in this sector of the Putumayo basin. Figure 8 to Figure 10 show the mud weight window built for planning and drilling Loro-31 well.

The main drilling risks at surface sections (26" and 16") are gumbo and bit balling in Orito-Belén formation (e.g., Loro-11), surface losses into non-consolidated deposits (e.g., Acaé-11), tight spots while tripping in Orito-Belén formation (e.g., Loro-9D, Loro-11 and Loro-12D with MW 10.0 ppg to 11.5

ppg), undergauge hole in Lower Orito-Belén by chemically reactive claystones (e.g., caliper of Loro-3 with MW 10.2 ppg), stepping and tight spots in Middle Orteguaza formation caused by interbedding of sandstone and coal with shale (e.g., Loro-12D) and packoff by shales failure (e.g., Loro-5A) with MW 11.2 ppg to 12.2 ppg in Orteguaza formation.

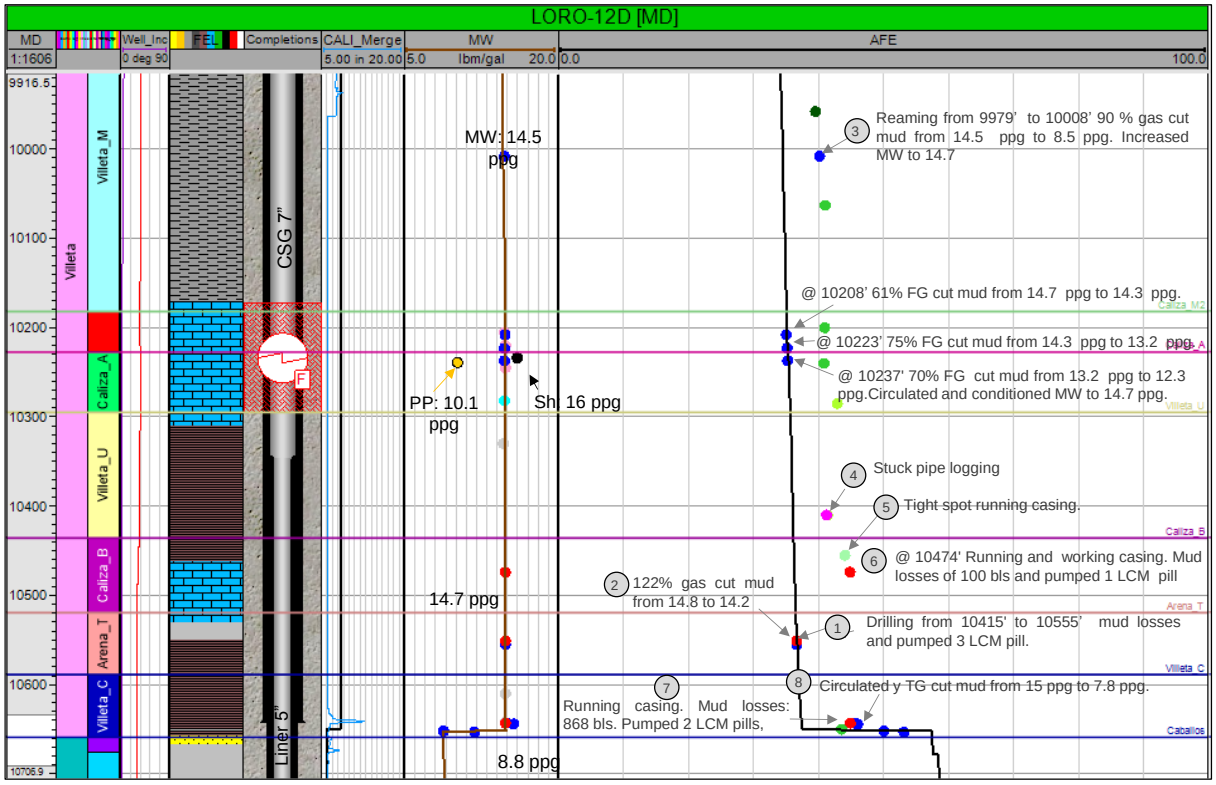

Figure 5. Drilling events presented in Loro-12D well, Villeta formation.

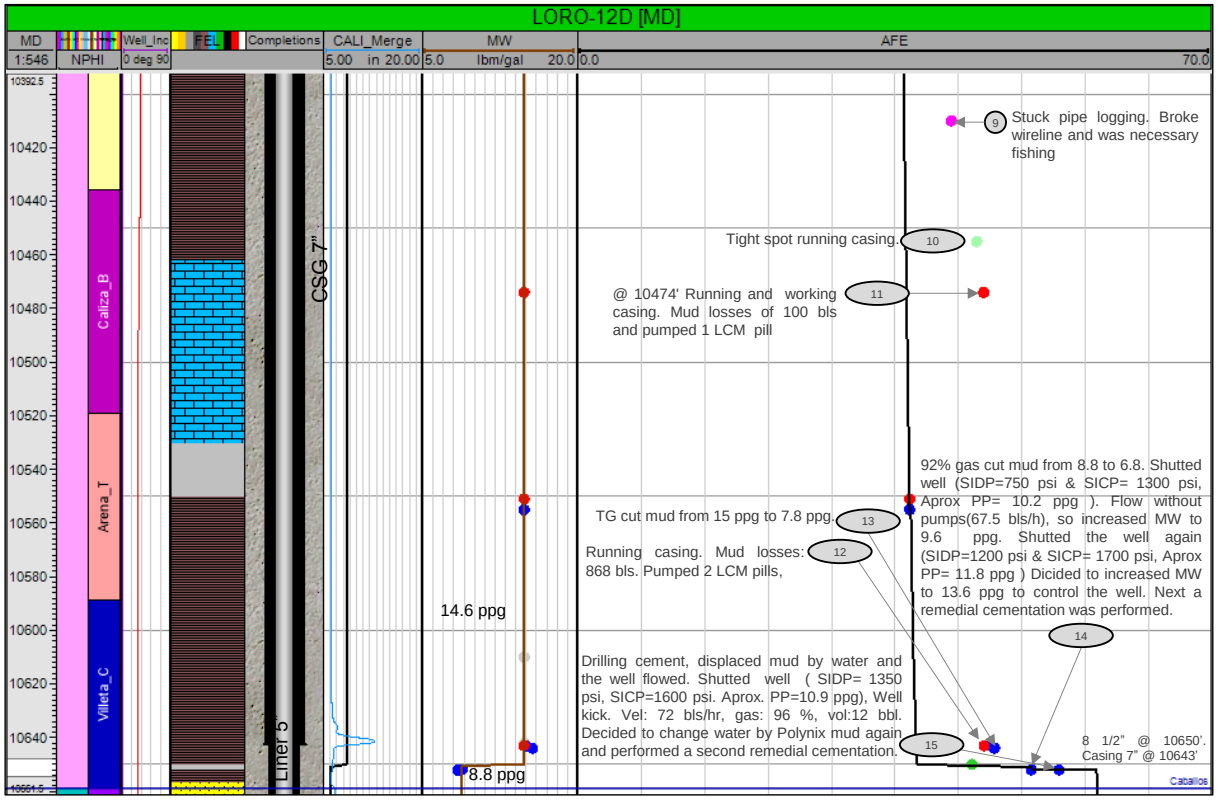

Figure 6. Drilling events presented in Loro-12D well, drillout Villeta – Caballos formations.

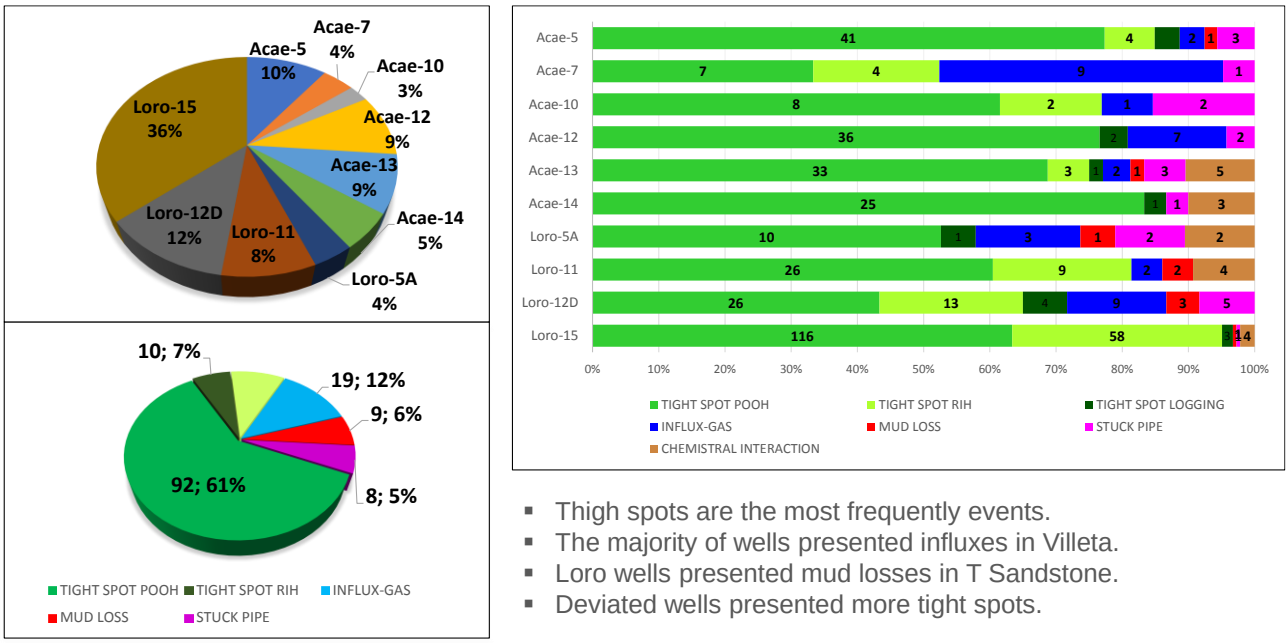

Figure 7. Drilling events overview in Loro-Acaé block.

Recommendations from geomechanics modelling to avoid or mitigate these drilling risks (Figure 8) includes the use a mud weight from 9.5 ppg to 11.7 ppg and the use semi-dispersed mud to drill Orito-Belén. Control of drilling parameters and mud properties when drilling Orteguaza to improve borehole condition and cleanliness, and the use of shale stabilizers, asphalt/graphite in this formation.

Figure 9 shows drilling risks for 12 ¼" intermediate section related to borehole enlargement in claystones of Pepino and Rumiyaco formations (Figure 9). Clay solubility was measured from 25% to 50 % (e.g., Loro-15 and Acaé-34). Tight spots (e.g., Loro-5, Loro-9, Loro-9D, Loro-11 and Loro12-D) and geometrical stuck pipe (e.g., Loro-12D) in Pepino´s conglomerates with MW from 10.0 ppg to 12.5 ppg. Differential stuck in Lower Conglomerate with MW 14.8 ppg (e.g., Loro-9D). Tight spot in Rumiyaco formation: Loro-12D with MW from 12 ppg to 13.5 ppg (wellbore deviation 30°), in Loro-9 with MW 11 ppg to 12.5 ppg, in Loro-9D with MW 11 ppg, in Loro-11 with MW 12.4 ppg. Stuck pipe in Rumiyaco formation (e.g., Loro-9 well with MW 11.0 ppg increases to 12.5 ppg). Continuous stucks forced a sidetrack drilled with 13.3 ppg. Hole tortuosity in Rumiyaco due to wellbore enlargement caused by soluble clays (in Loro-9D the wellbore reached up to 18" and in Loro-12D it exceeded 20"; BS = 8 ½"). The recommendations for this section include the use MW from 12.2 ppg in Pepino formation to 13.1 ppg in Rumiyaco formation. Also, filtrate control in Pepino´s conglomerates to avoid differential sticking risk. Additionally, well circulation while tripping before reaching the conglomerates. Lastly, use a non-dispersive mud to mitigate clay solubility.

Figure 10 shows operational window for 8 ½" and 6" production sections. Principal drilling risks are related to gas presence in Villeta: formation gas from M2, A, B and C Limestones, cut mud weight, mud losses in T Sandstone by induced fracture (e.g., Loro-15 MW 14.0 ppg, Loro-9D MW 15.2 ppg, Loro-11 MW 14.7 ppg, Loro-12D MW 14.8 ppg), differential sticking in T Sandstone (e.g., Loro-9D MW 15.2 ppg), wireline stuck in Villeta U Shale (e.g., Loro-12D MW 14.8 ppg), tight spots, high torque and overpull while tripping and casing running by interlayered shales, limestones and sandstones in Villeta formation, gas influx from Villeta C while drillout with MW about 9 ppg (e.g., Loro-9D, Loro-11 and Loro 12D) and mud losses in Caballos while well control operation (e.g., Loro-9D MW 14.0 ppg).

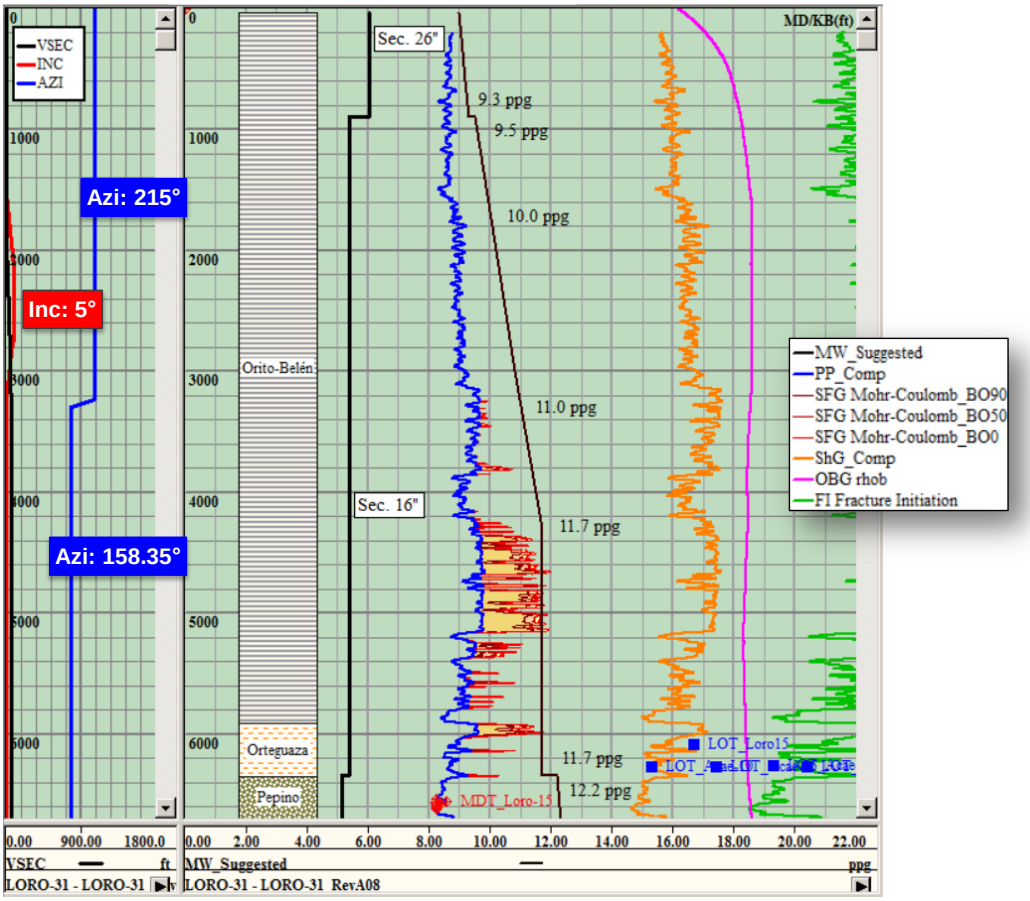

Figure 8. Mud weight window for surface sections (26" and 16").

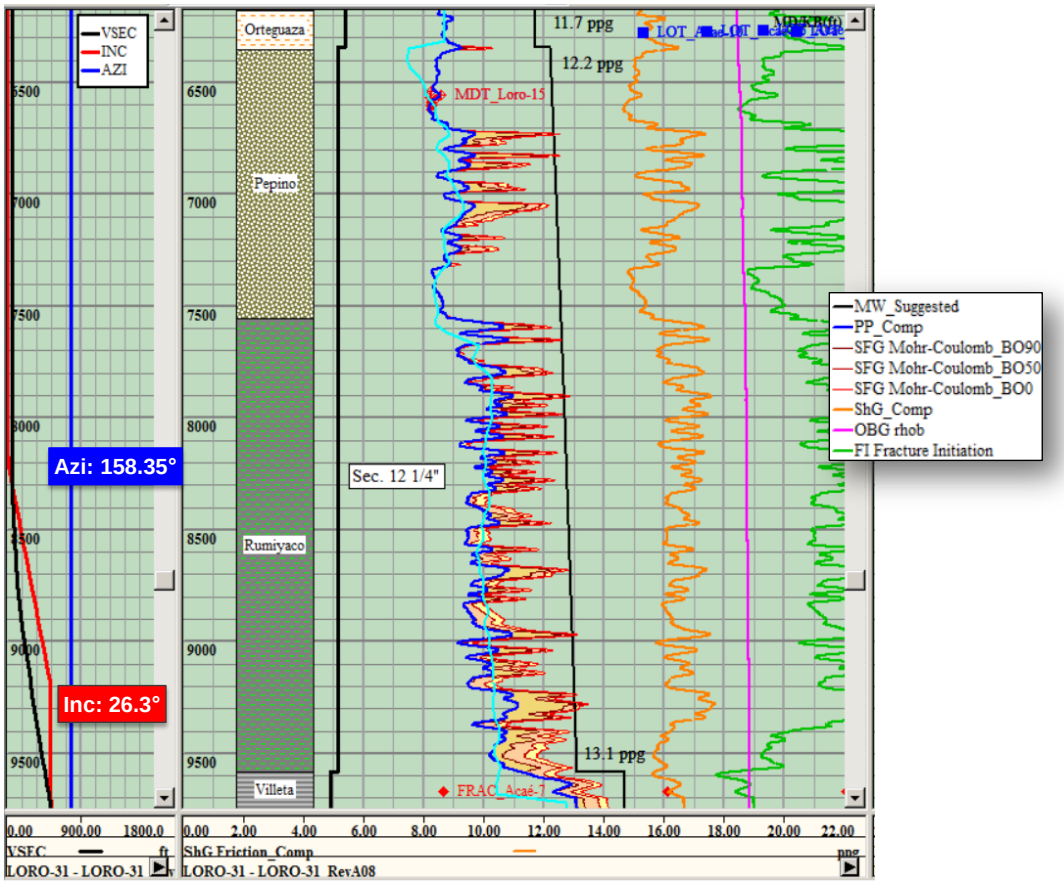

Figure 9. Mud weight window for intermediate section (12 ¼").

The recommendations for 8 ½" section (Villeta formation) include the use 14.7 ppg to control gas presence and shales instability (high attack angle up to 47° updip), filtrate control and shale stabilizers (graphite/asphalt). If cavings rate is over 3 bbl. /hour, it is necessary to increase MW to 14.8+ ppg. Also, it is necessary to set 7" Liner at least 10 ft within Caballos formation to avoid gas influx from Villeta C. Due to Villeta formation has a narrow window with high pore pressure (e.g, gas) and low fracture gradient (e.g., T Sandstone), it is required to consider a dynamic stress cage for T Sandstone, preventive LCM pills and to maximize drilling practices that allow an ECD under control. Also, in 6" section (Caballos formation) requires MW 9.2 ppg and filtrate control to minimize formation damage. Finally, it is recommended to increase MW up to 9.5 ppg in case of rock instability.

An attack angle analysis and a trajectory sensitivity analysis were done to define the optimum mud weigh to use in each drilling section, in addition to the calculation of the collapse gradient. Attack angle analysis includes well trajectory and dip direction & dip of formation beddings. Attack angle is defined as the resultant between normal vector to bedding plane and well trajectory vector. Values over 30° of attack angle are usually critical for stability in fissile rocks (e.g., shales). Updip, crossdip and/or downdip conditions are also evaluated.

Figure 11 is an example of attack angle analysis. Attack angle in Orteguaza shales is less than 5° up dip condition. However, it is recommended to use 11.7 ppg and mud properties control to improve cleanliness borehole condition (mud rheology). Villeta formation has an attack angle becomes critical (e.g., Villeta U Shale) with values from 23° to 47° updip condition. Recommendations include mud density of 14.7 ppg and filtrate control in Orteguaza shales. Lastly, increase MW to 14.8+ ppg in case of borehole instability.

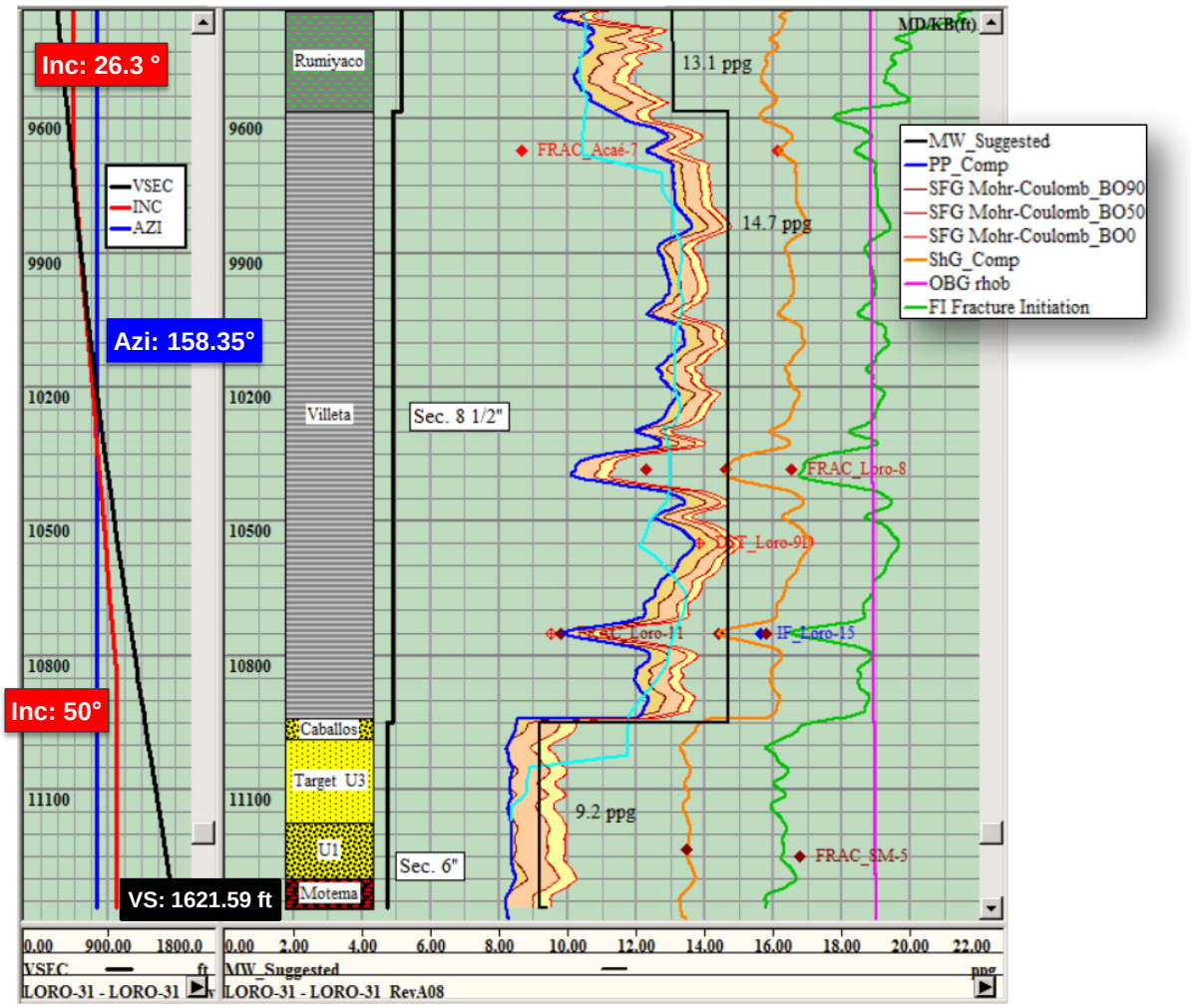

Figure 10. Mud weight window for production sections (8 ½" and 6").

Formation / Well LORO-31 RevA08	Well		Bed		Attack Angle	Relative Orienta-tion	Condition
	Incl	Azim	Dip	Dip - Azimuth			
ORTEGUAZA	0.0	158.4	3.5	370.0	3.49	328.35	Up-Dip
PEPINO	0.0	158.4	3.5	360.0	3.49	338.35	Up-Dip
RUMIYACO	0.0	158.4	3.5	370.0	3.49	328.35	Up-Dip
VILLETA	26.3	158.4	3.5	370.0	23.41	328.35	Up-Dip
CABALLOS U4	50.0	158.4	3.5	370.0	47.04	328.35	Up-Dip
MOTEMA	50.0	158.4	3.5	370.0	47.04	328.35	Up-Dip
TD	50.0	158.4	3.5	370.0	47.04	328.35	Up-Dip

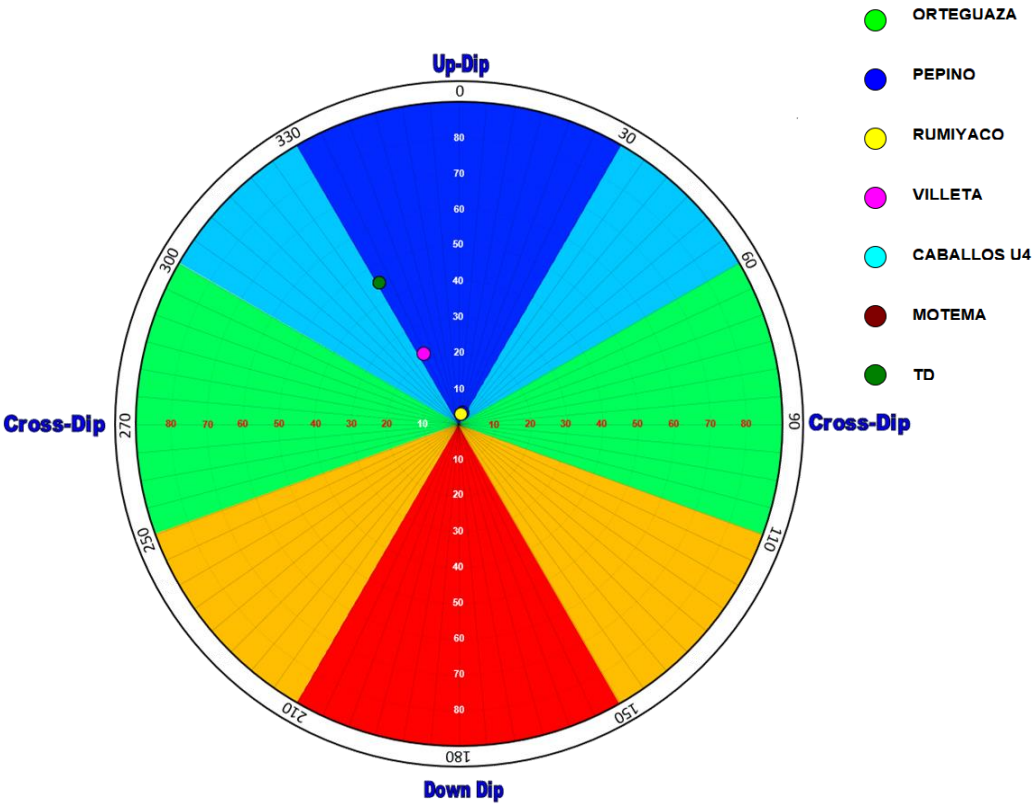

Figure 11. Example of attack angle analysis in Loro-Acaé block.

Figure 12 displays sensitivity analysis of well trajectory related to rock collapse to establish required MW to achieve enough stability for a breakout width of 50°. Likewise, Figure 13 shows a sensitivity analysis related to induced fracture performed in Villeta T Sandstone and Caballos Sandstones. These values were calibrated with induced fracture of Loro-15, MiniFRAC of Loro-11 and MiniFRAC of San Miguel-5 wells. ECD maximum allowed in 8 ½" sections is 16.5 ppg, it means, maximum MW of 14.8 ppg.

Figure 12 and 13 illustrate the maximum horizontal stress azimuth of 114°. This direction was stablished from breakouts analysis of Loro-9D, Acaé-6 and Acaé-9 wells, and fracture induced in T Sandstone of Loro-15 well. The mean value of SH is 114° ± 9°. It was compared with World Stress Map (Database Release 2016. GFZ Data Services. http://doi.org/10.5880/WSM.2016.001).

Orteguaza @5.990 ft MD

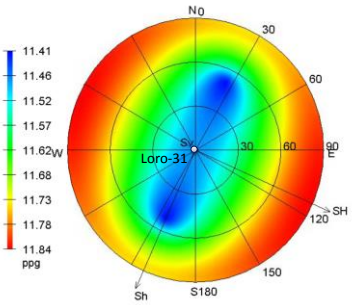

Inc: 0° Azi: 158.37
MW Required: 11.5 ppg
Maximum wade breakout allowed: 50°

Rumiyaco @9.295 ft MD

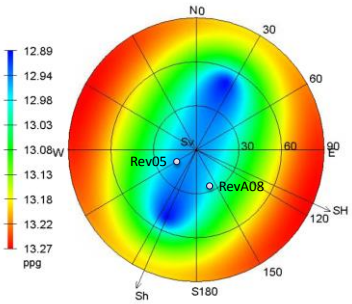

Inc: 26.33° Azi: 158.35
MW Required: 13.0 ppg
Maximum wade breakout allowed: 50°

Villeta U @10.550 ft MD

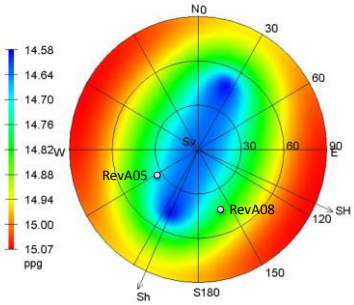

Inc: 43.91° Azi: 158.35
MW Required: 14.8 ppg
Maximum wade breakout allowed: 50°
(14.7 ppg BRKT 60°)

Figure 12. Sensitivity analysis of collapse.

Villeta Arenisca T @10.750 ft MD

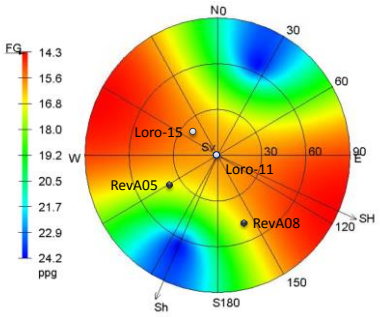

Inc: 47.97° Azi: 158.35°
ECD maximum allowed: 16.5 ppg

Fl Loro 15: 15.67 ppg (24°/314°)
FRAC Loro-11: 15.8 ppg (vertical)

Caballos @11.245 ft MD

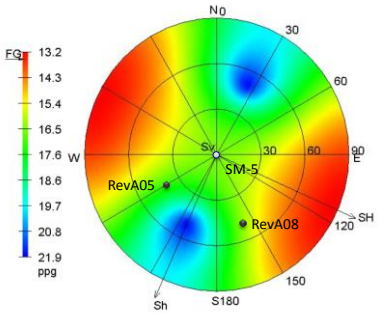

Inc: 50° Azi: 158.35
ECD maximum allowed: 16.2 ppg

FRAC SM-5: 16.73 ppg (vertical)

Figure 13. Sensitivity analysis of induced fracture.

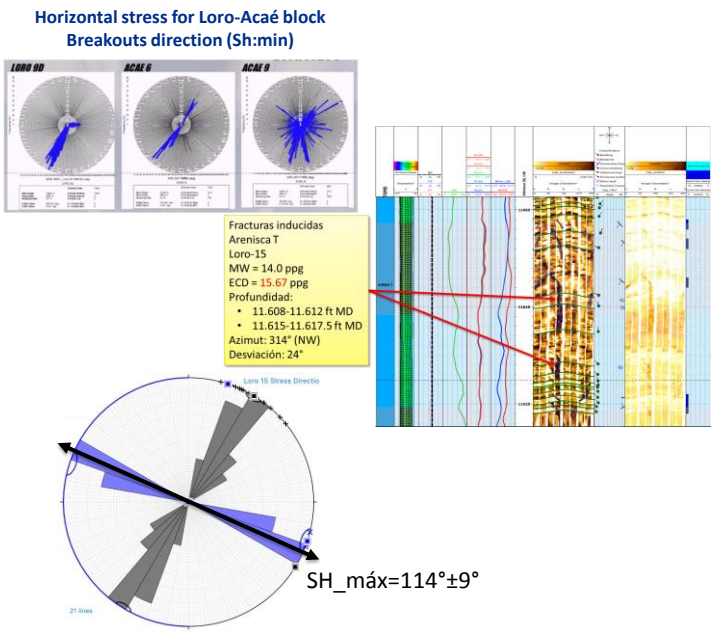

SH_máx=114°±9°

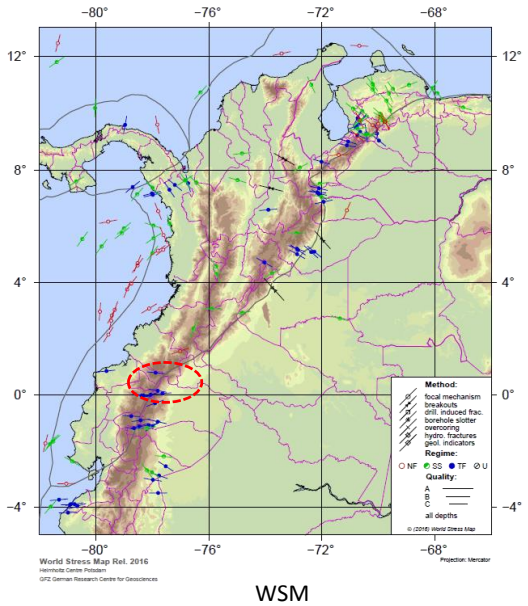

WSM
SH_máx: 94° ± 5°

Figure 14. Maximum horizontal stress direction for Loro-Acaé block.

5. 3D PORE PRESSURE MODEL

A 3D pore pressure model was developed in Loro-Acaé Block to stablish lateral and depth variations in Rumiyaco and Villeta formations. This model is currently being used during well planning to determine risks associated with gas influx, and therefore, establish better well trajectories and adequate mud weight to avoid issues related with gas presence.

Figure 15 illustrates 3D pore pressure calculation for Loro-Acaé block considering lithology types. For claystone formations was used methodology proposed by Eaton in 1975. The compaction train and the exponents identified and calibrated were used during the estimation of 1D pore pressure in the wells (upper image of Figure 15). For conglomerates and sandstones of the Pepino and Caballos formations were assigned a hydrostatic pressure and calibrated with pressure tests measurements and drilling events. For non-claystone zones of Villeta formation (e.g., limestones and sandstones) the pressure was estimated from correlation generated between the response of the P wave and the effective vertical stress at depths where there were measured pressure data (middle image of Figure 15). Finally, the 3D pore pressure volume is illustrated in the lower image of Figure 15.

Due to the pressure differences in Villeta formation between Loro, Hormiga, San Miguel and Acaé fields (identified through measured pressures and analysis of drilling events), it was necessary to perform a sectorization (e.g., Loro field) taking into account the geological structure (faults and folds) and different exponents application for Eaton's equation (Figure 16).

Figure 17 shows pressure heterogeneities with depth in the different formations. Pepino formation presents normal pressures ranging from 8.3 to 9.4 ppg. In claystones and siltstones of Rumiyaco formation (seal rocks of Villeta formation) the pressures range between 9.4 and 10.8 ppg. In Villeta formation the pressures vary both in depth and area from 9 ppg to 13.5 ppg in some sectors of Loro-Acaé block. Finally, Caballos formation shows normal pressure.

Figure 18 at left shows a cross section with the pressure variations of the upper units of Villeta formation (from N Sandstone to B Limestone) which range between 9 and 11.5 ppg for Acaé and Hormiga fields and from 10 ppg to 13.5 ppg for the Loro field. In right hand illustration the pressure observed in Villeta T Sandstone and Villeta C Limestone units are slightly lower than the other units of Villeta formation (9 to10.5 ppg).

There is a good match of the pore pressure profile extracted from the 3D Volume with the pore pressure curve from 1D modeling shown in Figure 9 and Figure 10 as a blue bright curve. However, in some areas there is a variation which is due to the differences between the inversion sonic log response and well original sonic log.

6. REAL TIME WELLBORE STABILITY ANALYSIS

Figure 19 is an example of a real time geomechanics monitoring event in the Acaé-34 well. The methodology for a real time monitoring includes a direct connection with the drilling rig established through communication protocol WITS0. Most of the operations data is received by Ecopetrol's EcoAge® software. This data capture includes: drilling parameters, drill bit position, operational events, cavings data log, cavings size and morphology, lithological log (formation evaluation log), survey, mud weight and ECD, MSE (mechanical specific energy), mud rheology, LWD logs and any additional information from different logs available in .LAS or .TXT formats containing variables based on time and depth (Mantilla, Saavedra, Arias and Osorio, 2019). Figure 19 shows an EcoAge® visual interface of a trip in an interval of the Rumiyaco formation. The tight spots events are often while put out of hole (POOH). The backreaming operation generates or increases the cavings production due to mechanical impact on shale intervals. It increases the rate of reworked morphology cavings. Based on that the real time suggestion is circulate out (bottoms-up) to clean the well avoiding a stuck pipe incidents. Run in hole (RIH) was a faster trip than previous POOH.

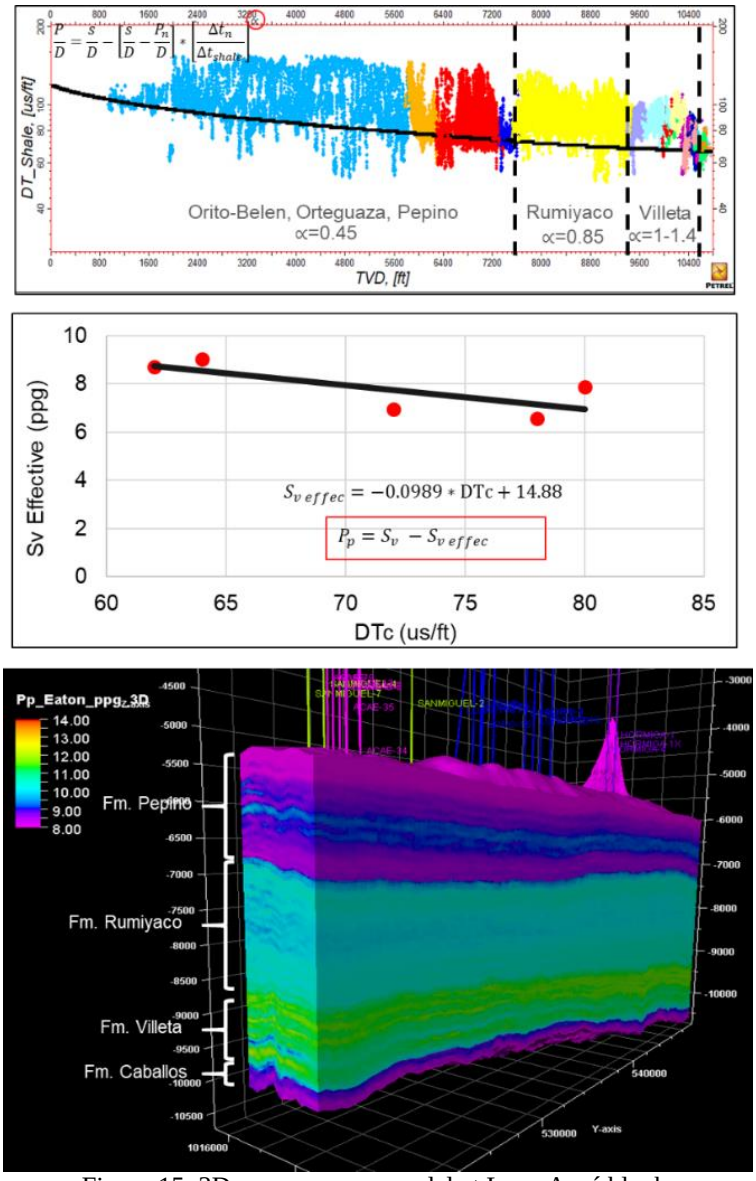

Figure 15. 3D pore pressure model at Loro-Acaé block.

Eaton exponent calculation (1.4) for a compartment of Villeta formation, Loro field

Eaton exponent calculation (1.0) for Acaé and Hormiga fields

Figure 16. Pore pressure in A Limestone, Villeta formation.

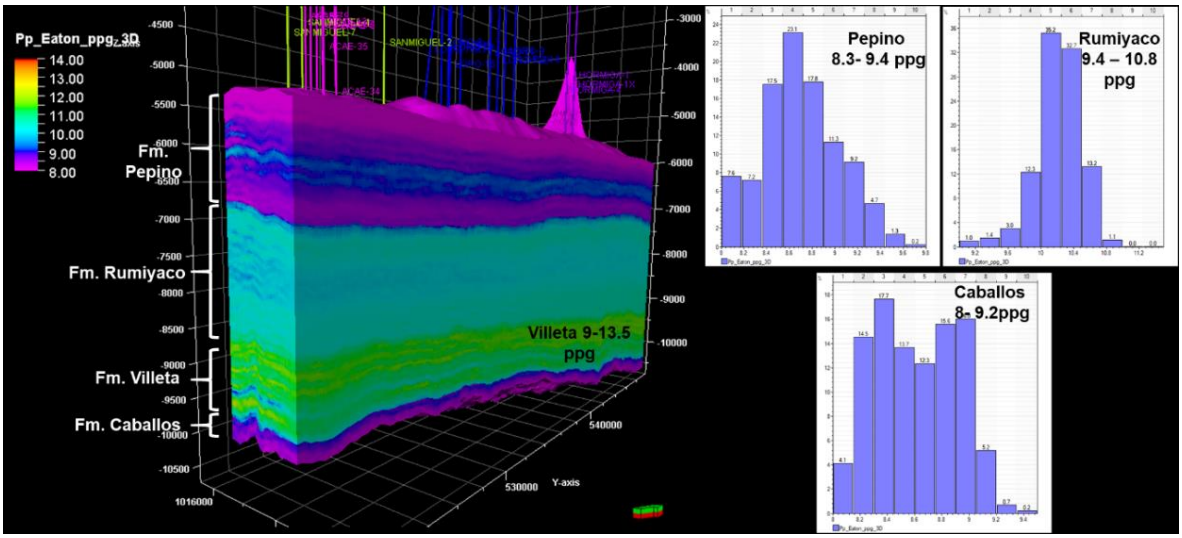

Figure 17. Magnitudes of pore pressure by formation at Loro-Acaé block.

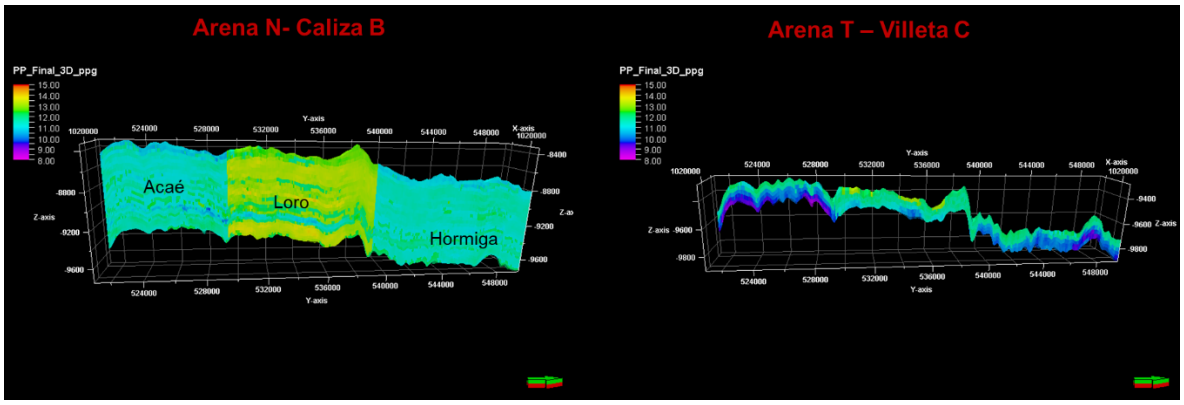

Figure 18. Pore pressure for [N Sandstone – B Limestone] and [T Sandstone – C Limestone] Units.

Figure 19. Example of real time geomechanics monitoring Acaé-34 well.

7. CONCLUSION

Although the Putumayo Basin is a passive basin with soft folding and dips that do not exceed 5°, there are multiple drilling problems related to lithological heterogeneity and strong gas overpressures (e.g., Villeta formation).

Due to the mineralogical composition of the Orito-Belén formation (high claystone content) it is advisable to drill it with a high HSI so that the hydraulic impact helps to enlarge the wellbore and the casing can be run without major inconveniences. Preferably use a native mud. This formation has a time-dependence behaviour.

Shales of Orteguaza formation are often susceptible at wellbore deviation. When it exceeds 20° these shales gradually decrease in stability. Therefore, the mud density to be used in Orteguaza must be determined according to well deviation and orientation. It is advisable to use filtrate control in these shales to help mitigate their instability. An adequate and constant mud weight to drill this formation will help mitigate stepping due to shale enlargement interbedded with sandstones and coals.

Drilling parameters must be controlled before reaching Pepino´s Conglomerates to prevent the sudden impact of the drill bit on this competent rock. It could damage its structure and impede its correct operation.

Circulations in the claystones near to the conglomerates should also be avoided to prevent the enlargement effect caused by hydraulic impact. It is advisable to drill the Villeta Formation with constant mud weight (as proposed in Orteguaza formation too) to prevent pressure variations caused by the drilling fluid on the rock. It could destabilize these shales.

For the Loro field a mud weight from 14.0 ppg to 14.8 ppg would help mitigate the risk related to gas influxes. However, the most appropriate MW to gas control will need to be evaluated while planning and drilling stages well by well.

It is not advisable to drill Pepino and Villeta formations in the same section. Villeta requires high mud weight to control instability and gas influxes. Pepino´s conglomerates have a fracture gradient and minimum horizontal stress gradient relatively lows. So, there would be a risk of fracturing them and inducing total drilling fluid losses and therefore well control problems. As well as its high permeability it is possible generate a differential sticking in these conglomerates.

In Caballos formation (zone of main reservoirs) no major problems are expected while drilling and a mud weight about 9 ppg should be enough to control wellbore stability.

ACKNOWLEDGEMENTS

A lot of people have participated in this project. Thanks to Ecopetrol for sharing the information to publish this work. Special thanks to Reinel Corzo, Paola Charry, Andrés Calle, Katherine León & Edgar Cáceres (Instituto Colombiano del Petróleo – Ecopetrol), Nelly Rubio (Vicepresidencia No Convencionales – Ecopetrol) and Francisco Cuervo, José Mondragón & Ignacio Acosta (Ingeniería de Perforación Vicepresidencia Área Sur – Ecopetrol).

REFERENCES

Aadnoy, B., Hareland, G., Kustamsi, A., De Freitas, T., & Hayes, J., 2009. Borehole failure related to bedding plane. *43rd U.S. Rock Mechanics Symposium and 4th U.S.-Canada Rock Mechanics Symposium.*

Abbey, C. P., Meludu, O. C., & Oniku, A. S., 2020. 3D modeling of abnormal pore pressure in shallow offshore Niger delta: An application of seismic inversion. *Petroleum Research*. https://doi.org/10.1016/j.ptlrs.2020.12.001

Agbasi, O. E., Sen, S., Inyang, N. J., & Etuk, S. E., 2021. Assessment of pore pressure, wellbore failure and reservoir stability in the Gabo field, Niger Delta, Nigeria - Implications for drilling and reservoir management. *Journal of African Earth Sciences, 173* (September 2020), 104038. https://doi.org/10.1016/j.jafrearsci.2020.104038

Baouche, R., Sen, S., Sadaoui, M., Boutaleb, K., & Ganguli, S. S., 2020. Characterization of pore pressure, fracture pressure, shear failure and its implications for drilling, wellbore stability and completion design – A case study from the Takouazet field, Illizi Basin, Algeria. *Marine and Petroleum Geology, 120* (June). https://doi.org/10.1016/j.marpetgeo.2020.104510

Fjær, E., Holt, R. M., Horsrud, P., Raaen, A. M. & Risnes, R., 2008. *Petroleum Related Rock Mechanics*. 2nd Edition. Hungary.

Heidbach, O., Rajabi, M., Reiter, K., Ziegler, M., WSM Team, 2016. *World Stress Map Database Release 2016*. GFZ Data Services. http://doi.org/10.5880/WSM.2016.001

Lee, H., Ong, S. H., Azeemuddin, M., & Goodman, H. (2012). A wellbore stability model for formations with anisotropic rock strengths. *Journal of Petroleum Science and Engineering, 96–97, 109–119*. https://doi.org/10.1016/j.petrol.2012.08.010

Mantilla, H., Saavedra, N., Arias, H., Osorio, A., 2019. Geomechanical monitoring in real time, a case study in Ecopetrol Onshore Wells. *Proceedings of ISRM 8th International Symposium Geomechanics, Bucaramanga, Colombia* (May 2019). ISRM-ISG-2019-06.

Okland, D., & Cook, J. M. (1998). Bedding-related borehole instability in high-angle wells. *Proceedings of the SPE/ISRM Rock Mechanics in Petroleum Engineering Conference, 1*, 413–422. https://doi.org/10.2118/47285-ms

Xie, Y., Ouyang, M., Zhao, H., Li, L., & Feng, Y. (2021). Wellbore pressure management of offshore wells during casing running in narrow safety pressure window formations. *Journal of Petroleum Science and Engineering, 199* (August 2020), 108284. https://doi.org/10.1016/j.petrol.2020.108284

Comprehensive evaluation of drilling events related to geomechanics in the Middle Magdalena Valley

Sandra Martinez[a], Nelly Rubio[a], Reinel Corzo[a], Laureano Jimenez[a], Sergio Ardila [b], Oscar Acevedo [b], Victor Porras[b]

[a,] *Ecopetrol, Bogotá, Colombia*
[b] *Ecopetrol contractors, Bogotá, Colombia*

ABSTRACT

Drilling upcoming wells in prospective areas of the Middle Magdalena Valley basin in Colombia requires knowing the drilling risks associated with wellbore instability events, in order to anticipate actions to mitigate or evade them, preventing non-productive times (NPTs) and increase in well costs. To achieve this, a comprehensive drilling evaluation of thirty-eight key wells has been performed, which include the visualization and classification of main drilling events related to geomechanics, the recognition of their potential root causes, the statistical analysis of these main events, and the qualitatively risk assessment on account of the definition of severity versus probability of occurrence of each main event by formation, providing clear understanding of mitigation plans, lessons learned and best operational practices for upcoming wells. The events evaluated in each well corresponded to those related to geomechanics, such as restrictions while drilling or logging operations, chemical instability, stuck pipe, mud losses and fluids influx.

KEYWORDS

Drilling Events Analysis; Qualitatively Risk Assessment; Operational Best Practices; Drilling Optimization

1. INTRODUCTION

Historically, the Middle Magdalena Valley (MMV) basin in Colombia has been one with the most important production contributions from Cenozoic petroleum systems exploited in different fields, and currently it has the option of incorporating reserves from the exploitation of unconventional deposits of Cretaceous formations. The drilling of wells over more than 50 years allows establishing an important source of information that can be used for well planning in prospective areas. Drilling upcoming wells in prospective areas of MMV basin requires knowing the drilling risks associated with wellbore instability events, to anticipate actions to mitigate or evade them, preventing non-productive times (NPTs) and increase in well costs. Taking that into account, this paper presents a comprehensive drilling evaluation that comprise an integral approach that has been applied in thirty-eight key wells in MMV basin. The integral approach incorporates the following aspects (Figure 1):

1. Drilling Events Evaluation
    a. Detailed revision of drilling daily reports.
    b. Identify and classify all main drilling events related to geomechanics. Generation of typical graphic of time-depth curve drilling.
    c. Recognition of potential root causes of these main drilling events.
    d. Statistical analysis of main drilling events: evaluation of the frequency of the events by formation/wells.
2. Risk Assessment
    a. Definition of the severity and the probability of occurrence by event (qualitative analysis). Identification of severity of these main events that can become a non-productive time (NPT).
    b. Results of risk assessment for Tertiary and Cretaceous formations
3. Definition of drilling mud strategy for key Cretaceous wells drilled by Ecopetrol S.A.

4. Clear understanding of mitigation plan by formation
5. Lessons learned for upcoming wells in MMV wells

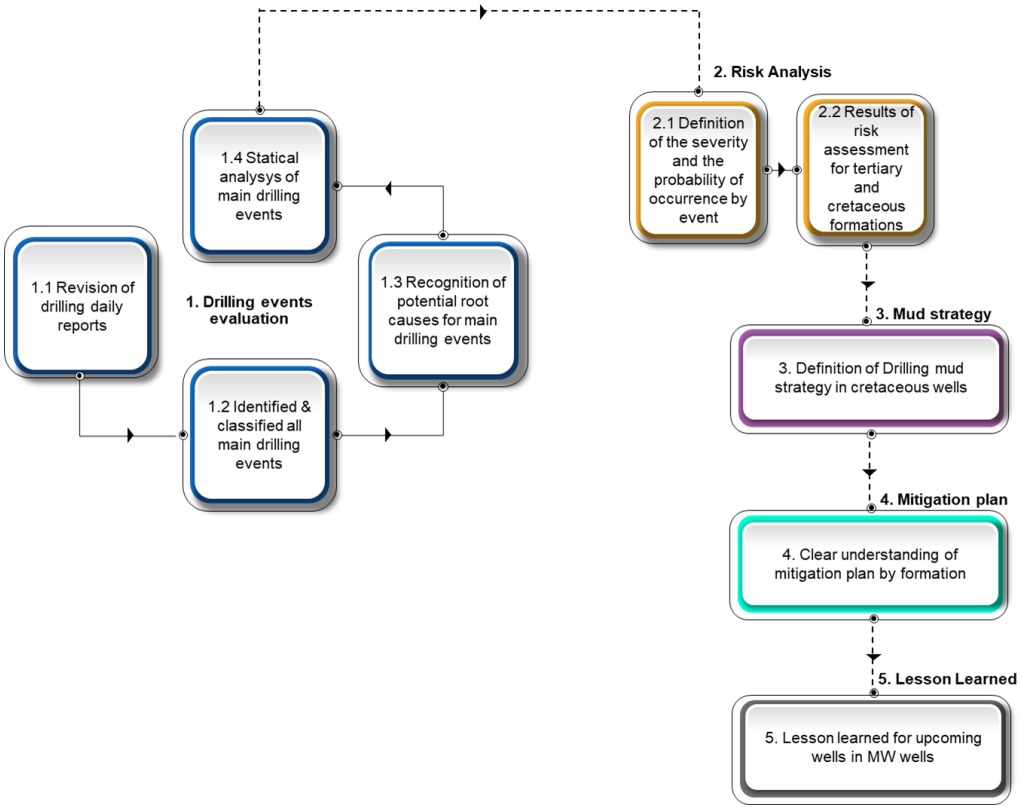

Figure 1. Diagram of proposed integral approach. It incorporates five aspects: on the left: drilling events evaluation, and on the right: risk analysis, mud strategy, mitigation plan and lesson learned. The definition of each one is referenced in the diagram.

This paper contains six sections. The first section is an introduction with the proposed methodology. The second section is an overview of the Middle Magdalena Valley (VMM) basin, and the description of a generalized chronostratigraphic chart of this basin. In the third section, the drilling events evaluation that includes: the identification and classification of main drilling events related to geomechanics, the recognition of their potential root causes, and statistical analysis by formation/well. In this section, examples of a typical graphics of time-depth curve drilling and bit position during real time monitoring are shown. The fourth section account for the qualitatively risk assessment performed. The fifth section present a definition of drilling mud strategy for Cretaceous wells in MMV basin. In the last two sections, the contributions of this study: mitigation plan by formation, the lessons learned, recommendations, and best operational practices for the upcoming wells in MMV basin.

2. MIDDLE MAGDALENA VALLEY BASIN: AN OVERVIEW

The Middle Magdalena Valley (MMV) basin is an intra-mountain basin with an approximate extension of 34,000 km^2, which is limited to the east by the Cordillera Oriental (Eastern Ranges) and to the west by the Cordillera Central (Figure 2). In the central part of the basin there are rocks from the Mio-Pliocene that are characterized by generating a gently undulating to steep sediment morphology. Quaternary sediments are formed by alluvial deposits from the Magdalena River and its tributaries, which give the land a smooth morphology. The MMV basin along with the Cordillera Oriental has been affected by three major tectonic events (Figure 3): 1) During the Late Jurassic and early Cretaceous, an extensional tectonic phase with development of grabens was established, in response to the “Pangea Rupture”; 2) During the Late Paleocene there was a compressive to transpressive tectonic that originated the uplift of the Cordillera Central and the structural highs of the MMV; and 3) From

the Middle Miocene, important compressive tectonic pulses began, which mainly affects the Cordillera Oriental and induced its uplift and inversion (Suarez et al., 2001 and Cespedes et al., 2014).

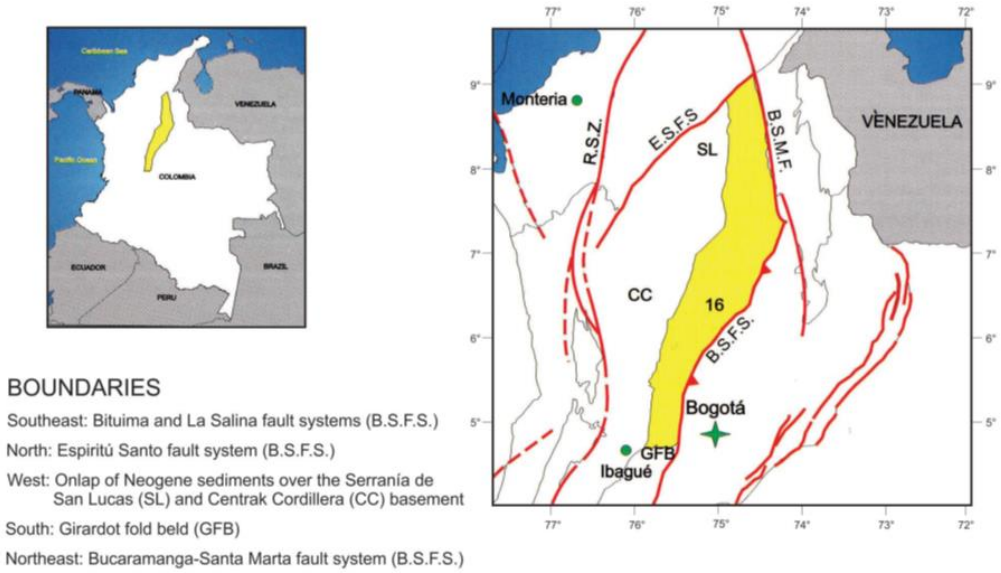

Figure 2. On the left: Location map of the Middle Magdalena Valley basin in Colombia. On the right: Main fault systems surrounding the Middle Magdalena Valley basin. Source: Agencia Nacional de Hidrocarburos, Colombia (ANH)

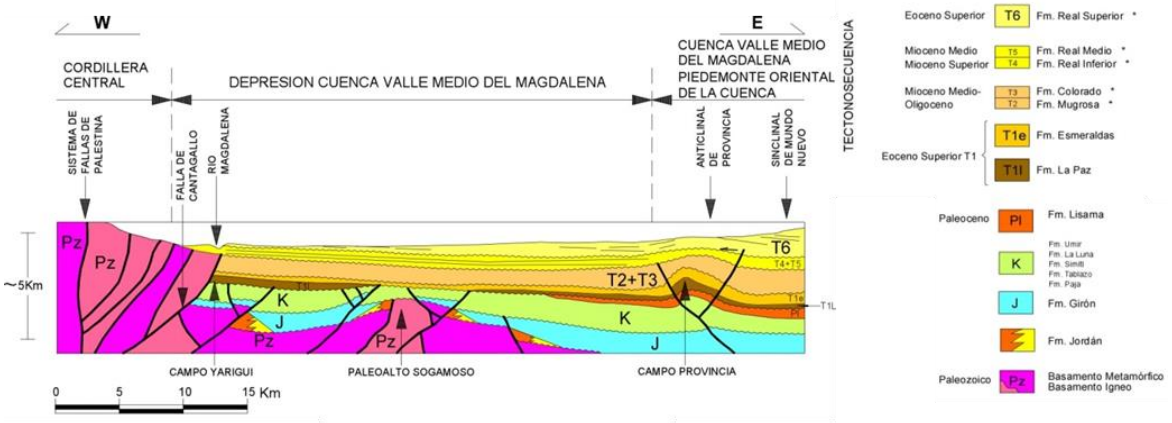

Figure 3. On the left: Diagram of tectono-stratigraphic evolution from the Middle Miocene to the present. On the right: the nomenclature used in the diagram, Tectono-sequences (T6 to T11: Tertiary formations), Paleocene, Cretaceous, Jurassic and Paleozoic. (Suarez et al., 2001).

Regarding to the Chrono-stratigraphic column of the MMV (Figure 4), the basal part of Cretaceous begins with the fluvial deposits of the Los Santos formation, which is composed of bioturbed sandstones, shales and sandy claystones. Next, the Cumbre Formation was deposited with bioturbed sandstones and cross-stratified sandstones and dark shales deposits to the top. The Rosablanca formation is composed of layerings of black clay, calcareous with gypsum, and limestone of varied textures (mudstone, wackstone, packstone). The environment is interpreted as marine platform deposits. The Paja formation are slightly calcareous, micaceous black shales with calcareous concretions. The Tablazo formation evidence clearly calcareous facies, which consist of interbedded biomicritic limestones with dark gray calcareous shales, which represent accumulations in a shallow carbonate platform. Limestones are most abundant towards the upper part of the formation. The Simití formation is concordant on the Tablazo formation and is composed of locally calcareous, carbonaceous, dark gray to black shales. The La Luna formation is subdivided into three members: Salada Member: calcareous, black, hard, laminar shales, with concretions, finely stratified limestone,

and pyrite. The concretions have ellipsoidal shape. Pujamana Member: Finely stratified gray to black calcareous shale. Galembo member: alternation of calcareous shales with thin layers of limestones and some layers of chert, siliceous shales, as well as glauconite and associated phosphates. Ecopetrol S.A. has been working on the definition of Olini group (Upper Lidita, Aico Shale and Lower Lidita) in the Upper Galembo member of La Luna formation. The Umir formation is accordant with the La Luna formation and is composed of interstratified gray shales with thin levels of siltstones, sandstones, siderite, and some coal mantles (Suarez et al., 2001).

Six tectonosequences deposited in alluvial and fluvial environments have been defined on the discordance of the Middle Eocene. These sequences include the T1 tectonosequence (La Paz and Esmeraldas formations), T2 tectonosequence (Mugrosa formation), T3 tectonosequence (Colorado formation) and T4 to T6 Tectonosequences (Real group) (Suarez et al., 2001).

- T1 tectonosequence (La Paz and Esmeraldas formations): La Paz formation represents the first fully continental deposition in the basin after the Cretaceous marine domain. It is the most important storage in the northern and eastern part of the basin. It is composed mainly of coarse-grained and conglomerate sandstones with intercalations of shales deposited in low-sinuous meandering fluvial systems. In the western part of the basin, it has a thickness of 2000', but in the central part it was not deposited due to a depositional termination on the paleo Sogamoso, and towards the eastern margin its average thickness is 650 feet. The lithology of Esmeraldas formation consists of thick intervals of dark shales and siltstones and thin coal beds deposited in meandering rivers. Fine-grained sandstones are also intercalated, and it has a transitional contact with the La Paz formation. In the Provincia area, the Esmeraldas formation exhibit a thickness of 1500’and varies up to 160 feet in the Yariguí-Cantagallo area.
- T2 tectonosequence (Mugrosa formation): Mugrosa formation is composed of intercalations of fine-grained sandstones and varicolored shales, accumulated within a paleo-environment of meandering river systems. Its thickness varies from 1900 'in the central and eastern sectors of the basin to 2400' to the west.
- T3 tectonosequence (Colorado formation): Colorado formation is constituted of massive shales with intercalations of fine to coarse-grained sandstones with a fluvial origin.
- T4 to T6 Tectonosequences (Real group): Real group is mainly composed of conglomerates and coarse-grained sandstones interbedded with varicolored claystones, deposited in continental environments.

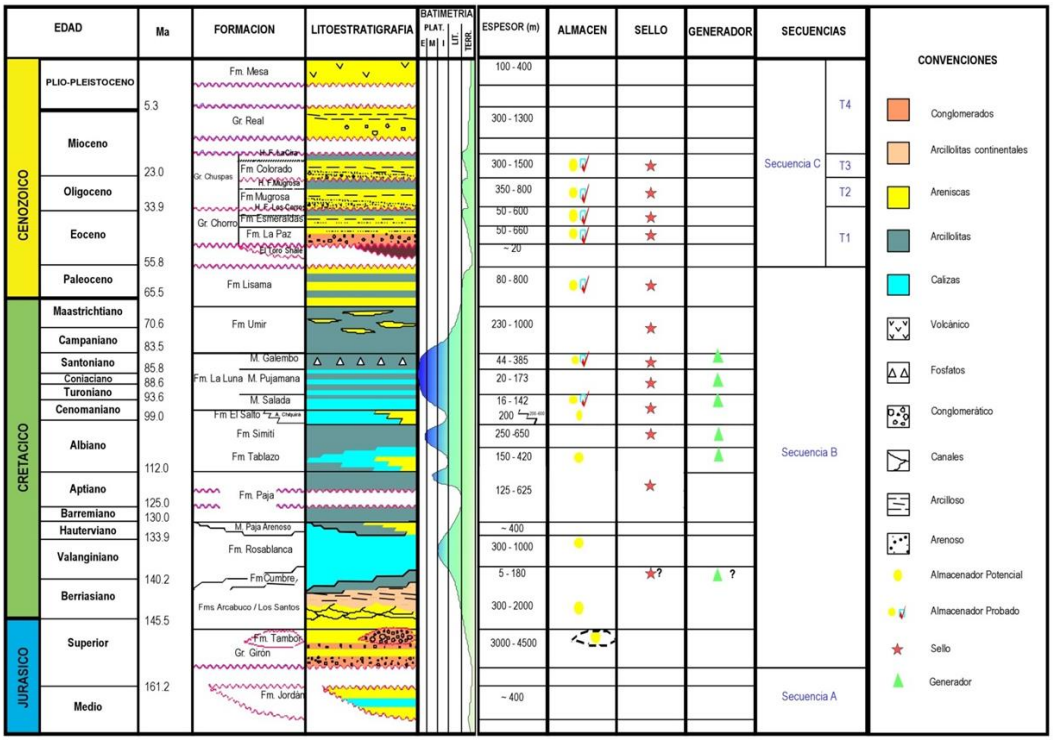

Figure 4. Generalized Chrono-stratigraphic column of the Middle Magdalena Valley. Source: Modified of L. Rolon et al., 2004.

3. DRILLING EVENTS EVALUATION

3.1. Main drilling events

Restrictions or tight hole do not necessarily lead to non-productive time (NPT), but they can be a symptom of problems that are most likely related to stability conditions, and it could materialize in a severe event such as a stuck pipe. Tight hole during drilling operations can be identified through running in hole (RIH), pull out of hole (POOH) and while running logging tools. Tight hole is identified in POOH trips when it is observed an increase in overpull above hole drag, and in RIH trips, the drill string weight loss or slackoff is evidenced. Tight hole is often easily overcome by working pipe to pass the restriction before the event causes a stuck pipe. However, in some cases of restrictions while running logging tools, the cable cannot pass the restriction at different speeds or the overpull is limited due to risk of cable damage or breakage, the wireline must be removed out of hole to perform a wiper trip and well conditioning, or in severe situation a fish operation must be required, giving rise to an NPT. To avoid restrictions during running logging tools, several actions are valued such as changing the wireline configuration and logging with through drillpipe logging (TDL) or logging while drilling (LWD). In case of severe restrictions, the consequence could be the inability of acquiring the planned information, and the loss of the logging tool. During the drilling is necessary to map all tight hole events that occur during the trips to establish along with complementary information, a diagnosis of the operational and stability conditions of the well. Figures 5 and 6 show the typical bit position curve during real time monitoring, and the typical time-depth drilling curve.

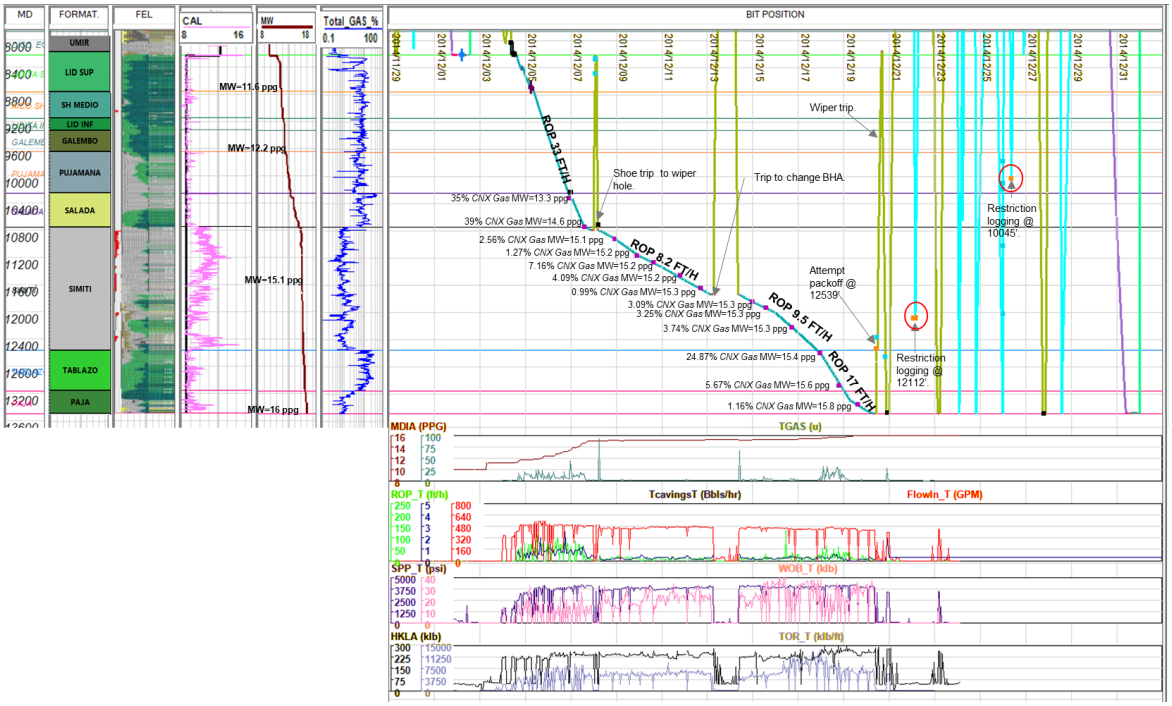

Figure 5. Typical bit position curve during real time monitoring. From left to right/from top to bottom: measured depth (in feet), formations, FEL, bit size and caliper (in inches), mud weight (in ppg), total gas (in %), bit position and main drilling events (time-depth curve). Drilling parameters: mud weight (MDIA in ppg), rate of penetration (ROP in ft/hr), standpipe pressure (SPP in psi) and hookload (HKLA in klb).

In real-time monitoring of drilling operations through bit position curves, all drilling events and mud logging records are positioned on the time and depth scale, where a database with information from multiple wells may be consolidated allowing the comprehensive analysis of the different events to establish the root cause and establish the recommendations to avoid or mitigate the future materialization of the event. Also, the integration of the historical information of drilling events from multiple wells can be used in the statistical analyzes of main drilling events, and their relationship with the geological characteristics of the formations.

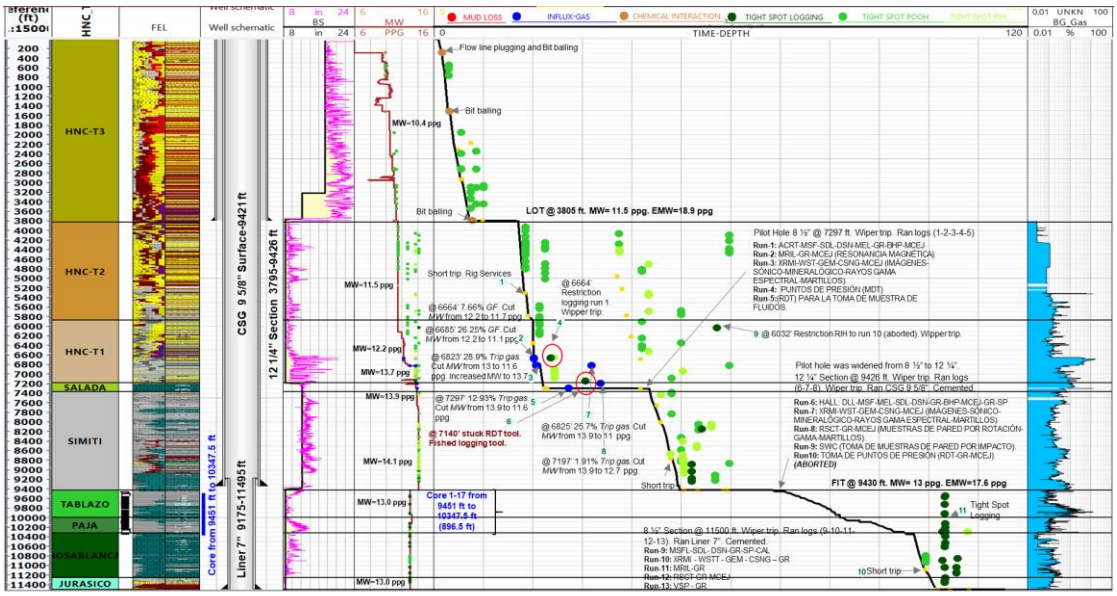

Figure 6. Typical time-depth drilling curve. From left to right/from top to bottom: measured depth (in feet), formations, FEL, well schematic, bit size and caliper (in inches), mud weight (in ppg), time-depth drilling curve with main drilling events. Brown dots stand for chemical interaction events, green dots represent tight hole events and blue dots symbolise gas influxes identified in the tertiary and cretaceous formations.

Figure 7 shows the caliper and the mineralogical composition of the clays from a well where an under-gauge hole has been evidenced throughout the analysis of the oriented caliper. This behavior was caused by chemical instability/swelling clays, and development of thick mud cake due to high permeability sands. As a consequence of this phenomena, some of the casings were placed out of the bottom in wells at the northern part of the basin. The presence of chert and coal in the tertiary formations that have been also identified as a potential causes of tight hole during trips.

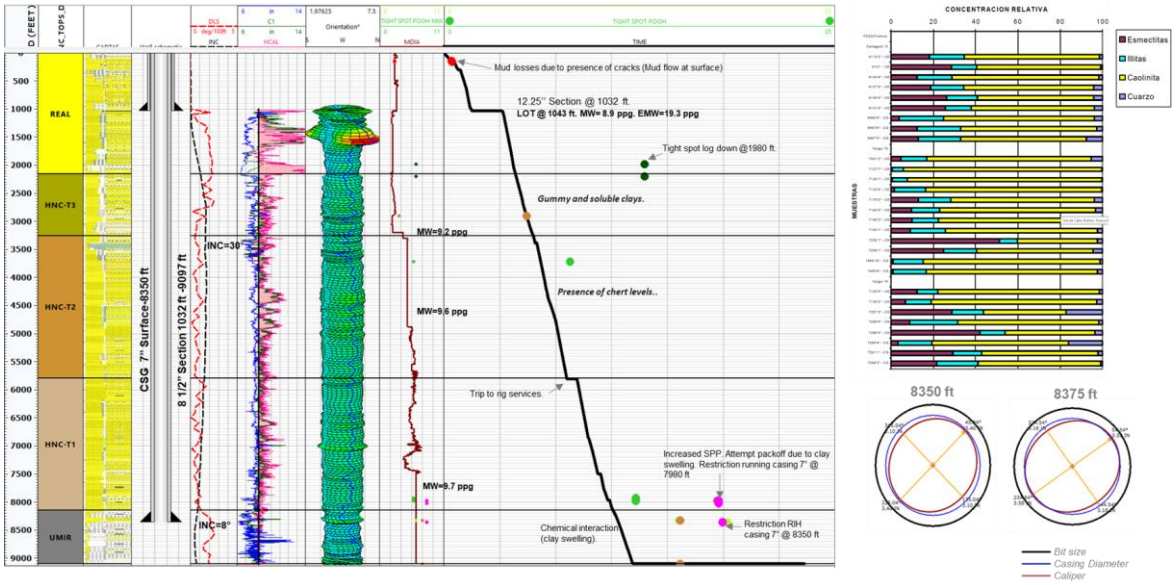

Figure 7. Chemical instability/clay swelling events due to the presence of reactive mineral clays in the tertiary formations. From left to right: measured depth (in feet), formations, FEL, well schematic, well deviation and dog leg, bit size and calipers (in inches), oriented caliper (in inches), mud weight (in ppg), time-depth drilling curve with main drilling events, XRD with mineral composition of formations and cross-sections of oriented caliper.

Partial and total mud losses are events that during drilling not only cause non-productive times, but also impact costs and can affect the safety of the operation. Mud losses can be understood as an

uncontrolled flow of mud within a formation. When mud losses event is not controlled effectively it could trigger other types of events such as pipe sticking, well instability or blowout. Mud losses can occur naturally due to formation characteristics such as fractured, unconsolidated, cavernous, high permeability and depleting rocks, or could be induced because of the increase on pressure of the circulation system has arisen the fracture pressure in an intact rock or a minimum horizontal stress in a fractured formation. Figure 8 shows the frequency of mud losses event in comparison with the total drilling events that has been identified in all thirty-eight (38) wells evaluated. In general, a low frequency of mud loss events has been observed. However, in the Real group (Tertiary formations) losses may represent ten percent (10%) of the drilling events identified, and in Lower Lidita (Cretaceous formation) up to thirty-seven percent (37%).

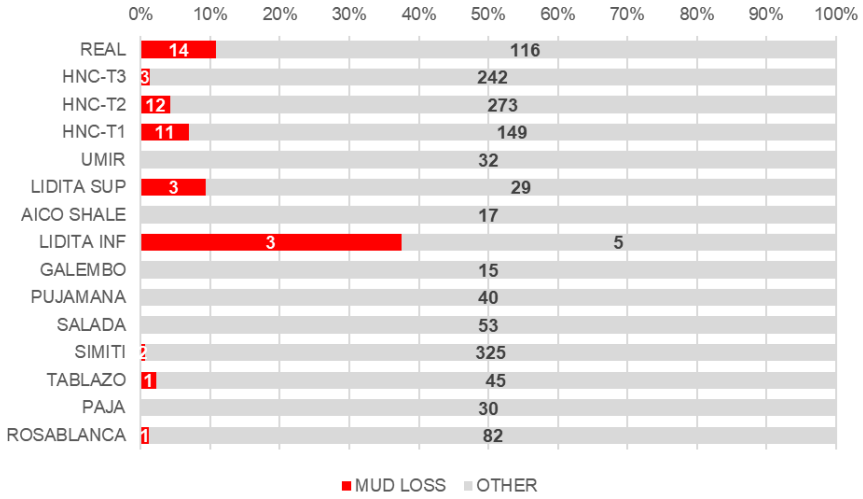

Figure 8. Frequency of mud losses event in comparison with the total of drilling events identified in the thirty-eight wells analyzed. From the chart: in the Real group (Tertiary), losses may represent ten percent of the drilling events identified, and in Lower Lidita (Cretaceous) losses represent up to thirty-seven percent of the total events.

3.2. Statistical analysis of main drilling events

Figure 9 shows the percentage distribution and frequency of main drilling events related to geomechanics by formation for six key Cretaceous wells drilled by Ecopetrol S.A. For this set of wells, eighty-five percent (85%) of the main events are tight hole during trips and logging. Most of the events are restrictions in roughly all formations, where the high frequency in the Tertiary formations is associated with tight hole –POOH, and tight hole-while logging in the Cretaceous formations. Restrictions during trips are presented by different causes, such as: the wellbore instability problems, clay swelling/chemical instability, hole cleaning, well tortuosity, BHA design, high vibrations, lithological characteristics, and mud fluid properties. In the tertiary formations, the main drilling events are mostly related to tight hole during trips. These formations are mainly constituted by interbedding of low thickness of claystones, siltstones, sands, and sandstones, where there is a high contrast of the rock properties for different lithologies which can cause tortuosity during trips. Chemical instability has been also identified as one of the causes of the restrictions, mainly while running casing operations. Chemical instability has been evidenced in the Tertiary formations where the composition of clay minerals is up to forty percent (40%) with significant presence of reactive minerals (Ecopetrol S.A. 1998-2014).

Along the wells in MMV basin, due to structural complexities and stratigraphic sections on the position of MMV key Cretaceous wells, is expected a variation in the pore pressure and mechanical behavior in the Cretaceous formations. The structure complexity, and the presence of Umir formation -acting as a seal- impacts pressures and stresses magnitudes in Olini Group and La Luna formations. Simiti is another important seal formation with high pressure and significant wellbore stability issues. Wellbore stability issues and restrictions in Upper Lidita and Aico Shale members of Olini Group, and

in Salada and Tablazo formations, potentially related to instability of planes of weakness/natural fractures. Connection gas and mud losses evidenced in the wells, could come from specific lithological units/layers, which have characteristics that do not represent the entire formation (permeability, natural fractures, and higher pore pressure). Pujamana, Simití and Paja formations present both, high pore pressure and mechanical instability, which generate most restrictions during trips and running logs (Rubio et al., 2020).

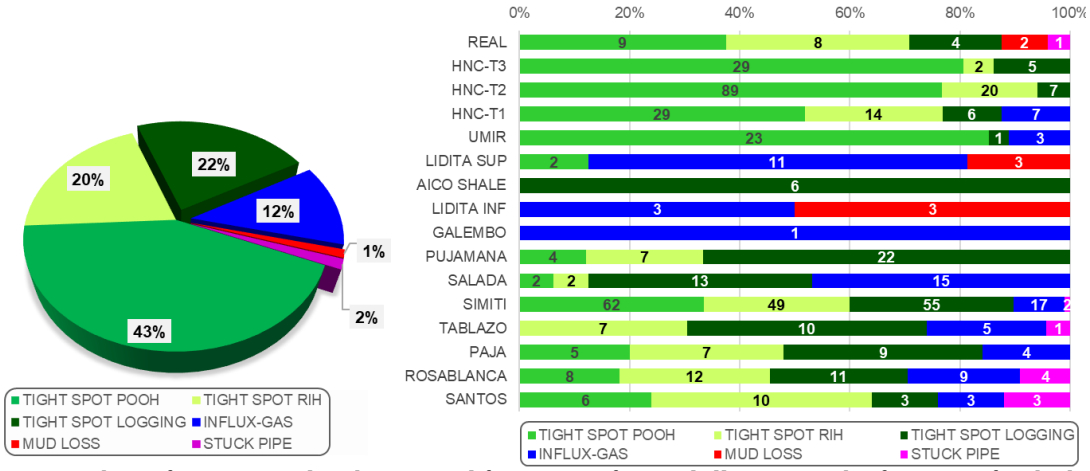

Figure 9. Pie-chart of percentage distribution, and frequency of main drilling events by formation for the key Cretaceous wells drilled by Ecopetrol S.A. Green color stands for tight hole events, blue color represents gas/water influxes, red color symbolizes mud losses and pink color represents stuck pipe events.

4. RISK ASSESSMENT

The risk assessment for each drilling event has been performed for all thirty-eight wells based on the definition of the severity and the probability of occurrence. These criteria were established according to the statistics obtained, and the field experience of the drilling engineers, considering the impact and management of each drilling event. Tables 1 and 2 present the criteria for defining the probability of each drilling event. The probability of tight hole event was defined with a normalized data for every 100 ft of formation, and the probability for other events such as: mud losses, influx, and stuck pipe as a function of the number of events by formation. The probability was defined into three categories such as: feasible, likely, and very likely. The severity implies the impact of each drilling event, and the potential consequence and it also was defined into three categories such as: light, moderate and strong (Tables 3, 4 and 5).

Table 1. Probability definition criteria for Tight hole events

Classification	Tight Spot POOH/RIH/ LOGGING
FEASIBLE	>10/100 ft
LIKELY	4-10 /100 ft
VERY LIKELY	1-3 /100 ft

Table 2. Probability definition criteria for Mud Losses, Influx and Stuck pipe

Classification	Mud Losses	Fluid Manifestations	Stuck Pipe
FEASIBLE	>3/formation	>3/formation	>3/formation
LIKELY	2-3/formation	2-3/formation	2-3/formation
VERY LIKELY	1/formation	1/formation	1/formation

Table 3. Severity definition criteria for tight hole events

Classification	Tight Spot POOH/RIH	Tight Spot LOGGING
LIGHT	Overpull / slackoff	Restriction
MODERATE	POOH / RIH with GPM	POOH cable and change setting tool / POOH and perform wiper trip
STRONG	Back reaming/ Reaming	Unable to run logs / Loss of tool/ fish operation

Table 4. Severity definition criteria for mud losses and influx

Classification	Mud Losses	Fluid Manifestations
LIGHT	Seepage Losses<10 Bls/hr	Gas Connection, Trip Gas, increased BGG
MODERATE	Partial Losses >10 Bls/hr	Control with MW increase up to 1ppg
STRONG	Total Losses	Control with MW increase above 1ppg

Table 5. Severity definition criteria for stuck pipe

Classification	Stuck Pipe
LIGHT	Attempts pack off
MODERATE	Pack off/working pipe/fishing operation
STRONG	Sidetrack

Figure 10 displays the color convention for the matrix of severity versus probability that has been used in the risk assessment of each drilling event. Severity can be light (L), moderate (M), and strong (S). Probability can be considered feasible (F), likely (L), and very likely (VL). The matrix of severity versus probability can be result in the combination of them, for instance: LF means light (L) in severity and feasible (F) in probability, in blue light color in the matrix.

		PROBABILITY		
		FEASIBLE	LIKELY	VERY LIKELY
SEVERITY	LIGHT	LF	LL	LVL
	MODERATE	MF	ML	MVL
	STRONG	SF	SL	SVL

Figure 10. Matrix of severity (light, moderate and strong) versus probability (feasible, likely, and very likely) for risk assessment of each drilling event.

Figures 11 displays the risk assessment results for twenty-eight wells drilled in the Tertiary formations. The twenty-eight wells were organized into 2 groups: wells drilled in the in the northern area (twelve tertiary wells); wells drilled in the southern zone (sixteen tertiary wells). In the northern area, the three events with most probability of occurrence and severity are related to mud losses (Real, HNC-T3, HNC-T2), stuck pipe (HNC-T1), restrictions and chemical interaction (all formations), while in the wells drilled in the southern area these three events with most probability of occurrence and severity are related to stuck pipe (Real, HNC-T3, HNC-T1 and HNC-T2), influx (HNC-T2) and restrictions (HNC-T1, HNC-T2 and HNC-T3).

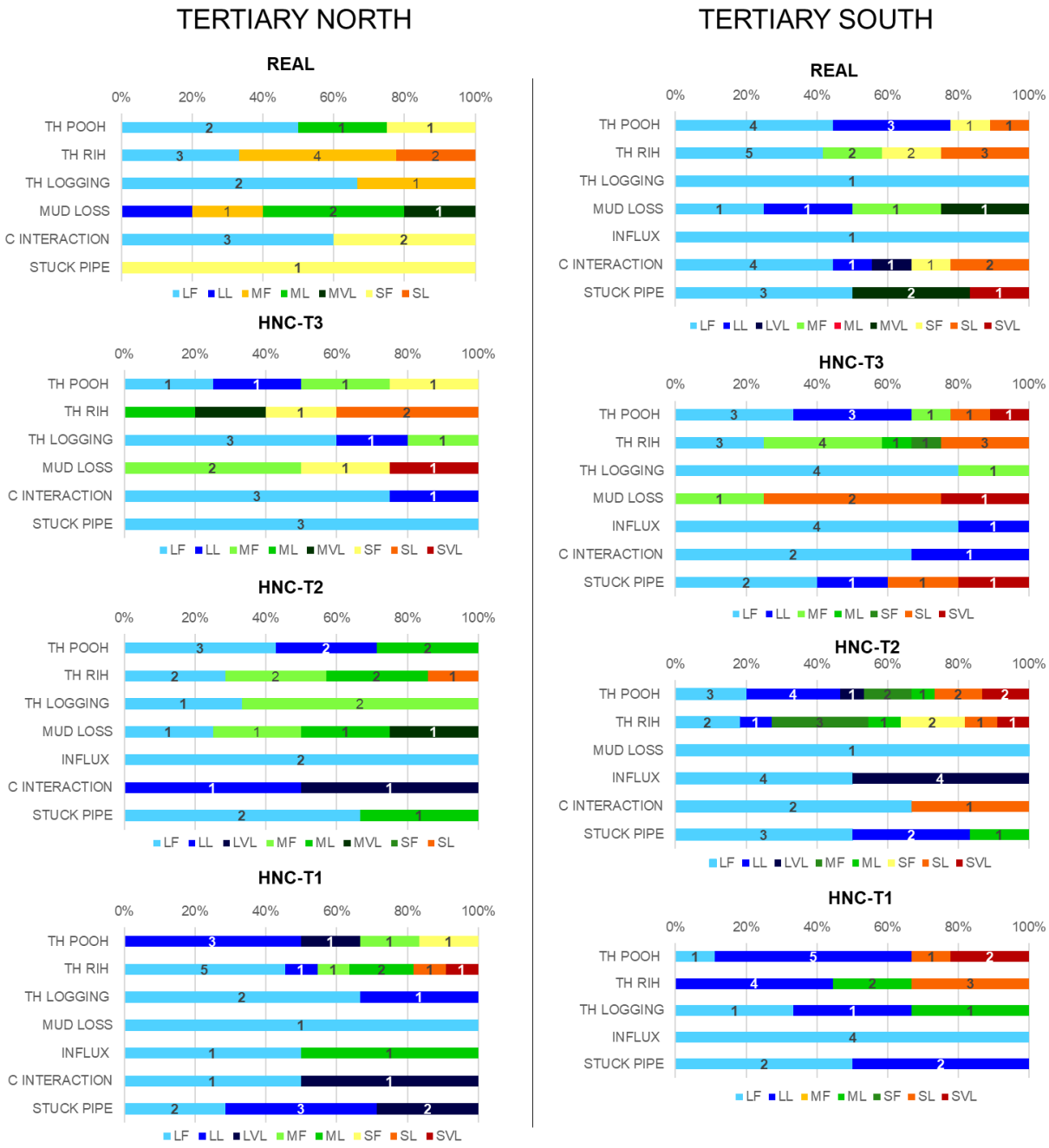

Figure 11. Risk assessment for twenty-eight wells drilled in the Tertiary formations.

Figure 12 shows the risk assessment results for twenty-eight wells drilled in the Cretaceous formations. The events with most probability of occurrence and severity in these wells are related to restrictions (all formations), and influx (all formations except Umir, Aico Shale and Pujama).

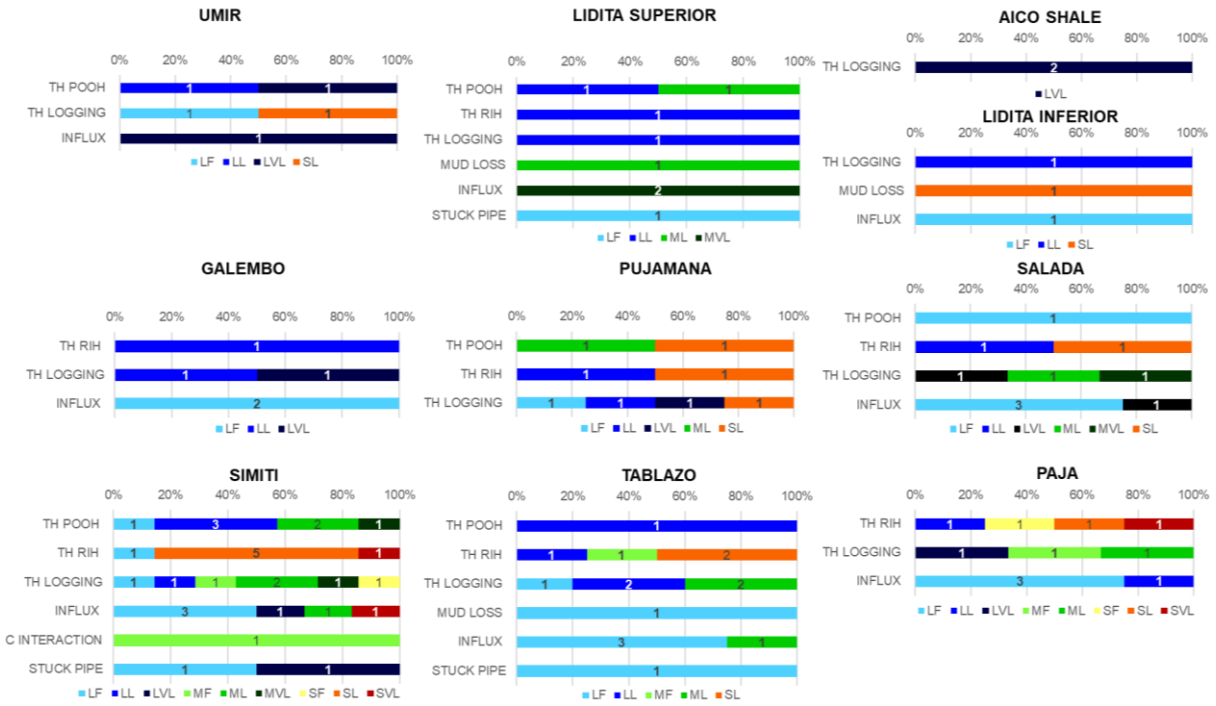

Figure 12. Risk assessment for ten wells drilled in the Cretaceous formations.

5. DEFINITION OF DRILLING MUD STRATEGY FOR KEY CRETACEOUS WELLS

The objective of mud formulation strategy was provided stability to the hole, in general terms, to handle chemical instability in Tertiary formations and mechanical instability in Cretaceous formations. During the 2014 drilling campaign in MMV, mineralogical information in the Tertiary formations was available in order to run the proposed reactivity protocol that is shown in Figure 13. The fluid company in charge also run a full protocol in the laboratory for three Catatumbo Cretaceous wells as part of the first phase. The first phase included the geomechanical model (rock properties, stress evaluation, etc.), evaluation of reactivity and cation exchange capacity in wells with similar formations, analysis of quantitative mineralogy of predominant shaly samples in the formations, the evaluation of reactivity curves. The second phase included the validation and adjustment of system property system performed in the ICP laboratories. The third phase included the prejob with the final fluid program.

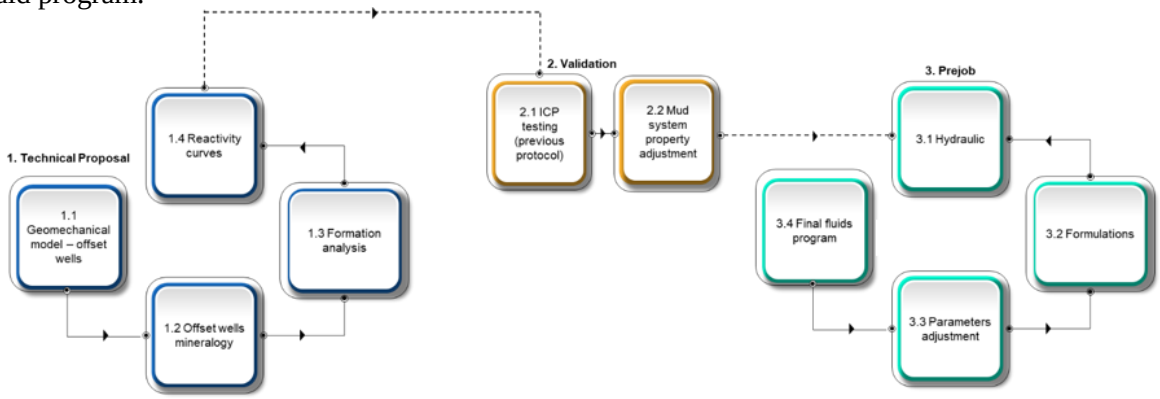

Figure 13. Three Phases Mud Strategy in Cretaceous wells.

In the analysis of events of La Luna formation of the first and third Cretaceous wells, were identified many events related with tight hole, and the measures taken in those wells was an increase in the mud weight assuming a wellbore instability issue. However, the fundamental factor for the fluid system design was sealing. This mud strategy fluid design was applied in the latest Cretaceous well with remarkable success. It is important to mention that were two different designs one for Tertiary another for Cretaceous.

6. STUDY CONTRIBUTION: MITIGATION PLAN BY FORMATION

This comprehensive drilling evaluation of the thirty-eight key in MMV wells allows the clear understanding of the potential root causes of the drilling events associated to structural aspects, lithological characteristics and operational practices for the Tertiary and Cretaceous formations. Table 6 summarizes the mitigation plan by formation for MMV wells.

Table 6. Mitigation Plan by formation for Middle Magdalena Valley wells

Formation	Events	Cause	Mitigation
REAL	•Mud losses in surface • Plugging of bit nozzles •Restrictions when running logging tools/Tight spots RIH, POOH	•Cracks presence •Presence of gummy and soluble clays •Interbeddings, high DLS	•Pumping pills with sealing material •Decreased mud flow in •Pumping visco-heavy pills to clean hole
HNC-T3	•Mud losses (Working pipe/Running CSG 7") •Bit balling •Stuck pipe attempt •Restrictions when running logging tools •Chemical instability		•Clay inhibitors (amine/glycol) •Pumping visco-heavy pills to clean hole •Reaming stands •Pumping LCM pills
HNC-T2	•ROP drop •Mechanical instability •Gilsonita influx •Mud losses •Tight spots RIH, POOH •Chemical instability •Restrictions when running logging tools	•Levels of Chert •Coal levels	•Control of drilling parameters to avoid bit damage •Clay inhibitors (amine/glycol) •Pumping visco-heavy pills to clean hole •Reaming stands •Use of lubricators
HNC-T1	•Tight spots RIH, POOH. •Differential sticking •Chemical interaction •Stuck pipe attempt •Restrictions when running logging tools. •Cut mud weight, •Mud losses running CSG 7"	•Gas connection.	•Do not keep drill string static. •Use of bridging material and reduce mud filtrate to avoid differential sticking. •Mud dilution •Pumping visco-heavy pills to clean hole •Reaming stands
UMIR	•Chemical interaction – Clay swelling •Mechanical Instability •Gas Influx, Cut mud weight •Restrictions (POOH and Logging)	•Intrinsic anisotropy due laminations. •Low mud density	•Clay inhibitors (amine/glycol) •Increase mud weight •Pumping visco-heavy pills to clean hole •Reaming stands
UPPER LIDITA	•Gas influx, cut mud weight, gas connection •Restrictions (RIH, POOH and logging) •Partial mud losses •Stuck pipe	•Complex geological structure •Presence of natural fractures •Presence of natural •fractures/geological uncertainties •Low MW and Cleaning hole	•Increase mud weight •Define casing point •Pumping pills with sealing material •Chemical & mechanical lubricants (3 – 4%) to ensure friction coefficient < 0.15.
AICO SHALE	•Restrictions (logging) •Mechanical Instability	•Intrinsic anisotropy due laminations •Low mud density	•Mantain mud-weight according to program •Pumping visco-heavy pills
LOWER LIDITA	•Restrictions (logging) •Partial mud losses and gas influx	•Complex geological structure •Presence of natural fractures	•Maintain mud-weight according to program •Pumping pills with sealing material

Table 6. Mitigation Plan by formation for Middle Magdalena Valley wells (Cont.)

Formation	Events	Cause	Mitigation
GALEMBO	•Restrictions (logging) • Gas influx	•Complex geological structure/heterogeneity •Low mud density •Presence of natural fractures	•Maintain mud-weight according to program •Pumping pills with sealing material •To keep enough material for weight up the mud any time is necessary
PUJAMANA	•Restrictions (RIH, POOH and logging)	•Intrinsic anisotropy due laminations/planes of weakness (PoW) •Cleaning hole	•Maintain mud-weight according to program •Chemical & mechanical lubricants (3 – 4%) to ensure friction coefficient < 0.15. •Pumping visco-heavy pills
SALADA	•Restrictions (RIH, POOH and logging) •Gas influx •Instability	•Intrinsic anisotropy due laminations/planes of weakness (PoW) •Low mud density •Presence of natural fractures	•Maintain mud-weight according to program •Cavings monitoring •Pumping pills with sealing material •Chemical & mechanical lubricants (3 – 4%) to ensure friction coefficient < 0.15. •Pumping visco-heavy pills
SIMITI	•Restrictions: reaming & back-reaming •Chemical interaction •Gas influx: well control •Mechanical instability	•Intrinsic anisotropy due laminations •Clay swelling •Low mud density	•Maintain mud-weight according to program •Cavings monitoring •Pumping visco-heavy pills
TABLAZO	•Restrictions (RIH, POOH and logging) •Partial mud losses •Gas influx •Stuck pipe	•Heterogeneity/Intrinsic anisotropy •Presence of natural fractures. •Low mud density •Instability/hole cleaning	•Maintain mud-weight according to program •Cavings monitoring •Pumping visco-heavy pills
PAJA	•Restrictions (RIH and Logging) •Gas influx •Mechanical Instability	•Heterogeneity •Hole cleaning •Low mud density	•Maintain mud-weight according to program •Cavings monitoring •Pumping visco-heavy pills

7. STUDY CONTRIBUTIONS: LESSONS LEARNED AND BEST PRACTICES FOR UPCOMING WELLS IN MMV WELLS

Based in the analysis events in MMV wells, the adequate fluid system must be following these conditions (MiSwaco, 2014):

- Mud system with seal for minimal pressure transmissibility (T: 250 ° F, P confinement 2500psi, ΔP 500psi)
- Mud system with HPHT filtration control for well pressure and temperature conditions (T: 250 ° F and ΔP 500psi)
- Mud system with effective seal strategy for well pressure and temperature conditions (T: 250 ° F & 1000 psi P differential), 5 / 35μm discs)
- Mud system with controlled API rheology for well pressure and temperature conditions
- Mud system with stable HPHT rheology for well pressure and temperature conditions (T: 250 ° F & P: 6000 psi)
- Mud system with dynamic HPHT filtering control for well pressure and temperature conditions
- Chemical inhibiting mud system (LSM - Linear welling)
- Mud system with good electrical stability

- Mud system with water phase salinity WPS (ppm Chlorides)
- Mud system that controls barite settlement after rolling at 250 ° F
- Mud system with low coefficient of friction

Table 7 displays a recommended fluid system for MMV wells in the Tertiary and Cretaceous formations.

Table 7. Recommended fluid system for MMV wells

Formation	Fluid Type	Drilling fluid objectives
TERTIARY	High performance WBM – Not dispensed - Inhibited	Avoid contamination of surface aquifers Control chemical instability Control gas/water superficial influx Ensure a proper cleaning of the hole Ensure a proper ROP
CRETACEOUS	Drill in (HPWBM) or Drill in (OBM Invermul)	Control mechanical hole instability Minimize fluid losses Maintain the chemical stability of shales Ensure a proper cleaning of the hole Ensure a proper ROP

The following operational best practices must be considered for mitigating tight hole drilling events:

- To perform monitoring of the torque and drag parameters to establish the free travel conditions. Once a tight hole is evidenced, work mechanically without forcing the string with excess overpull, reciprocating the pipe if necessary. In case of the mechanical work is unsuccessful, break gels by rotating the pipe and circulating at drilling flow.
- In the Cretaceous formations, reaming and backreaming should be avoided due to the existence of formations with planes of weakness such as high intensity of natural fractures in the limestones of the La Luna and Tablazo formations, and the shale laminations of the Simití and Paja formations, which can generate problems of cavings production (Yarim et al., 2010).
- Performing a short trip helps to remove the cutting bed and to improve the smoothness of the wall. Sometimes a short trip can be done when there is a long sliding section via a mud motor. It is beneficial to do so because sliding with the mud motor creates a lot of cutting beds that are not effectively removed.
- The rheological mud properties, filtering properties, formation bridging strategy, and chemical inhibition of clays improve formation stability conditions by avoiding travel restrictions.
- The control of the density must be according with the one established in the drilling program, indications of the presence of gas in the fluid, shape and size of the cuts.
- Control of rate of penetration (ROP) according to the flow used to avoid induced circulation loss events, taking in account possible faults and fractures in Olini group.
- It is recommended to perform constant monitoring of equivalent circulating density (ECD) to avoid inducing losses, if the increase of this ECD is related to an overload of cuttings is suggested circulate bottoms up to an acceptable value.
- Monitoring torque and drag conditions will be important to determine points of circulation or if it is requited to use lubricant.
- The pipe trip must be performed under the conditions to avoid a piston effect on the bottom and induce fractures into the formation or create a suction effect.
- The use of silica nanoparticles used in latest Cretaceous well is a new alternative for events during drilling operations due to loss of filtration and create thick retort that causes sticking and hole instability.

ACKNOWLEDMENT
The authors would like to thank Ecopetrol S.A. for all support to publish this paper.

REFERENCES

Céspedes, S. P., Forero, S. P., Cantisano, M.T., Marfisi, N., Zamora, W., and Corzo, R., 2014. *Oportunidad Exploratoria Lead Gala, Bloque de Exploración de Mares - Valle Medio del Magdalena*. Ecopetrol-internal document, Bogotá D.C., Colombia.

Ecopetrol S.A. 1998-2014. *Daily Drilling Reports*. Ecopetrol-internal document, Bogotá D.C. Colombia.

Rolón, L., F., 2004. *Structural Geometry of the Jura-Cretaceous Rift of the Middle Magdalena Valley Basin-Colombia* (Masters Thesis). West Virginia University, Morgantown, West Virginia, USA.

MiSwaco. 2014. *Drilling Fluid Recap.* Schlumberger, Houston, Texas, USA.

Rubio, N., Ardila, S., Martinez, S., Corzo, R., Quintero, Y., Mantilla, H., Carvajal, J., and Saavedra N., 2020. Ecopetrol Unconventional Key Wells: Drilling Analysis from Geomechanics Perspective. *1st Virtual Exploration Congress. Laying the Foundation. Ecopetrol, October 2020*. Ecopetrol, Bogotá D.C., Colombia.

Suarez, M. A., Córdoba, F., López, C., Rolón, L. F., Gomez, L.A., Buchelli, F., and Sotelo C. I., 2001. *Proyecto evaluación regional Cuenca Valle Medio del Magdalena - Cordillera Oriental, Colombia*. Ecopetrol, Bogotá D.C., Colombia.

Yarim, G., Ritchie, C. M., and May, R.B., 2010. A Guide to successful Backreaming: Real-Time Case Histories. *SPE Annual Technical Conference and Exhibition, Denver, 21-24 September*. SPE, Dallas, Texas, USA.

Numerical modeling of hydraulic fracture stimulation in unconventional reservoirs

J.A. Rueda[a, b], C. Mejia[a], D. Roehl[a, b]

[a] *Tecgraf Institute, Pontifical Catholic University of Rio de Janeiro, Brazil*
[b] *Department of Civil and Environmental Engineering, Pontifical Catholic University of Rio de Janeiro, RJ, Brazil*

ABSTRACT

The interaction of hydraulic and natural fractures limits the successful hydraulic stimulation treatments and enhanced production in unconventional reservoirs. In this context, the numerical models become indispensable for understanding hydromechanical mechanisms present in the hydraulic stimulation and the production of naturally fractured formations. This work presents a fully coupled hydromechanical approach to study the hydraulic fracture stimulation in naturally fractured formations and its effect on the production performance in unconventional reservoirs. The proposed methodology is based on the finite element method (FEM) and includes the coupling of fluid flow and geomechanics within the permeable rock formation and the fracture propagation process. An intrinsic mesh fragmentation technique is used to simulate non-planar fracture propagation with complex crack patterns. A pore cohesive zone model is used to simulate hydraulic fracture propagation, and the Mohr-Coulomb failure criterion is adopted to model closure/opening and friction/shear dilation of natural fractures. Several scenarios considering a complex fracture network are investigated to understand the dominant factors influencing hydraulic fracturing and the production performance in unconventional reservoirs.

KEYWORDS

Fractured rock; Hydraulic fracturing; Unconventional reservoir; Geomechanics.

1. INTRODUCTION

The hydraulic fracturing technique is dispensable in the development of unconventional reservoirs with ultralow permeability. The efficiency of hydraulic stimulation is strongly affected by the presence of geological discontinuities such as faults, joints, and natural fractures (Barbier, 2002; O'Sullivan et al., 2001). Geological discontinuities reduce the mechanical strength of the overall rock mass and alter the fluid flow characteristics. Pre-existing fractures can be partially or completely cemented. They can act as barriers for flow paths depending on the permeability of the filling material (Warpinski & Teufel, 1987). Sealed fractures can be stimulated by hydraulic fractures (HFs) and become preferential flow channels for oil/gas exploitation (Rueda Cordero, Mejia Sanchez, & Roehl, 2019a). In that sense, the hydraulic stimulation aims for the activation of natural fractures (NFs) and/or generation of new induced fractures to enhance permeability and well-reservoir connectivity (Shahid et al., 2016). However, the interaction of induced and pre-existing fractures increases the complexity of the hydraulic treatment and the geometry of the stimulated fracture network (Stephenson et al., 2018; Weng, 2015; Zhang et al., 2019).

Field and experimental observations showed different interaction types between induced and natural fractures (Jeffrey et al., 2010). Figure 1 illustrates the interaction process between fluid-driven fractures and pre-existing discontinuities. During the injection process, natural fractures can act as preferential paths for the growth of the hydraulic fracture network or arrest the hydraulic fracture propagation in some directions (Wang, 2016). In some cases, activated fractures can generate high proppant concentration and premature blockage of the proppant transport (screen out) (Potluri et al., 2005).

Several parameters as friction, cohesion, in-situ stresses, natural fracture aperture and orientation, fluid viscosity, and fluid injection rate can modify the final geometry of the stimulated fracture network (Mejia Sanchez et al., 2020; Rueda Cordero, Mejia Sanchez, Roehl, et al., 2019). In that context, numerical simulation of fracture propagation has become an essential tool to study and understand the interaction between hydraulic and natural fractures under different scenarios.

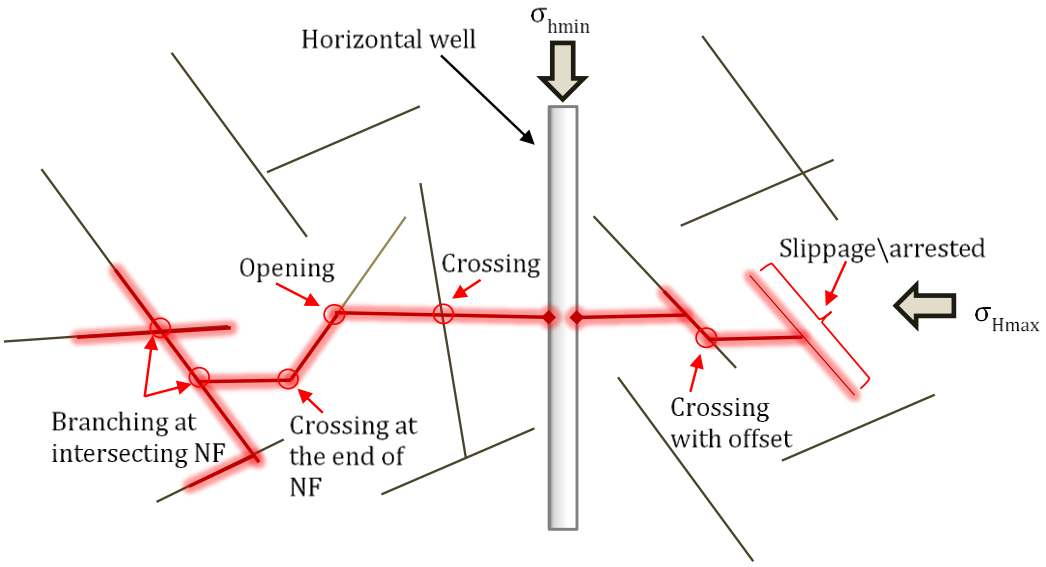

Figure 1. Schematic representation of the interaction between hydraulic fracture and natural fractures.

The development of representative models to simulate hydraulic fracturing is challenging due to the involved coupled-physics processes. In the last decade, robust numerical techniques have been developed to simulate fracture propagation in naturally fractured formations. Numerical approaches such as discrete element method (DEM) (Fatahi et al., 2017; Zhou et al., 2017), displacement discontinuity method (DDM) (J. Xie et al., 2018; L. Xie et al., 2016), extended and generalized finite element method (XFEM and GFEM) (Cruz et al., 2018, 2019; Gutierrez et al., 2019; Keshavarzi & Jahanbakhshi, 2013; Taleghani, 2009) have simulated the interaction between hydraulic and natural fractures successfully. However, those methodologies cannot assess the production performance of the hydraulically stimulated unconventional reservoir. This work presents a robust hydromechanical approach that integrates fracture propagation model and reservoir simulation based on finite element method (FEM). This approach allows studying several scenarios of hydraulic stimulation of fractured formation and its effect on production performance.

2. FRACTURE PROPAGATION IN NATURALLY FRACTURED FORMATIONS

2.1. Hydraulic fracturing

Fracture propagation and fluid migration in naturally fractured reservoirs is a complex process, and its numerical modelling represents a great challenge even in 2D cases. The difficulty arises mainly from fracture mechanisms and the non-linear coupling process. They include deformation of the rock induced by the fluid pressure on the fracture surfaces, fluid-driven fracture propagation, fluid flow inside the fracture, fluid leaked-off into the surrounding porous formation and the interaction between hydraulic and natural fractures. Those components were coupled in this work using finite element method (FEM).

The proposed approach simulates the hydraulic fracture propagation using the special triple-nodded interface element combined with the pore-pressure cohesive zone model (PCZM). This model defines the constitutive response in terms of traction separation law (TSL) and includes a fracture process zone ahead of a fracture tip (see Figure 2). The quadratic nominal stress criterion is adopted to predict the element damage initiation (Camacho & Ortiz, 1996), according to:

$$\left\{\frac{\langle\sigma_n\rangle}{\sigma_n^0}\right\}^2 + \left\{\frac{\tau_s}{\tau_s^0}\right\}^2 = 1 \quad (1)$$

where σ_n^0 and τ_s^0 are tensile and shear strengths; σ_n and τ_s represent the normal and shear tractions on the interface. After this point, linear softening behavior characterizes the progressive degradation of the material stiffness (see Figure 2b).

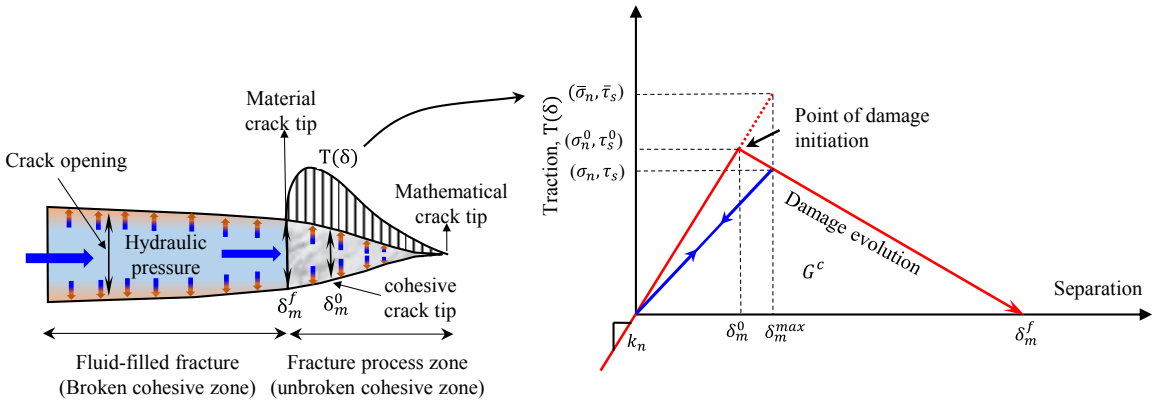

Figure 2. Schematic representation of the pore cohesive zone model (a) and traction separation response for the cohesive elements (b).

2.2. Natural fractures

The Mohr-Coulomb criterion with zero tension cutoff simulates the slip, opening, and shear dilation of the natural fractures, as shown in Figure 3. This model assumes that the NF activation occurs when the shear stress, τ_s, reaches the limit value τ_{slip} expressed in terms of the effective normal stress σ_n' (negative compression):

$$\tau_{slip} = c - \sigma_n' tan\phi \quad (2)$$

where c is the fracture cohesion, and ϕ is the friction angle.

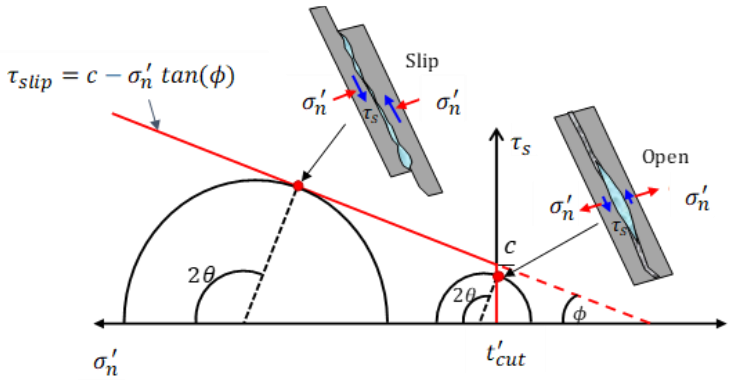

Figure 3. Mohr-Coulomb envelope

2.3. Fluid flow inside and across the fractures

We consider fluid flow along and across the natural fractures, as shown in Figure 4. The longitudinal flow $q_l$inside the fracture is considered incompressible and Newtonian, and it is defined as fluid flow through smooth parallel plates (i.e., Poiseuille flow):

$$q_l = -\frac{\delta_n^3}{12.\mu_f}.\frac{\partial p_i}{\partial s} \quad (3)$$

where μ_f is the dynamic viscosity of the fluid, p_i is the pore pressure inside the fracture parameterized with the curvilinear coordinate, s.

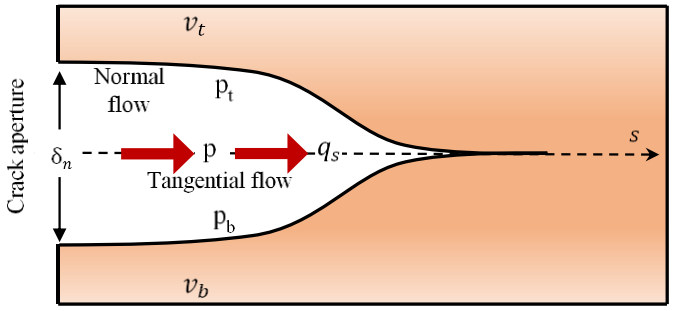

Figure 4. Fluid flow pattern inside the fracture

The normal flow may represent the infiltration of the fluid into the surrounding permeable rock formation, and it can be modelled through the pressure-dependent leak-off model:

$$v_t = c_t.(p_i - p_t) \quad (4)$$

$$v_b = c_b.(p_i - p_b) \quad (5)$$

where p_t and p_b are the pore fluid pressures at the top and bottom fracture surfaces and c_t and c_b are the top and bottom leak-off coefficients. The leak-off coefficients can be interpreted as the permeability of a finite layer on the fracture surfaces. In this study, these parameters have been assumed as constants.

2.4. Mesh fragmentation technique

We have used a novel intrinsic mesh fragmentation technique to simulate crack propagation with arbitrary paths. This technique is based on the insertion of interface elements at the edges of the continuum elements. The intrinsic mesh fragmentation has been successfully applied in hydraulic fracturing simulations in naturally fractured formations (Rueda, Mejia, Quevedo, et al., 2020), which is adopted in this work. More details of this technique can be found in the study presented by Rueda et al. (Rueda Cordero, Mejia Sanchez, & Roehl, 2019b).

3. RESERVOIR SIMULATION

Natural fractures play a critical role in the production of unconventional reservoirs. These natural fractures need to be characterized before the hydraulic fracturing design to optimize de production performance (Suppachoknirun & Tutuncu, 2017). Traditionally, explicit (discrete fracture models) (Rueda et al., 2019) or implicit methods (dual continuum approaches)(Mejia et al., 2021; Rueda, Mejia, Noreña, et al., 2020) are used to model these reservoirs. Dual continuum approaches are widely used for their reduced computational cost. The most popular dual continuum approach is based on the dual porosity and dual permeability (DPDP) model. This model simplifies the characterization of complex naturally fractured reservoirs, and it is preferred to history match fractured reservoirs and predict the production performance. However, this approach can not accurately simulate the effect of individual fractures indispensable to represent the fluid flow contribution of the stimulated and complex fracture network. Discrete fracture model (DFM) represents a naturally fractured system more realistically. This approach considers explicitly the effect of individual fractures on fluid flow and simulates the complex flow patterns in a fracture network more accurately. The fractures are represented by lines or surfaces

in 2D and 3D problems. By adopting an appropriate mesh discretization, the DFM can describe heterogeneities, anisotropy, and fracture distribution of the simulated fractured network. In this work, the discrete fracture model (DFM), based on FEM discretization, is adopted to simulate the hydraulically stimulated fracture network for production forecasting. The in-house framework GeMA (Geo Modelling Analysis)(Mendes et al., 2016) is used to simulate the reservoir production.

4. STUDY CASE

The numerical simulation consists of two stages. The first stage simulates the hydraulic fracturing of the deformable reservoir. Figure 5 illustrates the reservoir without NF and considering two fracture sets with strike angles of 30° and 120°. The second one investigates the impacts of natural fractures and fluid viscosity on the production performance of the stimulated reservoir. The reservoir of 60m x 60m x 12 m (length, width, and thickness) is under an initial pore pressure (P_0) of 45 MPa and initial effective stress (σ'_0) of 8 MPa. The walls are constrained in x and y-directions. The injector/producer well is located in the center of the model with an initial constant injection rate (Q_0) of 0.006 m^3/s for a period of 100s. After the fracture network stimulation, it is considered a producer well with constant pressure (P_w) of 40 MPa for a period time of 86400s. Table 1 summarizes the material properties of the rock matrix and fracture sets.

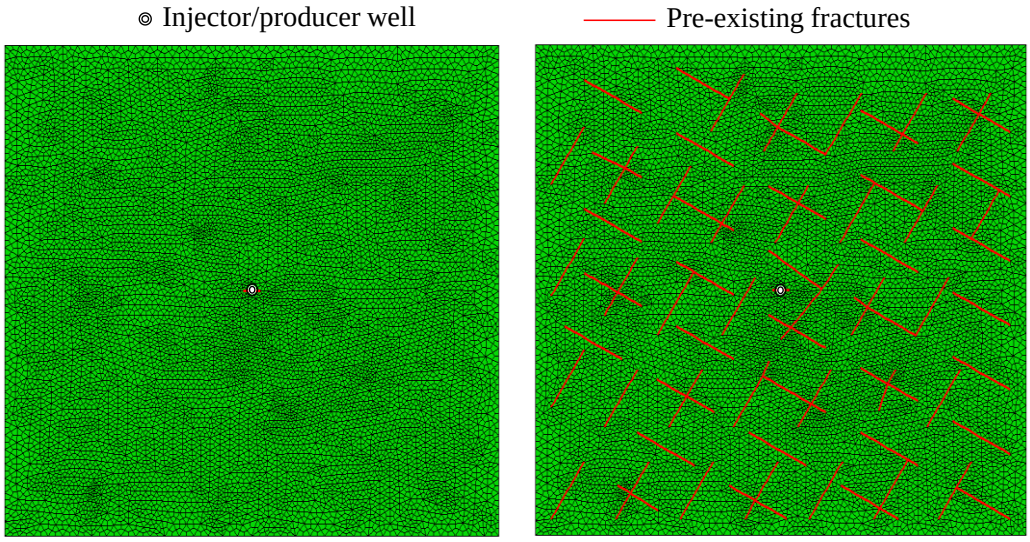

Case 1: Without NF **(a)**

Case 2: With two NF sets **(b)**

Figure 5. Reservoir model (a) without NF and (b) with two NF sets.

Table 1. Hydromechanical properties of the rock matrix and fracture sets.

Parameters	Units	Rock	NFs
Young's modulus, E	kPa	$1.7*10^7$	--
Possion's ratio, υ	---	0.22	--
Permeability k	mD	0.2	--
Porosity	--	0.25	--
Initial effective stress, σ'_0	MPa	8	8
Initial pore pressure, P_0	MPa	45	45
Bottom hole pressure at the producer, P_w	MPa	40	40
HF stiffness, $k_n = k_t$	kPa/m	--	$1.7*10^{10}$
NF stiffness, $k_n = k_t$	kPa/m	--	$1.5*10^9$
Fracture strike, θ_1 / θ_2 (°)	(°)	--	30/120
fracture aperture, a_0	m	--	$1*10^{-4}$

The first study investigates the effects of natural fractures considering a fluid viscosity of 10 cp for the stimulation stage and fluid viscosity of 1 cp for the production stage. Figure 6 shows the hydraulic fracturing results of the deformable reservoir without NF (Case 1) and considering two fracture sets (Case 2). Figure 6a shows the maximum principal stress distribution for each scenario. We can appreciate that the total HF length is higher in case 2 than those in case 1. The NF sets and the induced fracture network in case 2 affect the pore pressure distribution in the production stage, see Figure 6c. Owing to the stimulated fractures, the produced fluid rate and cumulative oil production in case 2 are higher than those without NF (case 1), as shown in Figure 7.

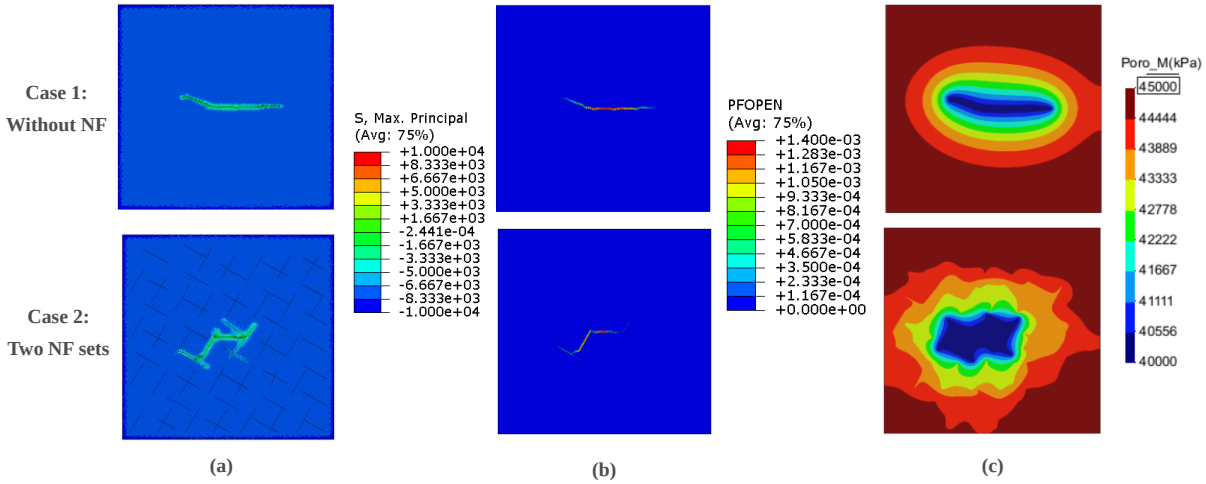

Figure 6. The hydraulic fracturing of the deformable reservoir (Case 1) without NF and (Case 2) considering two fracture sets.

Figure 7. Production performance, (a) oil production rate, and (b) cumulative oil production.

We also investigate the effect of the fluid viscosity (μ) on the NF stimulation and the production performance. We assess hydraulic fracturing treatment in Case 2 (Figure 5b) considering fluid viscosities of 1 cp, 10 cp, and 100 cp. The production stage considers a produced oil with a viscosity of 1 cp in all cases. Figure 8 depicts the case studies of hydraulic stimulation and production stages of Case 2a with μ =1 cp, Case 2b with μ =10 cp, and Case 2c with μ =100 cp. In case 2a, considering a fluid viscosity of 1 cp, the total HF length is shorter than cases 2b and 2c, as shown in Figure 8a. Figure 8b shows that the low viscosity also affects the final aperture of the induced fracture. This behavior is related to higher hydraulic conductivity for lower viscosities in the rock formation, which increases fluid leak-off from the induced fracture into the surrounded porous medium. Then, the relation of fluid viscosity and hydraulic conductivity affects the stimulated fracture network (Figure 8a), the fracture aperture (Figure 8b), the pore pressure distribution (Figure 8c), and consequently, the production

performance as depicted in Figure 9. Although a higher viscosity in case 2c induces a higher fracture aperture than in case 2b (Figure 8b), the total HF length in case 2b is higher than case 2a and 2c(Figure 8a). This effect results in a higher fluid production rate and cumulative oil production in case 2b than in case 2c. Therefore, a good balance between fluid viscosity and rock hydraulic conductivity is necessary to obtain an optimum production performance of the stimulated fractured formation.

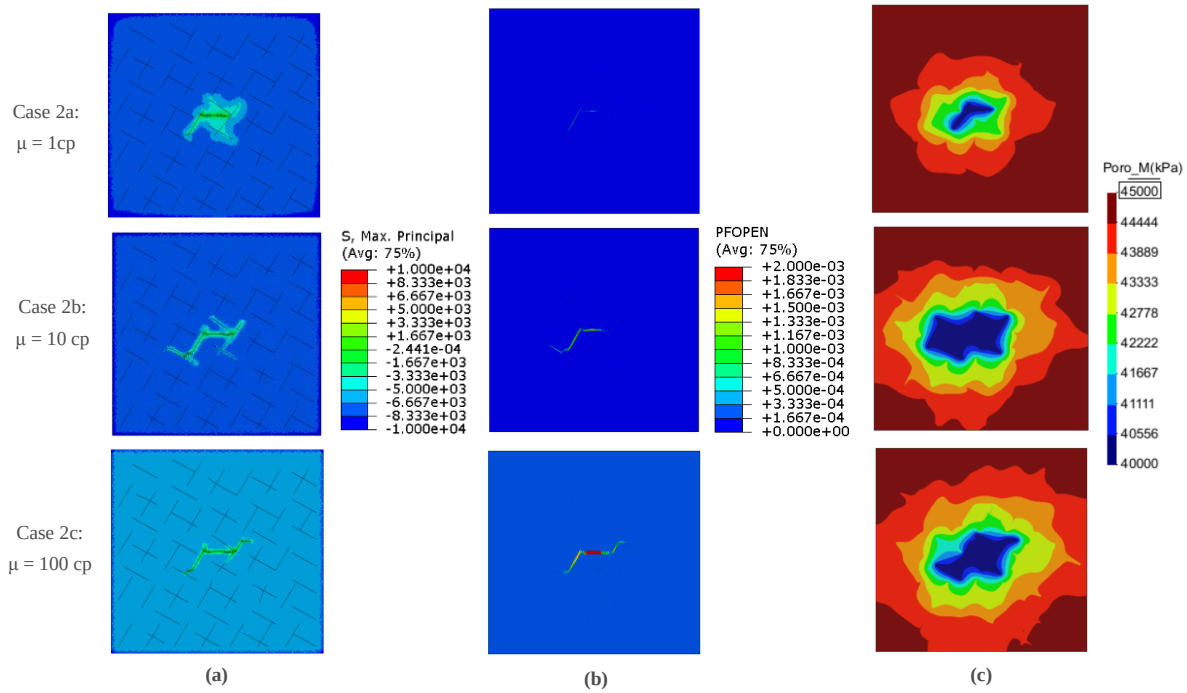

Figure 8. Case studies of hydraulic fracturing, (Case 2a) with μ =1 cp, (Case 2b) with μ =10 cp, and (Case 2c) with μ =100 cp.

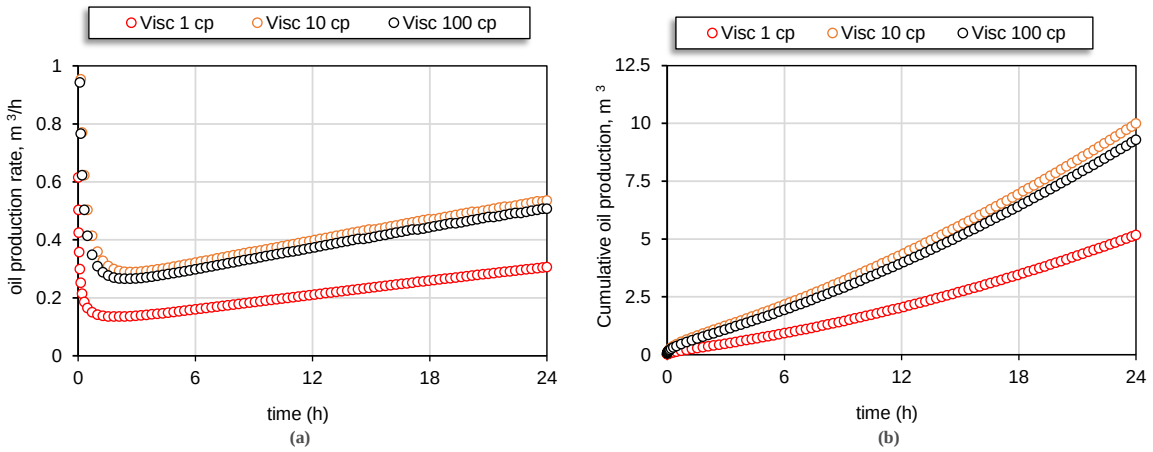

Figure 9. Production performance for different fluid viscosities, (a) oil production rate, and (b) cumulative oil production.

5. CONCLUSIONS

This paper presents a new methodology that integrates fracture propagation models and reservoir simulations to study the effect of natural fractures in the hydraulic stimulation and production performance of naturally fractured reservoirs. The proposed methodology is based on the finite element method (FEM). An intrinsic mesh fragmentation technique is used to simulate non-planar fracture propagation with complex crack patterns. Subsequently, the discrete fracture model (DFM) simulates the induced complex fracture network for production forecasting. Several scenarios considering a

complex fracture network were investigated to understand the dominant factors influencing hydraulic fracturing and the production performance in unconventional reservoirs. The results of the first case study show that natural fractures affect HF geometry and increase production performance. In the second study, the results show that de fluid viscosity used in hydraulic treatment plays an important role in the stimulation and production stages. Fluid with low viscosity induces fractures with a low aperture and vice-versa. Also, low viscosity fluids increase the hydraulic conductivity of the rock formation, enhancing fluid leak-off from the fracture into the surrounding porous media. Consequently, it also reduces fracture propagation. In contrast, high viscosity fluids induce fractures with higher aperture but tend to stimulate less natural fractures. Therefore, a good balance between fluid viscosity and hydraulic conductivity is necessary to obtain an optimum production performance of the stimulated fractured formation.

ACKNOWLEDGEMENTS

This research was carried out in association with the ongoing R&D project registered as ANP n° 20234-1, "SONAR" (PUC-Rio/Petrobras/ANP), sponsored by Petrobras. The authors also gratefully acknowledge support from the Brazilian Funding Agency: Fundação Carlos Chagas Filho de Amparo à Pesquisa do Estado do Rio de Janeiro (FAPERJ) – process E-26/202.928/2019 and E-26/200.781/2019.

REFERENCES

Barbier, E. 2002. Geothermal energy technology and current status: An overview. *Renewable and Sustainable Energy Reviews*, *6*(1–2), 3–65. https://doi.org/10.1016/S1364-0321(02)00002-3

Camacho, G. T., & Ortiz, M. 1996. Computational modelling of impact damage in brittle materials. *International Journal of Solids and Structures*, *33*(20), 2899–2938. https://doi.org/https://doi.org/10.1016/0020-7683(95)00255-3

Cruz, F., Roehl, D., & Vargas, E. do A. 2018. An XFEM element to model intersections between hydraulic and natural fractures in porous rocks. *International Journal of Rock Mechanics and Mining Sciences*, *112*(October), 385–397. https://doi.org/10.1016/j.ijrmms.2018.10.001

Cruz, F., Roehl, D., & Vargas, E. do A. 2019. An XFEM implementation in Abaqus to model intersections between fractures in porous rocks. *Computers and Geotechnics*, *112*(April), 135–146. https://doi.org/10.1016/j.compgeo.2019.04.014

Fatahi, H., Hossain, M. M., & Sarmadivaleh, M. 2017. Numerical and experimental investigation of the interaction of natural and propagated hydraulic fracture. *Journal of Natural Gas Science and Engineering*, *37*, 409–424. https://doi.org/10.1016/j.jngse.2016.11.054

Gutierrez, E. R., Mejía, S. E. C., Roehl, D., & Romanel, C. 2019. XFEM Modeling Of Stress Shadowing In Multiple Hydraulic Fractures In Multi-Layered Formations. *Journal of Natural Gas Science and Engineering*.

Jeffrey, R. G., Zhang, X., & Bunger, A. P. 2010. Hydraulic fracturing of naturally fractured reservoirs. *Thirty-Fifth Workshop on Geothermal Reservoir Engineering, Stanford University, Stanford, California*, 1–3.

Keshavarzi, R., & Jahanbakhshi, R. 2013. Investigation of Hydraulic and Natural Fracture Interaction: Numerical Modeling or Artificial Intelligence? *Effective and Sustainable Hydraulic Fracturing*, 1039–1058. https://doi.org/10.5772/56382

Mejia, C., Roehl, D., Rueda, J., & Quevedo, R. 2021. A new approach for modeling three-dimensional fractured reservoirs with embedded complex fracture networks. *Computers and Geotechnics*, *130*. https://doi.org/10.1016/j.compgeo.2020.103928

Mejia Sanchez, E. C., Rueda Cordero, J. A., & Roehl, D. 2020. Numerical simulation of three-dimensional fracture interaction. *Computers and Geotechnics*, *122*(March), 103528. https://doi.org/10.1016/j.compgeo.2020.103528

Mendes, C. A. T., Gattass, M., & Roehl, D. 2016. The gema framework - An innovative framework for the development of multiphysics and multiscale simulations. *ECCOMAS Congress 2016 - Proceedings of the 7th European Congress on Computational Methods in Applied Sciences and*

Engineering, *4*(June), 7886–7894. https://doi.org/10.7712/100016.2383.6771
O'Sullivan, M. J., Pruess, K., & Lippmann, M. J. 2001. State of the art geothermal reservoir simulation. *Geothermics*, *30*(4), 395–429. https://doi.org/10.1016/S0375-6505(01)00005-0
Potluri, N., Zhu, D., & Hill, A. D. 2005. Effect of Natural Fractures on Hydraulic Fracture Propagation. *Society of Petroleum Engineers*, *94568*. https://doi.org/10.2118/94568-ms
Rueda Cordero, J. A., Mejia Sanchez, E. C., & Roehl, D. 2019a. Hydraulic fracture propagation and its interaction with open and sealed natural fractures. *53nd U.S. Rock Mechanics/Geomechanics Symposium*.
Rueda Cordero, J. A., Mejia Sanchez, E. C., & Roehl, D. 2019b. Hydromechanical modeling of unrestricted crack propagation in fractured formations using intrinsic cohesive zone model. *Engineering Fracture Mechanics*, *221*, 106655. https://doi.org/10.1016/J.ENGFRACMECH.2019.106655
Rueda Cordero, J. A., Mejia Sanchez, E. C., Roehl, D., & Pereira, L. C. 2019. Hydro-mechanical modeling of hydraulic fracture propagation and its interactions with frictional natural fractures. *Computers and Geotechnics*, *111*, 290–300. https://doi.org/10.1016/j.compgeo.2019.03.020
Rueda, J., Mejia, C., Noreña, N., & Roehl, D. 2020. A three- dimensional enhanced dual porosity and dual permeability approach for hydro- mechanical modeling of naturally fractured rocks. *International Journal for Numerical Methods in Engineering*, 1–37. https://doi.org/10.1002/nme.6594
Rueda, J., Mejia, C., Quevedo, R., & Roehl, D. 2020. Impacts of natural fractures on hydraulic fracturing treatment in all asymptotic propagation regimes. *Computer Methods in Applied Mechanics and Engineering*, *371*, 113296. https://doi.org/10.1016/j.cma.2020.113296
Rueda, J., Mejia, E. C., & Roehl, D. 2019. Integrated discrete fracture and dual porosity - Dual permeability models for fluid flow in deformable fractured media. *Journal of Petroleum Science and Engineering*, *175*(December 2018), 644–653. https://doi.org/10.1016/j.petrol.2018.12.053
Shahid, A. S. A., Fokker, P. A., & Rocca, V. 2016. A review of numerical simulation strategies for hydraulic fracturing, natural fracture reactivation and induced microseismicity prediction. *Open Petroleum Engineering Journal*, *9*, 72–91. https://doi.org/10.2174/1874834101609010072
Stephenson, B., Galan, E., Williams, W., MacDonald, J., Azad, A., Carduner, R., & Zimmer, U. 2018. Geometry and failure mechanisms from microseismic in the Duvernay shale to explain changes in well performance with drilling azimuth. *Society of Petroleum Engineers - SPE Hydraulic Fracturing Technology Conference and Exhibition 2018, HFTC 2018*, 1–20. https://doi.org/10.2118/189863-ms
Suppachoknirun, T., & Tutuncu, A. N. 2017. Hydraulic Fracturing and Production Optimization in Eagle Ford Shale Using Coupled Geomechanics and Fluid Flow Model. *Rock Mechanics and Rock Engineering*, *50*(12), 3361–3378. https://doi.org/10.1007/s00603-017-1357-1
Taleghani, A. 2009. Analysis of hydraulic fracture propagation in fractured reservoirs : an improved model for the interaction between induced and natural fractures. *PhD Thesis, UT, 2004*. https://doi.org/10.5829/idosi.wasj.2013.28.11.2005
Wang, H. 2016. Poro-elasto-plastic modeling of complex hydraulic fracture propagation : simultaneous multi-fracturing and producing. *Acta Mechanica*, *227*, 507–525. https://doi.org/10.1007/s00707-015-1455-7
Warpinski, N. R., & Teufel, L. W. 1987. Influence of Geologic Discontinuities on Hydraulic Fracture Propagation. *Journal of Petroleum Technology*, 689–696. https://doi.org/https://doi.org/10.2118/13224-PA
Weng, X. 2015. Modeling of complex hydraulic fractures in naturally fractured formation. *Journal of Unconventional Oil and Gas Resources*, *9*, 114–135. https://doi.org/10.1016/j.juogr.2014.07.001
Xie, J., Huang, H., Ma, H., Zeng, B., Tang, J., Yu, W., & Wu, K. 2018. Journal of Natural Gas Science and Engineering Numerical investigation of effect of natural fractures on hydraulic-fracture propagation in unconventional reservoirs. *Journal of Natural Gas Science and Engineering*, *54*(September 2017), 143–153. https://doi.org/10.1016/j.jngse.2018.04.006
Xie, L., Min, K. B., & Shen, B. 2016. Simulation of hydraulic fracturing and its interactions with a pre-existing fracture using displacement discontinuity method. *Journal of Natural Gas Science and Engineering*, *36*, 1284–1294. https://doi.org/10.1016/j.jngse.2016.03.050
Zhang, F., Damjanac, B., & Maxwell, S. 2019. Investigating Hydraulic Fracturing Complexity in

Naturally Fractured Rock Masses Using Fully Coupled Multiscale Numerical Modeling. *Rock Mechanics and Rock Engineering*, *Vi*(May). https://doi.org/10.1007/s00603-019-01851-3

Zhou, J., Zhang, L., Pan, Z., & Han, Z. 2017. Numerical studies of interactions between hydraulic and natural fractures by Smooth Joint Model. *Journal of Natural Gas Science and Engineering*, *46*, 592–602. https://doi.org/10.1016/j.jngse.2017.07.030

© 2021 Universidad Nacional de Colombia – ISRM, ISSN 2805-6426 *Guillermo Alzate Espinosa (Ed.)*

Wellbore Performance Evaluation: From Reservoir Geomechanics to Near-Wellbore Geomechanics

Rene Alcalde [a]

[a] *BHP, Houston, USA*

ABSTRACT

One of the aspects that impacts wellbore's performance is the ductile behavior that a reservoir-rock can experience when subjected to high evolving compressive effective stresses resulting from depletion. During production, the reservoir-stress path can move within the elastic domain while at the same time, the Near Wellbore (NWB) stress path moves inside the plastic region. Poroelastoplastic deformations induce NWB damages leading to high skin evolution, lowering production, and in some cases forcing well shutins. This paper shows that cumulative stress-strain responses at the reservoir scale level need to be carried onto the near wellbore region to assess properly any productivity or injectivity loss. The goal is to understand better factors affecting NWB performance and provide geomechanical analysis tools to assist interpretation of skin evolution. The analysis shows that reservoir stress paths do not always follow the NWB stress paths. Hence, the NWB region cannot detach its performance from the field scale's response. Results indicate that skin evolution remains associated with pressure fluctuations via permeability changes and, most notably to Volumetric Strain Changes (VSC). This finding allows utilization of volumetric strains as a tracking tool of skin evolution similar to skin monitoring from PTAs. Therefore, it is possible to track skin evolution as an evolution of volumetric strain. Furthermore, VSCs can point out the length and preferential orientations of geomechanical formation damage. As a result, better-inform decisions can be made, for instance, on stimulation type selection, hydraulic fracture impairment, and drawdown pressure limits as part of the wellbore productivity enhancement processes.

KEYWORDS

Formation Damage; Skin; Well Performance; Near Wellbore.

1. INTRODUCTION

It is essential to understand the geomechanical impact of pressure changes in the near-wellbore region; such fluctuations alter the stress state and ultimately the reservoir rock's reaction. Ductile materials exhibit more pronounced effects than brittle rocks, particularly when in situ conditions are such that the wellbore is close to the rock yielding envelopes (Schutjens, P., 2001; Schultz, R., 2005). During production, the reservoir stress path can move within the elastic domain. Simultaneously, the Near Wellbore (NWB) stress path can move inside the plastic region, manifesting as an evolution of wellbore skin. Field observations indicate that NWB damage induced by rock deformations promotes high skin evolution over time, lowering production, and in many cases forcing well shut-ins (Ugoala, O., 2013). The industry faces the need for more applied geomechanics in coupling both reservoir and near wellbore region responses to better understand different field operational issues. For instance, tracking of mechanical skin evolution, estimation of flowing bottom hole pressure limits, completion damage, and induced deformation bands, among others, require geomechanical coupling between the reservoir and the altered zone around wellbores. Based on field observations, this paper illustrates that the stress-strain response at the reservoir-scale level needs to be carried onto the near-wellbore region to assess adequately any productivity loss. After evaluating and discarding all potential causes of skin

development, the cases presented here deal with stress-induced wellbore damage related to production as the only root cause of skin evolution.

2. NEAR WELLBORE REGION CONSIDERATIONS

During the production of a well, the ideal performance is to achieve pressure drawdowns that yield higher rates without productivity loss. However, such drawdowns induce stress distribution in the near-wellbore region producing mechanical damages. Mechanical damage is interpreted as irreversible degradation of strength or stiffness, or alteration of flow properties, due to permanent changes in material fabric for a giving pressure drop around the borehole (Dusseault M., 1992; Sabet, M.A., 1991). Wellbore mechanical damage develops from different drilling processes (fluids invasion, borehole stabilities, partial penetration, etc.), completions operations (fracturing, perforations, etc.), and production. In some cases, mechanical damage from each source can be present simultaneously. In this paper, mechanical damage from drilling and completions is treated as *initial* skin damage. It is possible to identify and assess most of the initial skin damage and incorporate it into reservoir simulations and well performance forecasts. However, skin damage development as production continues is a more challenging task as new wellbore damage mechanisms come into play. Among the potential causes of skin development attributable to production are: (i) asphaltene presence, (ii) scale precipitation, (iii) fines migration, (iv) relative permeability and viscosity changes, and (v) near-wellbore geomechanical yielding. This paper presents examples of accelerated skin development from three different wells. Although not shown here, independent workstreams evaluated all the previously mentioned wellbore skin mechanisms for all three examples. The outcome concludes that near-wellbore geomechanical yielding is the only potential root cause of such damage during production. Therefore, this paper focuses on mechanical damage related to stress-strain changes due to production.

Figure 1 illustrates the reservoir-scale stress path of a ductile reservoir in a Deepwater Gulf of Mexico (GoM) field. The stress trajectory suggests that the risk of shear failure is not of concern for the current depletion levels, but compaction will occur only for the last point of the projected depletion. Generally, from this result, engineers infer that productivity issues will not prevail only until the very end of the reservoir production life. If this behavior is correct, is it valid to assume that the near-wellbore region will follow the same performance as the reservoir-scale stress path? The following sections will try to answer that question.

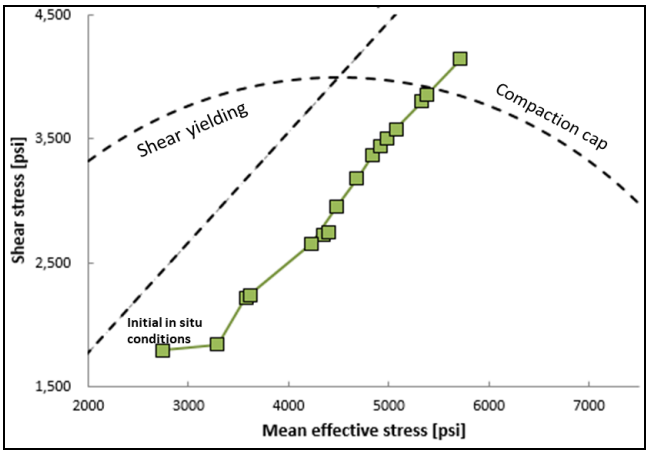

Figure 1. Stress path at reservoir scale for a Deepwater GoM field. The last point of the path indicates compaction. What would be the expected wellbore performance from this reservoir stress path?

3. GEOMECHANICAL MODELING SETUP AND APPROACH

It is essential to incorporate reservoir scale responses from depletion to evaluate stress and strain variations around the wellbore correctly. A 3D geomechanical finite element model was constructed

for a deepwater GoM field. The initial 1D mechanical properties and stress-state input come from drilling events, logs, and formation pressure tests. The magnitude of the minimum horizontal stress, S_{hmin}, was calibrated from leak-off tests (LOT) and mini-frac data and stress azimuth from borehole breakout data. Pressure and temperature from the reservoir at each timestep are upscale from the fluid flow dynamic model.

Figure 2a depicts a cross-section of the 3D pore pressure. The dash-dot black line represents the section gridded for the reservoir, and the outer black dash line refers to the boundaries of the external geomechanical grid. There are low pore pressures associated with salt bodies in the field (top left of Figure 2a) and compartmentalized reservoir sections where production is ongoing. Evidence of shear failure comes from the known presence of faults and deformation bands from image logs. Therefore, in addition to calibration of stress magnitudes and orientations, shear deformations have been used, as an extra parameter, to calibrate and benchmark the geomechanical model. Figure 2b shows the accumulation of total volumetric strains in the field after ten years of production. These deformations developed at the exact well locations where wellbore failures occurred as the confining pressure changed. As a last comment related to 3D far-field modeling, tuning of shear strains from the observed deformation bands provides proper calibration of strain levels pre and post-production. Coupling the wellbore region to the reservoir scale response is possible by explicitly incorporating the cylindrical wellbore geometry including casing and cement. Thus, cumulative strains from the reservoir scale serve as input data to the near-wellbore model. This paper aims to illustrate stress changes effects in the NWB region; therefore, it will not discuss the details of the 3D modeling any further.

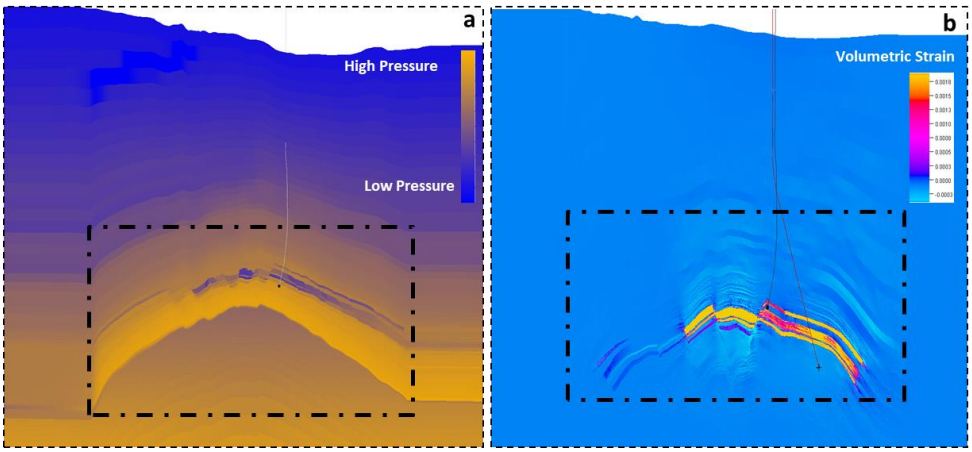

Figure 2. Cross-section of the 3D geomechanical grid after ten years of production for (a) Pore pressure and (b) Cumulative total volumetric strains. The dash-dot black line represents reservoir grid limits. The outer black dash line refers to the external geomechanical grid boundary.

3.1. General features of the constitutive rock behavior

As pore pressure changes due to production or injection, the shear and mean effective stresses will increase or decrease within the reservoir. Subsequently, the wellbore wall and regions near the wellbore will experience the same fluctuations because of the borehole's related pressure drawdowns. Once effective stresses reach the rock material's mechanical failure limits, plastic deformations at both reservoir and near wellbore scales will occur. The geomechanical yielding criterion used to describe far-field stresses also applies to NWB regions. The only difference is that an explicit wellbore geometry is utilized, and cumulative strains must be accounted for from far-field deformation as production progresses. Failure to carry out stress-strain responses from the reservoir scale level to the near-wellbore zone will underestimate borehole damage risks.

The selected modeling approach uses the modified Critical State Cam-Clay model to describe the rock's ductile constitutive behavior. It constrains the wellbore's geomechanical damage using the two typical rock yielding limits. (i) Shear yield behavior, including dilation bands with shear and (ii)

Compaction yield behavior with grain crushing and irrecoverable permeability reduction (pore collapse).

The yielding criterion is represented in the *p*-*q* space, where *p* is the mean effective stress, and *q* is the shear stress. The modified criterion can be written as follows (Zoback, M.D. 2007):

$$q^2 - M^2 p(2p_c - p) = 0 \tag{1}$$

Equation (1) represents a family of ellipses passing through the origin where *M* and P_c are material parameters (Figure 3). *M* characteries the material's shear strength and can be expressed as M=*q*/*p* (it defines the cap curvature). p_c is a strain hardening force evolving with loading, usually referred to as the critical state pressure; while *p* and *q* are given by:

$$p = \frac{1}{3}(\sigma_1 + \sigma_2 + \sigma_3) \tag{2}$$

$$q = \frac{1}{2}\sqrt{(\sigma_1 - \sigma_2)^2 + (\sigma_2 - \sigma_3)^2 + (\sigma_1 - \sigma_3)^2} \tag{3}$$

The maximum *q* value in the yield boundary is $q=M\ p_c$, which provides a straight line known as the critical state line (CSL). The yielding surfaces in Figure 3 mark the boundary between the elastic and plastic deformations domains. The intersection of the yield locus with the *p* axis defines the consolidation pressure *p** (*p**=2p_c) and establishes the onset of inelastic compaction. Increasing values of *p** will describe a series of end caps. The upper left part of the curve defines the shear localization domain with dilation above the CSL. In the examples presented here, the presence of wellbore failure for either of the two failure mechanisms allowed the M values' calibration.

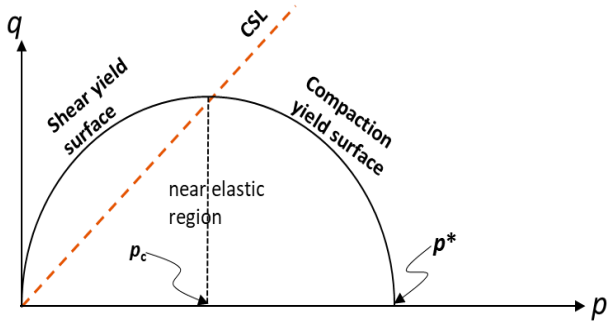

Figure 3. Modified Cam Clay yield surface in *p*-*q* space.

4. CASE STUDY DESCRIPTION

This section describes three examples of skin evolution over time and associated with geomechanics for wells in a deepwater GoM field where the reservoir rock behaves in a ductile manner. Case 1 and Case 2 exemplify accelerated damage from producers, and Case 3 shows skin stabilization from an injector.

4.1. Geomechanical skin in producers: Case 1

Case 1 relates to a producing well with an initial high skin of +43 units and initial high oil rates. Once in production, and according to PTA's monitoring, the skin gradually increases. After eight months of production, the skin builds to +180 units reducing the production rate by ~73%, leading to the well's shut-in. Figure 4 illustrates the reservoir scale stress path for Case 1 (here, reservoir scale refers to

approximately 500 ft radius). Notice that it is the same reservoir stress path shown in Figure 1. In Figure 4, a series of permeability end caps are plotted for increasing values of p^* to indicate permeability reductions. The orange triangle indicates conditions when the well was open to production. Offset depletion has induced permeability reduction (approximately 4%) from the initial in situ field conditions (A) to the time the well is drilled and open to production (B). Such permeability decrease would add some mechanical damage to the initial skin estimation. When reservoir compaction reaches the irreversible plastic limit represented by point C, the permeability will be reduced by 24%. Plastic compaction occurs only for the last reservoir depletion point (D). As mentioned earlier, there is no indication of productivity decline from this reservoir scale path during the first years of production. It does not provide insights into the well's accelerated skin development observed within the first year of production.

A better approach to infer the development of mechanical skin damage is to examine the stress path at the near-wellbore scale. High-stress concentration at the wellbore wall can also propagate in the NWB region when high loadings/unloadings are imposed on elastoplastic materials, which in turn may induce further damage away from the wellbore. This propagation occurs because ductile rocks may fail at sufficiently large plastic deformations and may not necessarily fail at the yield point. Such failure can be conclusive only with the adequate determination of stiffness and cumulative total strains in different zones of the interacting reservoir-wellbore system. Thus, geomechanical coupling of cumulative total strains from the reservoir scale with the NWB region provides better stress-strain estimations. Figure 5 shows the stress path at the near-wellbore scale for Case 1. When considering coupling to the NWB, the stress trajectory shows different failure states. First, the NWB zone is already under the shear damage regime (shear yielding shade area) when the well is open to production (point A). As production continues, the NWB region moves from point A to point B (when the well was shut-in), corresponding to the highest observed skin value. The mechanical skin damage in this well is due to shear failure associated with shear dilation bands. It does not necessarily mean that permeability will increase as it appears that the material's level ductility/brittleness and properties, such as porosity, control shear yielding. As shown by Zhu et al., 1997, when porosity is greater than 15%, permeability decreases under shear loadings. Therefore, this wellbore damage is most likely related to induced shear bands. The observed failure condition could also be a potential source of fines migration or sanding (the material is less ductile in this location), which are still valid mechanics under such shear yielding regime. However, no correlation or evidence has been observed in the field for any of those two damage mechanisms. Finally, if at some point in time, the NWB region reaches a condition below the critical stale line (C-D), it would be possible to increase pressure drawdowns until the second failure state occurs (point E, Figure 5). Such failure refers to the inelastic compaction limit, which is still applicable for the latest depletion point, similar to the forecast from the far-field stress path (point D in Figure 4).

Figure 6 plots total volumetric strain as a function of radial distance from the wellbore wall. It shows that volumetric strain increases over time from the initial drawdown until the well was shutin. Dilatancy (negative volumetric strains) of 1.5% is induced around the wellbore (approximately 3 ft). Away from the wellbore, volumetric strains become compressive, denoting shearing with potential permeability impairment up to a distance of approximately 170 ft. Beyond this distance, volumetric strains return to a zero value but only in the orientation of S_{Hmax}. It is essential to mention that these volumetric strain changes manifest in one preferential orientation and do not always develop circumferentially. Thus, a barrier separating a "dilation zone" from a "compressive zone" occurs at a short distance from the NWB zone.

Figure 7 illustrates the skin values from PTA and the average total volumetric strains as a function of time. Volumetric strains track the accelerated skin values from PTA over the well's entire monitoring period before the shutin (point B). The result implies that volumetric strain changes can fairly track skin evolution qualitatively. Although not presented here, it is worth mentioning that plotting only plastic strains will track skin development as well. Nevertheless, in that case, any skin build-up associate with elastic behavior would be miss from any interpretation.

For completeness of this case, reservoir surveillance from PTA is shown as independent analysis. For the well in Case 1, pressure build-ups (BU) do not suggest an impact of compaction (Figure 8). PTA modeling of the BUs response requires modeling reservoir geometry as parallel barriers opening up on each side of the well at a distance of ± 150 ft. It also requires having up to two times mobility and storability increases in the two unbound directions. It is worth noting that the PTA model resembles the geomechanical model's volumetric strain behavior at a similar radial distance.

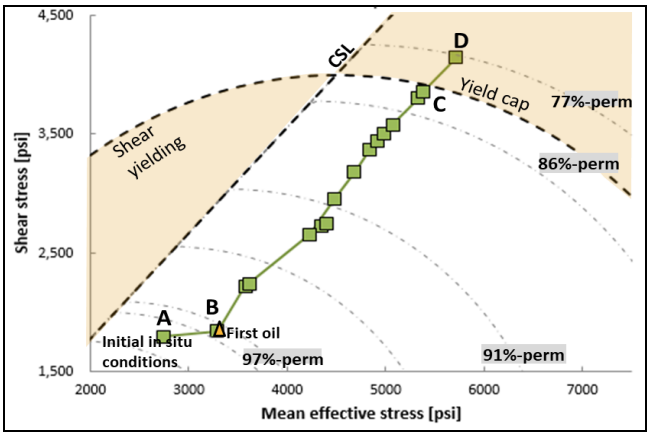

Figure 4. Reservoir-scale stress path for Case 1. The series of dash-dot curves indicate permeability degradation end caps for increasing values of p^*. Plastic compaction will occur only for the last depletion point (D).

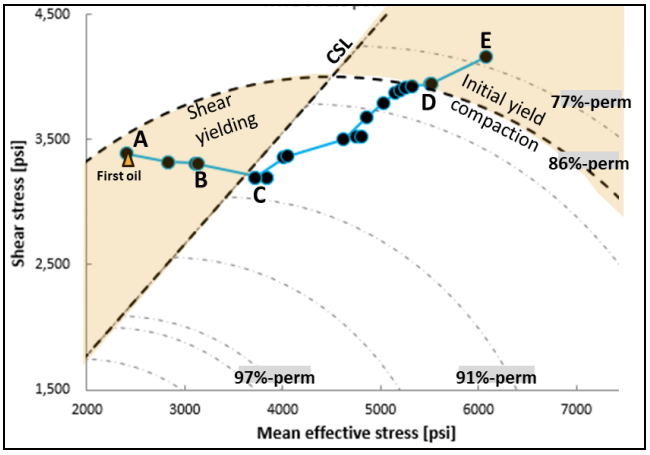

Figure 5. Near-wellbore scale stress path for Case 1. NWB region is under shear yielding at the onset of production. Well shutin at Point B. Plastic compaction will occur only for the last depletion point (E).

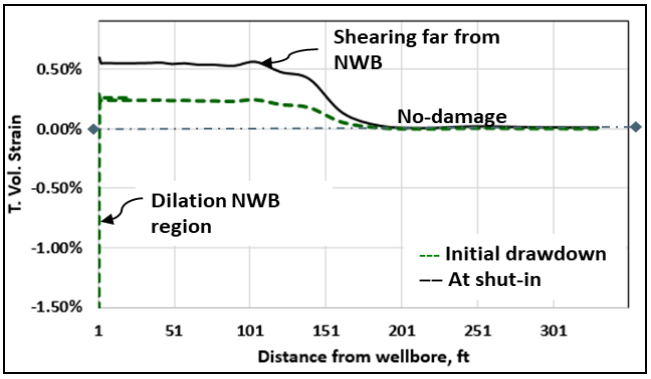

Figure 6. Total volumetric strain as a function of radial distance for Case 1. Changes in volumetric strain suggest shearing of rock material with permeability impairment for a distance of approximately 170 ft in S_{Hmax} direction.

4.2. Geomechanical skin in producers: Case 2

Case 2 relates to a producing well with an initial high skin of +6 units and initial high oil rates. According to PTA's monitoring after the well's start-up, the skin remains stable for about five months. After ten months of production, the skin builds to +150 units reducing its production rate by ~80%, followed by a well shut-in (point B).

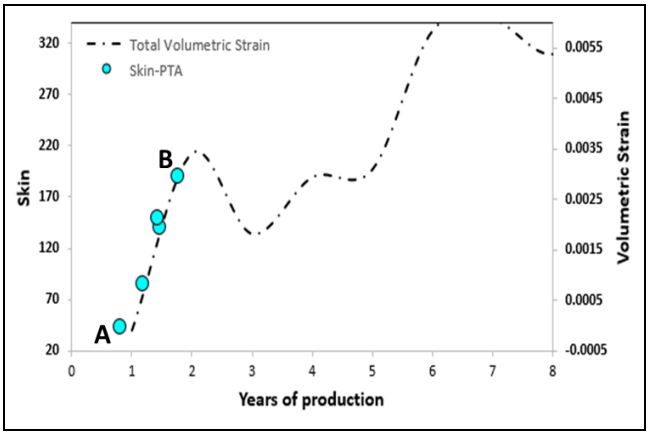

Figure 7. Tracking of skin evolution from PTA with volumetric strains for Case 1. Point B indicates well shutin.

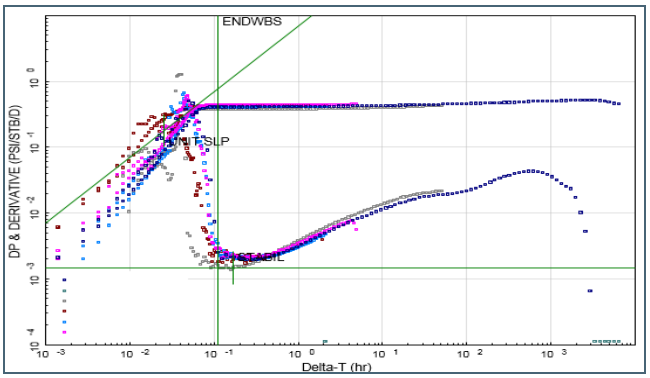

Figure 8. Pressure build-up (BU) and PTA modeling for Case 1. The modeling requires flow barriers to obtain a match, which resembles the geomechanical model's volumetric strain behavior at a similar radial distance.

Offset depletion induces a minor permeability reduction from the initial in situ field conditions. Once the wellbore is in production, elastic compaction occurs, reaching a permeability reduction of 22% without any plastic compaction for the last pressure depletion stage (point C). There is no indication of potential productivity loss within the reservoir's pressure depletion range from this reservoir stress path. As in Case 1, the current stress trajectory does not provide insights into the well's accelerated skin development and well shutin.

Figure 10 shows the stress path at the near wellbore scale for Case 2. There is no risk associated with compaction at the NWB scale in this path, which agrees with the reservoir scale stress path's prediction (C). However, at the start-up of the well, the NWB region is already under complete shear failure. As the pressure drawdown increases, localization of shear bands occurs as the wellbore region conditions move towards the CSL (B). This operation (A-B path) accelerates skin development and leads eventually to the well shutin.

The total volumetric strain as a function of radial distance from the wellbore wall is plotted in Figure 11. The compressive volumetric strain increases approximately 0.30% and gradually drops to zero volumetric strain for distances past 165 ft but only in the orientation of S_{hmin} (up-dip direction of the producing reservoir). As in Case 1, shear deformation is the leading cause of wellbore failure suggesting a permeability impairment within 110 ft from the wellbore.

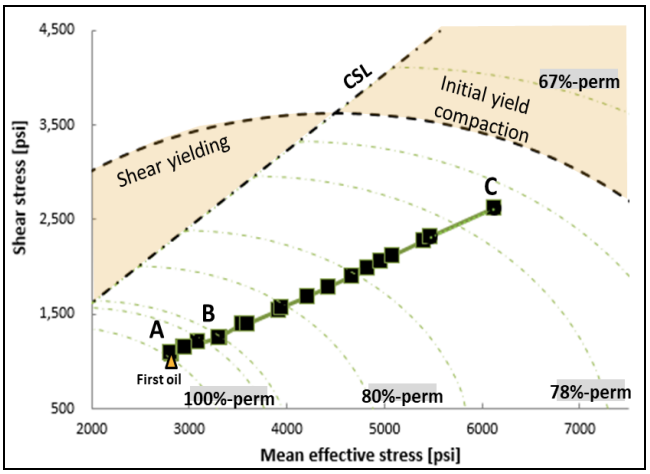

Figure 9. Reservoir-scale stress path for Case 2. The dash-dot curve series indicates end caps of permeability degradation for increasing values of p^*. Plastic compaction did not occur.

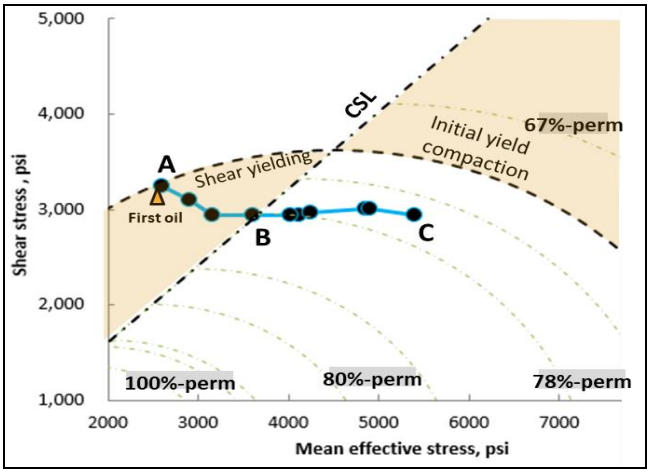

Figure 10. Near wellbore stress path for Case 2. NWB shear failure is already in place at the onset of production. Point B indicates when the well was shut-in.

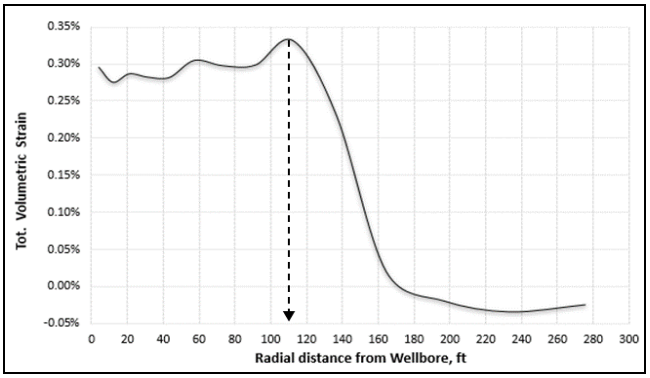

Figure 11. Total volumetric strain as a function of radial distance at the time of well shutin for Case 2. Changes in volumetric strain suggest shearing of rock material with permeability impairment up to a distance of approximately 110 ft in S_{hmin} direction.

Figure 12 illustrates skin values from PTA and total volumetric strains as a function of time. Skin assessments from PTA increase rapidly as pressure drawdown increases. There is a remarkable agreement of skin tracking compared to volumetric strain results. The idea of monitoring skin damage with volumetric strain changes as a predictive tool gets reinforce with this case. The corresponding independent PTA modeling requires the well to be between intersecting barriers located ± 500 ft with a

25% decrease in mobility and storativity. Such geometry implies the need for some sort of baffles at a distance from the wellbore wall to get a good match of the PTA response, as shown in Figure 13. Pressure BUs do not suggest an impact of compaction. At DeltaT of 200 hrs, the derivative re-stabilizes as indicative of a mobility increase, reflecting an improvement in the reservoir away from the wellbore, which correlates with the geomechanical model's strain behavior beyond 165 ft. Like Case 1, this deformation manifests on a particular wellbore orientation (it is not circumferential).

4.3. Geomechanical skin in injectors: Case 3

Case 3 relates to an injector well with an initial skin value of +1. Upon injection, wellbore skin starts to decrease and remains stable over the injection period. Figure 14 illustrates the reservoir scale stress path of this well. The orange triangle, point A, indicates the initial field in situ conditions, and point B indicates the beginning of injection operations.

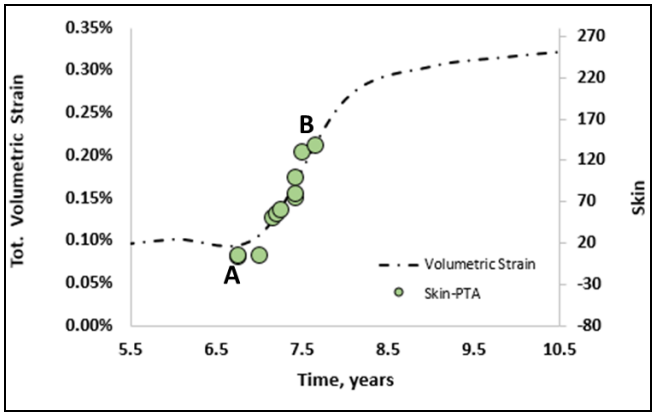

Figure 12. Tracking of skin with volumetric strains for Case-2. Well's shut-in at point B.

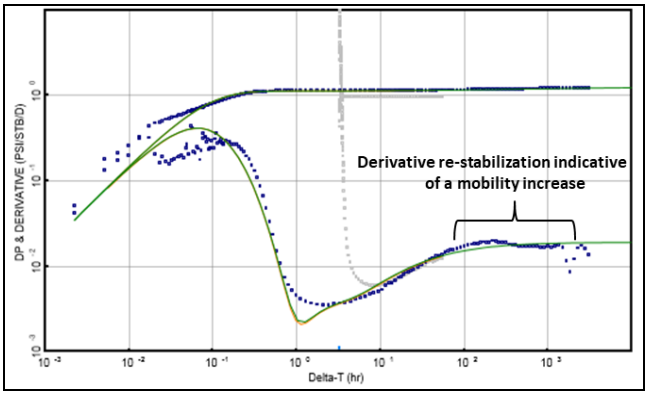

Figure 13. Pressure build Up (BU) and PTA modeling for Case 2. Restabilization indicates an improvement in the reservoir away from the wellbore. It resembles the geomechanical model results.

As injection pressure increases, the reservoir conditions move towards the critical state line (point C) and remain fluctuating on top of it as injection continues. In this particular case, the near-wellbore scale behavior under injection is very similar to the reservoir scale stress path. The dilatant limit is reached quickly with relatively small pore pressure increases due to the initial high pressure confining of the injector and the rock material's ductility. As a result, the points on top of the CSL are deformed at constant plastic volume as injection continues. Induced volumetric strains are under dilatancy conditions in the NWB region for a radius of 1.5 ft approximately. At radial distances greater than 10 ft, strains become compressive, showing radial symmetrical deformation away from the wellbore without preferential orientation in this case. Figure 15 shows skin values from PTA and the total volumetric strains as a function of time. It is important to mention that the well was hydraulically fractured initially before injection. That is why the skin is negative, and because the hydraulic fracture was not modeled, the volumetric strain does not decrease initially. Once conditions are in equilibrium,

volumetric strains fairly track skin stabilization for this injector. The volumetric strain curve forecasts a low risk of skin development in the forthcoming years.

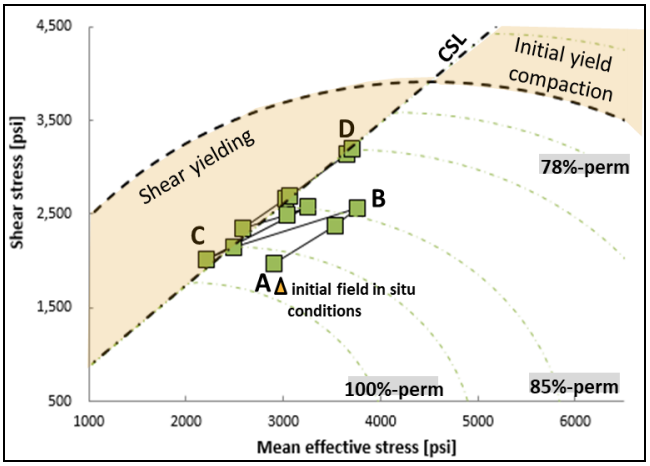

Figure 14. Stress path for Case 3. A-B path reflects offset depletion. (B-C-D) Stress path for both reservoir and NWB scale. Injection starts at point B. When conditions reach the CSL (C) deformation occurs at constant plastic volume.

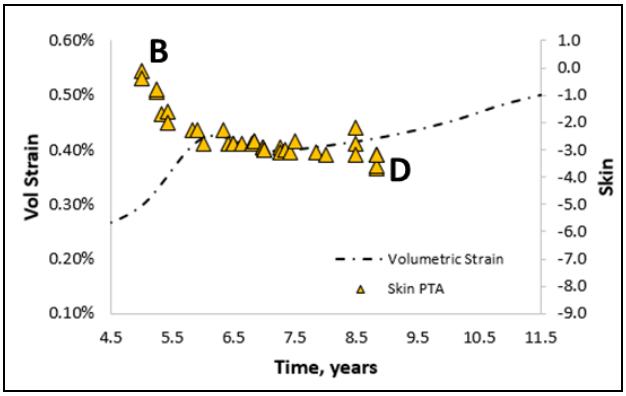

Figure 15. Tracking of skin evolution with volumetric strains for Case 3.

5. CONCLUSIONS

Field examples in this paper express the importance of coupling field stress-strain responses to near-wellbore modeling and the utility of using volumetric strain for monitoring wellbore skin. The general outcomes from the above discussion are:

1. In some instances, reservoir stress paths provide a decent forecast of failure risk at both reservoir and NWB scales. However, several factors affect the conditions under which the scale differences become more notable.
2. Shear dilation does not always lead to permeability improvement as field experience indicates that the material's ductility and porosity control it.
3. Initiation and propagation of plastic damage around the NWB region have been correlated with actual wells shut-ins in the field when other damage mechanisms have been discarded.
4. It is possible to track skin evolution due to production or injection using strain changes as a predictive tool, similar to PTA monitoring. Strain changes will not predict skin damage quantitatively, but it is expected to forecast skin tendencies.
5. Upper and lower limits of flowing bottom hole pressure must be defined during drawdown operations so that the near-wellbore region remains away from the dilatant and compacting yielding zones.

6. Most importantly, strain changes give the potential to determine the distance and orientation affected by deformations in the NWB region. Such understanding will facilitate the treatment of future completions.

REFERENCES

Dusseault, M.B. and Gray, K.E., 1992. Mechanisms of Stress-Induced Wellbore Damage. *SPE 23825. SPE intl. Symposium on Formation Damage control held in Lafayette, Louisiana, February 26-27, 1992.*

Fjær, E., R.M. Holt, P. Horsrud, A.M. Raaen, R. Risnes. 2008. *Petroleum Related Rock Mechanics*. 2nd Edition. Amsterdam. Elsevier.

Jaeger J.C., Cook, N.G.W., Zimmerman, R.W. 2007. *Fundamentals of Rock Mechanics*. Fourth edition. Blackwell Publishing.

Sabet, M.A., 1991. *Well Test Analysis. Contributions in petroleum geology & engineering; 8*. Gulf Publishing Company

Schultz, R., Siddharthan, R., 2005. A general framework for the occurrence and faulting of deformation bands in porous granular rocks. *Tectonophysics 411 (2005) 1–18.*

Schutjens, P., Hanssen, T., Hettema, M., Merour, J., 2001. Compaction-induced porosity/permeability reduction in sandstone reservoirs: data and model for elasticity-dominated deformation. *SPE 71337. SPE Annual Technical Conference & Exhibition held in New Orleans, Louisiana, 30 September–3 October 2001.*

Ugoala, O., Gad. K.H., Whittle, T.M., Stone, M., Butter, M., Mahmoud, H.S., 2013. Time Lapse PTA to Determine the Impact of Skin, Reservoir Compaction, and Water Movement on Well Productivity Loss: a Field Example from WDDM, Egypt. *SPE 164668. North Africa Technical Conference & Exhibition held in Cairo, Egypt, 15–17 April 2013.*

Zhu., W. and Wong T., 1997. The transition from brittle faulting to cataclastic flow: Permeability evolution. *Journal of geophysical research, Vol. 102, No B2, pages 3027-3041, February 10, 1997.*

Zoback, M.D. 2007. *Reservoir Geomechanics*. New York; Cambridge University Press.

Application of Seismic Attributes and Spectral Decomposition to Enhance Fault Interpretation, Case Study from Middle Magdalena Valley Basin, Colombia.

Mateo Acuña-Uribe[a], María C. Pico-Forero[b], Paul Goyes-Peñafiel[c], Darwin C. Mateus[d]

[a, b] *Escuela de geología, Universidad Industrial de Santander, Bucaramanga, Colombia.*
[c] *Escuela de Ingeniería de Sistemas e Informática, Universidad Industrial de Santander, Bucaramanga, Colombia.*
[d] *Instituto Colombiano del Petróleo - Ecopetrol, Piedecuesta, Colombia.*

ABSTRACT

Fault interpretation in seismic volumes is an essential task to understand the structural geology of the subsurface and a key role in decision-making related to well planning and reducing operational risks. During the last decades, it has developed seismic attributes based on different algorithms which preserving and highlighting amplitude discontinuities that typically are associated with faults. Moreover, distinct methodologies and workflows have been proposed to highlight and identify geological faults in seismic data as of the unification of those attributes. In the present project, we analyze different types of seismic attributes available in seismic interpretation software such as dip-steered median filter, structural smoothing, amplitude contrast, variance, dip illumination, fault likelihood and likewise integrates spectral decomposition by continuous wavelet transform and swarm algorithms to attenuate the random seismic noise, preserve the amplitude discontinuities, smooth the seismic reflectors and highlight the lineal features and finally skeletonize them. Through seismic data conditioning, edge detection and edge enhancement we obtain an ant-tracking volume in which geological faults, their locations, extensions, orientations are more accurately identified and at the same time enables the automatic extraction of fault planes. Additionally, owing to the good definition of the fault planes on the final ant-tracking it is possible to extract the density fracture attribute to identify qualitatively high fracture density zones to be avoided for future wellbore paths. The different seismic attributes and the spectral decomposition were tested by using a seismic volume of an oil field located in the Middle Magdalena Valley basin characterized by a high random noise level and complex geological structures. The final ant-tracking volume mainly distinguishes two fault systems with NW-SE trend: 1. Conjugate normal faults altogether with scissors faults and 2. High angle reverse faults associated with tectonic inversion events.

KEYWORDS

Seismic Attributes; Seismic Interpretation; Geological Faults; Automatic Fault Extraction.

1. INTRODUCTION

The new challenges of the oil and gas industry require the development of new techniques and technologies to reduce the risk failure during drilling operations. Using seismic data is possible to analyse the geological configuration of the subsurface. With the development of seismic attributes at the end of the last century, the way in which seismic interpreters elaborate geological models has changed. Seismic attributes reveal characteristics, relations, and patterns of seismic information that cannot be easily perceived (Chopra & Marfurt, 2007). Seismic attributes are tools to infer geology from seismic data (Barnes, 2001). Therefore, they help to solve dissimilar problems associated with the interpretation and characterization of the subsurface geological configuration. For instance, identifying fault patterns and structural styles. Furthermore, they contribute to the mitigation of a certain number of wellbore stability problems such as lost circulation or overpressure, that result in

non-productive times and economic effects. Planning the wellbore trajectory to avoid possible areas of fluid losses near faults is a way to prevent lost circulation. These areas could also be related to formations with natural fractures and areas surrounding fault planes where rocks tend to have a brittle behavior. So that, the presence of surrounding fractures allows the circulating fluid to filtrate through the formation, increasing the risk of lost circulation (Lavrov, 2016).

Fault networks play a fundamental role during drilling, and fault detection is one of the most important steps in seismic interpretation during exploration and development stages (Basir, 2013). Mainly, seismic interpretation is crucial in seismic volumes with a high presence of random noise where identification and fault characterization trace to trace becomes a complex task. In previous research, Dalley *et al.* (1989) developed two of the first attributes for structural interpretation, known as dip and azimuth. Since then, a series of attributes known as coherence, similarity and semblance were proposed to fault interpretation (Bahorich and Farmer, 1995; Marfurt *et al.*, 1998; Gresztenkorn and Marfurt, 1999; Randen *et al.*, 2000) which are based on algorithms to compare similarities between adjacent traces. Roberts (2001) and Al-Dossary & Marfurt (2006) demonstrated the effectiveness of the curvature attribute as a geometric measure seismic reflector for fault detection. More recently, other attributes were presented as a tool to delineate faults and predicting their structural trend as amplitude contrast (Aqwary & Boe, 2011), dip illumination (Aqwari *et al.*, 2012) and fault likehood (Hale, 2013). On the other hand, ant-tracking is an algorithm based on swarm intelligence (Colorni *et al.*, 1991; Dorigo & Gambardella, 1997) which sharpens the faults and optimizes the automatic extraction of the fault planes. Therefore, the use of different fault-sensitive seismic attributes allows fault networks to be identified easier and saving time and effort in fault interpretation.

2. GEOPHYSICAL DATA

The seismic data is a post-stack time migrated seismic volume that covered an area of approximately 44 km^2 in the Middle Magdalena Valley basin, Colombia. The seismic grid is composed of in-lines ranged from 270 to 450, and crosslines ranged from 270 to 570. A total of 180 inlines and 300 crosslines were used. The length of the inline was 6048.06 meters, and the interval of the inline was 40.3 meters. The length of the crossline was 7254.72 meters, and the interval of the crossline was 20.16 meters. The total record length was 5.9 seconds, and the sample interval was 2 milliseconds. The sample value format was the International Business Machines (IBM) floating point. The amplitude spectrum in the seismic data starts from 10 Hz to 95 Hz. The usable spectrum covers frequencies from 10 Hz to 70 Hz.

2.1. Data quality

Different time intervals are more susceptible to seismic noise than others. Moreover, they are associated with different frequency ranges. The resolution of the seismic data, the fault interpretation process and the quality of the extracted structural attributes are highly related to the frequency content. Signal, noise, and signal-to-noise ratio (S/N) attributes were extracted to determine the seismic noise distribution and the signal-to-noise ratio of the data (Figure 1). It is to be noted that the presence of seismic noise varies along the z-axis. The zone of interest 1 has the lowest ranges of signal-to-noise ratio and higher levels of seismic noise. In addition, the shallowest interval (0 - 500 ms) is where the highest levels of seismic noise are evidenced, which increases the uncertainty regarding the presence of faults. In contrast, the zone of interest 2 corresponds with low and intermediate values of seismic noise, resulting in medium-high values of the signal-to-noise ratio related to fault zones free of seismic noise. Moreover, on the S/N attribute, it is possible to detail certain linear features closely related to geological faults. Nevertheless, due to the high levels of seismic noise, these linear features are strongly masked, making the fault interpretation process more difficult on the original seismic data.

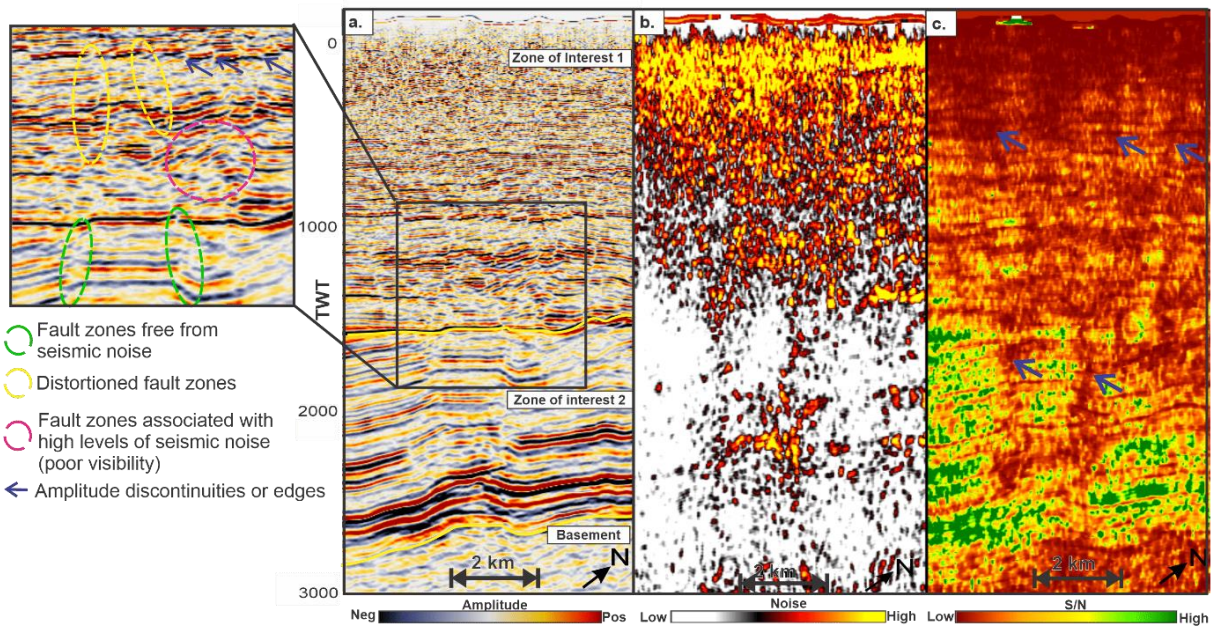

Figure 1. a) Crossline section of the original seismic data, b) noise attribute and c) signal-to-noise ratio attribute.

3. METHODOLOGY

The use of mathematical and geometric attributes (Tarner, 1999; Barnes, 2016) is important to identify accurately faults in complex geological structures and noisy seismic volumes. These kinds of attributes make possible the random seismic noise attenuation, amplitude discontinuities preservation, seismic reflectors smoothing, and linear features highlighting. Alternatively, to skeletonize amplitude discontinuities detected by the geometric attributes, the use of ant-tracking based on swarm algorithms has been demonstrated by Pedersen *et al.* (2002)**.**

A final ant-tracking volume is obtained through seismic data conditioning, edge detection, and edge enhancement. As a result, geological faults, their locations, extensions, and orientations are more accurately identified. Additionally, the final volume enables the automatic extraction of fault planes. Finally, due to the good fault definition, it is feasible to identify zones with a higher probability of fracture density with seismic attributes.

3.1. Seismic data conditioning

Seismic data conditioning is decisive to remove random noise that hides amplitude discontinuities associated with faults. To increase the signal-to-noise ratio within the seismic conditioning we have extracted different filters as the dip-steered median filter (DSMF) (Tingdahl, 1999), edge-preserving smoothing (EPS) (Luo *et al.*, 2002; AlBinHassan *et al.*, 2006), structural smoothing (Iske and Randen, 2005) and the fault enhancement filter (FEF) (Jaglan *et al.*, 2015). These mathematical attributes exhibit different seismic characteristics. For instance, on the structural smoothing, the lineaments lose definition and do not retain their linear expressions (Figure 2d). The FEF attribute has a high seismic noise sensitivity, considering that delineated amplitude discontinuities and slight changes on the reflectors continuity that were not precisely related to faults (Figure 2e). The obtained seismic events from the FEF attribute are more discontinuous and faulted, which are not related with the geological reality of the subsurface. In contrast, the DSMF attribute smoothed the seismic events without degrading or eliminating the fault expression (Figure 2b) and the EPS attribute generated a sharp effect in the linear features making easier its visualization (Figure 2c). These attributes are the most efficient in terms of seismic data conditioning among the evaluated filters. Alaei (2012) established that spectral voices could be associated with less random noise and better discontinuity details. Therefore, the spectral decomposition was employed by the Continuous Waveform Transform (CWT) method to attenuate the remaining seismic noise from the mentioned filters (Sinha *et al.*, 2005; Chopra

& Marfurt, 2018). The frequency decomposition was developed as follows: the EPS volume is spectrally decomposed into eight volumes of peak frequency with the highest power values (dB). The spectral voices 31.5, 39.5, 44.5, 50, 54.5, 61, 65, and 70 Hz of the usable spectrum are obtained owing to low association with random seismic noise. Each of these volumes is suitable for geometric and structural seismic attributes extraction.

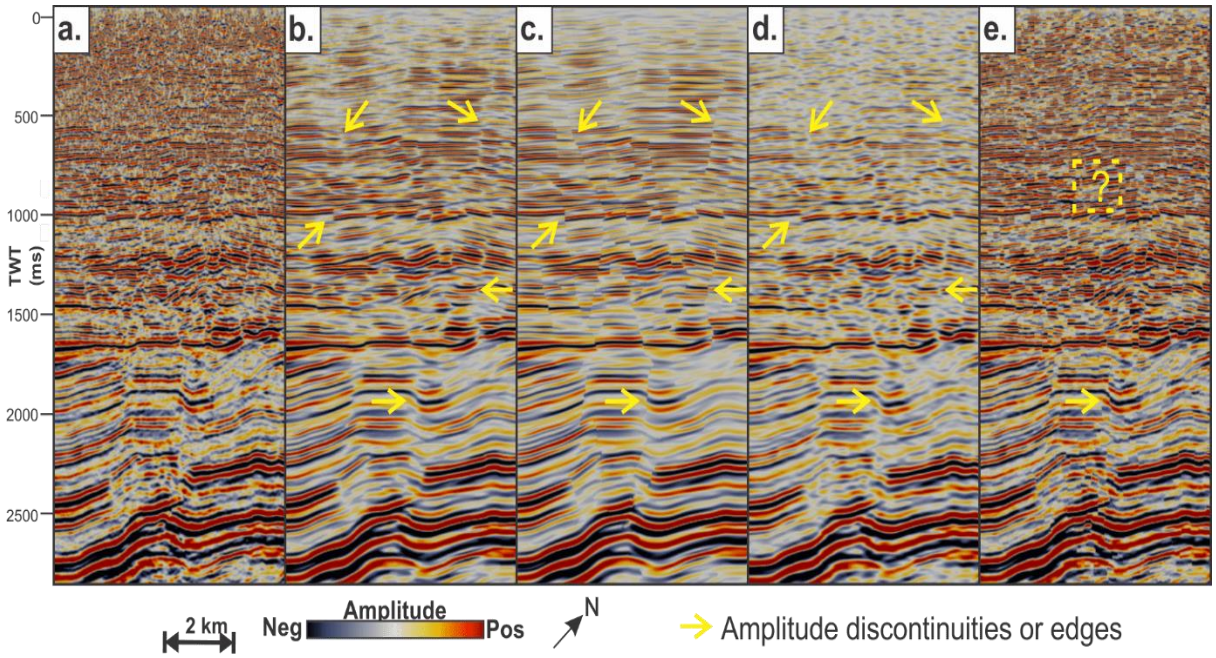

Figure 2. a) Raw seismic volume, b) dip-steered median filter, c) edge-preserving smoothing, d) structural smoothing and e) fault enhancement filter.

3.2. Edge detection

Structural, geometric or edge detection seismic attributes greatly accelerate the fault interpretation process. In addition, geometric attributes provide a quantitative measure of how significant a given discontinuity is in relation to others (Chopra *et al.*, 2014). After the data seismic conditioning process, the detection of amplitude edges associated with faults based on the geometric and structural attributes was developed. Similarity (Tingdahl and De Groot, 2003), semblance (Marfurt *et al.*, 1998), amplitude contrast (Aqwari & Boe, 2011), variance (Van Bemmel & Pepper, 2000), gradient magnitude (Schlumberger, 2007), dip illumination (Aqwari *et al.*, 2012), most positive curvature (Roberts, 2001), and fault likelihood (Hale, 2013) attributes were extracted in this stage. The peak-frequency volumes created in the last stage are used to compute each geometric attribute. Those volumes associated with the same attribute were combined via addition to obtain a frequency-limited volume. The addition process has been recommended in previous research by Dewet *et al.* (2016).

The similarity enhances seismic features not associated with faults (Figure 3a). The gradient magnitude algorithm is not computed along the dip reflectors, highlighting a large part of these (Figure 3e). While on the semblance and variance attributes, a large part of the lineaments lacks good vertical continuity (Figure 3b and 3d). In contrast, the dip illumination, amplitude contrast, most positive curvature, and the fault likelihood are the most efficient attributes in terms of detection of amplitude discontinuities. Since their algorithms are calculated along of the reflector immersion and subsurface structures, thus distinguishing seismic events unassociated with faults, and preserving the amplitude discontinuities generating fewer seismic artifacts. Consequently, the linear anomalies have been highlighted efficiently with a good vertical structural continuity. Frequency-limited geometric attribute volumes are the product of the present stage.

3.3. Edge enhancement

To improve the structural lineaments detected by the structural and geometric seismic attributes, we employed the ant-tracking attribute to enhance the linear features that are related to the general structural trend of the faults (Pedersen *et al.*, 2002; Schlumberger, 2007). The ant-tracking is extracted from the four volumes of band-limited attributes: amplitude contrast (Figure 4a-b), dip illumination (Figure 4c-d), most positive curvature (Figure 4e-f), and fault likelihood (Figure 4g-h). To integrate each of the characteristics represented on the four ant-tracking volumes, we have combined them via addition getting a final ant-tracking volume (Figure 4i-j). The result improves the continuity of the lineaments and attenuates the remaining artifacts from the independent ant-tracking volumes.

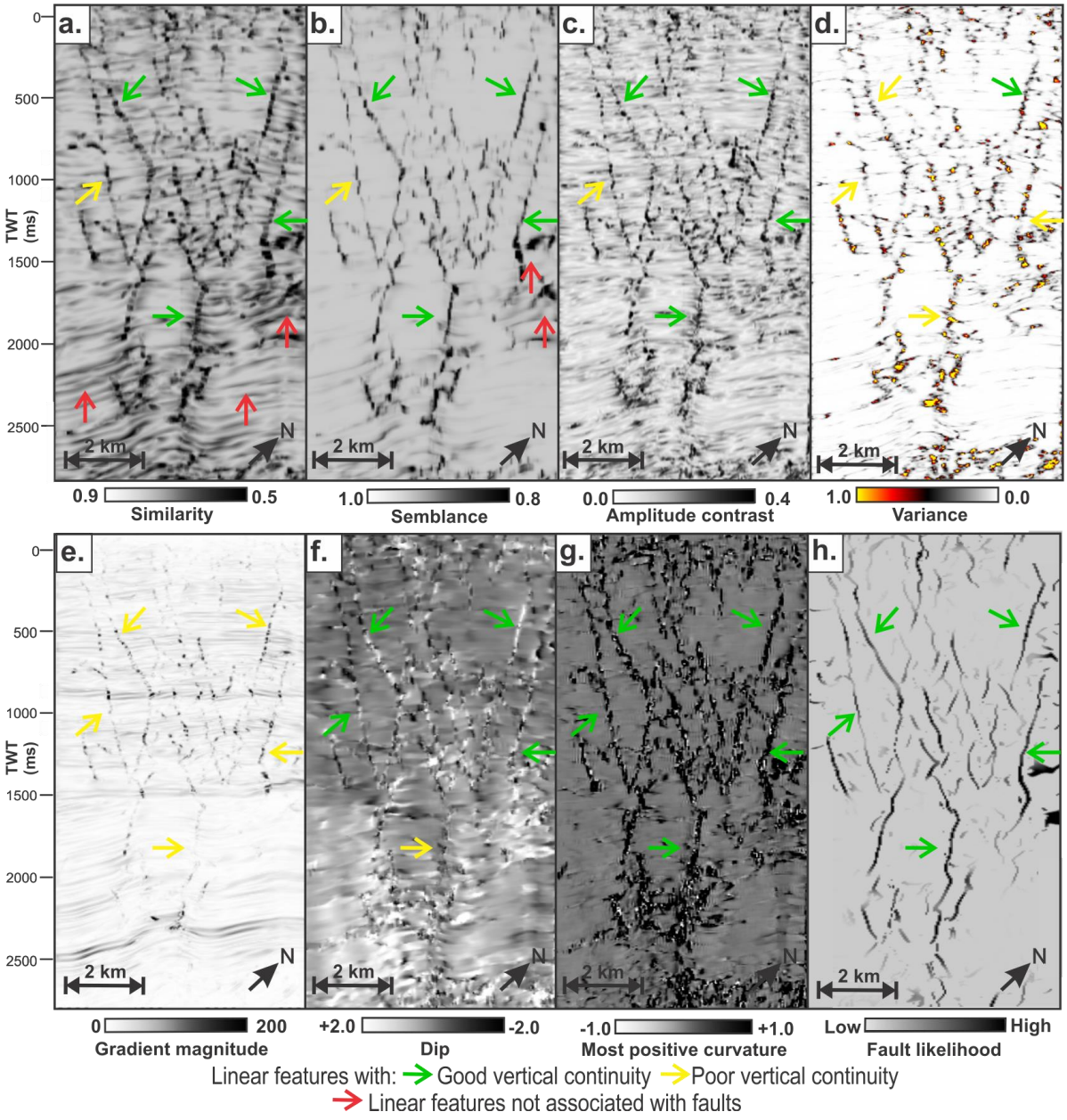

Figure 3. a) Similarity, b) semblance, c) amplitude contrast, d) variance, e) gradient magnitude, f) dip illumination, g) most positive curvature, h) fault likelihood.

3.4. Fault planes extraction

Due to the good vertical and lateral continuity of the highlighted and enhanced amplitude discontinuities, we extract the fault patches automatically that follow the structural lineaments. Some patches must be manually merged because they are associated with a unique fault plane. Figure 5 presents a comparison between the fault patches generated automatically, the edited fault patches, and the manually picked faults. It is to be noted that the size, shape, distribution, and orientation of the automatic faults are similar to the manual interpreted faults. Reliable fault planes are extracted automatically by the final ant-tracking volume, thus saving human effort and large amounts of time typically invested during the manually picked process of the faults.

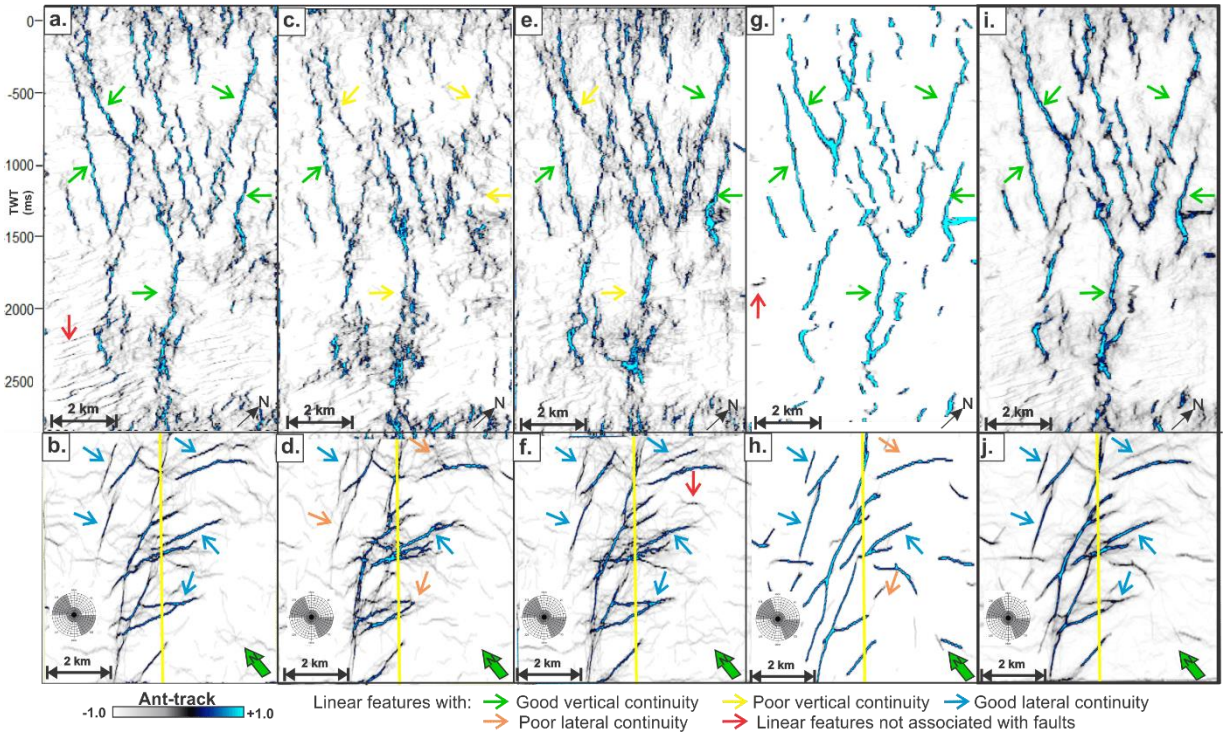

Figure 4. Ant-tracking extracted from: (a-b) amplitude contrast, (c-d) dip illumination, (e-f) most positive curvature, (g-h) fault likelihood and (i-j) final ant-tracking volume.

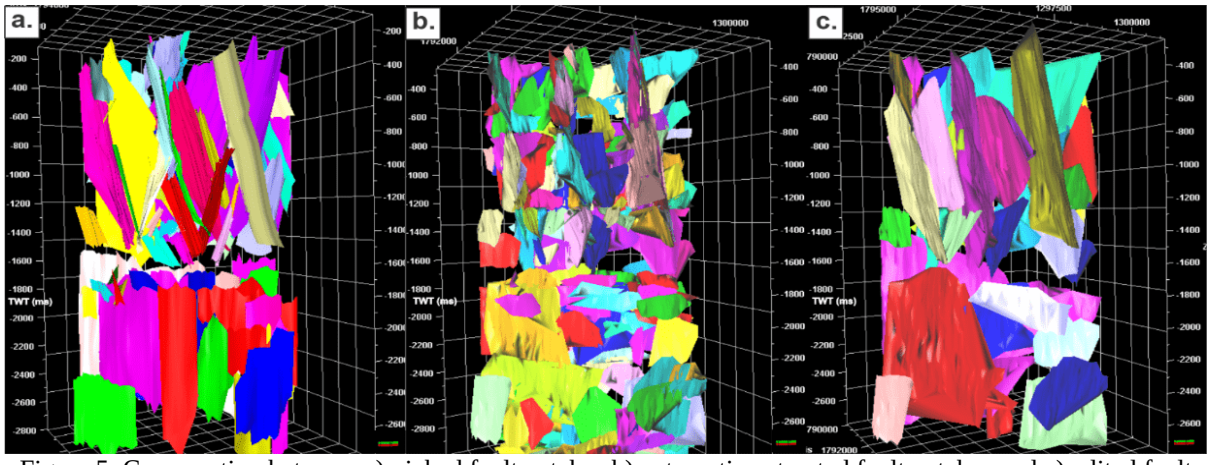

Figure 5. Comparation between a) picked fault patches b) automatic extracted fault patches and c) edited fault patches. It is to be noted the similarity between the planes in (a) and (c), this demonstrates the efficacy of final ant-tracking revealing the presence of faults.

4. RESULTS AND INTERPRETATIONS

We present a structural style analysis in the evaluated seismic volume located in the Middle Magdalena Valley basin using nine aleatory reflectors that are not related to geologic formations. The faults were interpreted using the final ant-tracking volume (Figure 6c). Two structural styles are evidenced: the first structural style is distinguished in the deep zone or zone of interest 2, between the time sections 1600 and 2600 ms. It is characterized by the presence of asymmetric anticline-synclinal pairs associated to reverse faults of high dip angle with slip that move reflectors up to 75 ms vertically (Figure 6a-b). The high dip angle suggests a change in the kinematics of the faults from normal to inverse. Predominantly, these reverse faults have strike between 180º-240º, 270º-315º and to a lesser extent 25º-45º and 115º-135º (Figure 6e). This kinematics change is related to the tectonic inversion event documented in the Middle Magdalena Valley basin by Sarmiento-Rojas (2001). The second structural style is associated with the shallowest zone, between the time sections 0 and 1600 ms. In the zone, a low relief anticline with a NE-SW trend stands out and conjugated normal faults and scissor faults characterized by their X-shape (Figure 7b-c). These faults have a high dip angle, opposite dip directions, and strike between 45º-90º and 210-255º, marking a NE-SW trend in this area as evidenced in the stereograms in Figure 6d. Furthermore, the slip reaches up to 40 ms vertically. The interpreted faults in the zone of interest 1 concur with the youngest faults of the Middle Magdalena Valley basin characterized by their normal kinematics evidenced by Mojica & Franco (1990).

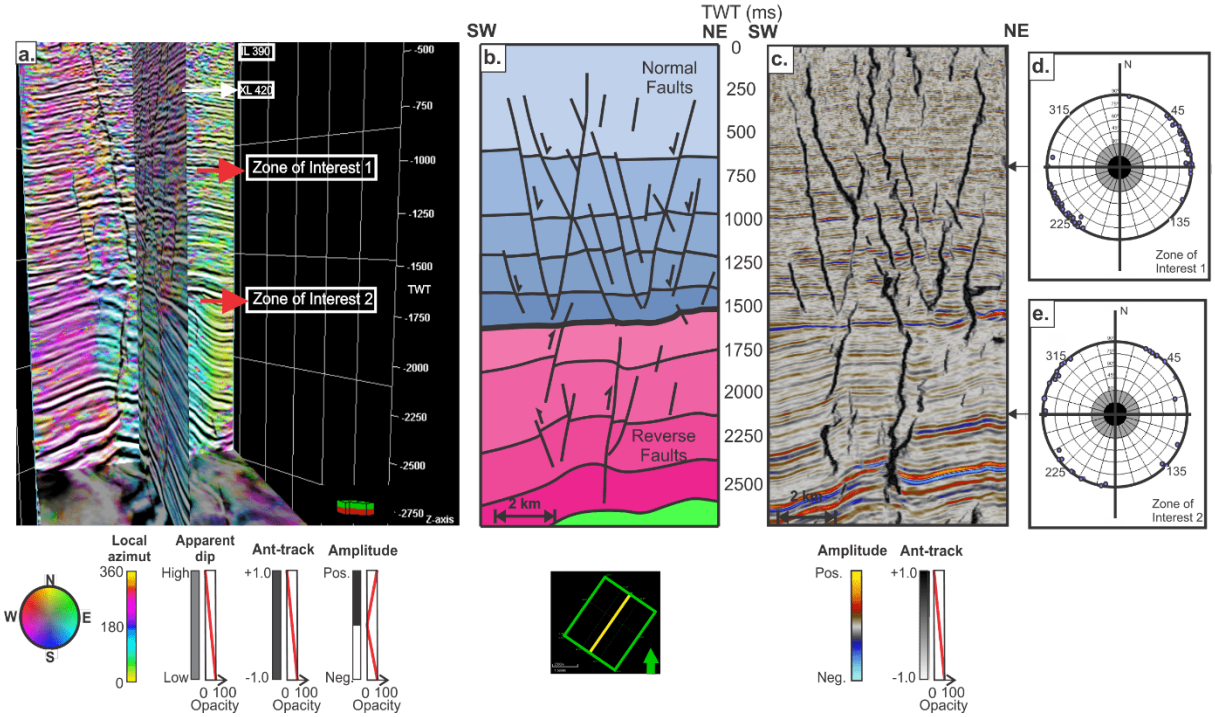

Figure 6. a) Vertical slices corendered with the final ant-tracking (blackish monochromatic palette), seismic amplitude (dichromatic palette), apparent dip (greyish monochromatic palette) and local azimuth (polychromatic palette) (Marfurt, 2015), b) fault model interpreted from the results obtained with the final ant-tracking, c) final ant-tracking, d) stereogram showing the distribution of faults in zone of interest 1 and e) stereogram of zone of interest 2.

Fault zones have complex internal architectures owing to the small-scale variations and high-density fracture areas, which can affect the wellbore stability (Fasching & Vanek, 2011). To identify the high-density fracture zones from a seismic point of view, we extracted the fracture density attribute from the final ant-tracking volume. The fracture density attribute is effective delineating the locations of the maximum number of fractures in a radius of 100 meters, representing areas with high probability of fracture density. These areas can be identified like regions with the highest risk to loss circulation (Jaglan *et al.*, 2015). Corendering the fracture density, the ant-tracking and the raw seismic volumes, the areas with the highest probability of fracture density are highlighted generally near to the fault

planes (Figure 7). Accordingly, those areas can be avoided in the well trajectory to mitigate loss circulation. The zones exposed in red and yellow tones are known as fault zone (Fasching & Vanek 2011). However, the zones with low or non-fracture presence are denoted with bluish and purple tones indicating low probability of fractures.

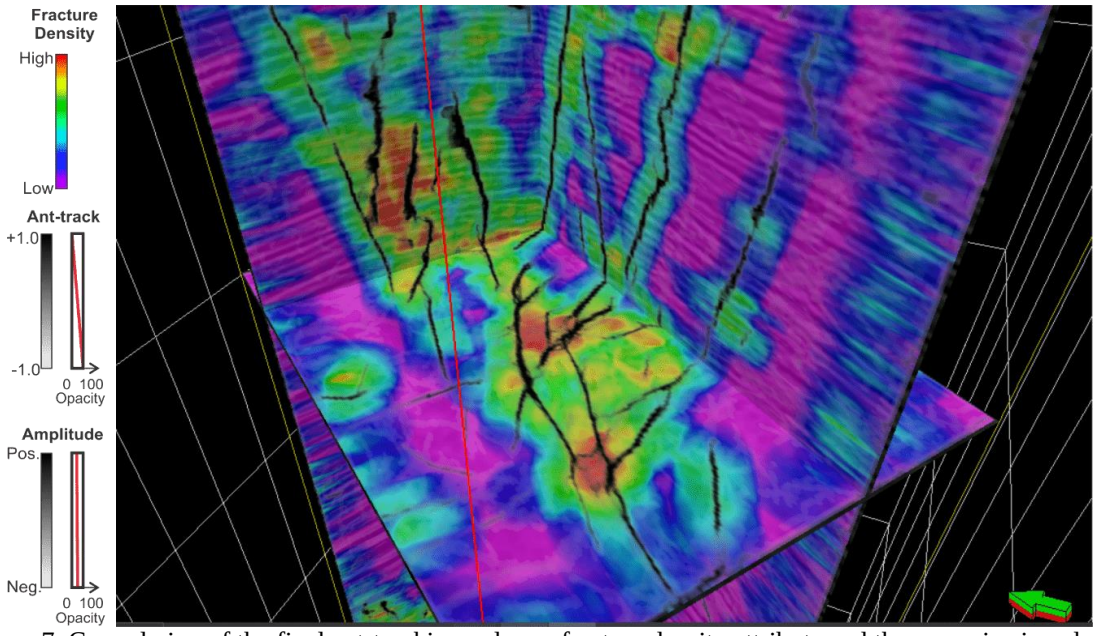

Figure 7. Corendering of the final ant-tracking volume, fracture density attribute and the raw seismic volume.

5. DISCUSSION

This study presents an application of spectral decomposition and seismic attributes for fault identification in seismic volumes with high levels of random noise, illustrated through a case study from Middle Magdalena Valley Basin. By combining diverse types of seismic attributes and spectral decomposition, it is generated a final ant-tracking that captures faults associated with amplitude discontinuities. Moreover, the attribute computation and fault extraction time were approximately four hours, which is less in comparison with the twenty hours spent in the manual fault interpretation. It is important to emphasize that the parameterization of the seismic attributes is relevant since each seismic data is different. Therefore, before computing or extracting each of the mentioned attributes, vertical window, spatial patterns, and the optimal parameters must be analysed. This process enhances the linear features associated with fault and while attenuating the random seismic noise. Some unexpected linear features have been highlighted by the different extracted ant-tracking volumes, especially those related to high noise level zones and which are unassociated with real faults. The use of seismic attribute workflows to enhance fault interpretation has been demonstrated by several authors (Basir *et al*., 2013; Dewet & Alissa, 2016; Kumar & Mandal, 2018). Besides, the final ant-tracking is efficient in comparison to other ant-tracking volumes result of past methodologies (Pepper & Bejarano, 2005; Zhang *et al*., 2017). Figure 8 illustrates the structural details, the delineation of faults is poorly imaged due to the random seismic noise and overlapped features that make the fault images chaotic. Nevertheless, the final ant-tracking generates a thinned amplitude discontinuities images where the fault details are enhanced. Additionally, in the fracture density volume the high-risk loss circulation zones are highlighted which are closely associated with fault planes.

The case study discussed above shows the importance of the use of seismic attributes to enhance the fault interpretation, obtaining improved images of geological structures from noisy seismic data. Finally, the computed attributes can be used to interpretation applications, such as identifying faults for overpressure, wellbore stability analysis, reservoir compartmentalization, and oil migration routes analysis.

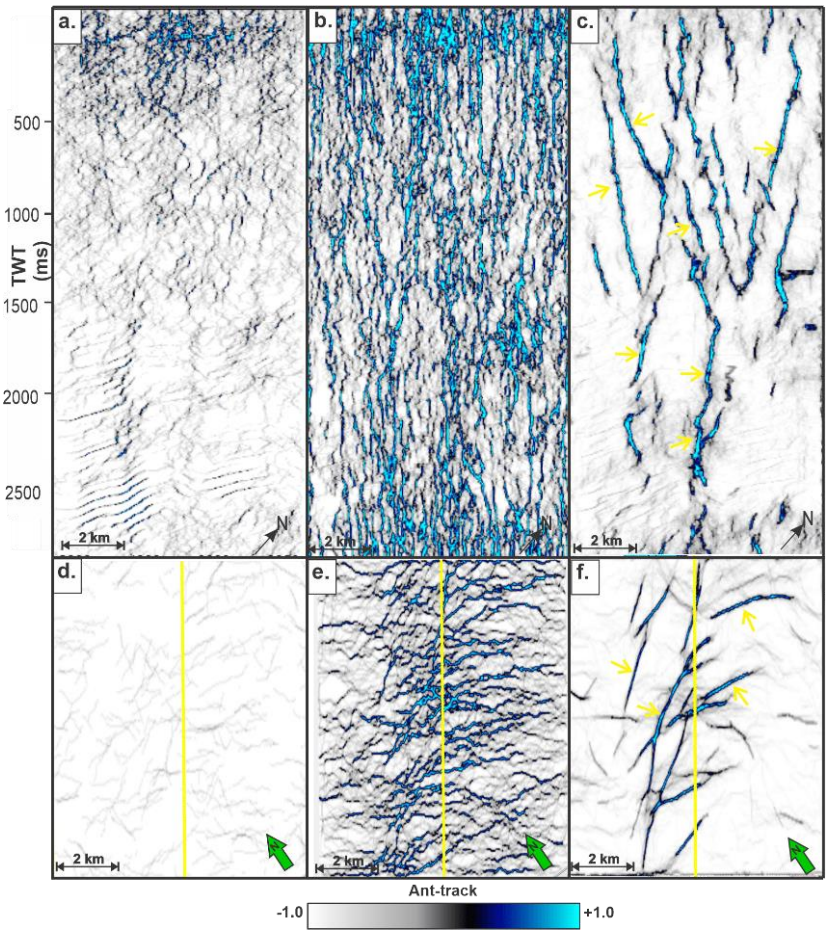

Figure 8. Comparation between other ant-tracking workflows: a) Pepper & Bejarano (2005), b) Zhang *et al*., (2017) and c) the final ant-tracking proposed in the present project.

6. CONCLUSIONS

The use of different types of seismic attributes and spectral decomposition reduces the spent time for the 3D fault interpretation in noisy seismic data and complex geological structures, generating a reliable fault model. Moreover, by means of fracture density volume and the final ant-tracking volume, the high-density fracture areas are delineated. These areas are identified as regions with the highest risk to loss circulation contributing to the wellbore trajectory planning.

Due to the considerable suppression of seismic random noise and the seismic attributes integration, a clear, coherent, and reliable ant-tracking volume is obtained in comparison with other ant-tracking volumes result from past seismic attribute methodologies.

From the geological fault model, two structural styles were interpreted. The first one is observed in the zone of interest 2 characterized by high-angle reverse faults associated with tectonic inversion events described in the Middle Magdalena Valley Basin by Sarmiento-Rojas (2001). The second structural style is observed in the zone of interest 1 dominated by conjugated normal and scissors faults evidenced in Mojica & Franco (1990).

ACKNOWLEDGEMENTS

The authors thank Ecopetrol S.A. for permission to publish the results of this work and for providing software licenses and the members of Wellbore Stability research group who provided valuable suggestions and edits.

REFERENCES

Alaei, B., 2012. Improved fault imaging by interpretation of frequency decomposition and fault attributes, example from Mid Norwegian Sea. *3rd International Conference on Fault and Top Seals - From Characterization to Modelling.*

AlBinHassan, N., Luo, Y., & Al-Faraj, M., 2006. 3D edge-preserving smoothing and applications. *Geophysics*, 5-11.

Al-Dossary, S., & Marfurt, K., 2006. 3D volumetric multispectral estimates of reflector curvature and rotation. *Geophysics*, 41-51.

Aqwari, A. a., & Boe, T. H., 2011. Improved fault segmentation using dip guided and modified 3D sobel filter. *SEG San Antonio 2011 Annual Meeting*, 999-1003.

Aqwari, A. A., Weinzierl, W., Daber, R., & Boe, T. H., 2012. Directional guided seismic attributes and their use in assisting structural, stratigraphic and lithological interpretation. *SEG Las Vegas 2012 Annual Meeting*, 1-5.

Bahorich, M., & Farmer, S., 1995. 3D seismic discontinuity for faults and stratigraphic features: The coherence cube. *The Leading Edge*, 1053-1058.

Barnes, A., 2001. Seismic Attributes in your Facies. *CSEG recorder*., 41-47.

Barnes, A. E., 2016. *Overview of poststack seismic attributes. En A. E. Barnes, Handbook of Poststack seismic attributes* (pags. 13-25). Yale: Society of Exploration Geophysicists.

Basir, H. M., Javaherian, A., & Yaraki, M. T., 2013. Multi-trace attribute ant-tracking and neural network for fault detection: a case study of an Iranian Field. *Journal of Geophysics and Engineering*, 1-10.

Brouwer, F., 2007. *Creating a good Steering Cube.* OpendTect dGB Earth Sciences website.

Chopra, S., & Marfurt, K., 2007. Seismic attributes for prospect identification and reservoir characterization. *Interpretation Journal - SEG*, 59-83.

Chopra, S., & Marfurt, K., 2018. Multispectral, multiazimuth and multioffset coherence. *Interpretation.*

Colorni, A., Dorigo, M., & Maniezzo, V., 1996. Distributed Optimization by Ant Colonies. *European Conference on Artificial Life*, Elsevier Publishing. , 134-142.

Dalley, R. M., Gevers, E., Davies, D., Gastaldi, C., Ruijtenberg, P., & Vermeer, G., 1989. Dip and azimuth displays for 3D seismic. *First Break.*

Dewet, D. T., & Alissa, H. A., 2016. *Spectral Similarity Fault Enhancement*. *Interpretation*, 149-159.

Dorigo, M., & Gambardella, L. M., 1997. Ant Colony System: A Cooperative Learning Approach to the Traveling Salesman Problem. *IEEE Transactions On Evolutionary Computation*, 53-66.

Fasching, F., & Vanek, R., 2011. Engineering geological characterisation of fault rocks and fault zones. *Geomechanics and Tunnelling* , 183-194.

Gersztenkorn, A., & Marfurt, K., 1999. Eigenstructure-based coherence computations as an aid to 3-D structural and stratigraphic mapping. *Geophysics*, 1468-1479.

Hale, D., 2013. Methods to compute fault images, extract faults surfaces, and estimate faults throw from 3D seismic images. *Geophysics*, 33-43.

Iske, A., & Randen, T., 2005. *Mathematical methods and modelling in hydrocarbon exploration and production.* Springer. Germany.

Jaglan, H., Qayyum, F., & Huck, H., 2015. Atributos sísmicos no convencionales para la caracterización de fracturas. *First Break*, 101-109.

Kumar, P. C., & Mandal, A., 2018. Enhancement of fault interpretation using multi-attribute analysis and artificial neural network (ANN) approach: a case study from Taranaki Basin, New Zealand. *Exploration Geophysics*, 409-424.

Lavrov, A., 2016. *Preventing Lost Circulation. En A. Lavrov, Lost circulation: mechanisms and solutions.* Gulf professional publishing (pags. 163-203). Gulf Professional Publishing.

Luo, Y., Marhoon, S., & Alfarajh, M., 2002. Edge-preserving smoothing and applications. *Acquisition - Processing*, p136-158.

Marfurt, K., 2015. Techniques and best practices in multiattribute display. *Interpretation*, B1-B23.

Marfurt, K. J., Kirlin, R., & Farmer, S. L., 1998. 3-D Coherency attributes using a semblance-based coherency algorithm. *Geophysics*, p1150-1165.

Pedersen, S. I., Randen, T., Sonneland, L., & Oyvind, S., 2002. Automatic Fault Extraction using Artificial Ants. *SEG Exposition and Exhibition 72nd Annual Meeting*. Salt Lake City, Utah , USA.

Pepper, R., & Bejarano, G., 2005. Advances in Seismic Fault Interpretation Automation. *AAPG Annual Convention.*

Randen, T., Monsen, E., Signer, C., Abrahamsen, A., Ove, H. J., Saeter, T., & Schlaf, J., 2000. Three-Dimensional Texture Attributes for Seismic Data Analysis. *SEG 2000 Expanded Abstracts.*

Roberts, A., 2001. Curvature attributes and their application to 3D interpreted horizons. *First Break,* 85-100.

Schlumberger., 2007. *Interpreter`s Guide to Seismic Attributes.*

Sinha, S., Routh, P. S., Anno, P. D., & Castagna, J. P., 2005. Spectral Decomposition of Seismic Data with Continuous-wavelet Transform. *Geophysics*, 19-25.

Tarner, M. T., 1999. *Seismic attributes, their classification and project utilization.* Rock Solid Images. Houston, Texas.

Tingdahl, K., 1999. Improving seismic detectability using intrinsic directionality. *Earth Sciences Centre, University of Gothenburg*, Paper B194.

Tingdahl, K., & De Groot, P., 2003. Post-stack-dip and azimuth processing. *Journal of Seismic Exploration,* 113-126.

Van Bemmel, P., & Pepper, R., 2000. *Seismic signal processing method and apparatus for generating a cube of Variance values.* United States Patent - 6,151,555, 1-24.

Zhang, T., Lin, Y., Liu, K., Aamer, A., & Stephen, G., 2017. Fault Visualization Enhancement Using Ant Tracking Technique and Its Application in the Taranaki Basin, New Zealand. *SEG Technical Program Expanded Abstracts 2017.*

© 2021 Universidad Nacional de Colombia – ISRM, ISSN 2805-6426 *Guillermo Alzate Espinosa (Ed.)*

Porosity and permeability behavior at different stress path and drainage condition in an uncemented and reconstituted porous medium

Juan C. Correa-Álvarez[a], Guillermo A. Alzate-Espinosa[a], Edson F. Araujo-Guerrero[a]

[a] *Universidad Nacional de Colombia, Medellín, Colombia*

ABSTRACT

The important participation of Colombian heavy oil fields at the country oil production and the current thermal recovery operations implemented for their exploitation have brought about the need of a proper characterization and understanding of the reservoir mechanical and petrophysical properties under different pressure and temperature conditions. According to this current demand, the present study aims to analyze and assess a set of 19 triaxial tests focusing on the behavior of petrophysical properties (porosity and permeability) in representative reconstituted samples of an uncemented formation. Among these triaxial tests, different condition of temperature, confining pressure, drainage, and loading conditions (DTXC, UTXC and DRTXC) are carried out in order to replicate the conditions occurring to the formation during thermal recovery processes and estimate the effects of these variations on sample's properties. The analysis shows a direct dependence between the petrophysical properties and the confining pressure. In tests carried out under high confinement (effectives stress greater than or equal to 4 MPa) the porosity decreases during shear stage, whilst under low confinement (effective stress of 0.4 MPa) porosity increases during shear stage. On the other hand, the permeability decreases before and after the shear stage in tests with high confinement, whilst at low confinement values, permeability increases. Lastly, an especial case of stress path for the undrained triaxial tests is presented which shows an asymptotic behavior in the stress path describing the Mohr Coulomb failure envelope. This especial case of stress path could be useful to evaluate Mohr Coulomb failure envelope using a single sample.

KEYWORDS

Heavy oil; Stress path; Triaxial test; Failure envelope; Petrophysical properties.

1. INTRODUCTION

Hydrocarbon reservoirs are subjected to different stress path during its productive life. Depending on the production/injection processes the rock can be subjected to a stress state where the horizontal stresses reduce (production) or increase (injection) (Morales-Monsalve et al., 2018). Besides, according to the redistribution of stress and pressure around the wellbore, the vertical stress might change (Ikogoll et al., 1989)

Steam injection is one of the most used methods for enhanced oil recovery (EOR) which, generates an increase in the reservoir temperature (Alvarez and Han, 2013) affecting the stress path and, therefore, the mechanical behavior of the formation (Brignoli and Di Federico, 2004), and the behavior of the petrophysical properties (Minde, 2018). Thus, properties such as permeability and porosity depend directly on conditions such as reservoir temperature, effective confining stress, and the stress path. The aim of this study is to assess the effect of the stress path and drainage condition on the porosity and permeability behavior of uncemented and reconstituted porous mediums. In this sense, 19 triaxial tests are presented, including drained triaxial compression tests (DTXC), undrained triaxial compression tests (UTXC) and drained triaxial expansion tests (DRTXC) at different temperature conditions and effective confinement stress. Additionally, due to the different temperature conditions, an analysis of

the variation of porosity and permeability during heating processes is presented as a function of the effective confinement stress.

2. SAMPLE PREPARATION

Triaxial tests are performed over reconstituted samples using soil from an outcrop of the Picacho formation, located in the Eastern Cordillera of Colombia. The sand is mainly composed of quartz (95%), and it has small amounts of kaolinite (4%) and pyrite (1%) (Arias, 2015). Samples are reconstituted to represent the behaviour of a typical Colombian heavy oil reservoir (ϕ = 27% and k = 250 mD), through a constant compaction method that does not include the addition of any type of cementing material. Additionally, the compaction process and subsequent cutting process (if needed) include the use of dry ice and thermal insulation to preserve the sample desired properties at low temperature. Besides, samples are taken to a typical confining condition of heavy oil reservoirs. Samples are saturated using brine (3% NaCl) in order to represent reservoir water. The pore pressure of each test is kept constant at 5.5 MPa during all the stages of the drained tests; the sample temperature is 20°C (ambient temperature), however, this temperature will increase depending on the test to be performed.

3. EXPERIMENTAL SETUP AND EQUIPMENT

The equipment used for conducting the tests consists of a servocontrolled electro-hydraulic loading frame, a triaxial cell with internal channels for connecting internal sensors, a high quality Quizx pump for controlling the confining pressure, a pump type syringe to monitor pore pressure, a Quizx pump to perform permeability measurements, and a data collector that receives data at a set frequency. White oil is used as confinement fluid, which resists conditions of high pressure and temperature. The entire triaxial cell is placed inside an environmental chamber to supply and control the temperature conditions contemplated in the experimental design. The lines and valves used are made of steel resistant to conditions of high pressure and temperature. The scheme in Figure 1 illustrates a diagram of the assembly inside the triaxial cell.

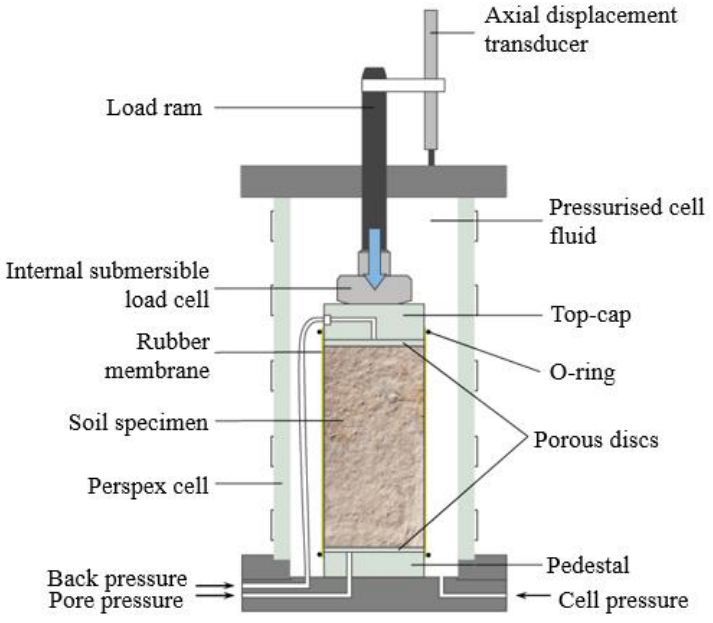

Figure 1. Diagram of the internal assembly of the triaxial cell.

Two axial displacement sensors and one radial displacement sensor are used as measuring instruments of LVDT type (Linear Variable Differential Transformer). Piezoelectric crystals on the triaxial cell pedestals are also employed for some shear and compressional wave velocity measurements. In the experimental assembly, two thermocouples aid to monitor temperature, one inside the cell and the

other inside the pore fluid pump. Finally, three pressure transducers are implemented to obtain a more accurate reading and avoid pressure losses in the lines.

4. TRIAXIAL TESTS

To complete this study, 19 triaxial tests of different types are carried out at different confining, temperature, and pressure conditions. Each test has three main stages, a first stage of isotropic consolidation to apply the desired confining pressure on the sample, a second stage of heating and a final stage of shearing. During the consolidation stage, each sample was consolidated to a confining pressure of 8.2 MPa (in situ mean effective stress) and then, unloaded to the desired effective confining stress. Permeability measurements were carried out at different temperatures and during various stages of the tests to evaluate the behaviour of the petrophysical properties.

Several drained triaxial compression tests (15 in total) are performed at 8.2, 4.0 and 0.4 MPa of effective confining stress and temperatures of 50 (reservoir conditions), 120, 180 and 230°C. Figure 2 **(a)** shows the scheme of the stresses applied during a drained triaxial compression test. During DTXC, the sample isotropically consolidated to the desired confining stress and, then axially loaded at a fixed pore pressure value until the sample is sheared to failure (Morales-Monsalve, 2018).

Two (2) drained reverse triaxial compression tests (DRTXC) are performed at 8.2 and 4.0 MPa of effective confining stress and 50°C of temperature. Figure 2 **(b)** shows the scheme of the stress applied during a drained triaxial extension test. During a DRTXC the sample is isotropically consolidated until reaching the desired confining stress, then, radial stress is reduced at a constant pore pressure value until sample fails by shear (Morales-Monsalve, 2018).

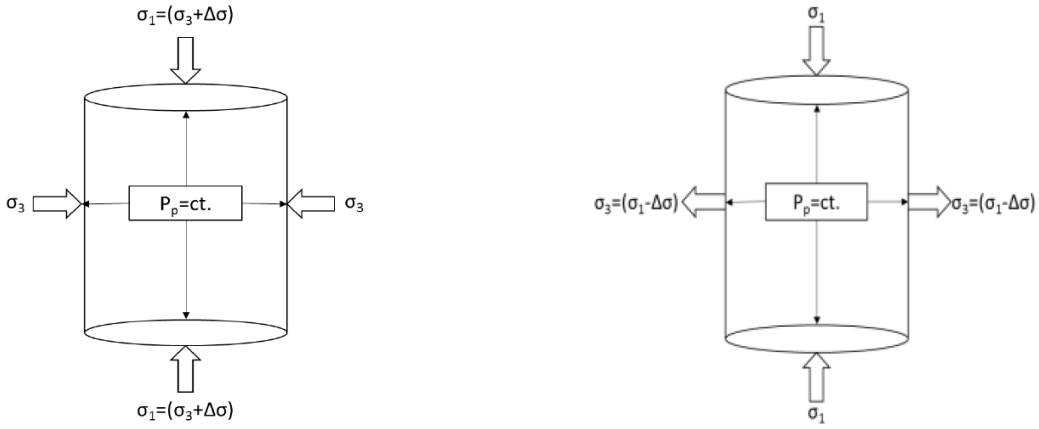

(a) **(b)**

Figure 2. Scheme of the stresses applied to the sample during: **(a)** DTXC and **(b)** DRTXC (Morales-Monsalve, 2018).

Two UTXC tests performed at 4.0 and 3.2 MPa of effective confining stress and 50°C of temperature. Figure 3 shows the scheme of the stresses applied during a UTXC test. During this test, the sample is loaded isotropically (consolidation) until reaching the desired confining stress, then, an axial loading is applied until the material fails in shear while the pore pressure varies depending of the applied load (Morales-Monsalve, 2018).

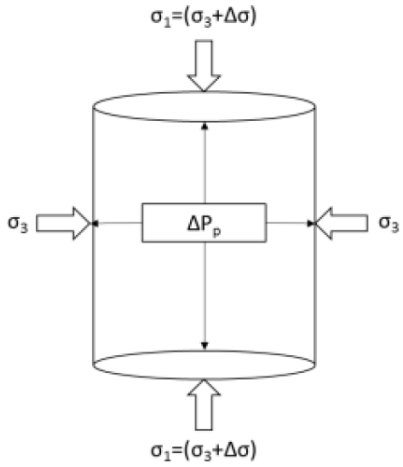

Figure 3. Scheme of the stresses applied to the sample during an UTXC test (Morales-Monsalve, 2018).

5. BEHAVIOR OF PETROPHYSICAL PROPERTIES WITH TEMPERATURE

5.1. Porosity

The change in porosity at heating stage of the test is related with the porous volume variation inside the sample due to the low coefficient of thermal expansion of the solid grains compared to the rock thermal expansion coefficient (Arias, 2015). Therefore, porosity during the heating stage is calculated from the volumetric strain of the sample, measured by LVDTs.

In this sense, it is observed that for the same temperature change, there is a lesser variation in the porosity of the samples subjected to high confinements (low slope of the tests at 8.2 MPa in Figure 3) since the expansion of the solid matrix of the sample occurs only within the porous space, due to the resistance imposed by the confinement pressure. Tests performed at low confinement have a greater variation in porosity when exposed to the same temperature change.

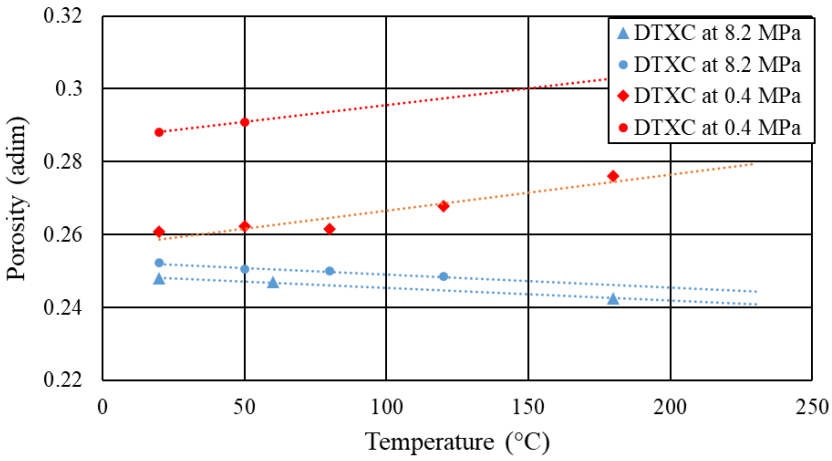

Figure 4. Behavior of porosity with temperature at different effective confining stress.

In addition, Figure 4 shows for high confinements tests, porosity tends to decrease. At low confinements, porosity increases due to temperature effect, as shown in the linear regression applied to the results.

5.2. Permeability

Each sample is saturated with a 3% NaCl brine and, considering that the pore pressure in the tests remains constant and equal to 5.5 MPa (except for the shearing stage of the UTXC tests). ASPEN software is used to determine the brine viscosity to each temperature test scenario, in order to calculate permeability by Darcy's law. See Figure 5 below.

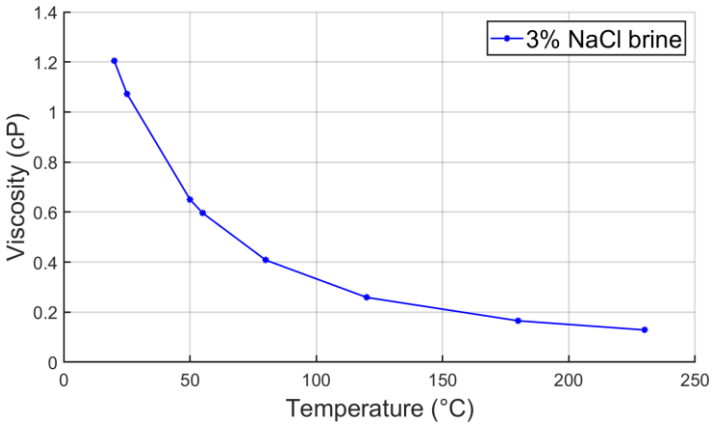

Figure 5. Viscosity changes with temperature.

Figure 6 **(a)** shows the behavior of permeability measurements (normalized) for all tests performed at an effective confinement of 8.2 MPa. Although the behavior of a DRTXC test is included, it only differs from the DTXC tests during the shearing stage. Therefore, results at the heating stage are comparable. In the different tests carried out at this high confining stress, permeability reduction is observed once temperature starts to increase, this behavior matches the tendency of an exponential curve with a correlation coefficient of 0.9496. These results in permeability behavior are consistent with what is observed in the porosity analysis. The less porous space the grater is the restriction of fluids through sample and, therefore, less permeability.

However, for low confinements tests the trend is not quite clear (see Figures 6 **(b)** and **(c)**). It is not possible to obtain a permeability model that includes the behavior of the different tests performed for the effective confining stress of 4.0 MPa and 0.4 MPa. The low consolidation of grains within the sample and, therefore, the possible migration of particles and plugging of pore throats during permeability measurements can explain this fluctuating trending behavior. Most tests carried out at 4.0 MPa report a significant increase in permeability when increasing the temperature from 20°C to 50°C, followed by subsequent permeability reduction at higher temperature values (see Figure 6 **(b)**). This permeability increase at the beginning can be explained by the low confining state where both the total volume and porous volume of the sample are allowed to expand freely increasing porosity. For tests performed at 0.4 MPa, only 3 data are available at 50°C, with opposite and inconclusive behaviors.

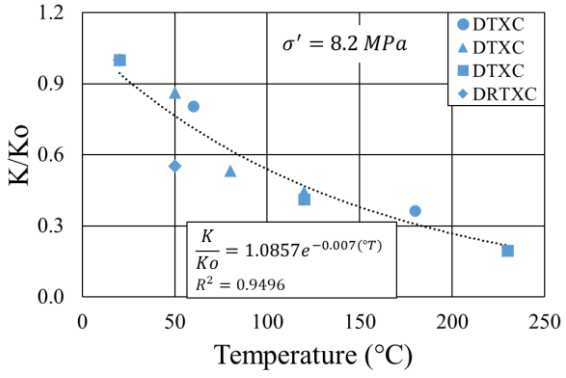

(a)

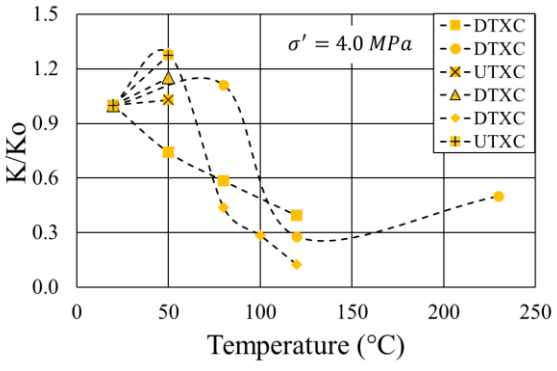

(b)

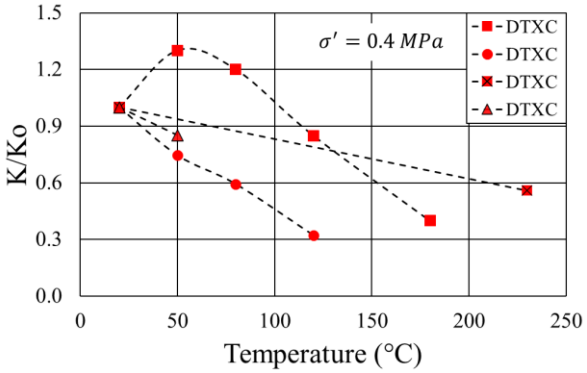

(c)

Figure 6. Behavior of permeability with temperature at different effective confining stress: **(a)** 8.2 MPa, **(b)** 4.0 MPa and **(c)** 0.4 MPa.

6. PETROPHYSICAL PROPERTIES AND STRESS PATH

To observe the effect of the stress path on changes in porosity and permeability during the shearing stage, a composite graph is proposed in *p*-*q* space (where *p* is average effective stress and *q* is deviatoric stress). On it is also, drawing the Mohr Coulomb failure envelope of the respective material; the highlighted values presented at the end of each stress path in Figures 7 and 8 correspond to porosity and permeability ratios calculated as the ratio of final to initial values.

6.1. Porosity

For DTXC tests (see Figures 7 **(a), (b), (c)** and **(d)**) high confinement prevents the sample from expanding radially. Considering the degree of consolidation of the rock matrix, the volume of the rock matrix will tend to remain constant while the porous volume decreases as result of the axial loading, which implies a decrease in the porosity of the sample (which is proportional to the void ratio, understood as the relationship between porous volume and matrix volume). For low confinements, the rock matrix is less confined, and the restriction imposed by pore pressure prevents the sample to expand reducing the porous volume. This behavior allows the porous volume inside the sample to remain constant while the volume of the matrix decreases by compaction of the axial load frame, implying an increase in porosity during the shearing stage.

During the two DRTXC tests, performed at 8.2 MPa and 4.0 MPa of effective confining stress, a porosity ratio greater than 1 is observed for both cases (see Figure 7 **(a)**), which implies an increase in porosity during the shearing stage. This result is consistent with what is expected for this type of test, since by reducing the confining stress during the expansional stage and maintaining the constant pore pressure, the porous volume of the sample will increase.

Finally, one of the UTXC tests (see Figure 7 **(a)**) shows a porosity ratio considerably greater than 1, implying an increase in porosity during the shearing stage; in this type of testing the undrained condition leads to variable pore pressure values and an almost constant porous volume. This trending behavior relates to an increasingly lower matrix volume due to the compression of the axial load frame, and significant increase in the sample porosity.

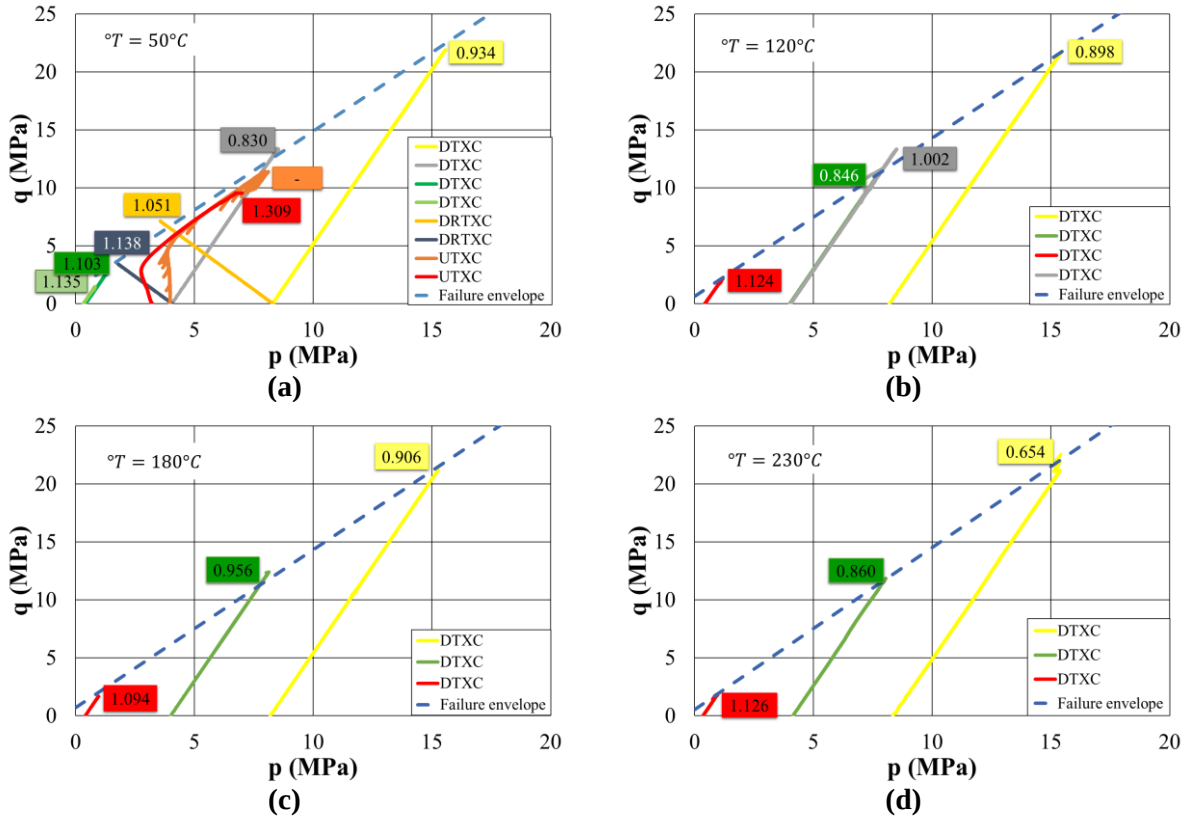

Figure 7. Behavior of porosity with stress path at different temperatures: **(a)** 50°C, **(b)** 120°C, **(c)** 180°C and **(d)** 230°C.

To sum up, the behavior of porosity depends on the confining condition to which the material is subjected. For instance, during the compressive tests performed, an increase in porosity is observed by the effect of shearing when low effective confining stress values are applied. For high levels of confinement there is a decrease in that property.

6.2. Permeability

For DTXC tests (see Figures 8 **(a), (b), (c)** and **(d)**) permeability ratio varies depending on the effective confining stress and the temperature of the test. For example, for tests carried out at 50°C (Figure 8 **(a)**) there is an increase in the permeability ratio, and therefore in the permeability of the sample. In tests carried out at high and low levels of confinement, there is a decrease in permeability during the shearing stage. However, tests conducted at 120 and 230°C show an opposite trend, at high effective confining stress, permeability decrease. For low effective confining stress, permeability increases, showing a consistent behavior with the aforementioned analysis porosity presented. The larger the porous space, less flow restriction and, therefore, greater permeability. This trending difference in permeability behavior during the shearing stage at different temperature conditions may be explained by thermal expansion of fluid and rock matrix, as wells as the creation of interconnected and non-interconnected porosity related to the compressive effect of the axial load frame.

For DRTXC tests (see Figure 8 **(a)**) a decrease in permeability is observed, at 8.2 MPa and 4.0 MPa of effective confining stress. Although such tests allow an increase in porosity (as demonstrated in the previous item), the lateral expansion of the sample may be associated with the creation of tortuous flow channels inside the porous space that are not aligned with the flow direction. Consequently, even if there is more porous space, the flow through the sample is restricted.

Despite the increase in porosity of one of the UTXC tests, in Figure 8 **(a)** a permeability ratio much lower than 1 is observed; which implies a significant decrease in sample permeability after the

shearing process; this behavior may be related to the collapse and creation of new flow channels into the porous medium due to undrained condition imposed on the sample, i.e. the absence of flow on the sample surface which allows the brine drainage might result in grain crushing and a rearrangement of the fluid and porosity in the vicinity of those surfaces. Thus, this phenomenon causes the creation of a larger porous space inside the sample, and the closure of flow channels on the surface, which result in a significant decrease in permeability during shearing stage of the test.

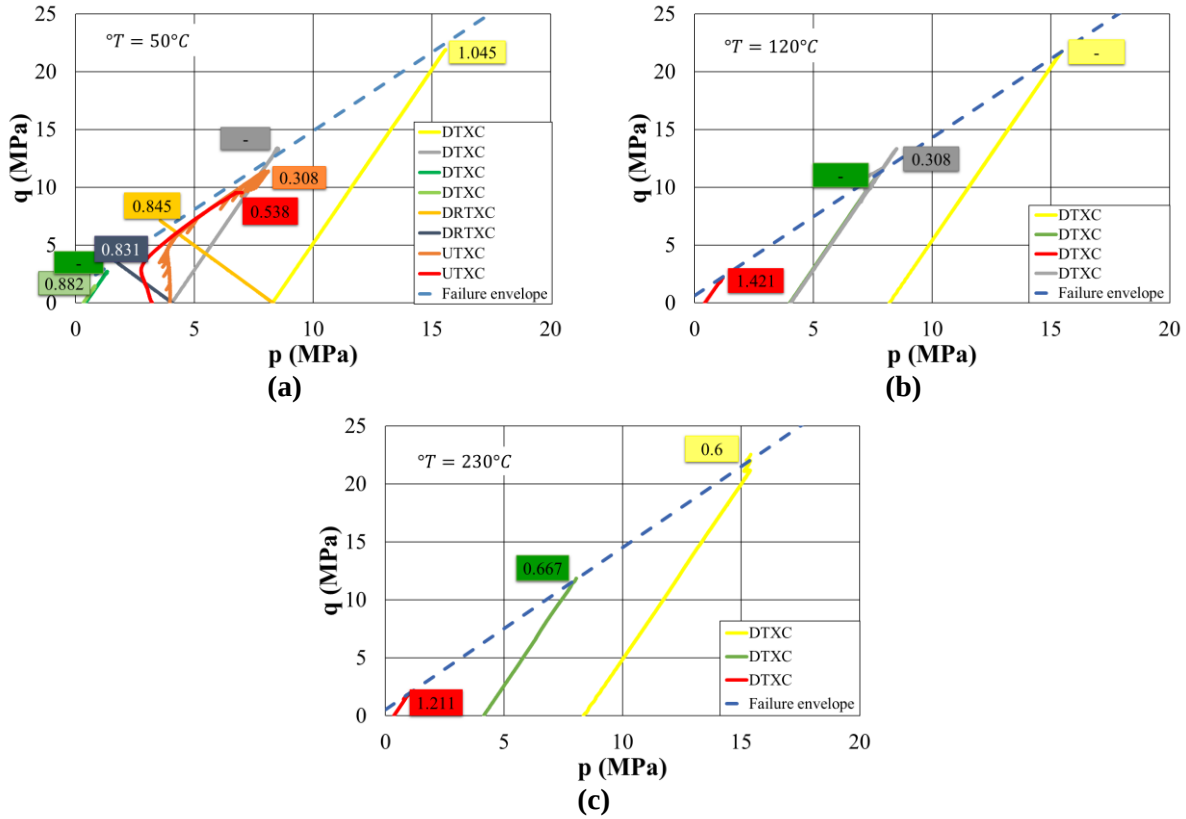

Figure 8. Behavior of permeability with stress path at different temperatures: **(a)** 50°C, **(b)** 120°C and **(c)** 230°C.

7. STRESS PATH OF UNDRAINED TRIAXIAL TESTS

The stress path of the two UTXC tests performed showed asymptotic behavior (see Figure 9) with respect to the Mohr Coulomb failure envelope; such tests, despite the slight difference in effective confining stress at the beginning of the shear stage, 3.2 MPa and 4.0 MPa respectively, they converge on the same line whose slope is equal to Mohr Coulomb failure envelope's. The stress path behavior of this type of test would allow the failure envelope of this type of material to be estimated from the performance of a single triaxial test.

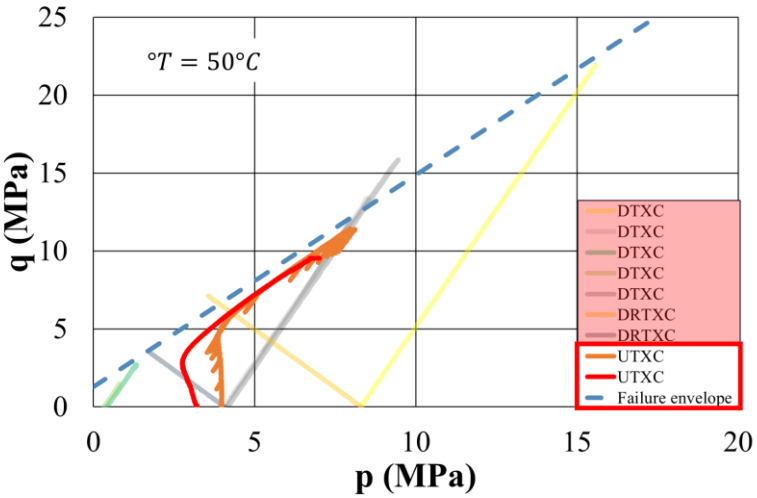

Figure 9. Behavior of stress path of the UTXC.

After saturation, each sample is isotropically consolidated to an effective confining stress of 8.2 MPa, then through a deconsolidation stage depending on the effective stress condition to which the test will be performed, an additional heating stage is also performed to finally perform the shear of the sample. These previous processes or stages can induce changes in the microstructure of the sample that affect the behavior of the stress path.

Furthermore, it is observed that the stress path of the UTXC tests represents a first stage in which p remains almost constant during this stage. The axial load frame approaches the sample, increasing the axial stress, but the effective confining stress reduces due to an increase in pore pressure inside the sample; compression simultaneously decrease the porous volume and volume of the rock matrix. However, the porous volume stops decreasing and offers a restriction that the axial stress applied mainly affects the matrix of the rock, grain compaction and a subsequent slight increase in porous volume, which is reflected in the decrease in pore pressure (see Figure 10) and the asymptotic behavior of the stress paths (see Figure 9).

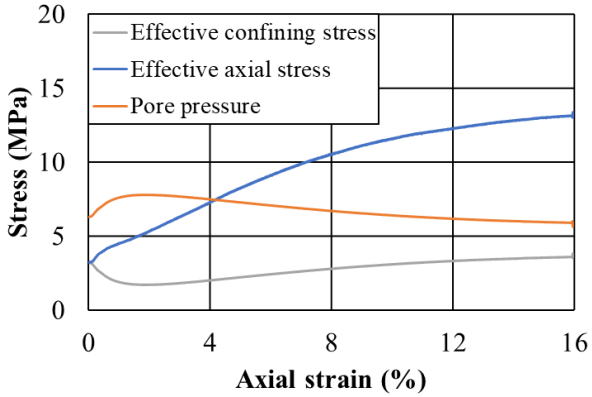

Figure 10. Behavior of effective stresses and pore pressure in UTXC.

8. CONCLUSIONS

- In a reconstituted and uncemented sample the behavior of porosity and permeability will depend directly on the level of confinement to which it is subjected. At a high level of confinement, both porosity and permeability decrease as temperature increases, whereas, for low confinement values, porosity increases as the temperature increases. This last effect is not evident in the permeability.

- In a compressive triaxial test, porosity decreases during the shearing stage when sample is subjected to high confining stresses, while for low confining stress, porosity increases.
- Extension or unloading tests (DRTXC) show an increase in porosity at high and low levels of effective confinement stress.
- In a reconstituted and uncemented porous medium, the stress path of an undrained test (UTXC) exhibits asymptotic behavior that can be used to estimate the behavior of the material's failure envelope.

REFERENCES

Alvarez, J., and Han, S., 2013. Current overview of cyclic steam injection process. *Journal of Petroleum Science Research,* 2(3), 1-12.

Arias, J., 2015. *Efecto de la temperatura en las propiedades mecánicas y petrofísicas de formaciones de crudo pesado. Master Engineering Thesis.* Universidad Nacional de Colombia, Medellín.

Brignoli, M., Di Federico, A., 2004. Compaction of unconsolidated sands and stress path effects: laboratory evidence. American Rock Mechanics Association (ed.), *Gulf Rocks 2004, the 6th North America Rock Mechanics Symposium (NARMS), Houston, Texas, 05 June 2004.*

Minde, W., Wang, W., Madland, M., Zimmermann, U., Korsnes, I., Bertolino, S., and Andersen, P., 2018. Temperature effects on rock engineering properties and rock-fluid chemistry in opal-CT-bearing chalk. *Journal of Petroleum Science and Engineering,* 169, 454-470.

Morales-Monsalve, C., Arbelaez-Londoño, A., Alzate-Espinosa, G., and Araujo-Guerrero, E., 2018. Effect of the stress path in the mechanical behavior of unconsolidated sands. International Society for Rock Mechanics (ed.), *VII Brazilian Symposium on Rock Mechanics-SBMR 2018, Brazilian, Brazil, 28 August-1 September 2018.*

Assessment of the effect of Cyclic Steam Stimulation (CSS) operational variables on well productivity including geomechanical modeling

Guillermo A. Alzate-Espinosa, Abel J. Naranjo-Agudelo, Edson F. Araujo-Guerrero, Carlos A. Torres-Hernández, Daniel Felipe Cartagena-Pérez, Camilo A. Benítez-Peláez, Mario A. Hernández-Ricaurte, Maria C. Herrera-Schlesinger, Elvis F. Higuita-Carvajal

Universidad Nacional de Colombia – Medellín campus, Research Group in Applied Geomechanics (GIGA), Colombia

ABSTRACT

A methodology is designed and implemented to explore the degree of impact of different operational variables of CSS on the productivity of a Colombian heavy oil field. Variables such as steam quality, steam rate, and duration of injection and soaking stages are assessed considering the geomechanical mechanisms related to the rock expansion due to temperature increases and the rock compaction due to the reduction of pore pressure in the production stage. For this purpose, a coupled modeling approach of fluid flow and geomechanics is carried out using STARS (CMG), including permeability multipliers controlled by volumetric strain. A directional permeability model and in-house software are used to obtain the relationship between permeability and volumetric deformation. Two sensitivity analyses based on experimental design and Sobol's method are performed in order to determine the influence of injection time, soaking time, injection rate, and steam quality on the cumulative oil production (Np) and oil-steam ratio (OSR). The first sensitivity analysis accounts for non-constant permeability, while for the second one, permeability is set constant. Once implemented this methodology, the operational variables that have a direct positive incidence on the Np increase are the injection time and the steam quality. The OSR behaves directly proportional to the steam quality and inversely proportional to the injection period. It is expected that the increase in Np due to the variation of operational parameters would be higher than 25%. Moreover, an analysis is accomplished to determine the degree of impact of permeability variations due to rock deformation on well productivity.

KEYWORDS

Cyclic steam stimulation; Experimental design; Operational variables; Geomechanics.

1. INTRODUCTION

1.1. Cyclic steam stimulation

Cyclic steam stimulation (CSS) is one of the most common thermal recovery methods used for heavy oil reservoirs. Unlike other techniques based on steam injection, such as Steamflooding and Steam Assisted Gravity Drainage (SAGD), CSS requires the least logistics for its execution since it is performed in a single well, which is both injector and producer. It consists of three stages: injection, soaking, and production. In the first stage, steam at high pressure and high temperature is injected into the well for a period that can last from a few days to a few weeks. In the second stage, the steam injection is stopped, and the well is shut down for a period. In this stage, there is heat redistribution in the reservoir that can alter the process's thermal efficiency depending on its duration (Sheng, 2013). Finally, in the production stage, the well is put on production until it reaches an economic limit. The objective of CSS is to reduce residual oil saturation through several reservoir drive mechanisms, usually related to the behavior of fluids and rock under temperature and pressure changes.

1.2. Drive mechanisms and operational variables in CSS

Drive mechanisms involving the reservoir fluids correspond to viscosity reduction, thermal expansion, and oil distillation (Luo et al., 2020). Concerning the rock behavior, the induced thermal stresses in the injection stage, especially near the wellbore, lead to rock thermal expansion and dilation. In the production stage, formation compaction occurs due to depletion and temperature reduction. These rock alterations imply changes in the rock's petrophysical properties like porosity and permeability (Shafiei & Dusseault, 2013), affecting the hydrocarbon production and formation injectivity.

Now, the relevance of each one of the drive mechanisms depends on the magnitude of pressure and temperature changes in the reservoir. These magnitudes are directly linked to operational variables such as injection time, injection rate, soaking time, and steam quality. The injection time controls the extension of the thermal front and the volume of stimulated reservoir. The injection rate is related to the injection pressure and the steam temperature. Finally, the steam quality defines the amount of energy injected per equivalent water barrel.

The relationship between the drive mechanisms and the operational variables in the three stages of the process is crucial to consider when designing an efficient CSS operation, especially regarding mechanisms like the permeability changes due to the volumetric deformation of the rock. In this paper, a methodology involving numerical simulation is proposed to determine the impact of operational variables over the well productivity, taking into account the geomechanical component implied in the process. This methodology is applied to a mature oil field in Colombia.

2. GEOMECHANICS IN CICLYC STEAM STIMULATION

Each of the three stages of CSS has implications on the reservoir rock behavior regarding its properties and stress state. A summary of these effects is listed in Table 1.

Table 1. Geomechanical effects on each stage of CSS.

Injection	Soak	Production
- Pore pressure increase: It derives into lower effective stress. - Dissolution of clastic cementation: It decreases the formation's strength. - Induced thermal stresses: Temperature differences create shearing stress that affects the rock behavior.	- Induced thermal stresses: Temperature differences create shearing stress that affects rock behavior. As time passes by, the heated area is higher, so the thermal stresses, including the caprock.	- Pore pressure reduction: It increases the effective stress. - The thermal front reduces its extension since heated fluids are produced. - Rearrangement of rock particles due to production: This affects mechanical properties.

The thermal expansion eventually leads to an increase of the shearing stress and rock dilation, which are considered the primary sources of the bulk permeability increase (Shafiei & Dusseault, 2013).

The elastic relationship between stress, strain, and temperature can be seen in Equation 1, where E is Young's modulus, υ is Poisson's ratio, ε_i is the strain component in direction i, $\Delta\sigma'_i$ and ΔT are the stress and temperature changes, and β is the linear thermal expansion coefficient. This expression involves Hooke's law and Terzaghi's effective stress principle.

$$\varepsilon_i = \frac{1}{E}\left[\Delta\sigma'_i - \upsilon(\Delta\sigma'_j - \Delta\sigma'_k)\right] + \beta\Delta T \quad (1)$$

This effect is graphically represented by Figure 1, highlighting the stress changes during the thermal operation between the reservoir and surrounding rocks. In Figure 1, the vertical equilibrium is illustrated as the addition of the areas A_1, A_2, and A_3 that represent the stress accumulation due to thermal stress.

Since the reservoir increases its temperature, the thermal stress (Area 3) increases within the reservoir layer meanwhile to make up for static vertical equilibrium the surrounding layers develop shearing stresses.

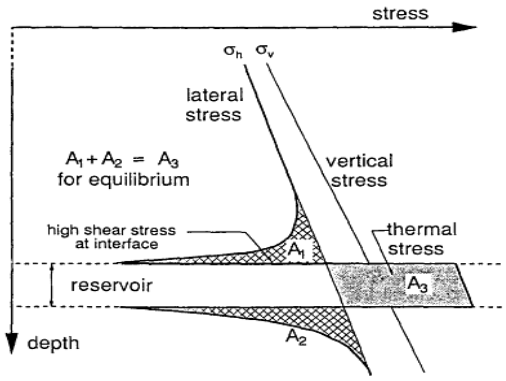

Figure 1. Stress equilibrium and shearing (Dusseault, 1993).

Furthermore, it should be pointed out that temperature changes directly impact the stress path during thermal operation. This effect of shearing is added to the one caused by production (Chalaturnyk & Li, 2004). Such combination gives a specific stress path in which grains' arrangement induces complex phenomena into the petrophysical properties (for instance, dilation).

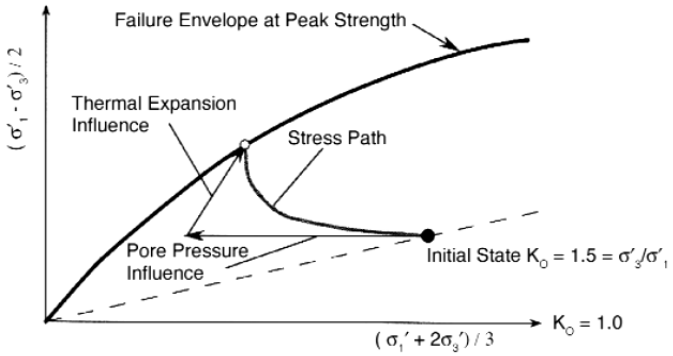

Figure 2. Theoretical stress path during heating and production (Chalaturnyk & Li, 2004).

As mention before, the combined effect of pressure and temperature derives into stress changes that lead to a modification in the rock fabric. This physical change directly impacts permeability since fluid flow paths are restricted or strongly modified in their tortuosity.

2.1. Permeability multipliers

The anisotropic nature of the strain and stress induced by CSS operations enforces the use of directional models to represent the reservoir's permeability evolution. For this purpose, a set of permeability multipliers controlled by volumetric deformation is obtained and included for the proposed sensitivities using STARS-CMG. This anisotropy comes from the fabric of the rock that creates differential strains during the heating process, this means that the same change in temperature makes the layer expands higher in the bedding direction than perpendicularly. Therefore, the pores' throats change their geometry with preference for a direction (anisotropic behavior) creating the requirement of directional model to describe the permeability evolution.

The permeability multipliers are estimated using a directional permeability model and in-house software. The permeability model calibration is achieved using linear regression from available experimental permeability data. Arias(2015) performs several sets of drained triaxial tests on reconstituted cores under variable temperature and confinement levels to obtain the petrophysical rock properties response.

To obtain the relationship between volumetric strain and vertical and horizontal permeability, the calibrated model is built up in GSIM, an in-house coupled with geomechanics reservoir simulator applied to thermal processes. The rock and fluid properties of the study case are used in addition to a highly refined radial grid near the wellbore to obtain assertive values of the stress, deformation, and permeability variations. The volumetric strain is calculated based on the strain results in *i*, *j*, and *k* directions. Finally, the vertical and horizontal permeabilities calculated with the directional model are normalized to generate the lookup multipliers table used in CMG. Figure 3 shows the impact of volumetric strain on permeability in the vertical and horizontal directions.

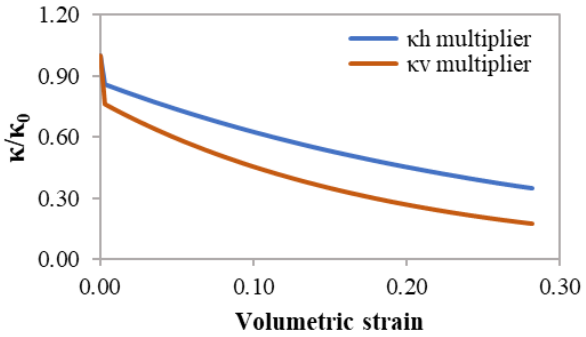

Figure 3. Relationship between volumetric strain and permeability multipliers.

3. METHODOLOGY

The Design of Experiments (DOE) is a statistical procedure used to study the significance of uncertain parameters with the minimum number of simulation runs. The variation of the uncertain parameters produces a response on the objective functions (outputs), which can be analyzed with variance-based procedures like the Sobol's method (Sobol, 1993). In this paper, DOE and Sobol's method are applied for two sensitivity analyses to determine the influence of CSS operating variables such as injection time, injection rate, steam quality, and soaking time on cumulative oil production (Np) and oil-steam ratio (OSR).

3.1. Sensitivity analysis with non-constant permeability

For the first sensitivity analysis, the permeability is considered as a non-constant parameter. The main objective functions selected are Np and OSR. The Np and OSR are used as indicators of well productivity and CSS efficiency, respectively. For this particular sensitivity analysis, where permeability is a function of volumetric deformation, two additional objective functions are used to study the effect of operational variables over permeability. The permeability objective functions refer to permeability magnitudes of two points located in regions near the wellbore in layers A2 and B2, recorded at the end of the production stage. They will be next referred to as κ(A2) and κ(B2) objective functions. These objective functions are adopted to determine the scenarios where the maximum and minimum permeability values are obtained by means of studying future well injectivity or productivity issues.

3.2. Sensitivity analysis with constant permeability

A second sensitivity analysis is performed with constant permeability. The permeability multipliers are removed from the base simulation model. Therefore, permeability remains invariable regardless of the induced volumetric deformation due to the steam injection and production. The main objective functions for this case are the same as the first sensitivity, that is Np and OSR. The permeability objective functions mentioned for the first sensitivity analysis are not evaluated.

CMG's thermal reservoir simulator (STARS), along with CMOST optimization tool, is used to carry out the sensitivities. The experiment set is created using the settings shown in Table 2. In the case of production variables such as total production rate, bottom hole pressure, and production time, the number of discrete values is 1; consequently, their values are fixed to a single magnitude. This is done in order to obtain representative results of Np and OSR.

Table 2. Operational variables values.

Variable	Value range	Number of discrete values
Injection rate (m^3/day)	350 - 445	7
Steam quality (%)	50 - 85	7
Injection time (days)	5 - 10	6
Soaking time (days)	2 - 5	4
Total production rate (m^3/day)	79	1
Bottom hole pressure (kPa)	4137	1
Production time (days)	180	1

4. STUDY CASE AND SIMULATION MODEL

The data used to construct the reservoir simulation model are obtained from a Colombian heavy-oil field located in the Mid-Magdalena Valley, which operates several wells under CSS. The reservoir embodies two well-differentiated sands, Zone A and Zone B, with interbedded shale layers. A single well model of the reservoir is generated with the rock and fluid properties listed in Table 3 and Table 4. The physical model consists of 40x10x30 blocks in the radial, tangential and vertical direction, respectively. A logarithmic length block distribution is used in the radial direction; meanwhile, a uniform distribution is used in tangential and vertical directions

Table 3. Petrophysical and thermal rock properties.

Property	Zone A	Zone B	Shale
Horizontal permeability (md)	1080	780	0
Vertical permeability (md)	360	206	0
Porosity (%)	29	28	0
Oil saturation (%)	80%	80%	80%
Water saturation (%)	20%	20%	20%
Thermal conductivity (W/m K)	62	62	69
Volumetric heat capacity (J/m^3 K)	2.51×10^6	2.51×10^6	2.75×10^6

Table 4. Oil properties.

Property	Value
Molecular weight (kg-mol)	272
Density (kg-mol/m^3)	980
Bubble pressure (kPa)	3447
Thermal expansión coefficient (1/K)	6.84×10^{-4}
Compressibility (1/MPa)	1.04×10^{-2}
Viscosity, Pa s @ 313 K	4.03
Volumetric factor (m^3/Sm^3)	1.04
Thermal conductivity (W/m K)	3.12

The mechanical properties and stress gradients used in the geomechanics module are shown in Table 5. Additionally, no-flow boundary conditions are imposed for the lateral, inferior, and superior reservoir boundaries, while no displacement conditions are set for the inferior grid layer.

Table 5. Mechanical rock properties and stress state.

Property	Zone A	Zone B	Shale
Cohesion (MPa)	8.83	8.83	13.79
Young's modulus (MPa)	17237	17237	1379
Friction angle (°)	30	30	40

Poisson's ratio	0.25	0.25	0.2
Rock compressibility (1/MPa)	3.90×10^{-4}	3.90×10^{-4}	5.03×10^{-4}
Thermal expansion coefficient (1/K)	1.20×10^{-5}	1.20×10^{-5}	1.62×10^{-6}
Vertical effective stress gradient (kPa/m)		12.44	
Minimum horizontal effective stress gradient (kPa/m)		8.82	
Maximum horizontal effective stress gradient (kPa/m)		14.02	

The model represents a vertical reservoir section in depths between 426.72 and 577.99 m and a drainage area of 70600 m^2. A cross-sectional view and the locations of Zone A and Zone B are shown in Figure 4, while the vertical discretization and layer thickness are shown in Table 6. For the injection and production stage, all sand layers are opened to allow fluid flow.

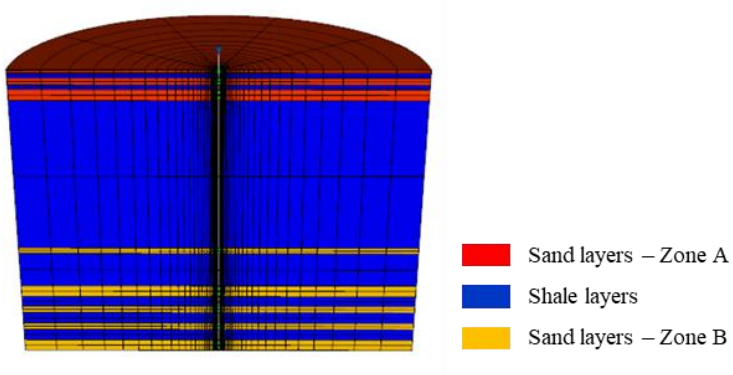

Figure 4. Radial model cross-sectional view.

Table 6. Vertical discretization.

Layer	Depth (m)	Thickness (m)
Sand A1	426.72	1.52
Sand A2	430.68	3.35
Sand A3	436.32	5.49
Sand B1	518.77	3.05
Sand B2	539.80	6.10
Sand B3	551.38	3.66
Sand B4	561.14	3.66
Sand B5	570.89	6.10

5. RESULTS AND DISCUSSION

The constant and non-constant sensitivity analyses require sets of 20 simulations, including the base case and verification runs. The experiment tables for both sets are equivalent; therefore, operational variables values for a particular experiment are the same for both sensitivity analyses allowing a practical comparison between cases.

5.1. Sensibility analysis results for the non-constant permeability case

The simulation model includes the effect of permeability variation with volumetric deformation. The four objective function curves are shown in Figure 5 and Figure 6; the best and worst-case scenarios and the base case (BC) are highlighted in red, black, and yellow, respectively.

The higher value for Np is obtained with experiment 19, with a cumulative production of 880 m^3. For OSR, experiment 14 represents the best-case scenario with a value of 0.2192. In regards to κ(A2) and κ(B2), experiment 14 also represents the best results, suggesting an initial link between the operating variables that control OSR and the ones controlling the permeability values near the wellbore. Experiments 10, 4, and 16 are the worst-case scenarios for Np, OSR, and the permeability objective

functions, respectively. The operating variables and their percentual variation respect the base case for experiments 4, 10, 14, 16 and, 19 are shown in Table 7.

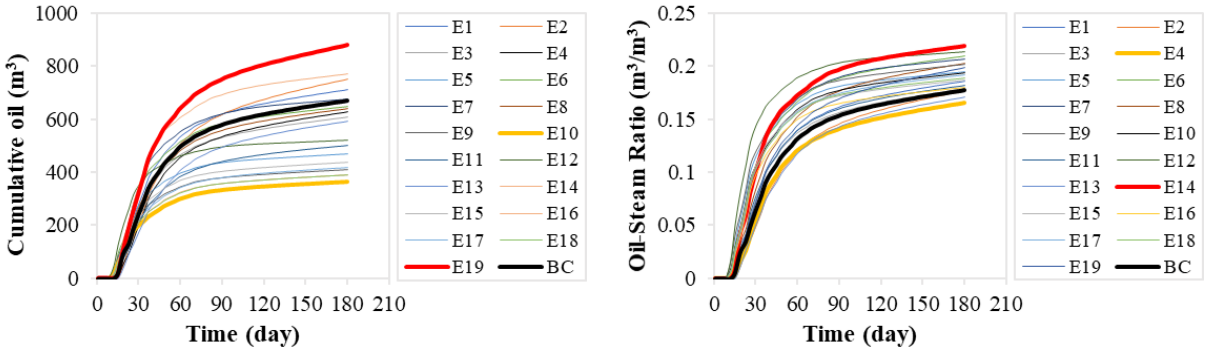

Figure 5. Cumulative oil (left) and Oil-Steam Ratio (right) curves.

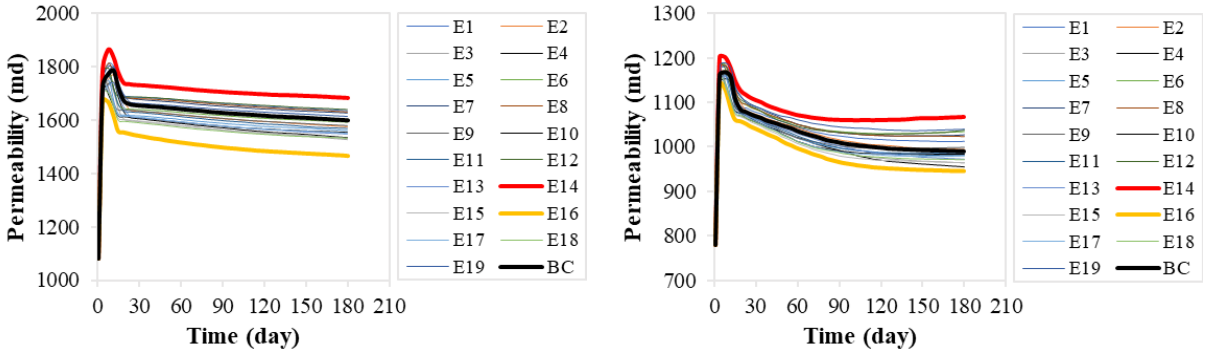

Figure 6. Near wellbore permeability curves for sands A2 (left) and B2 (right).

Table 7. Results for remarkable experiments.

Experiment	Injection rate (m^3/day)	Steam quality (%)	Injection time (days)	Soaking time (days)	Np variation (%)	OSR Variation (%)	κ(A2) Variation (%)	κ(B2) Variation (%)
BC	366	0.65	10	3	-	-	-	-
4	382	0.5	10	3	-6	-6	-4	-4
10	382	0.7	5	5	-46	10	-3	-1
14	445	0.85	8	4	15	24	5	8
16	366	0.55	6	4	-42	2	-8	-4
19	445	0.75	10	2	31	12	1	5

Concerning the permeability behavior, during the injection stage, the permeability rises at both near-wellbore points located in Sands A2 and B2. In production stage, permeability decreases at a low steady rate, lead by re-compaction due to temperature and effective stress reduction. At the end of the production stage, there's a high residual volumetric deformation accounting for rock expansion and dilation, which is linked to the final permeability values. Horizontal permeability values are shown in Table 8. For the point located near the wellbore in Sand A2, there's a maximum permeability change of 65%, while for Sand B2 is 38%.

Table 8. Horizontal permeability results for the base case.

Near wellbore point	Initial permeability (md)	Maximum permeability (md)	Final permeability (md)
Sand A2	1080	1786	1600
Sand B2	780	1079	990

The Sobol analysis results for the four objective functions are shown in Figure 7. Regarding OSR, steam quality represents the most crucial operating variable. This behavior can be explained by the fact that the amount of energy injected into the reservoir is dominated by the steam quality when the total steam

volume is fixed. Therefore, higher steam qualities represent more energy available to heat the heavy oil, leading to a production increment and a rise in OSR. Now, for Np, the most influencing factor is the injection time. In this case, for a fixed injection rate and steam quality, the injection time impacts the amount of steam injected into the reservoir. Higher injection time implies a larger steam front and a rise in temperature for oil-saturated zones far from the wellbore, which means a larger oil volume is heated (Torres, 2018).

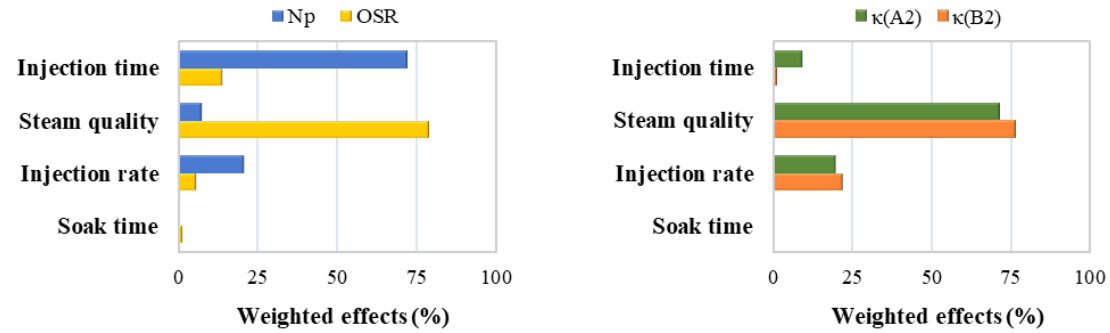

Figure 7. Influence of operating parameters on OSR and Np (left). Influence of operating parameters on permeability values for layers A2 and B2 (right).

Concerning the permeability objective functions, Figure 7 shows identical responses for both κ(A2) and κ(B2) under the four operating variables. The OSR, κ(A2), and κ(B2) are highly influenced by the steam quality, followed by the injection rate. The steam quality is related to the amount of energy injected by an equivalent water barrel, while the injection rate is associated with the overall steam volume injected and the steam temperature downhole. Once combined with a fixed production time, these effects imply higher temperature values at the end of the production stage, which are linked to thermal expansion and volumetric deformation that trigger permeability changes. These results are essential when planning future CSS cycles because the injectivity and production capacity of the reservoir is compromised by previous injection-production cycles.

5.2. Sensibility analysis of Np and OSR for the constant permeability case

The permeability lookup table is removed from the original simulation model to generate a new set of experiments. Thus, the results are not affected by permeability variations due to the volumetric changes of the rock, in that sense, this set of experiments is not a sensitivity study regarding permeability but a study of the Np and OSR's behavior with the influence of the operating parameters.

The Np and OSR curves for the 20 experiments are shown in Figure 8. The best and worst-case scenarios and the base case are highlighted in red, black, and yellow, respectively. Experiments 19 and 14 represent the best-case scenarios for Np and OSR, respectively. On the other hand, experiments 10 and 4 give the lowest values of Np and OSR. These results are equivalent to the non-constant permeability analysis. Nevertheless, there are variations in the magnitude of the objective functions.

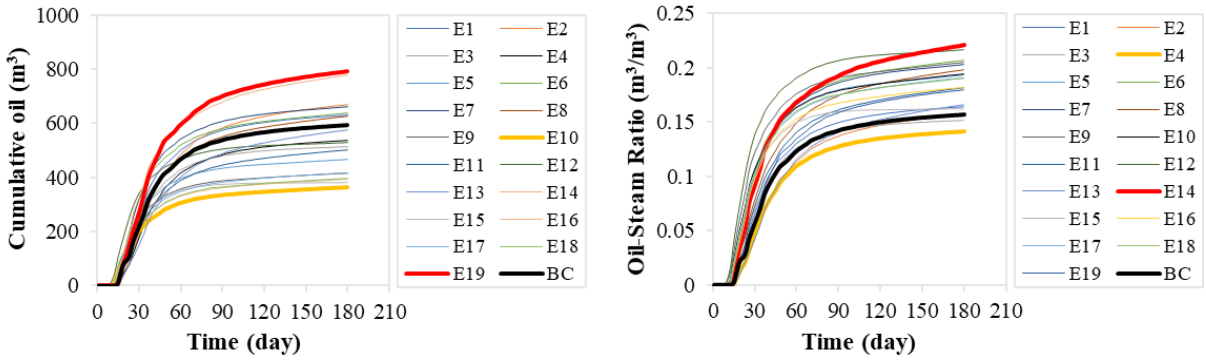

Figure 8. Cumulative oil (left) and Oil-Steam Ratio (right) curves.

Concerning the Sobol analysis, Figure 9 shows the effects of the four operating variables on Np and OSR. For both objective functions, the tendencies are similar to the results with non-constant permeability. The critical operating variable for Np is still injection time, while for OSR is the steam quality.

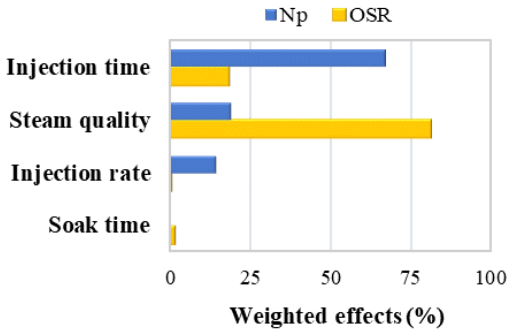

Figure 9. Influence of operating parameters on OSR and Np – Constant permeability.

In terms of Np, the curves of permeability shown in the non-constant permeability analysis indicate an enhanced flow capacity, at least for the near-wellbore zone for layers A2 and B2. Consequently, higher production is expected for the cases where permeability is a function of volumetric deformation. Table 9 indicates the Np and OSR corresponding to the operating values of the base case and the 19th experiment, for constant and non-constant permeability conditions. The 19th experiment refers to the run with the highest cumulative oil, which occurs to be the same experiment and operative conditions for both sensitivity analyses. If constant permeability is implemented on the simulation model, there's a cumulative oil underestimation of 11.6% for the base case and 9.7% for the 19th run. For the constant permeability scenario, Np increases 33% from the base case to the best-case scenario. For non-constant permeability rises 31%. These increments reflect the importance of selecting the proper operating variables magnitudes for CSS.

Table 9. Cumulative production for experiment 19.

Experiment	Type of sensitivity analysis	Np (m^3)	OSR (m^3/m^3)
Base Case	Non-constant permeability	671	0.1772
	Constant permeability	593	0.1781
19	Non-constant permeability	880	0.1992
	Constant permeability	794	0.1799

Table 10 shows the effects of operating variables over the Np and OSR for constant and non-constant permeability and its differences, where the base values correspond to the non-constant permeability cases. The results indicate that injection rate effects on Np and OSR are underestimated when permeability is set constant. The relevance of injection rate on permeability comes from its relationship with bottom-hole pressure and the temperature necessary to inject the steam with a specific quality. Regarding reservoir simulation, injection rate controls the steam temperature and indirectly the amount of volumetric deformation due to thermal expansion. On the other hand, the steam quality effect on Np and OSR is overestimated when the permeability is defined as constant.

Table 10. Effects of operating variables over Np and SOR for constant and non-constant permeability analysis.

Type of sensitivity analysis	Objective function	Soaking time effect (%)	Injection rate effect (%)	Steam quality effect (%)	Injection time effect (%)
Non-constant permeability	Np	0.02	21.00	7.60	72.00
	OSR	1.40	5.80	79.00	14.00
Constant permeability	Np	0.02	14.00	19.00	67.00
	OSR	1.40	0.01	81.00	18.00
	Np variation	0.00	7.00	-11.40	5.00
	OSR variation	0.00	5.79	-2.00	-4.00

6. CONCLUSIONS

- The soaking time has a minor influence over the cumulative oil production, oil-steam ratio, and the final values of near-wellbore permeability for both sensitivity analysis with constant and non-constant permeability.
- For Np and OSR, the crucial parameters are injection time and steam quality, respectively. The injection time becomes even more critical for Np when a non-constant permeability is addressed in the sensitivity. The same occurs with the injection rate related to the OSR objective function.
- For near-wellbore permeability objective functions $\kappa(A2)$ and $\kappa(B2)$, the effects of the operational variables have the same tendencies; in both cases, steam quality dominates. Nevertheless, for $\kappa(B2)$, where permeability values correspond to a deeper sand, steam quality increases its effect by 5%, while injection time reduces its influence by 9%.
- For both constant and non-constant sensitivity analyses, the Np increases around 30% from the base case to the best-case scenario. This value reflects the importance of selecting an adequate combination of operating variables in CSS. However, an optimization analysis is necessary to find the values of the operating variables which maximize both Np and OSR.
- The sensitivity analyses presented were done for a single CSS cycle. Studies over several cycles should be done to determine the changes in reservoir characteristics such as porosity, permeability, fluid saturations, and their impact on the influence of operating variables over the Np and OSR.

ACKNOWLEDGEMENTS

We record our appreciation to MINCIENCIAS and ANH for their support to project *FP80740-801-2019*, as well as CPIP and CMG for providing STARS licenses at Universidad Nacional de Colombia.

REFERENCES

Arias-Buitrago, J. A. 2015. *Efecto de la Temperatura en las Propiedades Mecánicas y Petrofísicas de Formaciones de Crudo Pesado (Master's Thesis)*. Universidad Nacional de Colombia, Medellín, Colombia. Retrieved from https://repositorio.unal.edu.co/handle/unal/57861.

Chalaturnyk, R. J., & Li, P. 2004. When Is It Important to Consider Geomechanics in SAGD Operations? *Journal of Canadian Petroleum Technology*, *43*(8), 31–35. https://doi.org/10.2118/04-08-discussion.

Dusseault, M. B. 1993. Stress Changes in Thermal Operations. Paper presented at *SPE International Thermal Operations Symposium*. Bakersfield, 8-10 February, U.S.A: Society of Petroleum Engineers. https://doi.org/10.2118/25809-MS.

Luo, E., Fan, Z., Hu, Y., Zhao, L., Bo, B., Yu, W., … Wang, J. 2020. An efficient optimization framework of cyclic steam stimulation with experimental design in extra heavy oil reservoirs. *Energy*, *192*, 116601. https://doi.org/10.1016/j.energy.2019.116601.

Shafiei, A., & Dusseault, M. B. 2013. Geomechanics of thermal viscous oil production in sandstones. *Journal of Petroleum Science and Engineering*, *103*, 121–139. https://doi.org/10.1016/j.petrol.2013.02.001.

Sheng, J. 2013. *Enhanced Oil Recovery Field Case Studies* (1st ed.). Waltham, MA: Gulf Professional Publishing. https://doi.org/10.1016/C2010-0-67974-0.

Sobol, I. M. 1993. Sensitivity estimates for nonlinear mathematical models. *MMCE*, *1*(4), 407–414.

Torres-Hernández, C. A. 2018. *Modelamiento del Perfil de Temperatura Dentro del Yacimiento Durante Procesos Recobro Térmico con Inyección de Vapor en Yacimientos de Crudo Pesado (Master's Thesis)*. Universidad Nacional de Colombia, Medellín, Colombia. Retrieved from http://bdigital.unal.edu.co/70310/1/1017216190.2018.pdf.

Evaluation of geomechanical and petrophysical parameters that affect fragility of shale gas reservoirs in different compaction trends during burial process

Dana C. Ángel Gómez[a], Maika K. Gambús Ordaz[a], Diego A. Vargas Silva[a]

[a] *Universidad Industrial de Santander, Bucaramanga, Colombia*

Abstract

Shale gas reservoirs are mainly characterized by their low permeability and by having geomechanical, petrophysical and geological characteristics different from conventional reservoirs. Successful production of this type of reservoir depends on two aspects, its hydrocarbon generation potential and the ease of extraction. Therefore, characterizing and determining the natural fracture zones that will be connected by the drill bit and hydraulic fracturing is essential before orienting and defining the well trajectory. This article will characterize reservoir properties in terms of its geomechanics and petrophysics, specifically rock brittleness, since they are the main determining factor for selection of shale gas reservoirs with potential to be exploited. Brittleness is determined from geomechanical properties, consequently, indicating higher brittleness values to rocks with high Young's modulus and low Poisson's ratio, which translates into rocks rich in quartz, and lower values to rocks with low Young's modulus and high Poisson's ratio due to its organic richness and high content of clay minerals. This brittleness index involves the following properties: elastic and resistance parameters, pore pressure, total organic matter content and porosity, which show changes according to the different compaction trends that the rock has undergone. Finally, the evolution of pore pressure and compaction trends as a function of time will be analyzed to determine rock brittleness at each stage of burial. Concluding that rocks prone to fracture present overpressure, a high Young's modulus, and a low Poisson's ratio, have low porosity values and TOC between 1% and 3%.

Keywords

Shale gas; Geomechanics; Petrophysics, Natural Fractures

1. INTRODUCTION

In recent years, shale gas reservoirs have been considered as a potentially economic resource, thanks to the high energy demand evidenced in countries such as the United States of America where natural gas consumption was 31.01 trillion cubic feet (EIA, 2019), and the technological development that has allowed its exploitation. However; the study and characterization of this type of reservoir turns out to be complicated, because they are reservoirs that have a matrix with ultra-low permeability and are notably different from conventional reservoirs, in terms of their geology, geomechanics and petrophysics (Dewhurst et al., 2015). In addition to their total organic matter content that makes them an interesting area. Therefore, to generate production from this type of reservoir, not only artificial fractures are required but also natural fractures, which constitute important flow channels (Nordeng, 2009), however, the little study of this type of fractures in reservoirs unconventional means that the success of its commercial production is not guaranteed.

Therefore, the need arises to characterize properties of shale gas in terms of geomechanical and petrophysical attributes that intervene in formation of fractures. The methodology developed will allow oil companies to correctly select the candidate strata to fracture and, therefore, to create flow channels to wells.

To carry out the evaluation of properties that affect fragility of shale gas-type reservoirs, each of petrophysical and geomechanical characteristics that are related to rock brittleness index will be studied, since this is the property that indicates the ease of a rock to break or fracture instead of deforming when an external force acts on it, to finally analyze the behavior of the aforementioned parameters under the different compaction trends that the reservoir presents as the sedimentation process occurs.
The properties to study are total porosity which is considered as one of the critical variables that directly controls the volume of free gas, the estimation of the adsorbed gas capacity and geomechanical properties (Bust, 2011); total organic content that defines the organic richness within the rock; Young's modulus (relationship between stress and strain); Poisson's ratio (ratio between transverse strain and axial strain); pore pressure which plays a central role in flow conduction; and rock compaction, which is defined mainly as loss of porosity due to increased burial.

2. RELATIONSHIP BETWEEN BRITTLENESS INDEX AND STUDY VARIABLES

Due to the lack of any standard definition and method, the term brittleness has been used for different practical uses. The most acceptable definition proposed by Hucka and Das (1974) indicate that fractures in brittle rocks begin at or slightly after the yield point.
From a geomechanical perspective, brittleness is related to Young's modulus and Poisson's ratio; brittle rock has a high Young's modulus and a low Poisson's ratio (Rickman, et al. 2008). From a mineralogical perspective, Wang and Julia (2009) indicate that quartz and dolomite are more fragile materials than organic matter and clay, this is why rocks rich in quartz minerals and carbonates tend to fracture rapidly and fractures remain stable after originating or being induced. In contrast, ductile rock, with its high content of clay and organic matter, is less easy to fracture since it requires greater energy or fracture pressure to break. From a petrophysical point of view, brittleness index is affected by porosity, that is, rocks with good porosity show a more ductile behavior than rocks with low porosity (Fjar, et al., 2008).

3. METHODOLOGY

The workflow adopted is divided into two main phases: first the quantification of petrophysical properties and second the calculation of geomechanical properties as shown in figure 1.

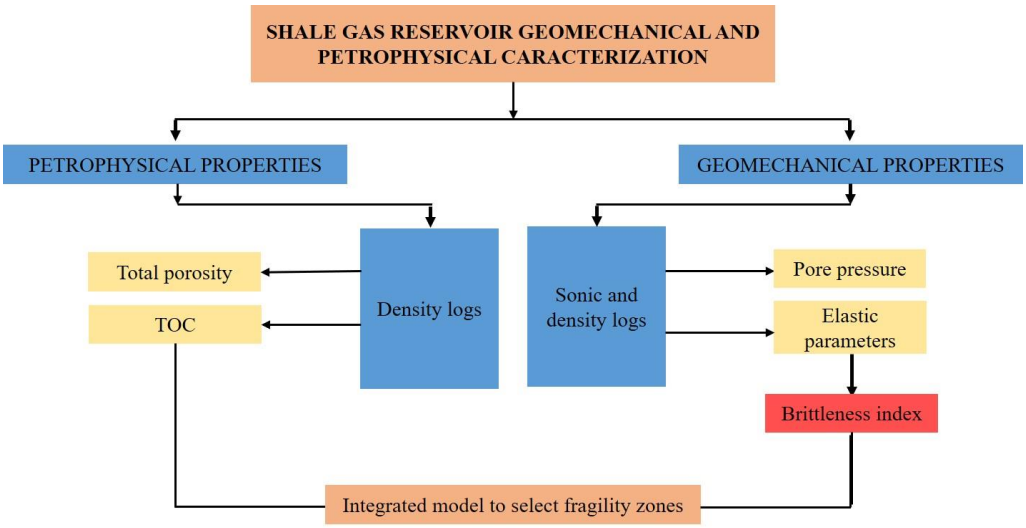

Figure 1. Methodology

The above properties are estimated using density and sonic logs, corresponding to a shale gas reservoir located in the Valley Middle Magdalena basin in Colombia, then the relationship between the brittleness index, geomechanical, petrophysical and compaction of the reservoir is studied, to finally determine which areas have good brittleness.

3.1. Estimation of total porosity

Gas storage in shale gas reservoirs (unlike conventional reservoirs where it is stored in the inorganic matrix and fractures) occurs in the adsorbed state within the kerogen, in the released or free state within the porosity of the kerogen, in the free state within the intergranular pore space (including microfractures), and in natural macroscale fractures (Bust, 2011).
The evaluation of porosity in shale gas reservoirs is largely based on density logs, which allows obtaining a value of this property through Equation 1 as shown below.

$$\varphi_D = \frac{\rho_{ma} - \rho_b}{\rho_{ma} - \rho_f} \quad (1)$$

where φ_D is density porosity, ρ_{ma} is matrix density, ρ_b is bulk density, ρ_f is fluid density, however, this value is affected by the kerogen content and the presence of the adsorbed gas.
A correct estimate from a density log can be achieved using a fundamental relationship between bulk density measured from log, ρ_b, and the densities of the various shale components as shown in equation 2, proposed by Bust (2011).

$$\emptyset_T = \frac{\rho_b - \rho_{ma} - w_k \rho_b \left(1 - \frac{\rho_{ma}}{\rho_k}\right)}{(\rho_g - \rho_{ma}) + (\rho_w - \rho_g) S_w} \quad (2)$$

where:ρ_g is overall gas density within total porosity, ρ_w is formation-water density, ρ_k is kerogen density, w_k is weight fraction of kerogen, and S_w is water saturation.

3.2. Estimation of total organic content (TOC)

Schmoker (1979) calculated the total organic content from density logs, TOC os expressed as a function of the difference between a reference density log response in the absence of kerogen and the actual density log response as shown in equation 3.

$$TOC \left(wt/_{wt}\right) = \frac{m}{\rho_b} + y \quad (3)$$

where the values of y, and m are obtained by equations 4 and 5 as observed below.

$$m = 1 \Big/ \left(\frac{1}{\rho_k} - \frac{1}{\rho_m}\right) \quad (4)$$

$$y = -\left(\frac{m}{\rho_m}\right) \quad (5)$$

3.3. Calculation of Young's modulus and Poisson's ratio

Elastic parameters measure the rock's ability to fail under stress (Poisson's ratio) and maintain fracture (Young's modulus). The combination of these two vital parameters is the main determinant of rock brittleness (Rickman, *et al.*, 2008). These parameters can be obtained through sonic and density logs. Dynamic Young's modulus can be obtained by means of equation 6, while dynamic Poisson's ratio can be calculated with equation 7.

$$E = \frac{\rho_b V_S^2 (3V_P^2 - 4V_S^2)}{(V_P^2 - V_S^2)} \quad (6)$$

$$\nu = \frac{(V_P^2 - 2V_S^2)}{2(V_P^2 - V_S^2)} \quad (7)$$

where E is dynamic Young's modulus, ν is dynamic Poisson's ratio, ρ_b is total density (g/cm^3), V_p is velocity of the compressional wave (km/s) and V_s is shear wave velocity (km/s).

3.4. Pore pressure estimation

Unconventional reservoirs are characterized by having high pore pressure, in some reservoirs such as Barnett (pore pressure 0.0117 MPa/m) and Marcellus (0.0136 MPa/m) there is a moderate overpressure and in others, such as Haynesville (pressure of pore 0.0181-0.0203 MPa/m), a considerable overpressure is evidenced, which occurs due to the ongoing or geologically recent maturation that seems to develop in the depth of reservoirs rich in organic matter (Zoback and Kholi, 2019).
Pore pressure can be estimated using Eaton's method expressed in equation 8 (Eaton, 1972).

$$P = \sigma_v - (\sigma_v - P_h)\left(\frac{\Delta T_n}{\Delta T_{log}}\right)^3 \quad (8)$$

Where P is pore pressure, σ_v is the vertical stress corresponding to the weight of the overburden, ΔT_n normal trend of sonic log transit time (μs/ft), ΔT_{log} is the value read from the sonic log (μs/ft) and P_h is the hydrostatic pressure.

3.5. Brittleness index

Rock brittleness index refers to the property of plastic deformation, which is not detected before the rock fractures, that is, the rock is easy to break or fracture under the action of an external force. According to Perez *et al*. (2013) Brittleness index can be used to classify reservoirs according to their mechanical behavior in:

- Brittle, if BI > 0.48
- Less brittle, if 0.32 < BI <0.48
- Less ductile, if 0.16 <BI <0.32
- Ductile, if 0 <BI < 0.16

Brittleness index can be estimated from geomechanical parameters using equation (9), as a function of Young's modulus and Poisson's ratio.

$$BI = \frac{E_N + \nu_N}{2} \quad (9)$$

E_N and ν_N can be calculated using equation (10) and (11)

$$E_N = \frac{E - E_{min}}{E_{max} + E_{min}} \quad (10)$$

$$\nu_N = \frac{\nu_{max} - \nu}{\nu_{max} - \nu_{min}} \quad (11)$$

3.6. Compaction of shale reservoirs

Sediment compaction is defined mainly as the loss of porosity due to increased burial, and includes mechanical and chemical compaction processes (Zadeh, 2016). The mechanical compaction of sediments begins just after their deposition in response to increased effective stress. Fine-grained clay

sediments show a very high initial porosity (60-80%) depending on the grain size, mineralogy and deposition environment. However, shales lose most of their porosity during the mechanical compaction stage.
At greater depth levels when the temperature reaches 343.15-353.15 ° C, chemical compaction begins, in which more thermodynamically stable minerals such as illite and quartz are produced through chemical reactions from smectite or the redistribution of minerals such as quartz and calcite, in addition this reaction produces quartz and water as by-products. The quartz produced precipitates as cement between the grains or at temperatures above 363.15 ° C as incipient flakes between the clay minerals. At deeper levels, when the temperature reaches 393.15 ° C, kaolinite will also be re-precipitated as illite and quartz in the presence of a potassium source (Thyberg, 2011).
To analyze the phenomenon of mechanical compaction, Athy in 1930 proposed a series of laws that allow to find the typical compaction parameter for each type of rock.

3.7. Athy's Law (1930) formulated with effective stress

Athy (1930) proposed a simple exponential decrease in porosity (ϕ) as a function of effective stress (σ'_z) for a given type of rock as presented in table 1, with only an initial porosity (ϕ_0) and a compaction parameter (k) using equation 12.

$$\phi = \phi_0 e^{-k\sigma' z} \tag{12}$$

Table 1. Typical parameters for each lithology

Lithology	ϕ_0	K (MPa^{-1})
Shale	0.7	0.096
Siltstone	0.55	0.049
Sandstone	0.41	0.0266

4. RESULTS

The methods described above are used to calculate petrophysical and geomechanical properties such as porosity, organic matter content, Young's modulus and Poisson's ratio in the case of study which corresponds to a source rock reservoir in Colombia, to evaluate the relationship of these properties with the rock brittleness index.

4.1. Relationship between brittleness index and total organic content (TOC)

Figure 2 shows that formations with TOC> 1% turn out to be brittle, formations with TOC> 3% are considered less brittle, TOC> 5% falls in less ductile regions and formations with TOC> 11% are considered ductile.

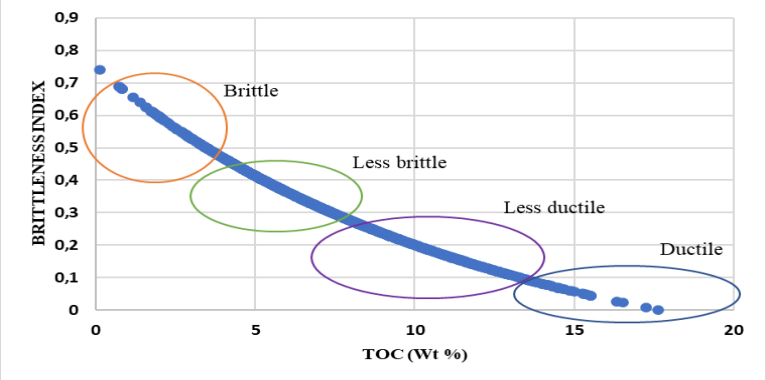

Figure 2. Relationship between brittleness index and total organic content (TOC)

This figure clearly indicates that the concentration of total organic content can mark brittle, less brittle and ductile areas, which is consistent with what was found by Wang and Julia (2009); that is, brittleness index of a shale-type reservoir decreases with increasing TOC.

4.2. Relationship between brittleness index and total porosity

Figure 3 (relationship between brittleness index and total porosity) shows that porosity values lower than 18% correspond to brittle regions, porosity between 18% and 27% indicates less brittle regions and finally porosity values greater than 27% fall in less ductile regions. This indicates that brittleness index of a shale gas reservoir decreases with increasing porosity.

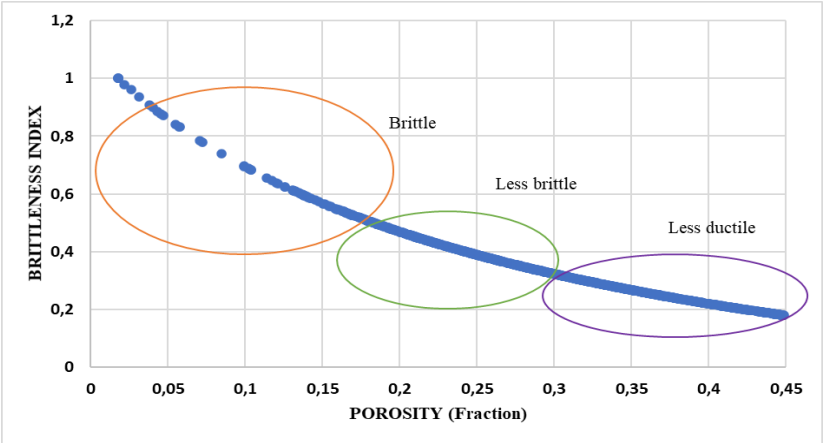

Figure 3. Relationship between brittleness index and total porosity

4.3. Relationship between brittleness index and Young's modulus

As can be seen in figure 4, rocks with high Young's modulus values turn out to be brittle, while rocks with a lower Young's modulus show ductile behavior.
Figure 4 also shows that for the shale under study, Young's modulus values between 40 and 100 GPa indicate that the rock is brittle, values between 20 and 40 GPa result in less brittle rocks and finally, Zones with a Yóung modulus less than 20 GPa turn out to be ductile.

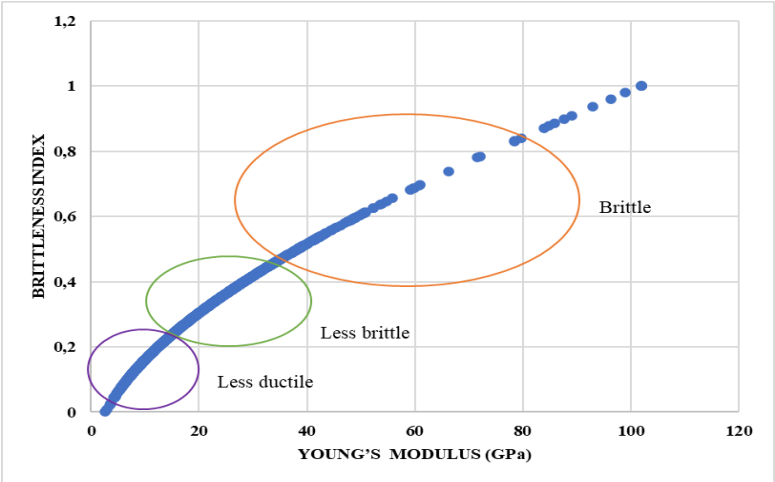

Figure 4. Relationship between brittleness index and Young's modulus

4.4. Relationship between brittleness index and Poisson's ratio

In figure 5 it is clearly observed that a lower Poisson's ratio translates into a higher brittleness index, and, on the contrary, a higher Poisson's ratio indicates that the rock behaves in a ductile manner, concluding that they are inversely proportional. Therefore, rocks with Poisson's ratio values less than 0.2 have good brittleness index, rocks with Poisson's ratio between 0.2 and 0.28 are less brittle, and rocks with Poisson's ratio greater than 0.28 are considered ductile.

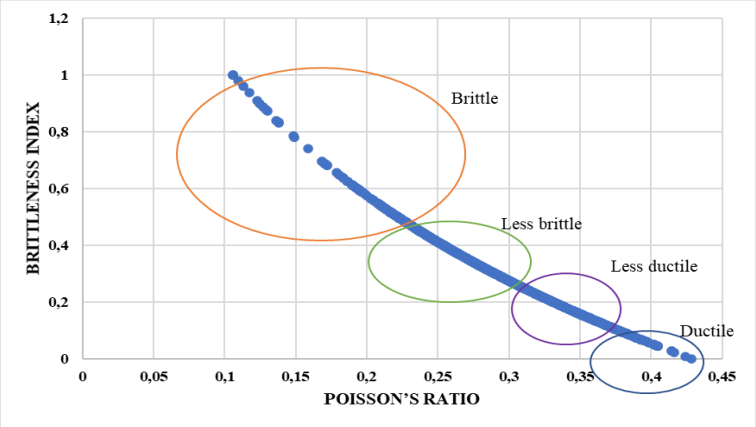

Figure 5. Relationship between brittleness index and Poisson's ratio

4.5. Relationship between brittleness index and pore pressure

In addition to TOC, porosity, and brittle minerals, pore pressure could be another parameter that influences fractures. Pore pressure affects the height and vertical growth of fractures in shale reservoirs (Iqbal, O. *et al.*, 2018). To see its effect on brittleness index, its relationship is represented in figure 6. This figure indicates that there is no significant relationship between brittleness index and pore pressure, except in some areas where brittleness index increases with an increase in pore pressure, but this may be due to the presence of brittle minerals.

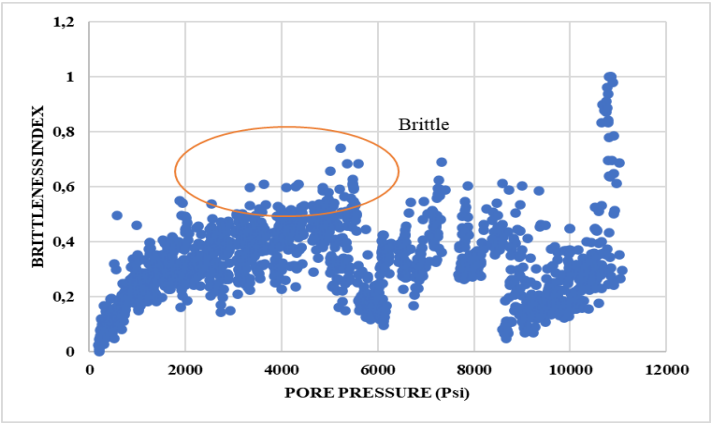

Figure 6. Relationship between brittleness index and pore pressure

4.6. Reservoir compaction

For the shale under study, the compaction trend is obtained as a function of the effective stress observed in figure 7, which is described by equation 13.

$$\phi = 0.7e^{-0.09*\sigma'_z} \quad (13)$$

That is, there is an initial porosity of 70% and a compaction parameter (k) of 0.09 MPa^{-1}, which is like the theoretical parameters for compaction of a shale proposed by Athy (1930) that are observed in table 1.

This trend obtained correctly describes the decrease in porosity up to an effective stress value of 20 MPa, however, at greater depths (and therefore greater effective stress) it does not correctly describe the compaction of that reservoir, which may be due to strata that correspond to a lithology different from the one studied or to chemical compaction processes.

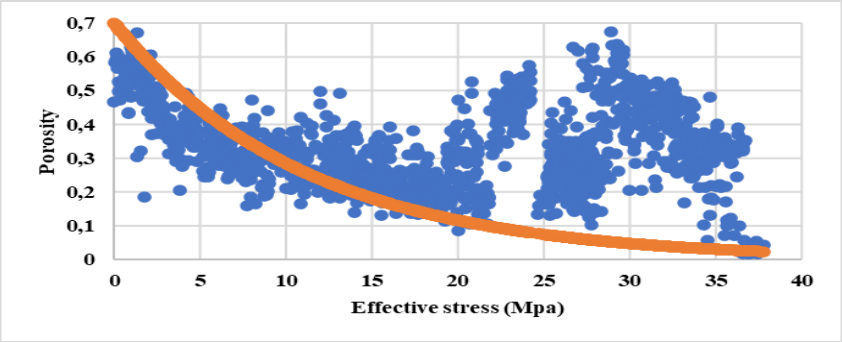

Figure 7. Compaction of a shale reservoir

4.7. Brittleness index as a function of compaction trends

Rock properties versus depth trends are important tools for investigating compaction processes during burial. Depth trends for total porosity and P-wave velocity are essential for estimating subsidence caused by sediment loading and for basin modeling analyzes. Compaction is considered normal when the sediments are progressively buried and are at their maximum depth of burial and the pressure of the formation fluid is hydrostatic (Zadeh, M. *et al.*, 2016).
P wave velocity (Vp) as a function of depth for the shale under study is shown in Figure 8, in which a general trend that increases with depth is observed. Three Vp trends (traced in red) are identified that are nearly linear with increasing burial depth.

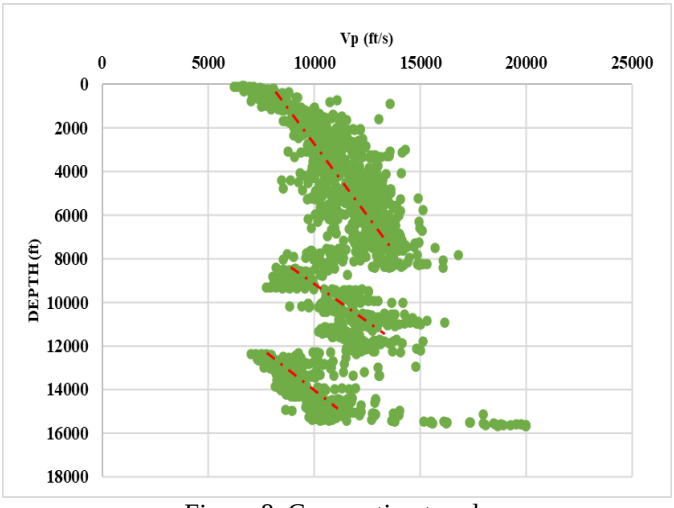

Figure 8. Compaction trends

Figure 9 shows the variation in brittleness index calculated using elastic parameters as a function of the different compaction trends suffered by the rock and which are previously indicated. Figure 9 clearly demonstrates a general trend of increasing brittleness regarding the burial, which is expected when Vp trends are analyzed.
The area with the highest brittleness index is that between a depth of 6000-8000 ft, which is mainly due to the high rock compaction at that depth, which caused a significant decrease in porosity, which, as mentioned has an inverse relationship with rock brittleness. In addition, the Young's modulus and

Poisson's ratio values for that depth turn out to be optimal to consider a shale as brittle, that is, a high Young's modulus (between 40-50 MPa) and a low Poisson's ratio (between 0.1 - 0.2).

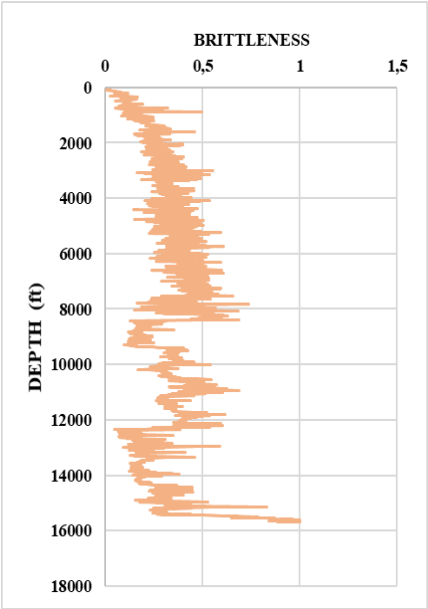

Figure 9. Brittleness index as a function of compaction trends

5. CONCLUSIONS

From the study, it is possible to demonstrate that porosity, total organic content, Young's modulus, and Poisson's ratio are parameters that can be used to classify reservoirs into brittle, less brittle, less ductile, and ductile layers.

Calculations indicate that brittleness is directly proportional to Young's modulus and increases with decreasing porosity, total organic matter content, and Poisson's ratio. Therefore, brittle formations have porosity less than 18%, TOC less than 3%, Poisson's ratio between 0.1 and 0.2, and Young's modulus greater than 40 GP. While formations with porosity greater than 27%, TOC greater than 5%, Young's modulus less than 20 GPa and Poisson's ratio greater than 0.28 present ductile behavior.

Considering the information analyzed, it is possible to show that as the depth increases, the rock formations become more fragile, due to the increased compaction of the rock.

REFERENCES

Aadnoy, B. and Looyeh, R., 2011. *Petroleum rock mechanics: Drilling operations and well design*. United States of America: Elsevier.

Athy, L., 1930. Density, porosity and compaction of sedimentary rocks. *American Association of Petroleum Geophysicists Bulletin*, (14):1–24,

Bust, V., Majid, A., Oletu, J. and Worthington, P., 2011. The petrophysics of Shale Gas Reservoirs: Technical Challenges and Pragmatic Solutions. *International Petroleum Technology Conference*, 1-16.

Dembicki, H., 2009. Three common source rock evaluation errors made by geologist during prospect or play appraisals. *American Association of Petroleum Geologist Bulelletin, 93(3),* 341-356. DOI:10.1306/10230808076

Dewhurst, D., Sarout, J., Delle Piane, C., Siggins, A., and Raven, M., 2015. Empirical strength prediction for preserved shales. *Mar. Petrol. Geol*. 67, 512–525.

Eaton, B.A., 1972. The effect of overburden stress on geopressures prediction from well logs. *Journal Petroleum Technology*. 2, 292–297. 24, SPE-3719-PA. DOI: https://doi.org/10.2118/3719-PA

Farghal, N. and Zoback, M., 2015. Identification of slowly slippling faults in the Barnett Shale utilizing ant tracking. *Technical Program Expanded Abstracts. 34.* 4919-4923. DOI: https://doi.org/10.1190/segam2015-5811224.1

Fjar, E., Holt, R., Horsrud, P., Raaen, A. and Risnes, R. (2008). *Petroleum Related Rock Mechanics* (2nd ed.). Hungary: Elsevier.

Gluyas, J. and Swarbrick, R., 2009. *Petroleum geoscience.* Malden: Blackwell Publishing.

Hucka, V. and Das, B., 1974. Brittleness determination of rock by different methods. *International Journal of Rock Mechanics and Mining Sciences & Geomechanics. 11.* 389-392. DOI: 10.1016/0148-9062(74)91109-7

Iqbal, O., Ahmad, M. and Kadir, A., 2018. Effective evaluation of shale gas reservoir by means of and integrated approach to petrophysics and geomechanics for the optimization of hydraulic fracturing: A case study of the Permian Roseneath and Murteree Shale gas reservoirs, Cooper Basin, Australia. *Journal of Natural Gas Science and Engineering (58).* 34-58. DOI: doi.org/10.1016/j.jngse.2018.07.017

Jarvie, D., Hill, R., Rubble, T. and Pollastro, R., 2007. Unconventional shale-gas systems: the Mississippian Barnett Shale of north-central Texas as one model for thermogenic shale-gas assessment. *American Association of Petroleum Geologist Bulelletin* 91 (4). 475–499.

Nordeng, S.H., 2009. The Bakken Petroleum System: an example of a continuous petroleum accumulation. *Dep. Miner. Resour. Newsl*. 36 19e22.

Perez, R. and Marfurt, K., 2013. Brittleness Estimation from Seismic Measurements in Unconventional Reservoirs: Application to the Barnett Shale. *SEG Houston annual meeting nro 2003.* 2258-2263. DOI: 10.1190/segam2013-0006.1

Perez, R. and Marfurt, K., 2014. Mineralogy-based brittleness prediction from surface seismic data: Application to the Barnett Shale. *Interpretation Oklahoma: Geoscience* 2(4). 1-17. DOI: doi.org/10.1190/INT-2013-0161.1

Rickman, R., Mullen, M. J., Petre, J. E., Grieser, W. V., & Kundert, D., 2008. A practical use of shale petrophysics for stimulation design optimization: All shale plays are not clones of the Barnett Shale. *In SPE annual technical conference and exhibition*. Society of Petroleum Engineers.

Schmoker, J., 1979. Determination of organic content of Appalaccian Devonian Shales from formation-density logs. *American Association of Petroleum Geologists Bulletin 63 (9)*. 1504-1573.

Soeder, D., 1988. Porosity and permeability of Eastern Devonian gas shale. *SPE Formation Evaluation.* 116-124. 53-63. DOI: http://dx.doi.org/10.1144/1354-079310-028

Thyberg, B. and Jahren, J., 2011. Quartz cementation in mudstones: sheet-like quartz cement from clay mineral reactions during burial. *Petroleum geoscience. 17 (1).*

U.S Energy Information Administration, 2019. Natural gas consumption. Available in www.eia.gov/naturalgas.

Wang, F. and Julia, G., 2009. Screening Criteria for Shale-gas Systems. *AAPG Bulletin*.

Yang, G., 2020. Developmental characteristics, and dominant factors of natural fractures in lower Silurian marine organic-rich shale reservoirs: A case study of the Longmaxi formation in the Fenggang block, southern China. *Journal of Petroleum Science and Engineering* (192). DOI:https://doi.org/10.1016/j.petrol.2020.107277

Zadeh, M., Mondol, N. and Jahren, J., 2016. Compaction and rock properties of Mesozoic and Cenozoic mudstones and shales, northern North Sea. *Marine and Petroleum Geology (76).* 344-361. DOI: https://doi.org/10.1016/j.marpetgeo.2016.05.024

Zoback, M. and Kohli, A., 2019. *Unconventional Reservoir Geomechanics: Shale gas, Tight oil, and induced seismicity.* UK: Cambridge University Press.

© 2021 Universidad Nacional de Colombia – ISRM, ISSN 2805-6426 *Guillermo Alzate Espinosa (Ed.)*

Modelling of coupled geomechanical and fluid flow behavior, including sand production criteria to diagnose, evaluate and predict sanding.

Edson Araujo-Guerrero[a], Jose G. Osorio-Gallego[a,b], Guillermo Alzate-Espinosa[a]

[a] *Universidad Nacional de Colombia, Medellin, Colombia*
[b] *Pluspetrol, Argentina*

ABSTRACT

Sand production in an oil and gas industry is a complex phenomenon causing operational costs to increase drastically, so controlling or managing sand has become very important in reservoir planning and development. During sand production, formation grains or chunks are detached from formation cavities due to mechanical loading processes, then transported to the wellbore by the flowing fluids, either oil, water or gas. This article presents a new model for sand production forecasts, which model couples the fluid flow and geomechanics and includes a sand production relationship. For the mechanical behavior an elastoplastic constitutive model and a sand production relationship is used, meanwhile, the fluid is slightly compressible and monophasic. The sand production relationship states that sand production occurs after high shear plastic strains are accumulated. FEM method is used for the numerical solution of the resulting system. To verify the model's behavior, results for a hypothetical case are compared with laboratory and previous reported in the literature related with sanding behavior. Among others results, is the relationship between the mechanical loading as a mechanism to promote sanding. Finally, in order to quantify the most important variables in sanding, a sensitivity analysis is performed. This analysis shows the effect of in situ stress state, sanding parameters and cohesion, being, after the sanding parameters, the cohesion as the most important variable for sand produced mass. The presented model has an important potential and its easy applicability positions it as an easy tool for matching and forecasting sand production.

KEYWORDS

Sand Production, Quantification, Forecast, Geomechanics

1. INTRODUCTION

Sand production is found in several reservoirs, commonly in poor or not cemented formations. Among sanding problems are: reduction or cessation of production, damage to the flow equipment either down-hole or in surface. Reason why sand management uses sand risk indicators to work with sanding, but when the risk is high (including economic impacts) then it is required the use of methods for sand control and mitigation.

There exist several ways to infer sand production potential such as dimensionless relationships (Bazanti & Desai, 1988), total compressibility to shear modulus ratio (Khamehchi & Reisi, 2015), neural network applications (Kanj & Abousleiman, 1999) and analytical solutions. Unfortunately, these methods do not predict sand production levels which are required to design properly the development plan for a wellbore or reservoir.

Numerical models are used to determine with higher detail the forecasts of sand production, and this way a numerical sand production model is presented accounting. The objective of the current work is to evaluate the influence of selected properties in sand produced mass. Ideally, sand production is a coupled problem which involves pressure changes, flow velocities, geomechanical behavior and sanding is a results of this variables changing during different operations.

2. SAND PRODUCTION OBSERVATIONS

Sand production causes can be found during drilling, completions or production and it can reach huge sand quantities capable of filling the wellbore with sand and generating a complete loose of the wellbore. Some sand production related problems are facilities and equipment erosion, required periodical workovers, sand separation and disposal, among others. All of these problems cause increases in project costs, reducing the project's viability. Despite of that, sand production increases the formation's permeability, therefore conductivity which at the same tame induce production increases. Field cases reported in Canada, Gulf of Mexico, and North Sea supports the hypothesis of increasing productivity due to sand production. (Palmer et al., 2000; Vaziri et al., 2000.)

Sand production requires mechanical stresses to generate plastic strains in the formation, then when sand grains are detached from the rock matrix, a fluid flow velocity is required to transport the solids from wellbore to surface. Sanding will not occur when dragging forces of fluid in movement are low (Nassir et al., 2015).

In experimental tests for sanding evaluation in hollow cylinder samples, it is concluded that sand production is caused by mechanical instability of the softened sample around cavities (caused by the effective stresses), moreover sand production could occur before mechanical failure. This helps to conclude that, fluid forces are not relevant in sand production phenomena, but are necessary to transport the produced solids (Tronvoll et al. 1997, Unnander et al., 1997).

3. SAND PRODUCTION MODEL DEFINITION

The current sand production model has two main components, the geomechanical and fluid flow equations which represent a coupled phenomenon. In addition, a sand production rule is included, which looks for including the behavior of the mentioned observations.

Based on the sand production evidences, the sand production rule aims to define the sanding conditions, and to quantify the sand production level. The main parameters in the sanding rule are the critical fluid velocity, the critical plastic strain, and the sand production to plastic strains parameter (μ_s). Critical fluid velocity refers to the minimum fluid velocity required to transport the detached sand grains, so if fluid velocity is lower that the critical value then sand grains are not transported and stays at the wellbore wall. Regarding to critical plastic strains sand production occurs only if the plastic strains are bigger than the critical value.

$$dm_s = \begin{cases} 0 & \varepsilon^{ps} < {\varepsilon_{cr}}^{ps} \\ \mu_s d\varepsilon^{ps} & \varepsilon^{ps} > {\varepsilon_{cr}}^{ps} \; ; \; v_f > v_{f\,cr} \end{cases} \quad (1)$$

Where dm_s is the ratio between the produced sand mass and the initial sand mass. The shear plastic strain ε^{ps} is defined as presented in Equation (2) and it is an accumulator of the plastic shear strains suffered by the formation. Moreover, the impact of sand production on the total strain tensor and the porous volume volumetric strain is given by Equations (3) and (4), respectively.

$$\varepsilon^{ps} = \int^{t} \sqrt{J(\underline{\dot{\varepsilon}}^{p})}\, dt \quad (2)$$

$$d\underline{\varepsilon}^{s} = \frac{k_s}{3} dm_s \underline{\delta} \quad (3)$$

$$d{\varepsilon^{s}}_{p} = \left(\frac{1-\phi-k_s}{\phi}\right) dm_s \quad (4)$$

Note that sand production causes an isotropic change in strain tensor. The sanding coefficient (μ_s) defines the sand production rate and the strain coefficient (k_s) defines the percentage of affectation of total volume due to sanding.

For the geomechanical problem three equations are integrated, the equilibrium equation, a constitutive relationship, and the consistency of displacements and strains (See Equations (5), (6) and (7) respectively).

$$\nabla \cdot (\underline{\sigma}) + \vec{F} = 0 \quad (5)$$

$$d\underline{\sigma} = \underline{\underline{C}}^e : (d\underline{\varepsilon} - d\underline{\varepsilon}^p - d\underline{\varepsilon}^s) + \alpha dp\underline{\delta} \quad (6)$$

$$\underline{\varepsilon} = \frac{1}{2}\left[\nabla \otimes \vec{u} + {}^t(\nabla \otimes \vec{u})\right] \quad (7)$$

The elastoplastic behavior of is modeled using the Drucker and Prager failure criteria with a not associated flow rule.

$$f(\underline{\sigma}) = \sqrt{J_2(\underline{\sigma})} - AI_1 - B \quad (8)$$

$$g(\underline{\sigma}) = \sqrt{J_2(\underline{\sigma})} - A^* I_1 - B^* \quad (9)$$

Plastic strains and sand production associated strains are presented in Equations (10) and (11) respectively. In those equations $d\lambda$ is the plastic multiplier. Note that sanding associated strains only occur when sanding conditions are reached.

$$d\underline{\varepsilon}^p = d\lambda \frac{\partial g}{\partial \underline{\sigma}} \quad (10)$$

$$d\underline{\varepsilon}^s = d\lambda \frac{k_s \mu_s \underline{\delta}}{3} \sqrt{J_2\left(\frac{\partial g}{\partial \underline{\sigma}}\right)} \quad (11)$$

The flow equation is the diffusivity equation (See Equation (12)), which accounts for the fluid material balance for a monophasic and compressible fluid, and introduce the geomechanically associated changes in porous volume, both elastic and plastic. Additionally, porous volume changes due to sanding are presented.

$$\nabla \cdot \left(\frac{\boldsymbol{k}}{B_o \mu} \nabla p\right) = A \frac{dp}{dt} - \frac{\alpha}{B_o} \frac{d\varepsilon_v^T}{dt} + \frac{(\alpha - 1)}{B_o} \frac{d\varepsilon_v^p}{dt} + \frac{(1 - \phi - k_s + \phi k_s)}{B_o} \frac{dm_s}{dt} \quad (12)$$

Where A is defined by Equation (13).

$$A = \frac{\left[\phi c_f - \phi c_s + (1 - \alpha)(c_{bc} - c_s)\right]}{B_o} \quad (13)$$

Permeability tensor is calculated as a function of porosity using the Kozeny-Carman relationship (see Equation (14)).

$$\boldsymbol{k} = \boldsymbol{k_0} \left(\frac{\phi}{\phi_0}\right)^3 \left(\frac{1 - \phi_0}{1 - \phi}\right)^2 \quad (14)$$

4. NUMERICAL SOLUTION

To solve numerically the system of equations, the finite element method is used. Note that cylindrical coordinates system is used because of the geometry of the problem (See Figure 1), especially because discretization is very efficient in this case with lower number of nodes required to solve the problem (Danielson & Noor, 1997). The radial size of the elements near the internal radius is small and increase exponentially as the elements are further from the internal diameter, which helps to have a higher resolution at the inner hole.

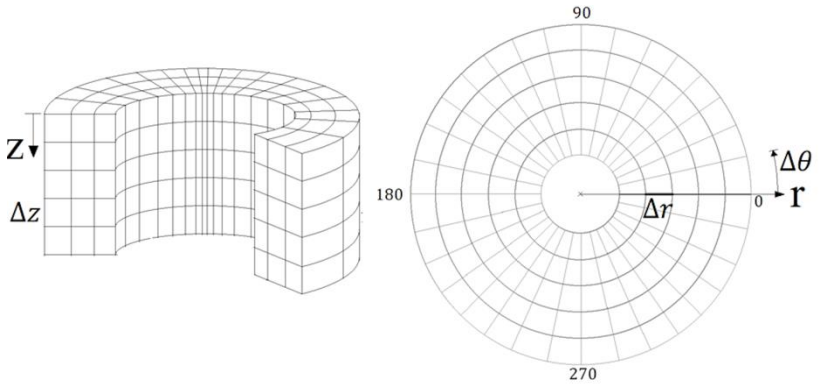

Figure 1. Physical model and Finite element grid.

Applying the FEM method in the coupled differential system (geomechanics and fluid flow), the local analysis for a single finite element results in Equation (15).

$$\begin{bmatrix} K_1 & C_1 \\ C_2 & K_2 \end{bmatrix} \begin{bmatrix} du \\ dp \end{bmatrix} = \begin{bmatrix} F_1 \\ F_2 \end{bmatrix} \quad (15)$$

Where C_1 is the geomechanics to fluid coupling term, C_2 is the fluid to geomechanics coupling term.

$$F_1 = \int_V B' C^e (d\underline{\varepsilon}^p + d\underline{\varepsilon}^s) dV + \int_S N' d\vec{T} dS \quad (16)$$

$$F_2 = -K_p p^n + \int_S N^{p'} (\vec{v} \cdot \vec{n}) dS - \int_V N^{p'} \left(C_i \frac{d\varepsilon^p{}_i}{dt} + D_i \frac{d\varepsilon^s{}_i}{dt} + \left(\frac{1 - \phi - k_s}{B_o} \right) \frac{dm_s}{dt} \right) dV \quad (17)$$

$$K_1 = \int_V B' C^e B dV \quad (18)$$

$$C_1 = \int_V B' \underline{\delta} N^P dV \quad (19)$$

$$K_2 = K_p + \frac{1}{\Delta t} \int_V N^{p'} A N^p dV \quad (20)$$

$$K_p = \int_V B^{p'} T B^p dV \quad (21)$$

$$C_2 = \int_V B^T \underline{\delta} N^P dV \quad (22)$$

Where $\vec{T}$ y $\vec{v} \cdot \vec{n}$ are respectively traction and flow velocity at the boundary, N is the shape function matrix and B are the spatial derivates of the shape functions, super index p refers to the pressure equation. The shape function 3D finite elements with 12 calculation nodes. The variables pressure and displacements, and their gradients expresses in terms of the shape functions are presented in Equations (23) , (24), (25) and (26).

$$\vec{U} = N_i \vec{u}_i \quad (23)$$

$$P = N^P{}_i p_i \quad (24)$$

$$\nabla \cdot \vec{U} = B_i \vec{u}_i \quad (25)$$

$$\nabla \cdot P = B^P{}_i p_i \quad (26)$$

5. RESULTS AND DISCUSSION

For the model application a hypothetical base case in open hole conditions is defined. In this case an isotropic in situ stress state is defined (See Table 1). Additionally, the ε_{cr}^{ps} value is cero, which means that the sand production starts at the same time that plastic strains are triggered. Note that this condition is equal to the analytical model conditions for sanding onset. During modelling the case is controlled with wellbore pressure, such that p_{wf} decreases to 1690 psi during 40 minutes. Sand production is accumulated and presented. Note that simulations always fulfill the condition of critical velocity to transport disaggregated sand grains.

Table 1. Base case properties.

Property	Value	Units
Reservoir pressure	2590	psi
$\sigma_h = \sigma_H = \sigma_v$	6000	psi
Thickness	30	ft
Fluid viscosity	5	cP
Fluid compressibility	8E-6	psi^{-1}
Isotropic permeability	600	mD
Bulk density	2.3	g/cm^3
Porosity	30%	--
Bulk compressibility C_{bc}	1E-6	psi^{-1}
Shear Modulus	600000	psi
Biot's coefficient	1.0	
Cohesion	1000	psi
Friction angle	10	°
Dilation angle	20	°
ε_{cr}^{ps}	0	--
Sand production parameter μ_s	0.1	--

Note that four different variables are analyzed. The effect of the variables ε_{cr}^{ps}, μ_s , horizontal to vertical stress anisotropy, horizontal stress anisotropy and cohesion on sand production level is reviewed. The used ranges for these variables are presented in Table 2.

All simulated cases have the same program in wellbore pressure reductions. Sand production quantity is mainly controlled by the μ_s parameter. Different simulation cases varying μ_s , show that the level of sand production increases proportionally to this variable, but a huge increase of sand production level is caused for μ_s values bigger than 1. Moreover, sand production level starts changing its behavior producing at higher rates. Along with produced sand mass is the productivity index. Note that

productivity index increases similarly to sand produced mass, which is aligned with the expected behavior of permeability increase due to sanding (increasing) and corroborates field observations.

Table 2. Base case properties.

Property	Values	Units
ε_{cr}^{ps}	0, 0.001, 0.002, 0.003	--
μ_s	0.01, 0.05, 0.1, 0.5, 1, 2, 10, 100, 1000	--
σ_h/σ_v ($\sigma_h = \sigma_H, \sigma_v = 6000$ psi)	0.8, 0.866, 1.0, 1.1, 1.2	--
σ_{h1}/σ_{h2} ($\sigma_h = \sigma_v = 6000$ psi)	0.8, 0.866, 1.0, 1.1, 1.2	--
Cohesion	800, 1000, 1200, 1400	psi

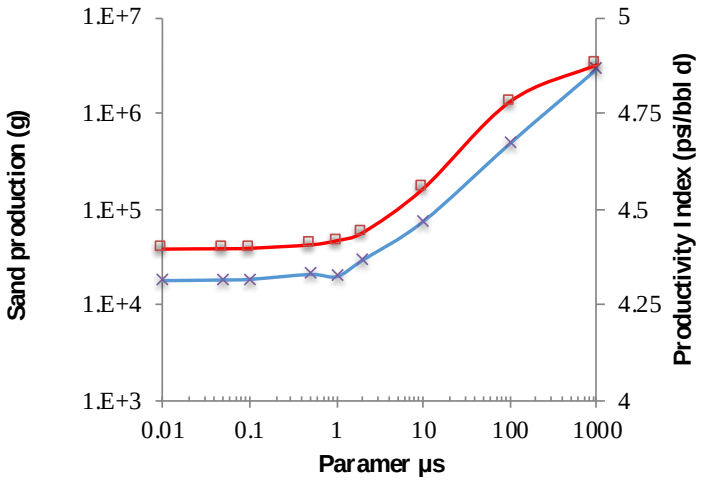

Figure 2. Effect of μ_s parameter in modelled sand production mass and productivity index.

In the case of horizontal to vertical stress anisotropy, sand production increases proportional to the anisotropy level. Note that this stress anisotropy sensitivity modifies the stress state regime from normal to inverse. Additionally, ε_{cr}^{ps} parameter is changed from 0 (base case) to 0.003, showing a reduction of the sand production levels. The effects of the two variables are presented in Figure 3. Note that each dot in the plot represent a complete simulation case. Additionally, the behavior is as expected, ε_{cr}^{ps} controls the onset of sand production, if ε_{cr}^{ps} is bigger, sand production onset is delayed, and at the end of the simulation cases produced sand is reduced. Although, sand production levels appear to be small, for real cases, the effect of sand production volumes in facilities erosion rates must be verified. This because, the sand production rate is not important at all, what really matters is the erosion and risks caused by sanding. Then, if the risks of producing sand are low, and surface system can stand sand production, then producing with sand is the best option.

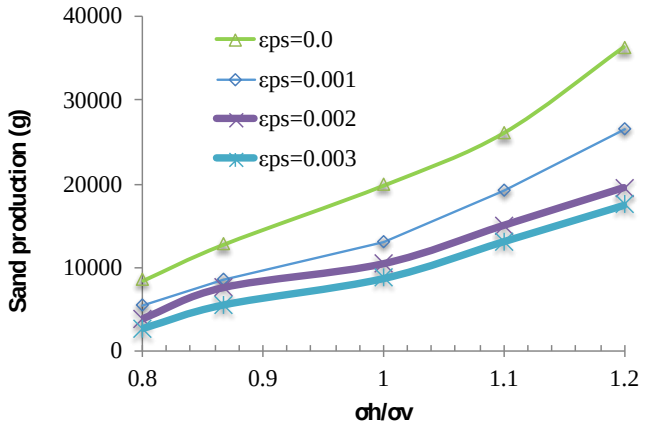

Figure 3. Effect of σ_h/σ_v ratio and ε_{cr}^{ps} on modelled sand production mass.

Regarding to the magnitude of horizontal stresses anisotropy, sand production increases when horizontal stress ratio increases too (See Figure 4). Note that at the highest horizontal stress ratio, one of the horizontal stresses is assumed constant equal to 6000 psi. This effect shows that sand production is higher when the difference between initial reservoir pressure and in situ stresses is higher too. Higher sand production is explained by higher plastic strains which is a requirement of sand production.

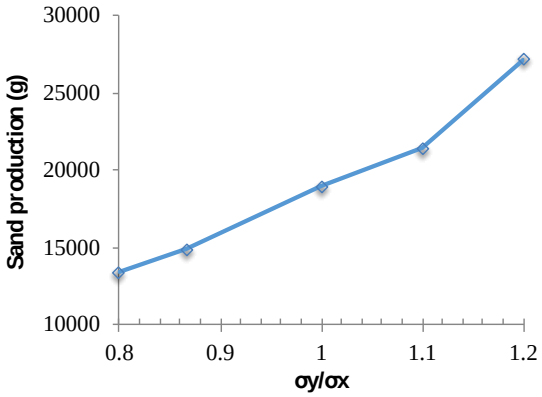

Figure 4. Effect of σ_{h1}/σ_{h2} ratio on modelled sand production mass.

Effects presented in Figure 3 and Figure 4, highlights mechanical stresses as one of the most important variables controlling sand production levels. Additionally, mechanical unload at the wellbore due to production of fluids, causes a new stress distribution around wellbore that generates sanding.

The last sensitivity analysis is related with cohesion values (See Figure 5). Note that the failure envelope is reduced or increased, then a formation with a lower or higher strength is modeled accordingly. Current effect shows how the mechanical stability of the formation affects the sand produced mass. The range of sanding was from 10000 to 50000 grams during 40 minutes simulated. This effect implies that cohesion has a not linear relationship with sanding, which is aligned with the expected behavior but highlights its importance. This fact forces a better characterization of formation strength parameters to predict more precisely sanding levels.

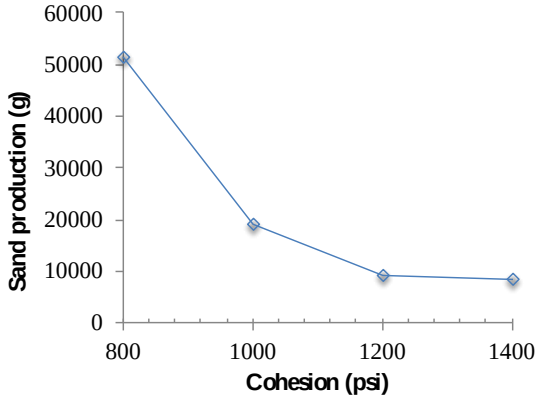

Figure 5. Effect of cohesion parameter on modelled sand production mass.

6. CONCLUSIONS

A numerical coupling model for sand production prediction is presented. The model couples fluid flow with geomechanics including a sand production rule, which is based in sand production observations. Parameters such as the elastoplastic limit and critical velocity for sanding are accounted.

Through this model, the sand production level can be evaluated. So, some sanding related effects were evaluated such as strength parameters, in situ stresses and sand production variables, among others. A hypothetical case and a sensitivity analysis in variables presented helps to determine that sanding rule parameters are highly important to model and match sand produced masses. The in-situ stress state sensitivity shows that higher sand produced masses are reached when horizontal stresses are higher, both for isotropic and anisotropic horizontal stresses. Finally, sand produced mass shows an exponential behavior with changes in cohesion parameter, which implies the need of a better characterization in formation strength parameters for precise sand production matching and forecasting in field and laboratory cases.

Further research must include real sand production cases to define sand rule parameters to match and validate model behavior on field conditions cases.

ACKNOWLEDGEMENTS

The authors acknowledge the support by MINCIENCIAS and ANH to Project 015-2016 "*Modelamiento geomecánico para el diagnóstico, evaluación y manejo de la producción de arena en pozos offshore*" as well as the support by GIGA group and Universidad Nacional de Colombia.

REFERENCES

Bazanti, M. S., & Desai, S. 1988. Sand production model for Safania field. *Society of Petroleum Engineers.* SPE-19035-MS.

Danielson, K. T., & Noor, A. K., 1997. Three-dimensional finite element analysis in cylindrical coordinates for nonlinear solid mechanics problems. *Finite Elements in Analysis and Design* (1997), 27(3), p 225–249.

Khamehchi, E., & Reisi, E., 2015. *Sand production prediction using ratio of shear modulus to bulk compressibility (case study). Egyptian Journal of Petroleum*, 24(2), 113–118. https://doi.org/10.1016/j.ejpe.2015.05.002.

Kanj, M. Y., & Abousleiman, Y., 1999. Realistic sanding predictions: a neural approach. In *SPE Annual Technical Conference and Exhibition*, October 3–6, Houston, Texas, USA: Society of Petroleum Engineers. https://doi.org/10.2118/56631-MS.

Nassir, M., Walters, D.A., Yale, D.P., Chivvis, R., Turak, J., 2015. 3D modeling of sand production in waterflooding by coupled flow/geomechanical numerical solutions. In: *49th US Rock Mechanics/Geomechanics Symposium*, June 28–July 1, San Francisco, California, USA: ARMA. ARMA-2015-426

Palmer, I.D., McLennan, J. D.; Vaziri, H.H., 2000. Cavity-like completions in weak sands. In: *Proceedings - SPE International Symposium on Formation Damage Control*, February 23–24, Lafayette, Louisiana, USA: Society of Petroleum Engineers. https://doi.org/10.2118/58719-MS

Tronvoll, J., Skjærstein, A., & Papamichos, E., 1997. Sand production: Mechanical failure or hydrodynamic erosion?. *International Journal of Rock Mechanics and Mining Sciences*, 34(3–4), 291.e1-291.e17. https://doi.org/10.1016/S1365-1609(97)00195-0

Unander, T. E., Papamichos, E., Tronvoll, J., & Skjærstein, A., 1997. Flow geometry effects on sand production from an oil producing perforation cavity. *International Journal of Rock Mechanics and Mining Sciences*, 34(3–4), paper No. 293. https://doi.org/10.1016/S1365-1609(97)00217-7

Vaziri, H. H.; Lemoine, L., 2000. Strong support for significant productivity boost through sand production. In: *4th North American Rock Mechanics Symposium*, July 31–August 3, Seattle, Washington, USA: ARMA. ARMA-2000-0295.

A new methodology for selecting sand control or sand management as strategy in wells with sand production potential

Edson Araujo-Guerrero, Guillermo Alzate-Espinosa, Yurladys Cross-Arroyave, Yeltsin P. Vega-Niño, Daniel Felipe Cartagena-Pérez, Abel J. Naranjo-Agudelo

Univerisdad Nacional de Colombia, Medellin, Colombia

ABSTRACT

Several reservoirs experience the phenomenon of producing fluids with some quantities of formation solids. This phenomenon, known as "sand production", occurs and affects many of the processes performed in a wellbore/reservoir and is one of the main factors causing problems related to project increasing costs with early equipment and facilities deterioration, low hydraulic conductivity detween wellbore and reservoir and sometimes complete well lose. The objective of this article is to present a methodology for selecting sand control or sand management as strategy to implement in sanding wells. This methodology, based on literature experiences, accounts for reservoir properties, fluid characteristics and completion variables for the selection of a strategy. In order to select correctly the strategy to implement in sanding wells either sand control or sand management, a two steps methodology is proposed. The first step allows to identify the better option between sand control or sand management for each case. Based on the previous step, the second step allows to identify the best way to implement each strategy. The present methodology helps to solve the difficult decision of either implement sand control or sand management through easy steps. This, using direct information of wellbore production and reservoir variables. The use of this methodology will allow for a better and faster decision making related to sanding wellbores treatment, reducing complex and unnecessary studies when those are not required.

KEYWORDS

Sand Production; Sand Control; Sand Management; Decision Methodology.

1. INTRODUCTION

Sand production occurs mainly in Poorly or unconsolidated formations, when forces of fluids in movement are enough to drag grains from formation sand. Produced solids can come from either the formation face or cavities or they can be fines coming from inside the reservoir. These solids can be produced for different reasons, therefore, to face sand production it is important to know the mechanisms involved in sanding. Some variables causing sand production are: pressure drop, depletion, in situ stresses, the water weakening effect, completion, drilling, and operational conditions (Araujo, 2015). For sanding wells, three options should be analyzed: Management, control or prevention. Sand Management refers to producing fluids with sand (with equipment erosion risk) improving porosity and permeability, hence productivity. Sand Control implies including filters in the bottom hole to prevent the transport of sand along with the fluid using mechanical or chemical means (Venkitaraman, Manrique, & Poe,. 2001). Sand Prevention does not involve control methods and depends on predictive models to identify the best drilling and production parameters that can delay sanding onset as much as possible in the life of the well (Venkitaraman, Manrique, & Poe,. 2001).

According to the results of a sand prediction model, sanding could start in the long term, therefore some operators prefer to produce the well without any control method installed initially looking not to decrease productivity, and once sanding begins, a sand control system is installed. This option of readjusting the well (retrofit), in some cases could be impractical, e.g. in offshore environments.

Sand production causes operational problems both at the bottom hole and at the surface, adding costs in sand handling, disposal, remediation, cleaning and equipment maintenance. Salehi Moorkani, *et al.*, (2010) mention some problems related to sand production:

- Downhole sand accumulation generating declination or cessation of production. See Figure 1.
- Sand accumulation in surface surpassing the facilities capability.
- Equipment erosion, which is dependent on the amount of sand, flow rate and type of fluid.
- Collapse of formation or casing due to high sand production.

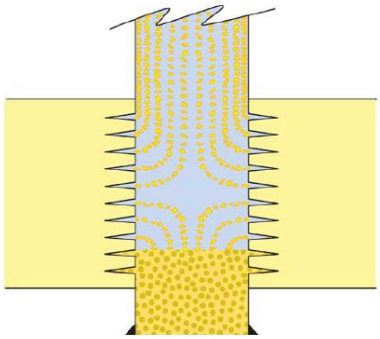

Figure 1. Solid production and bottom accumulation. Taken from Bellarby (2009).

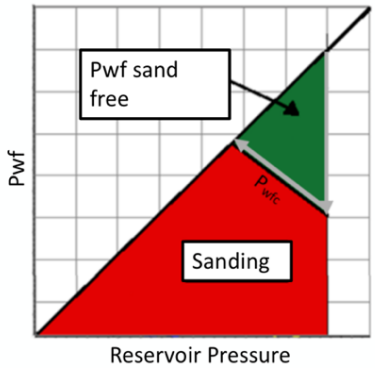

Figure 2. Sand production envelope. Taken from Araujo-Guerrero (2015).

1.1. Sand production prevention methods.

Methods of completion and production strategies to delay or avoid sanding without using sand control methods. They require a sanding model to predict the sanding onset. A well designed prevention method includes a contingency plan for sand control, that is, foresee possible sand control alternatives if necessary. Some sand prevention methods are listed below:

- Rate restriction by keeping the bottom hole pressure within the free of sand range (See Figure 2). It is appropriate in horizontal wells, whose productivity is not critically affected due to the high contact area between formation and well. Jaimes, *et al*, (2014a) presents a successful Colombian case, in which this technique was a technical and economical alternative.
- Selective perforating of the stronger intervals, isolating the sand prone intervals. Some conditions to classify intervals are: mechanical resistance and lower critical bottom pressures for sanding onset (CBHP) (Jaimes, *et al.*, 2014b).
- Oriented perforating: perforations are aligned to the directions of maximum mechanical stability, that is, in the direction where the stress contrast is the lowest (Jaimes et al., 2014b; Venkitaraman, Manrique, & Poe, 2001).

1.2. Sand Control Methods. Usage, limitations and advantages.

Stand alone screen (SAS) is the simplest and most economical method. SAS`s are screens with a grooved surface (free flow spaces), to filter the solids, except fines. They are installed without gravel, leaving a free annulus between screen and formation, which can be filled by formation collapse once production starts (total/partial collapse). After SAS installation, a good natural pack is achieved if the well is started with low rates. A total collapse eliminates the annular flow, meanwhile in a partial collapse, annular flow occurs and the screen may fail. The partial or total formation collapse (autopack) causes an additional skin that is critical if there is a high fines content or a highly heterogeneous formation (autopack damage) (Haskell *et al.*, 2010). The formation skin is obtained from a sand retention test and if it is high, another control method should be chosen. During SAS design, its internal diameter must be maximized as possible (minimum pressure drop inside the screen) and perform particle size distribution (PSD) tests, blocking tests, retention and integrity tests in high depletion scenarios (Han, Tallin, &

Wong, 2015). SAS application is recommended in formations with a D_{50}> 75 μm and a net-to-gross (NTG) > 80%.

To improve its performance, SAS is used with inflatable packers (zones isolation and reduction of annular flow), inflow control devices or ICDs, (uniform flow, reduction of hot spots and annular flow), slidding sleeves (to manage production from individual intervals in OH), among others devices (Chavan, *et al.*, 2011). The higher screen inlet area (percentage of external surface open to flow), the lower is the potential for blocking and erosion, and the longer is its useful life (Regulacion, *et al*. 2011). Some SAS's inlet areas are: Slotted Liner 1 to 4%, Wired Wrapped Screen 6.3 to 25%, Prepacked Screen <5%, Mesh Rite 40% and Premium 31 to 69%. Finally, SAS is not recommended in high rate vertical gas wells as the screen is easily eroded.

Expandable screen (ESS) is a screen that expands in the hole, adjusting itself to the hole diameter, which requires an ingauge hole (not to use in washed out wells). The expanded screen supports the formation to collapse and eliminates the annular flow (advantage over SAS). Additionally, the occupied section of the well diameter and frictional losses are minimized (Ripa, Bowen, & Conte, 2010). ESS is composed of an expandable perforated base pipe, a filter medium and an expandable cover to protect the filter. ESS inlet area ranges between 30 and 60% (Rahim, Al-Malki, & AlKanaan, 2010). For ESS design it is required retention and blocking tests, and to account for screen mechanical integrity during depletion (Ripa, Bowen, & Conte, 2010). ESS is recommended in formations with D_{50}>75 μm, and it has shown good performance in high rate gas wells whether horizontal or vertical (Ripa, Bowen, & Conte, 2010).

ESS is easier to install, less expensive, presents low damage, and offers a higher maintenance of productivity compared to SAS and open hole gravel pack systems (Deilami, Salehi-Moorkani, & Ghasemzadeh, 2010; Jones et al., 2005). Including expandable packages, ESS allows to isolate shale, gas or water intervals, which is the most important advantage over OHGP systems (Lau et al., 2004). Furthermore, selecting ESS over OHGP, can save 10 days of rig usage (Ripa, Bowen, & Conte, 2010). Its biggest limitations are: the system remains permanently in the hole after installation (Salehi-Moorkani, *et. al.*, 2010), and it is not recommended in cased holes (Bellarby, 2009).

Gravel pack (GP) is the most widely used method to control sanding and even fine sand production. It is applicable in open and cased holes (not for wells with diameter<5 in). It consists of filling with gravel (filtering medium) the annular between formation and screen (in open hole), or the annular between screen, casing and perforatings (in cased hole). Most GP failures are associated to productivity reduction, this due to filling an incomplete gravel packing with formation sand, which can be avoided using the High Rate Water Packing (HRWP) technique. HRWP allows to have more effective perforations, higher productivity and high useful life times (Mathis & Saucier, 1997). For gravel design, Saucier (1974) proposes that for achieving a balance between filtering, blocking, and maximizing permeability, the gravel's D_{50} should be between 5 to 6 times greater than the formation's D_{50}. Regarding to GP thickness, it must lay between 3 in (limit of low sand retention) and 5 in (maximum technical limit) (Matanovic *et al.*, 2012). Additionally, the resistance of the gravel must guarantee that it will not be crushed due to the increased stresses during depletion.

In open holes, with high fines content (> 10%), it is recommended to use horizontal wells or to use GP with an underreamed hole, this to reduce flow velocities. In cased hole, to reduce flow restriction, high perforation density and large diameters are required (penetration depth is less critical) (Oyeneyin, 2015). In case that flow velocities cannot be reduced (high rate and high permeability formations), pressure loss in packed perforatings would cause important production losses. Additionally, GP is not recommended in cased hole wells with an inclination angle higher than 60º due to the complexity and costs of packing vertical perforations (Bellarby, 2009). According to Burton & Hodge, (2010) the GP retained permeability ranges between 4 and 95%, depending on gravel permeability, drilling fluid composition and type of cleaning treatment, so it can generate high skins.

Frack Pack (F&P) or gravel packed fracture technique is designed for high permeability reservoirs with sanding. It seeks, rather than stimulating the formation, to generate short and wide fractures, and to pack

the fractures, perforatings and the annular between casing and screen with gravel, mitigating the loss of productivity through bypassing the damaged area around the well and controlling sand production. F&P could stimulate formations with low permeability (<10 mD) (Mathis & Saucier, 1997). It is appropriate in formations with high fines content (> 10%), due to the reduction of flow velocity and turbulence (allowing higher flow rates at lower pressure drops). It works well at intervals of less than 60 ft (Ali et al., 2002). In reservoirs with longer productive intervals, good vertical propagation is obtained by using screen with shunts (Behrmann & Nolte, 1998), or by fracturing multiple smaller zones (requires more equipment and is expensive). The gravel size should be 8-10 times the formation's D_{50} (Bellarby, 2009). F&P is not used when: there is a risk of the fracture contacting nearby gas or water zones without a competent barrier (Sanchez & Tibbles 2007), the casing diameter is lower than or equal to 5 in, there is a risk of casing failure or when well inclination angle is > 60° (Mathis & Saucier, 1997). In highly transmissible reservoirs it can become a flow restriction (Ali *et al*, 2001).

Chemical consolidation: It seeks to strengthen the near wellbore area by injecting a chemical treatment (resin) through perforatings, in order to bound sand grains. The challenge of this method lies in ensuring enough formation's mechanical strength while minimizing its impact on formation permeability. To implement it, it is recommended to guarantee: that wellbore is well cased, enough injectivity and good estimates of fracture pressure. It requires to carry out previous laboratory studies to correctly design the injecting process, fluids properties, chemical reactions, and the expected skin. In offshore cases, it is better to use water based resins (ABR) than solvent based resins (SBR) since they are less flammable (Foo, Bhasker & Foo-Karna, 2013; Songire et al., 2014). In cases with swelling clays that exceed 4%, it is difficult to obtain good compressive strength and retained permeability (Rama *et al.*, 2016). To dissolve these clays, an acid pretreatment must be carried out in the region near the well (Parlar et al. 1998).

This method is more successful on intervals lower than 15 ft (Chaloupka *et al.*, 2012) and requires efficient treatment of all perforations to avoid sanding (Parlar *et al*. 1998). It has a useful life from 1 to 2 years for epoxy resins (Chaloupka *et al*., 2012) and 1 year for resins type Furan (Parlar *et al*. 1998). It is restricted to clean formations (NTG ≥ 75%) and formations with permeability greater than 500 mD (Matanovic *et al*., 2012; Marfo *et al*., 2015). Among the advantages are: it does not generate additional restriction to the flow, it is economically favorable over GP and FP for short intervals and reservoirs with short productive life. It has been used successfully in gas wells and it does not require rig in the process (uses coiled tubing) (Marfo *et al*., 2015; Songire *et al.*, 2014).

Regarding the associated skin of each method, it was presented a skin from 1.8 to 2.2 for SAS and from 1.7 to 3.9 for GP (Burton, & Hodge, 2010). While for ESS, Bellarby (2009) presents an average skin of 0.9 (for 70 installed ESS), while Jones et al. (2005), found a skin of 0.3 (for 340 installed ESS). In table 3, damages reported for other sand control methods are presented. Jaimes, *et al.* (2014b), present the skin for CHGP (+5 a +10), HRWP (+2 a +5), F&P (-2 a +5), Chemical consolidation (+2 a +5).

Regarding to the percentage of failure of the sand control methods, Burton, & Hodge, (2010) shows for GP and SAS at open hole conditions, failure has reduced with time up to values near 12 – 14% in 2009. In cased hole completions, both GP y F&P reached failure of 8% (Burton, & Hodge, 2010). In the case of ESS, the failure percentage is found between less than 4.7% among 340 installations, even less than 2% if the screen is correctly dimensioned and installed (Jones et al., 2005).

2. NUMERICAL MODELLING OF SANDING AND PRODUCTIVITY LOOSES

For modeling of sand production phenomena and the productivity changes associated with well completion and sand control methods, a numerical simulation tool is used in this methodology. This numerical simulator allows modelling coupled processes of single-phase fluid flow and reservoir geomechanics with a poroelastoplastic behavior for the formation. This model combines the equilibrium equation, the elastoplastic constitutive equation, the diffusivity equation and a sand production criterion in a single tool. The proposed solution is developed in an in-house software in a fully coupled way, but iterative for convergence in plastic strains. It is solved through the finite element method (FEM) and the

physical model is in the cylindrical coordinate system due to geometric convenience. It is was implemented in FORTRAN language due to its high computational demand, although the complete methodology is implemented in Python language.

Naturally, being in cylindrical coordinates, this tool can model open hole completions, but a special feature of this tool is that it allows to include different types of flow restrictions inside the wellbore associated with completion. One of the most important is the possibility of configurating different types of cased hole completions, where the thickness and properties of the casing and cement can be introduced, this in addition to include perforating designs varying parameters such as perforation density (SPF), phase, average radius and penetration. Regarding to the sand control methods, it allows including the different methods mentioned in this document (SAS, ESS, OHGP, CHGP), accounting for their main characteristics as flow and mechanical properties, among others.

3. SELECTION OF SAND CONTROL OR SAND MANAGEMENT

This section presents a decision tree (See Figure 3), which helps to decide if it is better to implement sand control or management. Each result in message is present below. In the message 5, both methods must be analyzed.

- **Msg. 1**: In gas, condensate or HPHT wells, Sand Management is not advisable. Serious safety problems are generated by erosion at surface facilities. Control methods are mandatory. (Tronvoll, et. al., 2001)
- **Msg. 2**: Control methods reduce productivity and are expensive, then, Sand Management is recommended to induce highly favorable skins improving production rates. (Tronvoll, et. al., 2001)
- **Msg. 3**: In case of asphaltene or scale precipitation, the associated permeability losses are reduced allowing sanding. Still, it is possible to use control methods. (Tronvoll, et. al., 2001)
- **Msg. 4**: In Heavy and Extra Heavy oil wells, it is more profitable to allow sanding, as this increases permeability, e.g. CHOPS wells. If sand production volume at facilities is not tolerable, a sand control method with low impact in flow rates can be adopted. (Tronvoll, et. al., 2001)
- **Msg. 5**: There is no preliminary recommendation, so the analysis of both Control and Management will help to compare results and account for the technical and economic implications of each method.

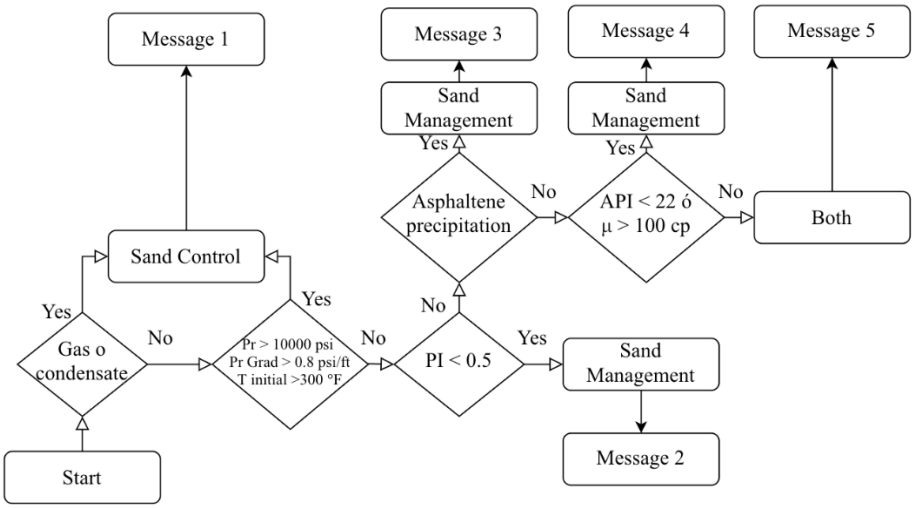

Figure 3. Decision tree for Sand Control or Sand Management selection.

4. SAND CONTROL METHOD SELECTION AND EVALUATION

This section presents a methodology to select the best sand control method, an initial assessment, based on the collection of empirical criteria and field experiences. Generally, the selection of a control method

is influenced by granulometry, mineralogy, flow velocity, damage around the well, fluid type, reservoir permeability, design and completion integrity, economic factors, logistics, associated risks, among others. For this reason, additional to the result of this methodology, it is important to perform a deeper analysis for each well. This way, the process of sand control method selection involves the next stages:

1. Data: mineralogy, particle size distribution (PSD), shale laminations, contacts, reservoir, well completion.
2. Prediction of onset, sand volume and sanding mechanism. Predictive models.
3. Preselection based on well, reservoir, environmental and operational conditions.
4. Quantify the impact. Determine the impact on PI or flow efficiency for each control method.
5. Economic analysis: Economic impact of the reduction of productivity in the short and long term.

In literature there are several methods for selecting the sand control method (Tiffin et al., 1998; Mathis & Saucier (1997); Price-Smith et al., 2000; Farrow, Munro, & McCarthy (2004); Haskell et al., 2010; Degos et al., 2010), but these do not group all types of technologies, some are horizontal wells, others only refer to GP and SAS, and do not account for chemical consolidation. As a contribution, the proposed methodology for selecting a sand control method groups the criteria of several authors to obtain a more robust and complete methodology. This is divided into three decision trees:

1. Cased hole wells with angle of inclination <60º (See Figure 4),
2. Open hole wells with inclination angle> 60º (See Figure 5), and
3. Open hole wells with inclination angle <60º (See Figure 6).

In the decision tress, Sc refers to the classification coefficient of sand and is defined as D_{10}/D_{95}. Meanwhile Cu is the uniformity coefficient of sand defines as D_{40}/D_{90}. If Cu <3 sand is uniformly classified; 3<Cu<5 is not uniformly classified and Cu>5 is highly not uniform sand. D_{10}, D_{40}, D_{90} and D_{95} are parameters from the PSD data.

Note that no method is recommended in cased holes with inclination angles > 60º due to its complexity and related high costs. This methodology allows, according to well conditions, reservoir and type of fluid, determining the appropriate control method. The required data is: PSD, NTG, expected production rate, fluid velocity near the well, fluid type, Skin, formation permeability, productive interval thickness and distance from the productive interval to contact zone.

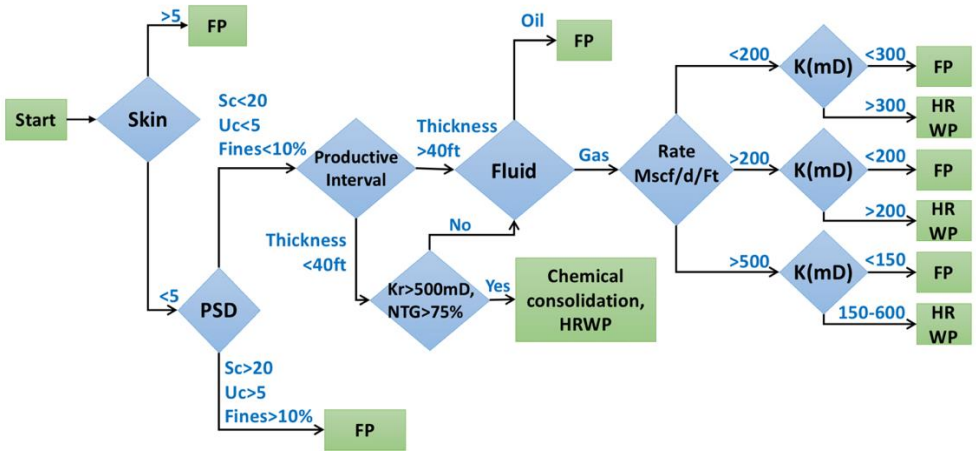

Figure 4. Decision tree for cased and perforated hole with inclination <60º.

For cased hole wells with inclination angle <60º (See Figure 4), according to field experience, up to 50% of perforations do not contribute to the flow due to collapse, blockage or damage, which turns out the number of effective perforations a variable that must be accounted. According to Welling (1998), productivity does not suffer significant reduction by perforatings filled with gravel, but when an incomplete packing is carried out, then solid (fines, sand and residues) will fill the voids reducing

productivity considerably. As mentioned before, HRWP is the most effective technique to pack the gravel in a cased hole (conventional packing results in a reduced effective perforation density and permeabilities between 50 and 5000 mD), and based on that, in GP, the decision tree will mention HRWP. Besides, for selecting between chemical consolidation and GP, it should be considered: hole diameter (GP limit is 5 in), injectivity (resin must enter the formation), zonal isolation, logistics, and treatment longevity.

For small thicknesses (< 40 ft), F&P is recommended with low viscous fluids or the WaterFrac technique (Mathis & Saucier, 1997). Open hole is recommended when well produces gas at a high rate (Q > 500 Mscf/d/ft) with k> 600 mD. If the hole is cased, maximizing the effective perforatings is the priority.

For open hole wells with inclination > 60º or horizontal wells (See Figure 5), sanding is minimized due to the lower pressure drops and lower flow velocities. In high productive formations (> 500 Mscf/d/ft) and k> 600 mD for gas, and for oil (>100 bpd/ft) and k> 900 mD), horizontal open holes or inclined completions are recommended to obtain optimal productivity and avoid reduction of flow efficiency, as a consequence of the restrictions and turbulence caused by the perforations Ali et al, (2001). Note that when Sc >10, Uc > 5 y Fines > 5%, ESS and GP are appropriated methods. Besides, for choosing one method: 1. use ESS when hole diameter <5 in, underreaming is expensive for long horizontal wells, 2. avoid using ESS in wells with high dogleg (>6°/100 ft). ESS installation is expensive and delayed.

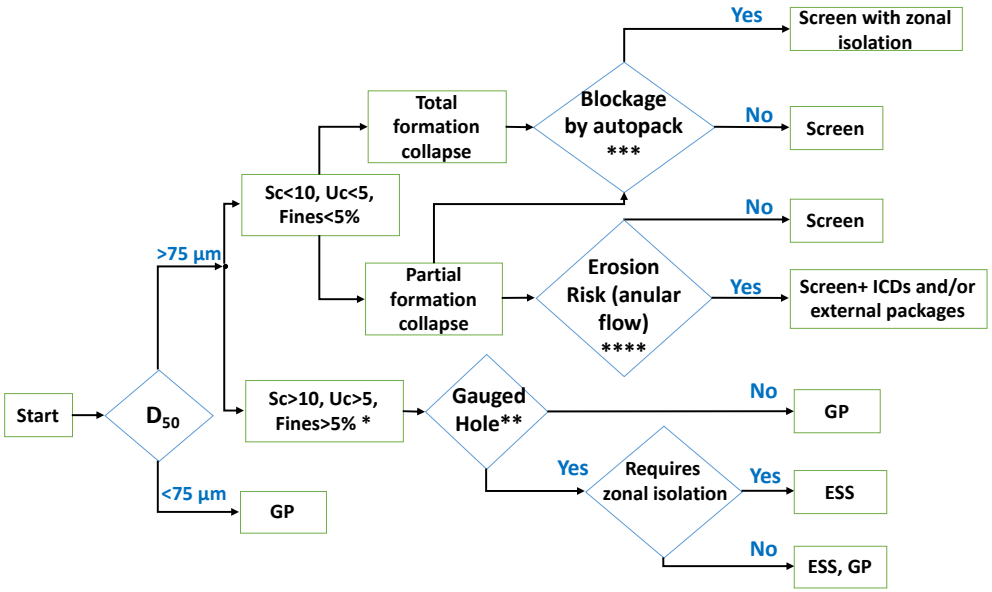

Figure 5. Decision tree for open hole completions well inclination >60º or horizontal.

For open hole wells with inclination < 60 º (See Figure 6), although the flow velocity limit and sand content for eroding the facilities must be determined for each case, for open hole vertical wells, SAS systems are not recommended if the fluid is gas due to the high flow velocities.

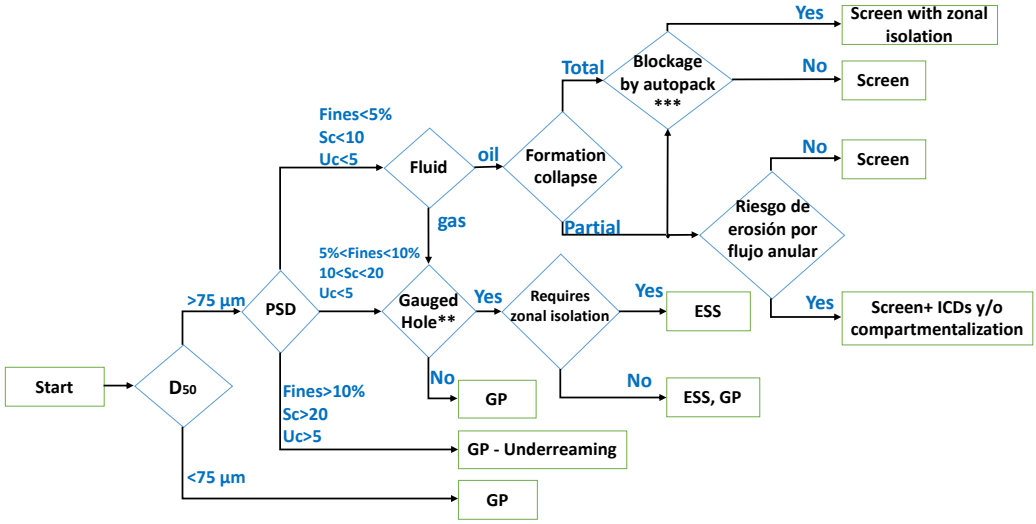

Figure 6. Decision tree for open hole completions well inclination <60º.

**gauged hole: Hole diameter equal to bit size (without collapse).
***Autopack blockage: Due to an heterogenous formation with shale zones causing production reduction. So, SAS should be implemented in homogeneous intervals with NTG > 80% or isolated sections.
****Annular flow erosion risk: Control sand transport using isolating packages and inflow control devices (ICD's).

After using this methodology, different optional sand control methods may be obtained to apply for the sanding problem. At this stage, a final analysis is proposed to limit the number of options. The main idea is to evaluate the impact on productivity of each of the optional sand control methods, so, with that information and knowing costs related to each control method, determine which one brings the biggest profit. This analysis is required because accounting for the global costs and total profit for each sand control method, rather than only productivity, it is the best tool for making decisions.

For evaluating the impact of the sand control methods on productivity, the model presented above is used, which allows modeling the poroelastoplastic behavior of the formation and determining the final productivity for each the case, this including the reduction in productivity associated with the different sand production control methods or wellbore completion. Reservoir, fluid and formation properties are presented in Table 1, Table 2 and Table 3 respectively. An example, of this analysis is presented in Table 4, where the PI ratio is presented. The PI ratio is the ratio between the current IP compared to the IP at open hole conditions.

Table 1. Reservoir properties.

Property	Value
Initial pressure	2200 psi
Depth	5000 ft
Vertical stress gradient	1.0 psi/ft
Horizontal stress gradient	0.9 psi/ft
Height	20 ft
Wellbore radio	4 in
External radio	50 ft
Permeability	600 mD
Porosity	30%

Table 2. Fluid properties.

Property	Value
Compressibility	$3.0x10^{-6}$ psi^{-1}
Viscosity	0.5 cp
Formation volumetric factor	1.2 RB/BN
API	30º
Height	20 ft

Table 3. Reservoir rock properties.

Property	Value
Young Modulus	$8.0x10^6$ psi
Poisson Ratio	0.25
Biot coefficient	0.99
Cohesion	1500 psi
Friction angle	20^o
Critical plastic strain	$1.0x10^{-5}$

Table 4. Productivity index ratio for different completions and sand control methods.

Sand Control/Completion	Description	IP/IP_0
Cased Hole 1	4 SPF and penetration 8 in	0.85
Cased Hole 2	12 SPF and penetration 14 in	1.23
ESS	Thickness 1.5 in, Effective k = 10 D	0.79
GP	Screen ID = 3 in, OD = 3.5 in, k_{gravel} = 10 D	0.74
CHGP	Cased Hole 2, k_{gravel} = 10D	0.85

5. SAND MANAGMENT IMPLEMENTATION

In the sand management method, sand is produced along with fluids, so the objective of this strategy is to produce with sand accounting for the related risks, and perform a proper management, handling and disposal of the produced solids. This methodology requires a constant monitoring of sand production rates and a broad understanding of the effects of sand production on surface and bottom equipment, especially the erosion rate and its relationship with the flow rate. For this, some severity scales of sand production have been proposed, especially based on sand concentration in the produced fluids. An additional measure is based on the effects of sandblasting such as the severity matrix proposed by Gupta et al (2016), which takes into account the abrasion rate and the rate of sand production. For the implementation of a sand management type process, it is necessary to have an appropriate knowledge of the formation's geomechanical behavior and of the sand production phenomenon just to predict as closely as possible both sanding conditions and the expected level of sand production (rates and volumes), and to quantify of the risk of sand production, including estimates of erosion rates at facilities as a function of fluid velocity and produced volume of sand.

Note that in the proposed method, in Figure 3, sand management is an option when: $PI \leq 0.5$, there is asphaltene precipitation, or fluid has low API and viscosity > 100 cP, which is a conservative filter to classify the cases where sand management is applicable. Accounting this, the methodology proposed for the sand management is focused on the produced sand volume. For this, an unmanageable sand batch parameter is proposed. An unmanageable sand batch is defined as the maximum volume of sand (in surface) produced during a short period of time, such that the designed surface facilities can manage it. This parameter must be determined for each case and should account for the erosion rate, the capabilities of the sand management and disposal system.

Usually, a sand production batch occurs when the conditions of flow are modified, e.g. sand production onset occurs when bottom hole pressure is reduced below its critical value. Using the numerical model, the sand batch value is required to obtain a minimal bottom hole pressure (P_{min}), for which the simulated sand production batch is equal to the sand batch value. Note that P_{min} is lower than the CBHP and P_{min} is calculated for different levels of depletion. For P_{min} calculation, a reservoir pressure (P_r) value is fixed, then wellbore pressure is reduced below the CBHP until the simulated sand production is equal to the sand batch volume. In Figure 7, three zones in the sand production envelope are shown, a sand free zone, a manageable zone and an unmanageable zone. The manageable and unmanageable zones are limited

by the P_{min} pressure. Lately, an economic analysis would permit to find an optimal pressure ($P_{min} < P_{opt} < CBHP$) which accounts for the flow conditions to reach the best profit.

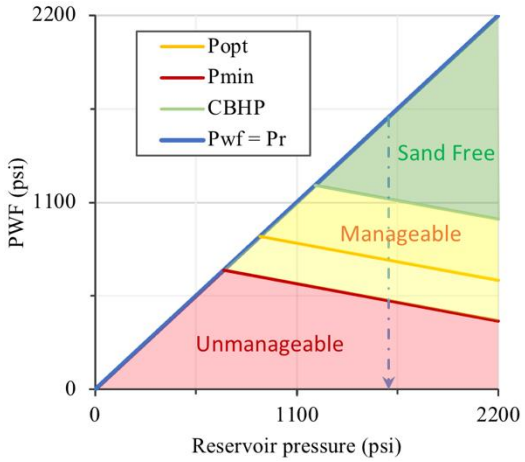

Figure 7. Sand production areas for sand management in sand production environment.

6. CONCLUSIONS

A methodology for identifying the best option between sand control or sand management is proposed. Although this methodology is conservative, it will help to users to easily classify a sand production case into one of the two options. Additionally, a methodology for selecting a sand control method is proposed this accounting for the favorable and unfavorable environments of each sand control method. Special emphasis is done in the sand control methodology, because several of the reported failures in the methods are related to mistakes in the selection of the method. Therefore, before selecting a sand control method it is necessary to perform a screening of the methods accounting for the limiting aspects of each method.

Related with the sand management methodology, it is recommended in cases there is a high confidence that sandblasting is not a big issue or where the facilities system is designed for handling sand production. Additionally, the way of calculation of an optimal pressure for sand management is presented, which will assure the correct application of the sand management technology.

Related with installing and using a sand control method, it is seen as a direct loss of productivity but it could result in an increment of productivity. This due to the increasing confidence of producing at bigger rates avoiding at the same time sanding problems, although, special care must be taken with fines content, because fines migration is a big enemy of all sand control methods, so avoiding fines migration and accumulation is mandatory to reduce skin and increase the performance of the sand control method. Initially, without performing previous tests, GP is the sand control method with higher confidence, but through rigorous tests and analysis, sand control method selection can be improved both technologically and economically. Although chemical consolidation has high requirements and important limitations, success is possible by means of an intense formation characterization and laboratory tests to increase the confidence in the method.

NOMENCLATURE

PI	=	Productivity Index
Pr	=	Reservoir pressure
Pr Grad	=	Reservoir pressure gradient
PSD	=	Particle size distribution
T initial	=	Reservoir temperature
μ	=	Fluid viscosity.

ACKNOWLEDGEMENTS

The authors acknowledge the support by MINCIENCIAS and ANH to Project 015-2016 "*Modelamiento geomecánico para el diagnóstico, evaluación y manejo de la producción de arena en pozos offshore*" as well as the support by GIGA group and Universidad Nacional de Colombia .

REFERENCES

Ali, S., Dickerson, R., Bennet, C., Bixenman, P., Parlar, M, Price-Smith, and Troncoso, J., 2001. High-productivity horizontal gravel packs. *Oilfield Review*. 13.

Ali, S., Norman, D., Wagner, D., Ayoub, J., Desroches, J., Morales, H., & White, S., 2002. Combined stimulation and sand control. *Oilfield Review*, 14(2), 31-47.

Araujo-Guerrero, Edson Felipe, 2015. Modelo de predicción y cuantificación de la producción de arena en yacimientos de crudo pesado *(Master's Thesis)*. Universidad Nacional de Colombia - Sede Medellín.

Bellarby, J., 2009. Well Completion Design. *Developments in Petroleum Science* (Vol. 56). 1-711. https://doi.org/10.1016/S0376-7361(08)00203-3.

Burton, R. C., & Hodge, R. M., 2010. Comparison of inflow performance and reliability of openhole gravel packs and openhole stand-alone screen completions. In *SPE Annual Technical Conference and Exhibition*, September, Florence, Italy, Society of Petroleum Engineers. https://doi.org/10.2118/135294-MS.

Chaloupka, V., Descapria, R., Mahardhini, A., Coulon, D., Tran, Q., Haekal, M., Nusyirwan, A., 2012. Sand consolidation in the Mahakam Delta: 3 years later. *Society of Petroleum Engineers*. doi:10.2118/151488-MS.

Chavan, C. H., McKenzie, T., Wenk, A. D., Tandon, R., & Bhat, S., 2011. First time application of stand alone screens with sliding sleeves in the giant Mangala field, Rajasthan India. In *International Petroleum Technology Conference*, November, Bangkok, Thailand. International Petroleum Technology Conference.

Degos, X., Bourgoin, S., Furgier, J. N., Marpaung, F., & Dufour, P., 2010. Expandable screens: Field cases in deepwater environment. In *SPE International Symposium and Exhibition on Formation Damage Control*, February, Lafayette, Louisiana, USA. Society of Petroleum Engineers. https://doi.org/10.2118/128046-MS

Deilami, F., Salehi-Moorkani, R., & Ghasemzadeh, A., 2010. Successful applications of expandable sand screen in Persian oil fields, Part 2. In *SPE Asia Pacific Oil and Gas Conference and Exhibition*, June, Tunis, Tunisia. Society of Petroleum Engineers. https://doi.org/10.2118/133364-MS.

Farrow, C., Munro, D., McCarthy, T., 2004. Screening methodology for downhole sand control selection. In *SPE Asia Pacific Oil and Gas Conference and Exhibition*, October, Perth, Australia. Society of Petroleum Engineers. https://doi.org/10.2118/88493-MS

Foo, I., Bhasker, R., & Foo-Karna, A. F.-F., 2013. Successful application of aqueous-based formation consolidation treatment introduced to the North Sea. In *SPE/ICoTA Coiled Tubing & Well Intervention Conference & Exhibition*, The Woodlands, Texas, USA, March. Society of Petroleum Engineers. doi:10.2118/163880-MS.

Han, Y., Tallin, A. G., & Wong, G. K., 2015. Impact of depletion on integrity of sand screen in depleted unconsolidated sandstone formation. In *49th US Rock Mechanics/Geomechanics Symposium*, San Francisco, California, June. American Rock Mechanics Association. ARMA-2015-301

Haskell, J. B., Toelsie, S., & Mohan, A., 2010. Optimization of sand control for unconsolidated, shallow, and low-pressure sandstone reservoirs: A Suriname case study. In *Trinidad and Tobago Energy Resources Conference*, Port of Spain, Trinidad, June. https://doi.org/10.2118/133461-MS

Jaimes, M. G., Quintero, Y. A., & Contreras, G. Y., 2014a. Drawdown management: A Technical and economic alternative for sand control in wells: A Colombian field application. In *SPE Latin America and Caribbean Petroleum Engineering Conference*, Maracaibo, Venezuela, May. Society of Petroleum Engineers. https://doi.org/10.2118/169376-MS.

Jaimes, M. G., Quintero, Y. A., Martin, D. P., & Puentes, M. S., 2014b. Design and implementation of software tool to select and evaluate sand exclusion and management alternatives, during the stages of

drilling, completion and production: A Colombian field application. In *SPE Latin America and Caribbean Petroleum Engineering Conference*, Maracaibo, Venezuela, May. Society of Petroleum Engineers. https://doi.org/10.2118/169398-MS.

Jones, C., Tollefsen, M., Metcalfe, P., Cameron, J., Hillis, D., & Morgan, Q., 2005. Expandable sand screens selection, performance, and reliability: a review of the first 340 installations. In *Middle East drilling technology, IADC/SPE*, Dubai, United Arab Emirates. SPE/IADC.

Lau, H. C., VanVliet, J., Ward, M., Morin, D., Djamil, A., Kuhnert, P., … Shanks, S., 2004. Openhole expandable-sand-screen completions in Brunei. *SPE Drilling & Completion*, 19(1). Society of Petroleum Engineers.

Marfo, S. A., Appah, D., Joel, O. F., & Ofori-Sarpong, G., 2015. Sand consolidation operations, challenges and remedy. In *SPE Nigeria Annual International Conference and Exhibition*, Lagos, Nigeria, August. Society of Petroleum Engineers. https://doi.org/10.2118/178306-MS.

Matanovic, D., Cikes, M., & Moslavac, B., 2012. *Sand control in well construction and operation.* Springer, New York.

Mathis, S. P., & Saucier, R. J., 1997. Water-fracturing vs. frac-packing: Well performance comparison and completion type selection criteria. In *SPE Annual Technical Conference and Exhibition*, San Antonio, Texas, October. Society of Petroleum Engineers. https://doi.org/10.2118/38593-MS

Oyeneyin, B., 2015. Integrated sand management for effective hydrocarbon flow assurance. *Developments in Petroleum Science*, 63, 288.

Parlar, M., Ali, S. A., Hoss, R., Wagner, D. J., King, L., Zeiler, C., & Thomas, R., 1998. New chemistry and improved placement practices enhance resin consolidation: Case histories from the Gulf of Mexico. In *SPE Formation Damage Control Conference*, Lafayette, Louisiana, February. Society of Petroleum Engineers. https://doi.org/10.2118/39435-MS

Price-Smith, C., Parlar, M., Bennett, C., Gilchrist, J. M., Pitoni, E., Burton, R. C., Dickerson, R., 2000. Design methodology for selection of horizontal openhole sand-control completions supported by field case histories. In *SPE European Petroleum Conference*, 24-25 October, Paris, France. Society of Petroleum Engineers. https://doi.org/10.2118/85504-PA.

Rahim, Z., Al-Malki, B., & AlKanaan, A., 2010. Selection of completion strategy for sand control and optimal production rate-field examples from Saudi Arabia's' Unayzah sandstone reservoir. In *SPE Asia Pacific Oil and Gas Conference and Exhibition*, Brisbane, Queensland, Australia, October. Society of Petroleum Engineers. https://doi.org/10.2118/131078-MS.

Rama, M. S., Songire, S., Meher, P., Kristanto, T. A., Latief, R., & bin, Z. M. H., 2016. Effective resin consolidation treatment methods and compositions for clay-laden formations. *Society of Petroleum Engineers.* doi:10.2118/178998-MS.

Regulacion, R., Seno, A., Safiin, N. B., & Suryana, N. Z., 2011. Optimized stand-alone screen design for the'J' Field, Malaysia. In *SPE Production and Operations Symposium*, Oklahoma City, Oklahoma, USA, March. Society of Petroleum Engineers. https://doi.org/10.2118/141461-MS.

Ripa, G., Bowen, E. G., & Conte, A., 2010. Years of success with premium expandable screen system through managed applications and installation. In *SPE Annual Technical Conference and Exhibition*, Florence, Italy, September. Society of Petroleum Engineers. https://doi.org/10.2118/132959-MS.

Salehi-Moorkani, R., Safian, G. A., & Mirzaei Paiaman, A., 2010. Successful applications of expandable sand screen in Persian oil fields, Part 1. In *SPE Production and Operations Conference and Exhibition*, Tunis, Tunisia, June. Society of Petroleum Engineers. https://doi.org/10.2118/133364-MS.

Sanchez, M., & Tibbles, R., 2007. Fracturing for sand control. *Middle East and Asia Reservoir Review*, 37-49.

Saucier, R. J., 1974. Considerations in gravel pack design. *Journal of Petroleum Technology*, 26(2), 205–212. http://doi.org/10.2118/4030-PA.

Songire, S., Hassan, A., Amer, M., Farid, S., Luijkx, J.-M., & AbdelKhaleq, M., 2014. Successful field application of aqueous-based formation consolidation treatment implemented in Nile Delta, Egypt. In *SPE Saudi Arabia Section Technical Symposium and Exhibition*, Al-Khobar, Saudi Arabia, April. Society of Petroleum Engineers. https://doi.org/10.2118/172214-MS.

Tiffin, D. L., King, G. E., Larese, R. E., & Britt, L. K., 1998. New criteria for gravel and screen selection for sand control. In *SPE Formation Damage Control Conference, 18-19 February, Lafayette, Louisiana* (pp. 201–214). Society of Petroleum Engineers. http://doi.org/10.2118/39437-MS.

Tronvoll, J., Dusseault, M. B., Sanfilippo, F., & Santarelli, F. J., 2001. The tools of sand management. In *SPE Annual Technical Conference and Exhibition*, New Orleans, Louisiana, September. Society of Petroleum Engineers.https://doi.org/10.2118/71673-MS.

Venkitaraman, A., Manrique, J. F., & Poe Jr, B. D., 2001. A comprehensive approach to completion optimization. In *SPE Eastern Regional Meeting*. SPE Eastern Regional Meeting, Canton, Ohio, October. Society of Petroleum Engineers. https://doi.org/10.2118/72386-MS

© 2021 Universidad Nacional de Colombia – ISRM, ISSN 2805-6426 *Guillermo Alzate Espinosa (Ed.)*

Wellbore stability analysis using drilling parameters

Uribe-Patiño, J. A.[a], Araujo-Guerrero E. F.[b], Villabona-Camacho J. A.[c]

[a, b] *RocMec S.A.S, Medellín, Colombia*
[c] *Ecopetrol S.A., Bogotá, Colombia*

ABSTRACT

This paper proposes a practical and cost-effective procedure to perform a wellbore stability analysis, including the elaboration of a safety mud window and the evaluation of the wellbore trajectory using drilling data (drilling reports, drilling parameters, mud properties, and mud-logging samples) that are routinely gathered in every well. The workflow includes the estimation of the rock geomechanical properties through a back analysis from the drilling parameters and the geomechanical events. These steps comprise the calculation of the pore pressure and stress state using the classical D-exponent method and Eaton's equation, along with the generation of a safety mud window and the evaluation of the wellbore trajectory using the Mohr-Coulomb (MC) failure criteria and the Kirsch's equations. Since the output of the proposed method depends on parameters that are not exactly known, significant engineering criteria and geomechanical expertise are crucial to achieve a quantitative analysis. The proposed approach was evaluated in a study case in a well drilled in the south-west of Colombia. The results were compared to those obtained from a wellbore stability analysis using geomechanical properties estimated from offset well logs, obtaining general agreement in magnitude and trend of the values. These findings suggest that drilling data, when properly used, can provide a reliable wellbore stability analysis for assisting post-drill studies, pre-drill forecasting, and decision making in real-time during the drilling operation. Moreover, the systematic application of the proposed methodology in several wells might allow updating the 3D geomechanical parameters at the reservoir scale.

KEYWORDS

Wellbore stability analysis, One-dimensional mechanical earth model, Drilling parameters, D exponent.

1. INTRODUCTION

Wellbore stability analysis has demonstrated to be an important aid for reducing drilling risks and costs related to unwanted drilling events such as loss of circulation, kicks, tight hole, stuck pipe, and hole collapse. The core of a wellbore stability analysis is an accurate one-dimensional mechanical earth model (MEM), whose accuracy is highly affected by the amount of information available for determining the rock geomechanical properties; which are the input parameters of the MEM. Oftentimes, the scarce available information is associated with the high costs of logging, coring, and lab testing programs that in some cases correspond to a large fraction of the total cost of the well; while in other cases, the lack of information is attributed to unsuccessful logging and coring runs in wells with high inclination or instability issues. The use of drilling data for estimating the geomechanical parameters of the drilled formations have been recognized since the 1960s (Cunningham and Eenink, 1959; Combs et al., 1968). A handful of models for estimating the pore pressure from drilling parameters have been proposed (Bourgoyne and Young 1974; Majidi et al. 2017), among these models the more traditional is the D-exponent method (Jorden and Shirley, 1966; Rehm and McClendon, 1971). Despite the theoretical assumptions needed to normalize the rate of penetration (ROP) and the neglect of drilling hydraulics, the D-exponent method is the most widespread in the industry, mainly due to its practicality and the low amount of information required for its implementation. Acknowledging the limitations of the D-exponent method and due to practical purposes, in this paper the D-exponent method will be

implemented in order to outline the procedure for achieving a wellbore stability analysis from drilling data. The D-exponent method allows defining qualitative trends in the pore pressure and the stress state. However, the great challenge is to obtain quantitative information from these trends, since there is significant uncertainty in the geomechanical parameters and in the simplifying assumptions of the model. From the drilling operation, many events and observations can be used to constrain the geomechanical parameters of the underground formations. Therefore in this paper, events such as cavings production, inflows, fluid losses, and FIT/LOT tests will be used to calibrate the computation of wellbore stability variables such as the breakdown pressure, the collapse pressure, and the fluid loss threshold.

2. THEORY

The D-exponent method is a classical empirical model for estimating the formation pore pressure from drilling parameters (Jorden and Shirley, 1966; Rehm and McClendon, 1971). It relies on the definition of a normal-compaction trend line (NCT); thus, deviations of the D-exponent from the NTC may indicate over-pressured or sub-pressured zones. Its main limitations are that it was developed for tricone drilling bits and it ignores bit hydraulics and bit wear. The D-exponent is defined by:

$$D = \frac{\log\left(\frac{R}{60N}\right)}{\log\left(\frac{12W}{1000d_b}\right)} \frac{MW_{norm}}{ECD} \tag{1}$$

Where R = rate of penetration ROP (ft/hr), R = RPM = revolutions per minute, W = weight on bit WOB (klb), d_b = bit diameter (in), MW_{norm} = normal hydrostatic gradient (ppg), and ECD= current equivalent circulation density (ppg). As most conventional methods for determining pore pressure, the pore pressure gradient can be estimated comparing the measured D-exponent with D-exponent under normal consolidation conditions (NCT) as follows:

$$g_p = g_n \frac{D_{norm}}{D} \tag{2}$$

Where g_p= pore pressure gradient (psi/ft), g_n = normal pore pressure gradient (psi/ft), and D_{norm} = D-exponent under normal consolidation conditions. The minimum horizontal stress can be estimated from the Eaton's equation:

$$\sigma_{hmin} = \frac{\mu}{1-\mu}\sigma'_v + p \tag{3}$$

Where σ_{hmin} = minimum horizontal, μ= Poisson's ratio, σ'_v= effective vertical stress, and p= pore pressure. The vertical stress is defined by:

$$\sigma_v = \int_0^z \rho_b g dz \tag{4}$$

Where ρ_b bulk's density. The variable ρ_b can be estimated knowing the density of the rock matrix ρ_s and the density of the pore fluid ρ_f, like that:

$$\rho_b = \rho_s(1-\phi) + \rho_f\phi \tag{5}$$

Where ϕ = porosity. The porosity is often modeled with a simple exponential function (Athy 1930):

$$\phi_n = \phi_a + \phi_b e^{-kz} \tag{6}$$

If it is assumed that diagenesis and complex burial history have not considerably altered porosity, unconsolidated formations will have higher porosity than normally consolidated formations; therefore, the deviations of the actual porosity from a porosity under NCT can be accounted in a similar way to the Eq. (2), like that:

$$\phi = \phi_n \frac{D_{norm}}{D} \tag{7}$$

The model for calculating the mud window is mainly based on the application of Kirsch's equations for inclined wellbores presented by Fjaer et al. (2008) and it has two main components:

1. Stress rotation to wellbore coordinates
2. Calculation of collapse pressure and breakdown pressure for each depth.

In the case of stress rotation, the in situ stress state is rotated to the wellbore coordinates. The initial stress state is aligned with a Cartesian system (x', y', z'), that is, the maximum horizontal stress $\sigma_{Hmax}$is parallel to x', the minimum horizontal stress σ_{hmin} is parallel to y' and the vertical stress σ_z is parallel to z'. A second coordinated system (x, y, z) is aligned with wellbore direction and inclination such that the wellbore axis is parallel to z, the x axis points toward the lowermost radial direction, and the y axis is horizontal. The transformation between (x', y', z') to (x, y, z) requires two operations. First, a rotation around the z' axis, then, a rotation around the y axis. The rotation matrix is presented in Eq. (8)

$$\underline{L} = \begin{bmatrix} \cos a \cos i & \sin a \cos i & -\sin i \\ -\sin a & \cos a & 0 \\ \cos a \sin i & \sin a \sin i & \cos i \end{bmatrix} \tag{8}$$

The stress tensor transformation from in situ condition to wellbore coordinates is performed using Eq. (9).

$$\underline{\sigma}^0 = \underline{L} \cdot \underline{\sigma}^{insitu} \cdot \underline{L}^t \tag{9}$$

With the stress tensor in wellbore coordinates, the next step is the calculation of the collapse and breakdown pressures. In this calculation, we use an application of Kirsch's equations for inclined wellbores at the wellbore wall (Fjaer et al., 2008) (See Eqs. 10 to 15). To obtain the collapse pressure at a specific depth, the wellbore pressure is decreased until the resulting stresses at the borehole wall cause a failure for the Mohr Coulomb failure criteria (See Eq. 16). In the case of the breakdown pressure, the wellbore pressure is varied until the resulting stresses at the borehole wall cause a failure by the tension criteria (See Eq. 17).

$$\sigma_r = p_{wf} \tag{10}$$

$$\sigma_\theta = \sigma_x^0 + \sigma_y^0 - 2\left(\sigma_x^0 - \sigma_y^0\right)\cos 2\theta - 4\sigma_{xy}^0 \sin 2\theta - p_{wf} \tag{11}$$

$$\sigma_z = \sigma_z^0 - \nu\left[2\left(\sigma_x^0 - \sigma_y^0\right)\cos 2\theta + 4\sigma_{xy}^0 \sin 2\theta\right] \tag{12}$$

$$\sigma_{r\theta} = 0 \tag{13}$$

$$\sigma_{\theta z} = 2\left(-\sigma_{xz}^{0}\sin\theta + \sigma_{yz}^{0}\cos\theta\right) \tag{14}$$

$$\sigma_{rz} = 0 \tag{15}$$

Where, P_{wf} is the wellbore fluid pressure, stress tensor components with the superscript 0 refers to the stress tensor in wellbore coordinates, θ is the angle of evaluation measured from the x axis, ν is the formation's Poisson ratio.

$$\sigma_1^{'} = UCS + \sigma_3^{'}\left(\frac{1+\sin\varphi}{1-\sin\varphi}\right) \tag{16}$$

$$\sigma_t = \sigma_{min}^{'} \tag{17}$$

Where, UCS= unconfined compressive strength, φ= internal friction angle, and σ_t= tensile strength. The UCS can be estimated from the porosity curve using the Eq. 18 which is correlation used for the sandy formations (Zoback, 2007) and the Eq. 19 which is a correlation for shaly formations (Horsrud, 2001).

$$UCS = 277\exp(-10\phi) \tag{18}$$

$$UCS = 2.922\phi^{-0.96} \tag{19}$$

3. METHODOLOGY

Figure 1 outlines the methodology to perform the wellbore stability analysis using drilling information. The blue boxes are the input parameters, the red boxes are the internal processing steps, and the green boxes are the outputs from each step. The workflow, from left to right can be explained as follows:

a. The first red box involves the calculation of the D-exponent which allows estimating the pore pressure, the minimum stress, and the overburden stress. To yield those results the drilling parameters should be gathered, cleaned, and prepared for the analysis, also the information about the stratigraphy of the drilled formations should be accounted for. In this step, the drilling parameter curves along with the D-exponent trend can be plotted, while the pore pressure and the stresses need to be calibrated in the next step.
b. In the middle red box the calibration is performed, in which the drilling events and regional geomechanical variables are accounted for. In this step, empirical correlations, engineering criteria, and geomechanical expertise are required to estimate the rock's elastic and mechanical properties such as the UCS, the Poisson's ratio, and the internal friction angle.

c. In the last red box, the stability variables are calculated to obtain the mud window and the polar plots. In this step, the results are compared with the events and observations reported during drilling which allows to back-calculate the elastic and mechanical parameters to meet the field observations.

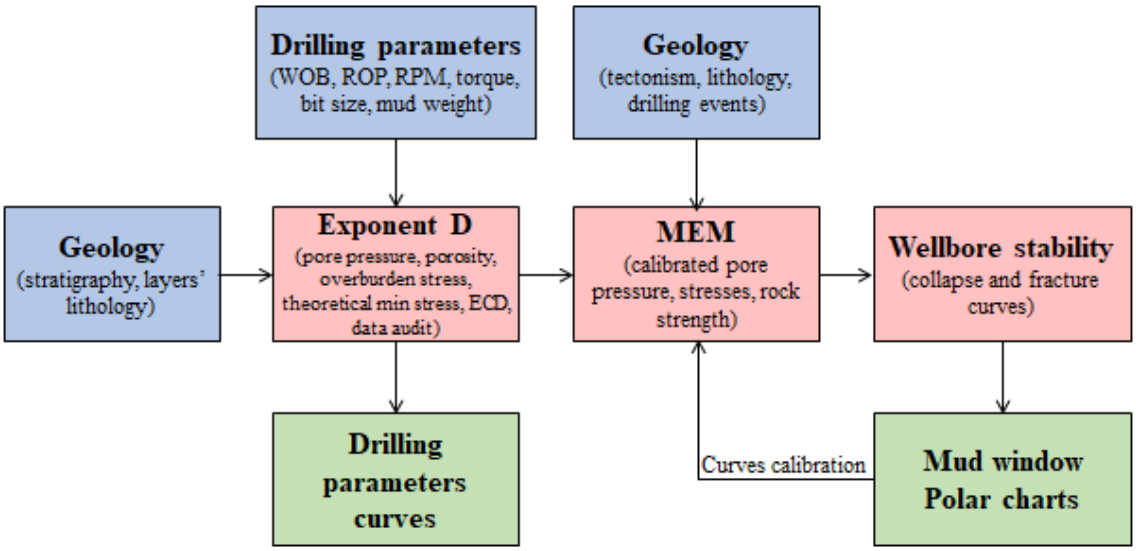

Figure 1. Work flow of MEM estimation from drilling parameters.

4. FIELD EXAMPLE

To demonstrate the proposed procedure, the following case of study is considered. The well is located in the south-west part of Colombia. It was drilled across the following formations with main characteristics:

- Formation A: Quaternary alluvial deposits composed mainly by conglomerates and igneous and chert clasts.
- Formation B: Altelnarting Miocene sequence of claystone and siltstone.
- Formation C: Oligocene intercalations of thick layers of siltstone and thin layers of fine-grained quartz sands.
- Formation D: Late Eocene sequence of conglomerates and sands in the upper part, siltstone and claystone which grade to fine-grained sands in the mid part, and conglomerates in the lower part.
- Formation E: Late Maastrichtian - Paleocene mainly claystone with siltstone intercalations and a minor proportion of sand.
- Formation F: Albian - early Maastrichtian mainly shale with intercalations of limestone.
- Formation G: Aptian – Albian sequence of quartz sandstone and sand.

The figure 2 shows the reported drilling parameters along with the computed D-exponent (Eq. 1).

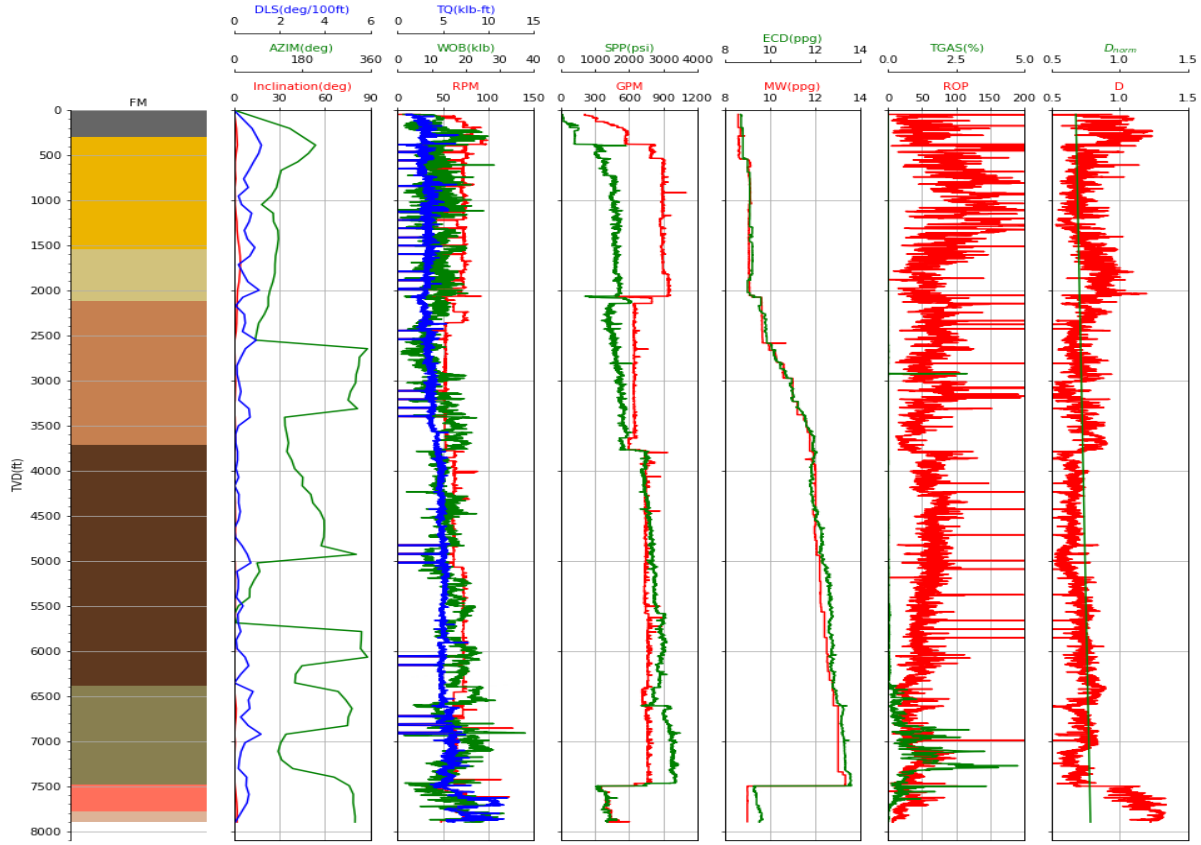

Figure 2. Drilling parameter and D-exponent.

Using the drilling parameters in the figure 2 the pressure gradient can be estimated with Eq. 2 and the minimum horizontal stress gradient with Eq. 3. As an initial guess, it was assumed a constant Poisson's ratio of 0.33 and the overburden gradient was assumed to be 1 psi/ft. The figure 3 presents the first estimation of the underground parameters; however, it is necessary to account for the field observations in order to calibrate the results.

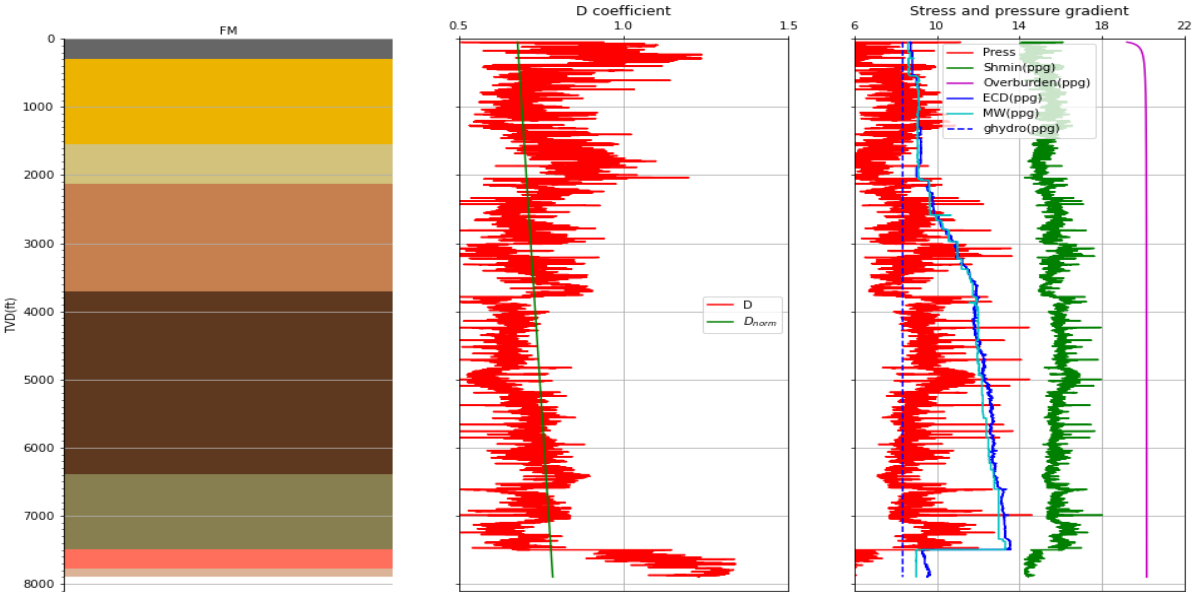

Figure 3. Preliminary pore pressure and stress results.

Outstanding information for refining the results presented in the figure 3:

- There are different zones where the estimated pore pressure gradient is lower than hydrostatic pressure gradient (blue dashed line); even though, the reservoir is known to have a low pore pressure, there is not known reasons for the pore pressure gradient to be lower than the hydrostatic pressure gradient in formations other than the reservoir. For this reason, values of pore pressure gradient lower than the hydrostatic pressure gradient will be omitted.
- It can be observed various pore pressure gradient values which overcome the mud weight, there were not inflows reported in the operation; therefore, values of pore pressure gradient greater than the mud weigh will be disregarded.
- From the depth of 5000 ft, there is a change in the in the pore pressure gradient trend, that is, above 5000 ft the pore pressure gradient trend is increasing with depth, but below 5000 ft the trend is decreasing. Apparently, this behaviour seem to be erroneous; since there is not reason to expect a progressive pore pressure reduction from that particular depth. That prediction of the model seems not to be directed correlated to a natural response of the formations. This misleading result evidences one the main disadvantages of the D-exponent method which is that it interprets any change in the drilling parameters as it were the result of variations in the rock properties; and this is mainly caused due to not considering other variables such as bit type, bit wear, mud type, drilling hydraulic, etc.
- During the drilling operation, it was observed, at the measured depth MD of 7182 ft, an increasing trend in the background gas, along with an increasing percentage of splintery cavings in the Shale shakers (up to 50%) sizes 50-70mm (figure 4). It was necessary to increase the mud weigh from 13.0 ppg to 13.3 ppg to manage the event. This observation indicates that at the depth of 7182 ft the mud weight was close the pore pressure, which severs as a calibrations point. Likewise, this observation proves false the decreasing pore pressure trend predicted by the D-exponent method in the figure 3.
- At the depth of 2077 ft a FIT test was carried out resulting an equivalent mud weigh of 15.7 ppg, which can be used as lower limit value for the minimum horizontal stress.

Figure 4. Observed splintery cavings.

Accounting for the above notes and observations, the pore pressure was calibrated and the depending variables were recalculated, the results are presented in the figure 5, with the purple star showing the depth of the FIT test and the red star showing the depth of the splintery cavings production.

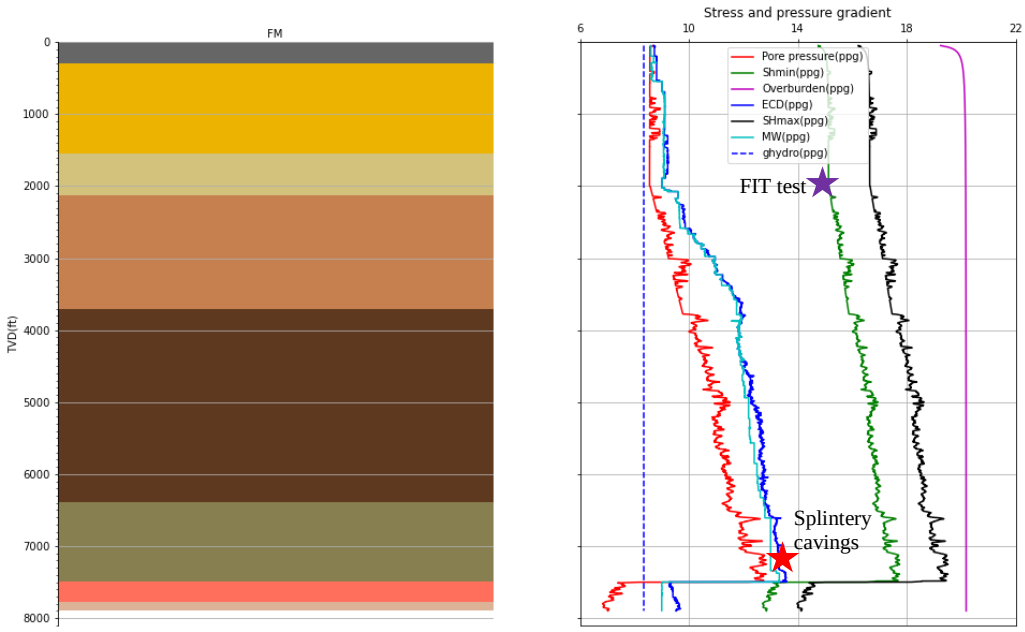

Figure 5. Calibrated stress and pore pressure results.

The stress state shown in figure 5 is used then to compute the mud window presented in figure 6, the following assumptions were made in order to achieve the reported results.

- The results were obtained after several iterations to define the limits in the elastic and strength parameters (figure 7); the result is an estimated mud window which best represent the field observations. The UCS of the material was calculated, based on the porosity curve (Eq. 6 with values of $\phi_a = \phi_b = 0.2$ and k = 0.0035), using Eq.18 for the sandy formations and Eq. 19 for shaly formations. Subsequently the USC values were approximated with a cubic function in order to avoid abrupt changes that may affect the mud window computations.
- Additionally, the friction angle was also assumed lithological dependent using 35° and 30° for sand and shale, respectively. Furthermore, the Poisson's ratio was assumed 0.28 sandy formations 0.28 and 0.30 for shaly formations.
- Based on the information related to the tectonics of the area available in the World Stress Map (Heidbach et al. 2016), it was assumed a normal faulting stress regimen (Sv>SHmax>Shmin) and a maximum horizontal stress (SHmax) azimuth of approximately 100°.
- The minimum horizontal stress was calibrated using a Formation Integrity Test (FIT) performed in the wellbore during drilling, as mentioned earlier.
- To estimate the magnitude of the maximum horizontal stress, different levels of anisotropy were evaluated taking into account that the basin is considered passive, therefore low anisotropy is expected. Finally, an anisotropy level of 1% was used with good results in the reproduction of drilling events.
- It was necessary to increase the overburden gradient to 1.1 psi/ft to improve the mud window results.

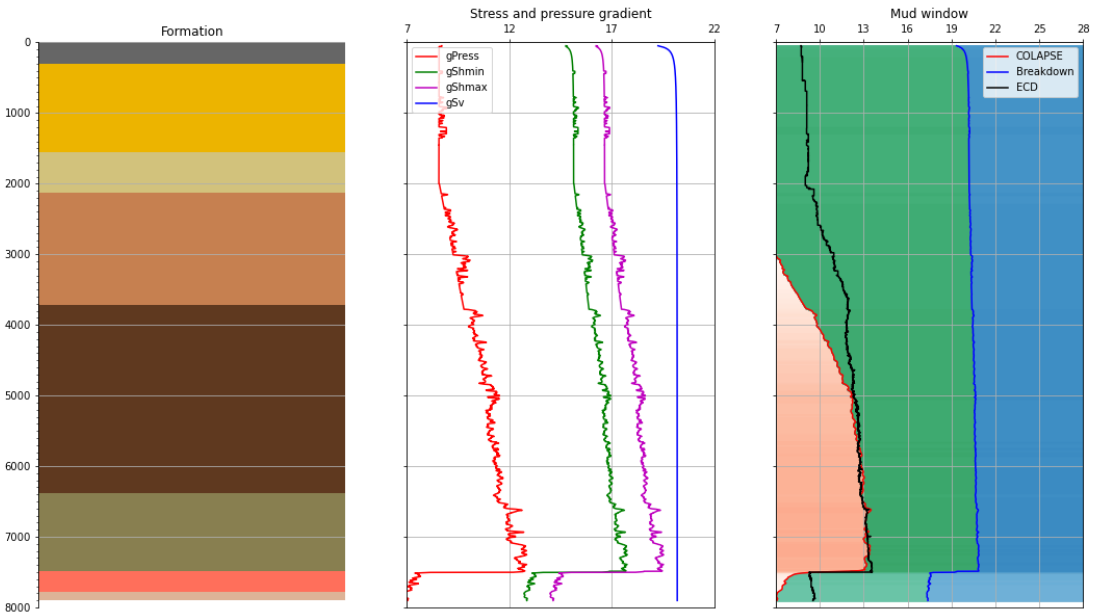

Figure 6. Mud window.

The estimated mud window displays a zone where the ECD is closed to the collapse pressure (4800 ft to 7500 ft); it was decided this behaviour was in accordance with the field observations, since in that particular depth interval, it was reported a content of breakouts cavings ranging from 15% to 30% (figure 7). The overall breakout during drilling was 15%; even though this values was low during the drilling operation, the more problematic wellbore instability events occurred during pulling out of hole and run in the hole trips, which was responsible for significant accumulated non-productive times. It was reported an event, during a trip, where the caving production reached a value of 8 bph and 80% of breakout content (figure 8).

Figure 7. Characteristic breakout during drilling.

Figure 8. Characteristic breakout during trips.

Additionally to the mud window, figure 9 shows the polar plots for two selected depths of interest. This plot was performed varying the wellbore direction 360 degrees from the North and the wellbore inclination from vertical to horizontal. In the figure 9, the maximum horizontal stress has an azimuth of 100°. As it was expected, the most stable inclination was for a vertical well. Drilling through sub-horizontal layers and little stress anisotropy leads to relative little differences in stability with azimuth.

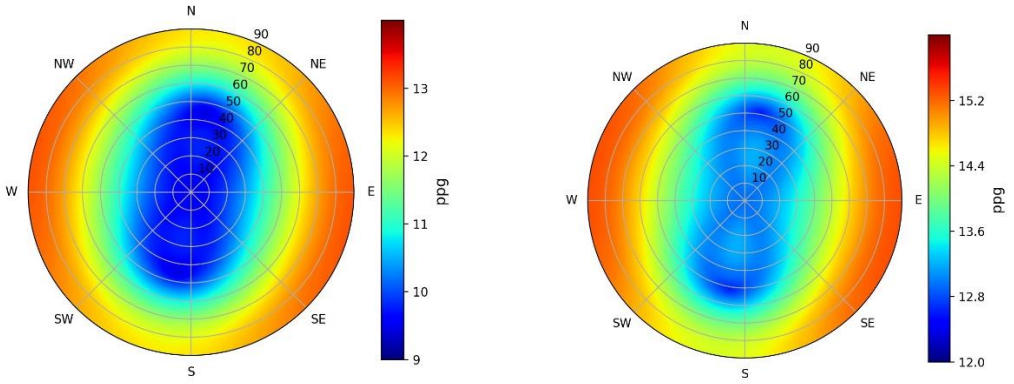

a). Polar plot at 3826’ b). Polar plot at 5845’

Figure 9. Polar plots at different depths (the wellbore is located at the center of the plot).

The wellbore stability analysis from the drilling parameters (estimation of the stress state, mud widow, and back-analysed strength parameters) is then compared to the results computed from offset well logs. The figure 10 shows that, in general, the trend of the values estimated from drilling parameters (solid lines) agree with the values computed from offset well logs (dashed lines). In the analysis from drilling parameters, the maximum horizontal stress gradient was calculated from a constant anisotropy factor; which may explain the deviation with the values calculated from offset well logs, which uses a more complete source of information for estimating these values. Additionally, it can be observed in figure 10 that the collapse and breakdown curves from drilling parameter resulted in more conservative values compared to the one from offset well logs, which is a good thing regarding that there is more uncertainty involve in the wellbore stability analysis form drilling parameters than from offset well logs.

The comparison of the back-analysed strength parameters is presented in figure 11. Even though there is important deviation between the magnitude of values obtained from drilling parameters and the values obtain from offset well logs, it can be argued that the results obtained from the proposes approach might be helpful to constrain the real values. It is interesting to note how the proposed UCS captured relatively well the trend of the values calculated with offset well logs; this is because in interval from 4000 ft to 6000 ft the UCS had to be reduced to avoid excessive predicted borehole collapse, which indicated a weak zone, whereas as the high UCS values were related to zones with no breakout reports, the smooth effect was achieved by the fitting the values with a cubing polynomial function.

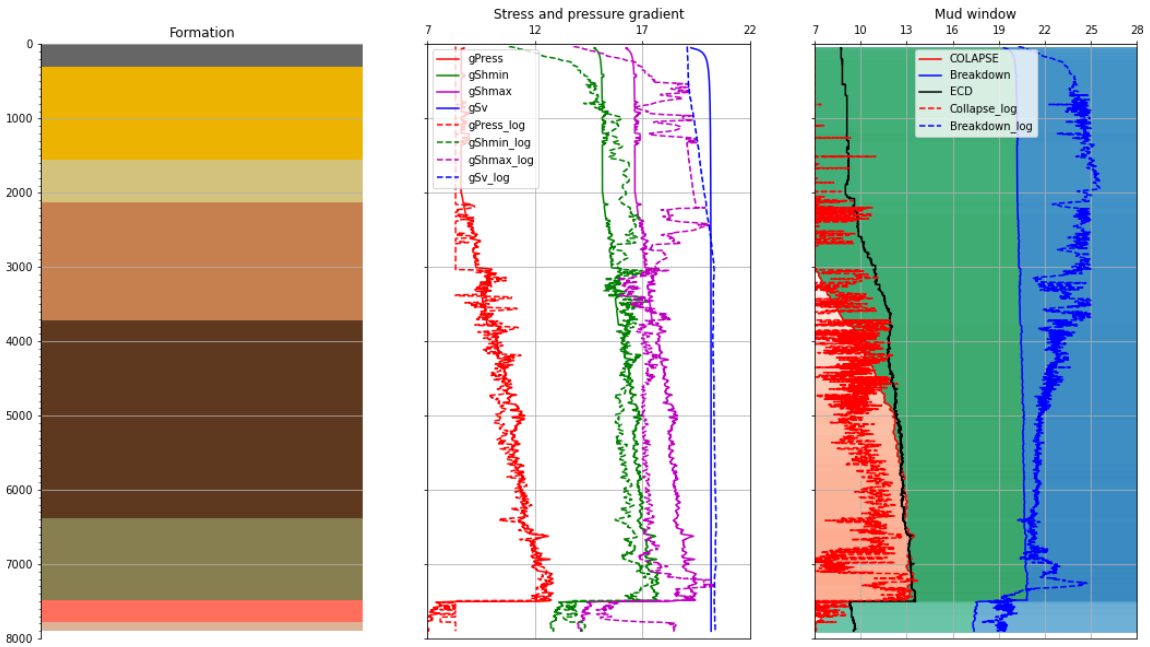

Figure 10. Comparison between results from drilling parameters and offset well logs.

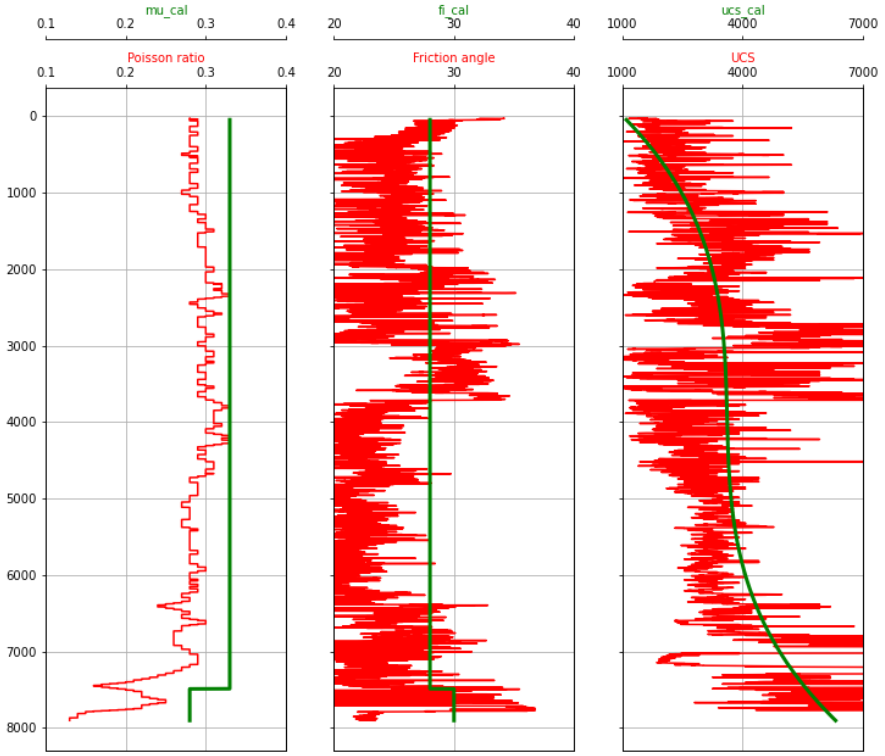

Figure 11. Elastic and strength parameters from drilling parameters vs. from offset well logs.

Important assumption were made to achieve the wellbore stability analysis from drilling parameters, despite of the fact that it was observe significant deviations from the values computed with offset well logs; it may be argued that the results obtained in this paper may be of substantial help to constrain the real stress state and rock strength parameters, particularly in the case of having limited o non available information. This article is not intended to propose a substitution for the wellbore stability analysis computed from well logs; however, the methodology presented in this document might be a valuable way for condensing and making sense of geomechanical information gathered during the drilling operation. It might be more practical to present the geomechanical drilling information in the condensed format of figures 6, 9, and 11 than presenting it as a pile of reports and drilling parameters logs.

5. CONCLUSIONS

- By implementing the D-exponent, a methodology for performing a wellbore stability analysis using drilling data was presented and demonstrated to be useful.
- The estimated mud window generally agrees in magnitude and trend with the mud window estimated from offset well logs.
- Despite the recognized limitations of the classical the D-exponent, the results were coherent, which can be attributed to the verticality of the studied well and that it is was possible to define an NCT in the formation E, which is mainly a massive claystone interval
- Even though the results were coherent with the results obtained from logs, it is important to consider more advanced techniques to estimate the pore pressure and stresses from the drilling parameters, since the well geometry, the drilled formations, the drilling hydraulics, drilling bit type, and the degree of overbalance might affect the results.
- The analysis was performed as a function of depth, it is important to consider the time effect in the wellbore stability, because there are many geomechanical events that might occur in operations other than drilling which can contribute to the constraining of the geomechanical parameters, for instance during tripping in/out the wellbore.
- Due to the limited information, the analysis was performed averaging the geotechnical parameters by formation, however, it is crucial to discretize the formations by rocks; because inside each formation might be significant variations in the geomechanical properties.
- It is advisable to apply the proposed methodology to multiple wells in the same region, since an overall analysis might be useful to reduce the uncertainty in the elastic and mechanical parameters of the rocks.

ACKNOWLEDGEMENTS

The authors are grateful to Ecopetrol S.A for permission to display and publish the data presented in this paper.

REFERENCES.

Athy, L. F. 1930. Density, porosity, and compaction of sedimentary rocks. *AAPG Bulletin*, 14(01), 1–24.

Bourgoyne, A. T. Jr. and Young, F. S. Jr. 1974. A Multiple Regression Approach to Optimal Drilling and Abnormal Pressure Detection. *SPE Drilling & Completion.* 14 (4), 371–384. SPE-4238-MS.

Combs, G. D. (1968). Prediction of Pore Pressure from Penetration Rate. *Presented at the Fall Meeting of the Society of Petroleum Engineers of AIME, Houston, 29 September–2 October.* SPE-2162-MS.

Cunningham, R. A. and Eenink J. G. 1959. Laboratory Study of Effect of Overburden, Formation and Mud Column Pressures on Drilling Rate of Permeable Formations. *Transactions of the Society of Petroleum Engineers*, 217, 9–17. SPE-1094-G.

Fjaer, E., Holt, R. M., Horsrud, P., Raaen, A. M., and Risnes, R. 2008. *Petroleum Related Rock Mechanics*, 2nd Edition, Elsevier, Amsterdam.

Heidbach, Oliver; Rajabi, Mojtaba; Reiter, Karsten; Ziegler, Moritz; WSM Team 2016. *World Stress Map Database Release 2016*. V. 1.1. GFZ Data Services.

Horsrud, P. 2001. Estimating Mechanical Properties of Shale from Empirical Correlations. *SPE Drilling & Completion.* 16(2), 68-73. SPE-56017-PA.

Jorden, J. R. and Shirley, O. J. 1966. Application of Drilling Performance Data to Overpressure Detection. *J Pet Technol*, 18(11), 1387–1394. SPE-1407-PA.

Majidi, R., Albertin, M. and Nigel, L. 2017. Pore-pressure estimation by use of mechanical specific energy and drilling efficiency. *SPE Drilling & Completion*, 32(02), 97–104. SPE-178842-PA.

Rehm, B. and McClendon, R. 1971. Measurement of Formation Pressure from Drilling Data. *Presented at the Fall Meeting of the Society of Petroleum Engineers, New Orleans, 3–6 October*. SPE-3601-MS.

Zoback, M. D. 2007. *Reservoir geomechanics*, Cambridge University Press, New York, USA.

Practical approach for wellbore stability modelling in a tectonically and geologically complex area: Colombian foothills field case

Cesar F Lopez[a], Jefferson S Mateus[a], Henry Arias[a], Aura M Roa[a], Juan D Puerta[a], Alexander Lopez[a],

[a] *Ecopetrol, Bogota, Colombia*

ABSTRACT

Piedemonte fields (Floreña and Pauto) are located in a tectonically and geologically complex area in the Colombian foothills, characterized by rugged topography, deep reservoirs, highly folded layers, high magnitudes and anisotropy in the stresses, presence of natural fractures and interbedded shale and sand sequences. The aforementioned features result in elevated drilling costs related to severe wellbore stability problems associated with high production of cavings, hard tripping, stuck pipe and sidetracking issues.

Geomechanical and wellbore stability modeling are important tools to reduce drilling costs related with operational problems by setting adequate mud weights, evaluating well trajectories and casing designs and identifying operational risks. In the Piedemonte fields, this kind of modelling represents a big challenge considering that every well needs a specific wellbore stability model due to the geological complexity, additionally, the information required can be limited due to operative or cost constraints of logging, coring or performing leak off tests and the risks associated.

The present work describes a methodology for the construction of confident geomechanical and wellbore stability models despite the lack of relevant information in the overburden formations. This methodology allows the integration of the most relevant information regarding mud weights, wellbore trajectories, attack angles evaluation, drilling parameters, a comprehensive cavings monitoring and detailed drilling event analysis for the building of probabilistic wellbore stability models that incorporate the uncertainty of the geomechanical model. This work has contributed to the improvement of the well planning phases, reduction of the uncertainty in the geomechanical parameters and the identification of root causes of the drilling events while minimizing the likelihood of its occurrence.

KEYWORDS

Wellbore Stability; Geomechanics; Drilling; Foothills; Probabilistic models; Cavings

1. INTRODUCTION

Despite tremendous efforts and developments in the analysis of wellbore stability problems, unplanned drilling events and operational problems continue causing considerable extra costs in many drilling projects around the world. Drilling wells in the Pauto and Floreña fields, known as the *Piedemonte* fields, represents a big challenge due to its geological and geomechanical conditions. First drilling campaign in the Floreña and Pauto fields was between 1994 and 1998. Deterioration of the hole and severe wellbore stability problems led to performing 21 side tracks in eight wells drilled (N. Last et al., 1995). Geomechanics understanding and wellbore stability modelling have helped to decrease hole problems. However, drilling wells is still an expensive activity, mainly due to operational problems related with wellbore instability. In the last drilling campaign 21 wells have been drilled in the Piedemonte fields evidencing several problems related with high cavings production, stuck pipe, hard tripping among others resulting in 17 side tracks and over costs above 80 MM USD.

2. GEOMECHANICAL CONTEXT

Piedemonte fields are located in a tectonically area evidenced by high folded layers, interbedded shale sand sequences, stress anisotropy and presence of natural fractures. Estimates of the stress magnitudes suggest that the stress regime present in the field is strike slip with some evidence of normal stress regimes especially in the reservoirs sections. Maximum horizontal stress is oriented from 100 to 160 degrees in azimuth along the field. Reservoirs are the *Mirador*, *Barco* and *Guadalupe* sandstones characterized by exhibiting low porosity, low matrix permeability and high compressional strength. Wells in the Piedemonte field reach depths between 14000 ft and 21000 ft. Figure 1 shows a typical well design for a well in these fields. Wells can be divided in two parts, overburden and reservoirs sections. The overburden sections go from surface to the top of the first reservoir found, reservoir sections from there to TD. Major wellbore stability problems occur in the overburden drilling through sand mudstone intercalated formations known as the *Carboneras* due to the presence of coal levels, being the most problematic of the *Carbonera* C7 and *Carbonera* C8. Wellbore stability problems during drilling reservoir formations are unusual due to its high UCS (>20000 psi). Most of the wells have to drill two or more reservoirs, so it is necessary to drill hard and soft rocks in the same sections rising mud weight to avoid soft rocks collapse but increasing reservoir damage and the risk of having mud losses. The principal historic operational problems in the overburden and the reservoir sections are also summarized in Figure 1.

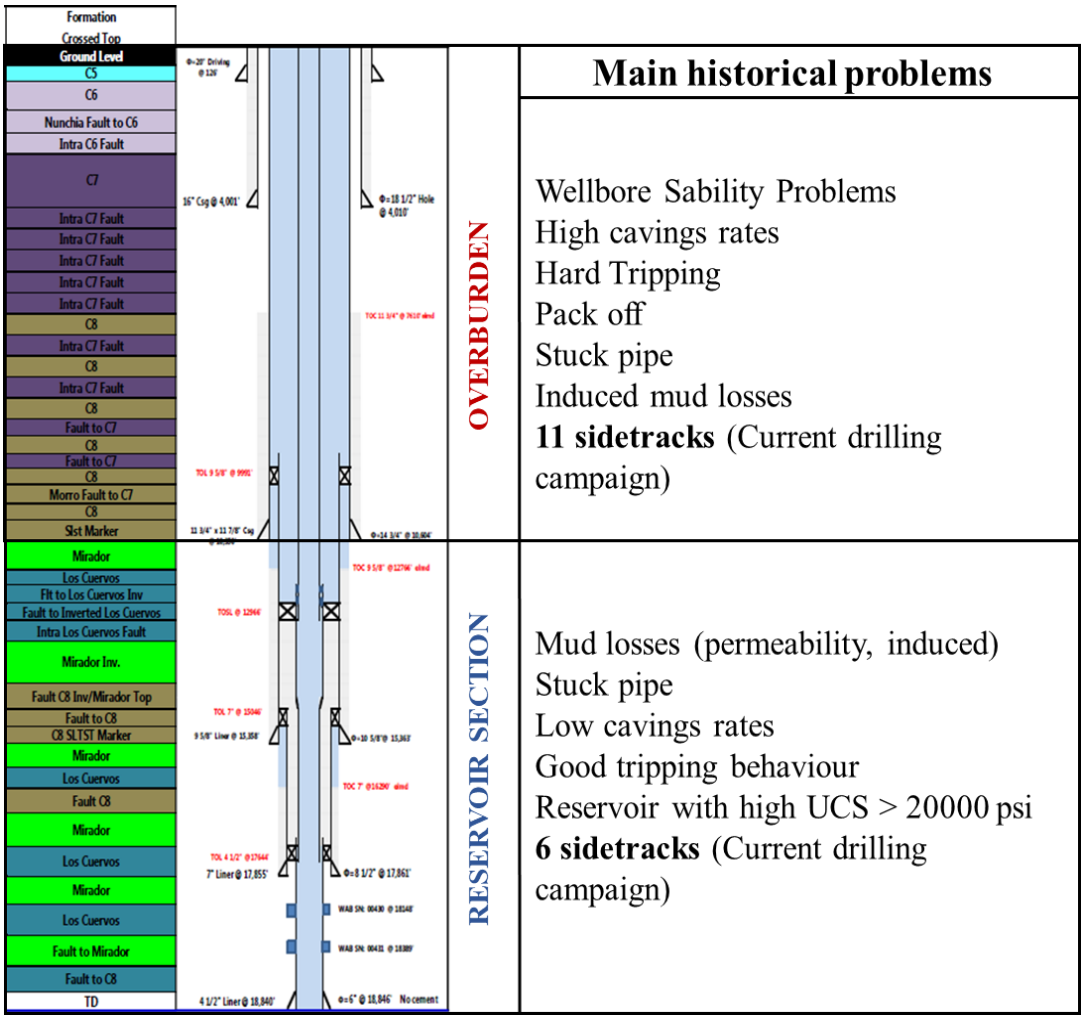

Figure 1. Typical well design in the *Piedemonte* fields.

3. WELLBORE STABILITY MODELING STRATEGY

Wellbore stability modeling has become an essential tool to use in the planning and execution of drilling projects in the *Piedemonte* fields. Conventional wellbore stability modeling require a geomechanical model composed by an estimation of pore pressure, vertical and horizontal stresses magnitudes and orientations, strength properties as unconfined compressive strength (UCS), internal friction angle or cohesive strength and elastic properties as Poisson's ratio or Young's modulus. Geomechanical models combined with the well trajectory results in a wellbore stability model that defines the safe operational mud weight window for a specific trajectory. To build a comprehensive and confident geomechanical model it is necessary to have measurements of the geomechanical parameters at many different depths along the well, this ideal situation is very uncommon for any drilling project. Due to lack of direct measurements, it is necessary to use correlations based on electrical logs to estimate pore pressure, stresses and rock properties. Methodologies to estimate geomechanical parameters have been developed for specific regions, types of rocks or other considerations that can be similar or not with the analyzed field. One of the important responsibilities of the geomechanical engineer is to determine which ones of these are best fitting in the field.

In the *Piedemonte* fields, there is a considerable lack of direct information to estimate geomechanical properties. Key information about stresses such as hydraulic fracture operations or image logs, pressure measurements or samples to perform lab tests are just available in reservoirs where the wellbore stability problems are insignificant. Well logs are not very common in the overburden section; also, the geological complexity and areal variation make the logs extrapolation a very difficult and uncertain task. In this situation of lacking direct measures and well logs, the best way to estimate geomechanical properties and build a confident wellbore stability model is using a kind of information available and abundant in all the *Piedemonte* wells, drilling events.

The key to build a confident wellbore stability model is the understanding of the drilling events and the identification of its cause (Helio Santos and Roberto Perez, 2001; B. McIntyre and R. Dixon, 2009). Conventional wellbore stability models are integrated by a pore pressure profile, fracture gradient and collapse pressures; collapse pressure allowing a certain amount of breakout is sometimes included, these curves define the safe window of mud weight to avoid influx from formations to the hole, wellbore collapse or mud losses by exceeding fracture gradient. That means conventional wellbore stability models talk about mud weight. A critical activity is to recognize if each event is related or not with low or high mud weight, even not having drilling events is a very good indicator to calibrate wellbore stability models. Integration and analysis of all the relevant information as mud properties, cavings data, operational parameters and bit position represents a good alternative to analyses principal drilling events**.** A time depth plot as shown in Figure 3, is an excellent tool to integrate information, gives a general view of the performance of drilling and the interpretation of the main events. They can reveal where (depth or formation) or during which operational activity (drilling or tripping) events occurred (J.C. Almeida et al., 2015). Additionally, it is possible to know the mud weight, cavings rates and morphologies or operational parameters at any time or depth. Sometimes, to have a more precise interpretation of the events it is necessary go deep into the details using the incident logs, daily reports, directional parameters, etc. If the correct cause of drilling events is known, it is possible to improve the calibration of wellbore stability models of wells with geological similarities. It is important to use the same correlations and parameter adjusting criterions for all the wells analyzed according to geological understanding assuring geomechanical representability for predictions in new wells.

Cavings monitoring in real time is essential to know both, the severity of wellbore stability problems and the kind of rock failure mechanism occurring downhole. Cavings rates give an idea about the severity of wellbore stability problems and morphology characterization suggest the kind of failure. Cavings morphologies can be classified as splintery, angular, tabular, blocky or reworked. Splintery carvings are often produced due to using lower mud weight than pore pressure in very low permeability rocks. Angular cavings are generally associated with shear failure due to low mud weight. Tabular cavings, are usually produced during drilling laminated formations as the shales, high amounts of tabular cavings may be associated to the use of low mud weight in highly dip formations or to the excess of

mud invasion in the weak planes when the mud weight is excessively high or mud seal properties needs to be adjusted. Blocky cavings are produced when laminar or naturally fractured formations are drilled, high production of this kind of cavings are related to excess mud invasion or mechanically interaction between drilling string and borehole, especially while tripping. Presence of reworked cavings is related with poor hole cleaning or bad hole quality conditions (Gaynor et al., 2001). When the cavings monitoring is available in historic wells it is very useful to analyse drilling events.

Conventional analytical wellbore stability models, also known as deterministic models, use unique values of geomechanical parameters at different depths. These models are only reliable if the input data are reasonably accurate, a situation not very common in the Piedemonte fields. An adequate interpretation of the drilling events help to adjust wellbore stability models. However, there are many different combinations of geomechanical properties leading to a well-calibrated wellbore stability model, but there will be high uncertainty in the parameters that could affect predictions of mud weight requirements in complex and unexplored trajectories. Probabilistic models become an important tool to maximize the possibility of adopting the correct decision involving the key parameters uncertainty (Aadnoy, B. and Looyeh R., 2010; D. Moos et al., 2003). Combination of drilling information integration, correct interpretation of events and probabilistic models represent a powerful methodology to evaluate and avoid wellbore stability problems in the *Piedemonte* fields.

4. FIELD CASE

According to the development plan of the Piedemonte fields, building new locations to drill new wells is an uneconomical activity due to the rugged topography in the area. This situation leads to proposing complex trajectories for new wells that must be drilled from existing locations. Wellbore stability modelling becomes a critical tool to evaluate new projects and avoid problems during operations. Three new wells are planned to be drilled in a particular area where operational problems have been recurrent in the overburden section and it is necessary to have confident geomechanics and wellbore stability models. The work presented in this document consists in the analyses of four wells drilled from location "A" in the overburden as it was the most problematic section during drilling these wells. Figure 2. Shows a plant view of the wells in the location "A".

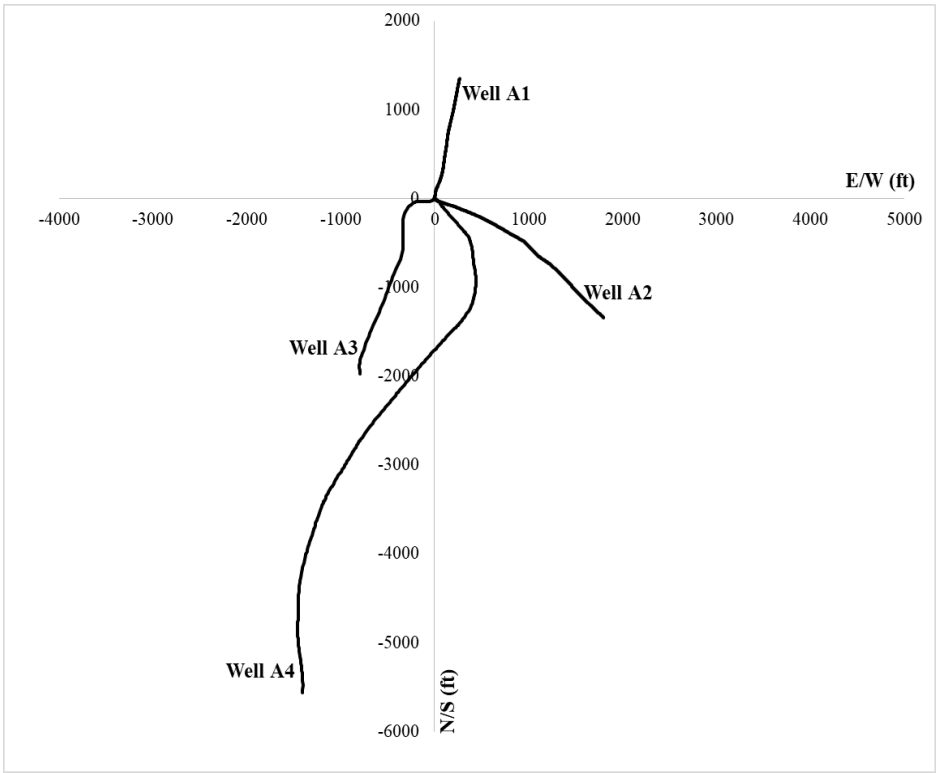

Figure 2. Plant view of Wells drilled in location "A"

4.1 Events analysis

Well A1 was the first well drilled in the location A, most of problems occurred in section 14 ¾" in the overburden, Figure 3 shows a time depth plot integrating several parameters this section in the well A1. In the first track is represented bit position in red giving information about drilling and tripping performance, in this same track is represented the cavings rates in blue shadow correlated with bit depth data. Principal axis (left) shows cavings rate and secondary axis (right) is the depth reference for bit depth and formation tops. Second track show sizes cavings information, blue shadow represents minimum sizes of cavings analyzed, yellow the most common size and red shadow the highest sizes. In this track is plotted as well mud weight changes in time. Cavings sizes scale is referencing in the principal axis (left) and mud weight in the secondary axis (right). In the third track cavings morphologies distribution is represented by color bars, red bars represent the portion of reworked cavings in the shakers, splintery in blue, angulars in yellow, blocky in dark green and tabulars in light green. Fourth track represents the portion of cavings respect to the total amount of cavings and cuttings measured at the shakers. Last track plots some operational parameters as SPP, flow and ROP. In this kind of plot, it is possible to include any other parameter in time to correlate with the bit position and cavings behavior.

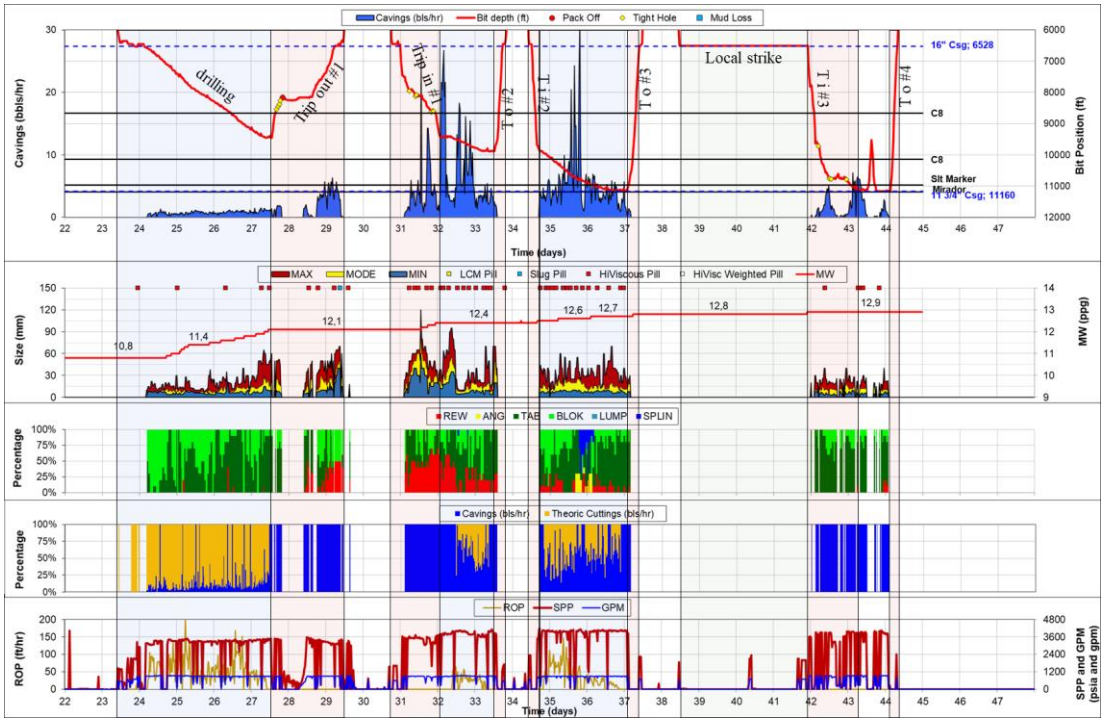

Figure 3. Time depth plot for well A1

According to Figure 3, the 14 ¾" section start to drill with a mud weight of 10.8 ppg, during drilling mud weight was increased to 12.1 ppg before starting first trip out (trip out #1) at 9450 ft. Cavings rates were below 1 bph, sizes lower than 2.5 cm. In the trip out #1, pulled out of hole in elevators to 8550 ft where tight hole are reported (yellow dots in bit depth plot), and a stuck pipe at 8160 ft (red spot), worked string for a few hours until the pipe got free and continued tripping out. After the pipe was free, cavings rates increased from 1 bph to 5 bph, maximum cavings size increased as well and reworked cavings began to be reported. In the trip in #1 there were some restrictions, cavings rates increased up to 25 bph, cavings sizes continued increasing and reworked cavings were present in a proportion above 50% of the total sample. Mud weight was raised to 12.4 ppg to reach the bottom and continue drilling in a shale rock. Continue drilling 440 ft of new hole, cavings rates increase to 15 bph. Next tripping out (trip out #2) was free without restrictions; trip in #2 was good behavior as well. Casing point was reached at 11160 ft, during drilling was reported cavings rates picks over 25 bph and splintery and angulars cavings, mud weight was increased to 12.8 ppg. Tripping out was free without problems. The well was closed for 3.5 days due to a local strike, a conditioning trip was performed to assure the well was in good condition to run the casing. This trip and the casing running were done without problems, final

mud weight before casing running was 12.9 ppg. Event analysis of this section suggest that increments in mud weight helped to improve hole condition after trip out #1 and trip in #1. Additionally, there are not long time dependent wellbore stability problems, evidenced by the good performance during wiper trip after 3.5 days of exposure time without circulation.

Well A2 was the second well drilled in the location "A". Figure 4 shows the time depth plot for well A2 in the similar depth interval that was analyzed in the well A1. As in the well A1, low cavings rates were reported during drilling, mud weight was increased to 12.8 ppg while drilling before performing first tripping out, expecting to have free trips as in the well A1 after the mud was increased. Tight hole, restrictions and high cavings rates were evident as much in trip out #1 as in the trip in #1, trip out #2 was performed without restrictions or tight holes. As in the well A1 trip out #2 and casing running were without important restrictions, but in this well, mud weight could not be increased to perform the trips. Hole condition improved after perform trip out #1 and trip in #1 without increasing the mud weight. Apparently, problems observed in the trip out #1 and trip in #1 are not due to low mud weight, this is a very important information to calibrate geomechanical and wellbore stability models.

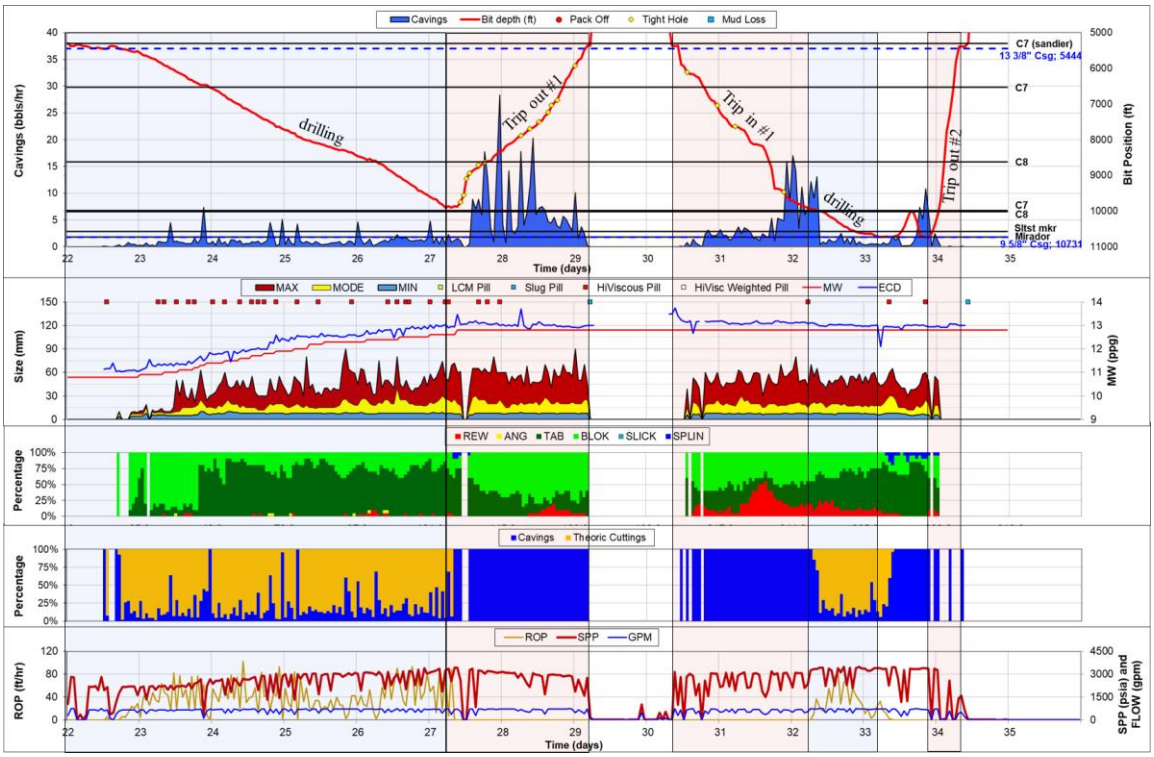

Figure 4. Time depth plot for well A2

Third well in the location "A" was well A3. This well had a very similar behavior in the analyzed section that previous wells, cavings rate were low during drilling and increase during trip out #1and trip in #1. Casing point in this well was reached in one bit run, mud weight before start trip out #1 was 12.5 ppg, during trip out #1, there were a lot of tight holes, stuck pipe and induced mud loses (blue squares). Mud weight was increased until reach 13 ppg at the end of trip in #1 (See Figure 5**)**.

Well A4 is the last well that has been drilled in this location. Several operational problems lead to performing 4 side tracks while drilling through 14 ¾" section. Original hole began to drill with a mud weight of 10.7 ppg and was increased to 11.5 before tripping out. During the trip in, pipe got stuck at 6200 ft and mud losses were induced leading to drill a first sidetrack. New hole (ST1) starts at 4825 ft (KOP), using mud weight of 11.7 ppg (see figure 6), while drilling at 5725 ft occurred a stuck pipe and induced mud losses, pipe was worked for 8 days having some string movement from 5725 ft to 5222 ft, where decided to cut the pipe leaving a fish of 193 ft. This situation reveals that hole was in bad

condition, but it is not clear the pipe got stuck due a strong pack off because of the string movement of 503 ft while working the pipe. Next sidetrack (ST2) used a 11.7 ppg mud weight at 4550 ft, 549 ft below the casing shoe. Hole observed in very bad condition, decided to abandon the 14 ¾" old hole and start a new sidetrack just below the 16" casing shoe. A multidisciplinary team identified that the main problems in these sections were associated with wellbore stability due to exposure time, micro fractured coal layers instability and poor mud condition. Main change to start the third side track (ST3) was to review mud condition; adjust mud weight, rheological properties and using nano technology to improve sealing strategy. Figure 7 shows the cavings monitoring for ST3, cavings characterizes and tripping behavior was very similar to previous wells. Final MW for the section was 12.6 ppg, drilling with the last BHA, reservoir was intercepted at 10590 ft, total mud losses were reported with a differential stuck as consequence, pipe was cut at 10490 ft leaving a fish of 100 ft. After the remaining pipe was on surface, there were necessary to perform a wiper trip to assure the casing running, wiper trip was done without difficulties, casing was run and the next section began as a ST. This event of total mud losses and differential sticking represent a very valuable source of information to calibrate both geomechanical and wellbore stability models. Total mud losses represent a decrease in the ECD and the fact that wiper trip after cut the string did not present considerable restriction and the casing was run to the top of the fish gives an idea that mud weight used was far enough to avoid hole collapse. Due to the typical naturally fractured shales found in the Piedemonte fields, it is very common to have production of tabular and blocky cavings. Reworked cavings have been produced in some wells, mainly associated with complex geometries resulting of drilling complex structures and interbedded formations.

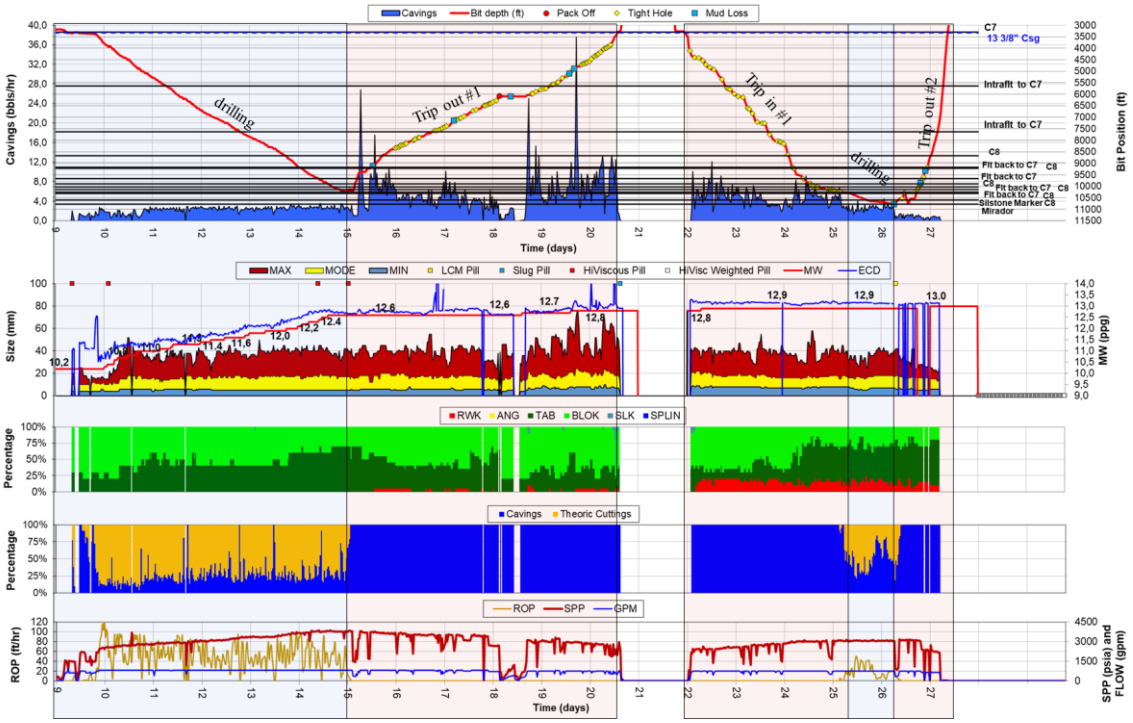

Figure 5. Time depth plot for well A3

4.3 Wellbore stability modeling

Geomechanical model was built based on a short section of sonics logs in the well A2, complementary information was extrapolated from far away wells. Well A4 was used as the main well to adjust geomechanical and wellbore stability model due to this well used the lowest mud weight (12.6 ppg) and the interpretation that mud weight was right. Pore pressure estimations were made using Eaton's methodology adjusted according to mud weight used and the events interpretation (Aadnoy, B. and Looyeh R., 2010). Horizontal stresses were estimated by the poroelastic equations, minimum horizontal

stress was calibrated with a hydraulic fracture data at reservoir depth, no leak off test data were available in the area, maximum horizontal stress orientation of 120 degs was interpreted from image logs available in the reservoir section. McNally (1987) and Freyburg (1972) correlations (Zoback, M., 2007) and Mohr-Coulomb failure criteria were used to estimate strength properties. UCS and maximum horizontal stress were modified to adjust the wellbore stability model according to event interpretation. Figure 8 shows a polar diagram to identify the relative differences in mud weight requirements to avoid hole collapse in a Carbonera formation depending on well trajectory. Well A4 requires 0.1 ppg less mud weight that the other wells. Wells 1, 2 and 3 require the same mud density to avoid hole collapse.

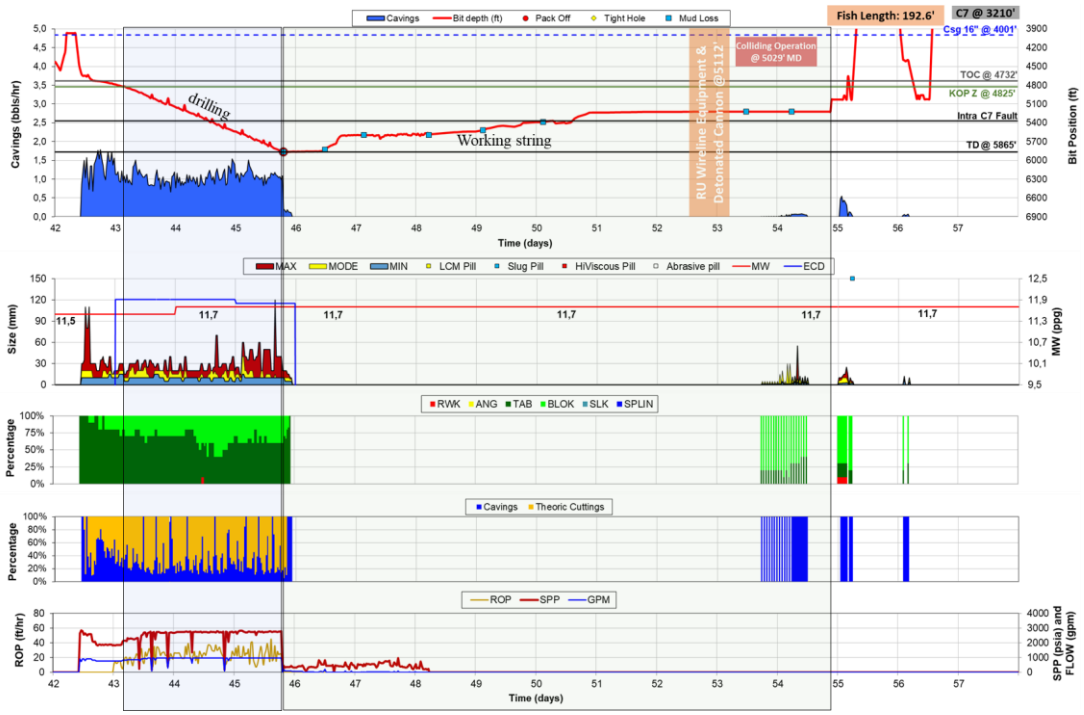

Figure 6. Time depth plot for well A4 ST1

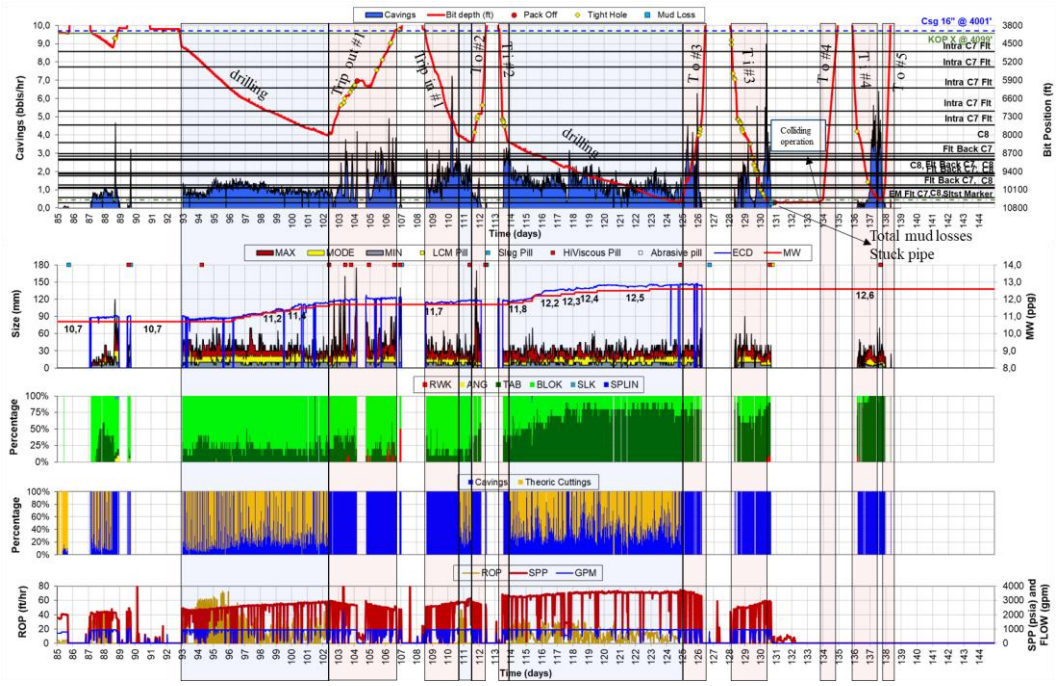

Figure 7. Time depth plot for well A4 ST3

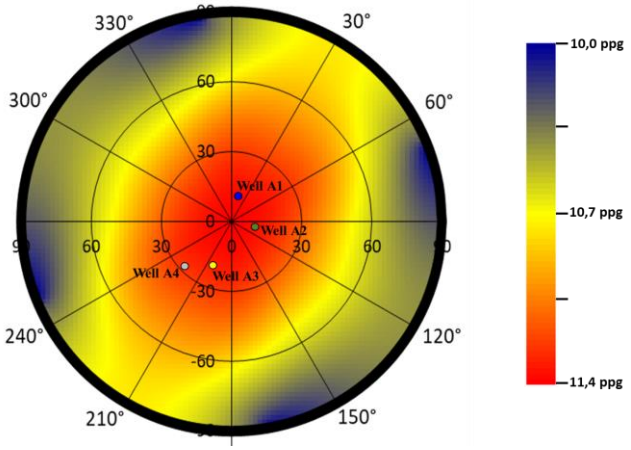

Figure 8. Mud weight requirements for Carbonera formation in the location "A" in a polar diagram.

4.4. Probabilistic models

The probabilistic model used in this work has been based on the Montecarlo simulation, generating 10000 random values of the geomechanical parameters with a normal distribution in an uncertainty range. Same amount of wellbore stability models were obtained using the Kirsh equations to estimate the hoop stresses and Mohr Coulomb failure criteria (Fjaer et al., 2008). Based on the interpretation that MW was enough in all the wells of the location "A", probability of success or having no hole collapse due to low mud weight is 100 %. For the current analysis that probability has to be as minimum 95% with breakout zero. Table 1 shows the range of uncertainty for the most critical depth in the section. Probabilistic model was run at the depth and trajectory of well A4, this well used the lowest mud weight in the location "A". Figure 9 shows the results of the histogram of collapse pressure resulting from Montecarlo simulation and the cumulative frequency using the data of table 1. This cumulative frequency represents the cumulative likelihood of avoiding wellbore collapse for any mud weight. Analysis of results show that using MW of 12.6 ppg, the probability of success is 96%, that means that the uncertainty ranges are adequate. Figure 10 shows a sensitive analysis for each parameter in the wellbore stability model; each plot in Figure 10 represents the variation in collapse pressure changing the analyzed parameter in the uncertainty range described in the Table 1, keeping constant the other variables. Higher inclinations of the lines (blue for breakout zero and red using a wide breakout of 70 degrees), represents high effect in the collapse pressure, flat lines represent little or no effect. UCS, SHmax magnitude and pore pressure have the biggest effect in the collapse pressure, future information acquisition should be focused to minimize the uncertainty of these parameters. In the other way, parameters such as Poisson's ratio, friction coefficient ratio or vertical stress have minimum effect in the wellbore stability model results.

Table 1. Geomechanical parameters used in the probabilistic model

Parameter	**Mean**	**Min**	**Max**
Vertical Stress (Sv) (psi/ft)	1	0.92	1.08
Minimum horizontal stress (Shmin) (psi/ft)	0.83	67	4
Maximum horizontal stress (SHmax) (psi/ft)	1.1	1	1.2
Orientation of SHmax (degs)	120	100	140
Pore pressure (Po) (psi/ft)	0.57	0.52	0.62
Unconfined Compressive Strength (UCS) (psi)	1150 0	800 0	1500 0
Friction coefficient (u)	0.85	0.7	1
Poisson Ratio (v)	0.2	0.15	0.25

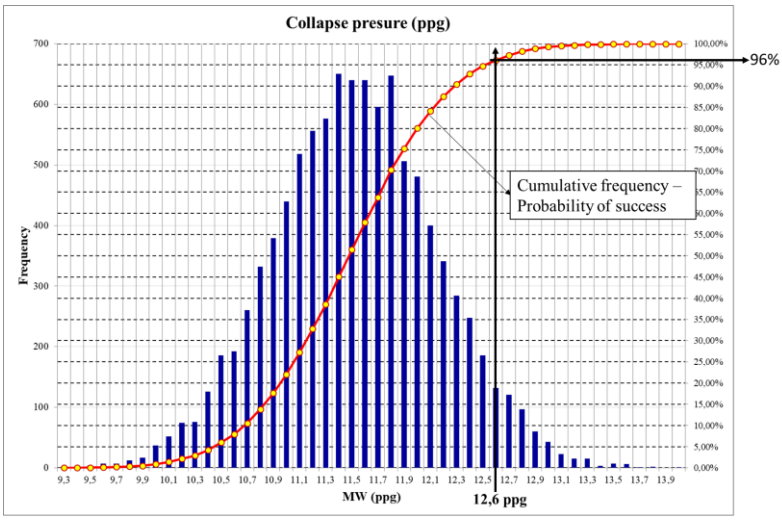

Figure 9. Probabilistic analysis for well A4

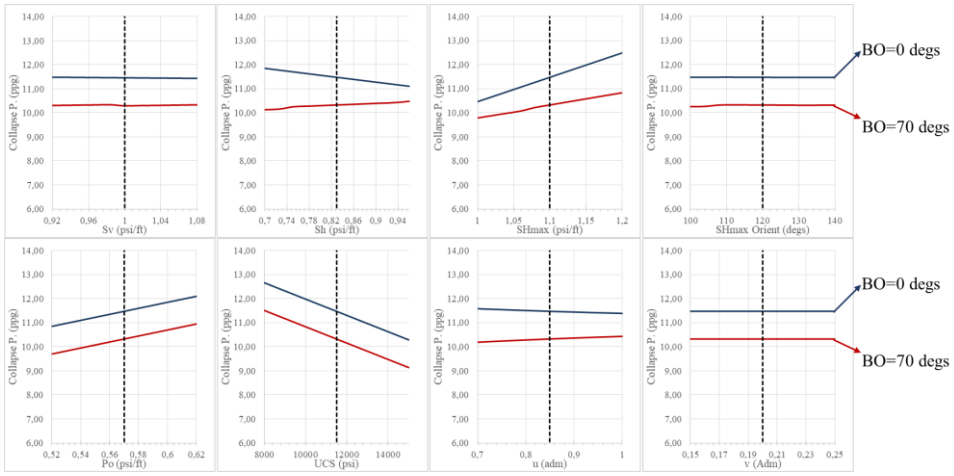

Figure 10. Sensitive analysis for well A4

Same uncertainty ranges determined in the probabilistic model of well A4 were used to evaluate mud weight requirements for the remaining wells of the location "A" involving geomechanical uncertainty due to the lack of information. Probabilistic models for wells 1, 2 and 3 were run using specific depth formation and trajectories of each well. Evaluation of probabilistic model for well A2 is shown in the Figure 11, mud weight used of 12.8 ppg has a 96% of probability of success, it means that mud weight used was enough to avoid hole collapse and there is a high probability that tripping problems were not related with low mud weight.

Montecarlo simulation is a very important tool to define safe mud weights especially in highly uncertain environments as in the Piedemonte fields. Drilling events analysis presented in this document suggest that mud weights used in the wells were adequate to avoid hole collapse and results shown in Figure 9 and 11 confirm that affirmation. In this work, a probabilistic model in association with event analysis helps to reduce the range of uncertainty of the geomechanical parameters that will be used to evaluate mud weight requirements for future trajectories in the Piedemonte fields.

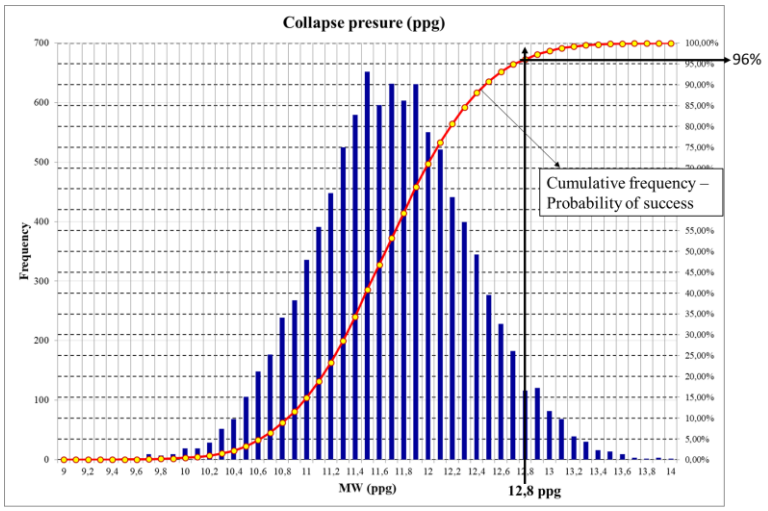

Figure 11. Probabilistic analysis for well A2

5. CONCLUSIONS

- It is possible to build confident geomechanical and wellbore stability models with few geomechanical information in mature fields by using integration of drilling information to have a comprehensive event analysis and by using probabilistic models.
- Geomechanical and wellbore stability modeling in Piedemonte fields help to define safe mud weight windows, especially to identify actual situations where high mud weight is required.
- Montecarlo simulation is a very important tool to define safe mud weights especially in highly uncertain environments as the Piedemonte fields. Probabilistic model in association with event analysis helped to reduce the range of uncertainty of the geomechanical parameters that will be used to evaluate mud weight requirements for future trajectories in the Piedemonte fields.
- UCS, SHmax magnitude and pore pressure have the major effect in the collapse pressure, future information acquisition should be focused to minimize the uncertainty of these parameters.
- According to this document, severe and continuous operational problems in the wells drilled in the location "A" are not related to using low mud weights. Identification of the correct cause of the operational problems will be the key to obtain a considerable reduction in drilling costs.
- It is highly recommended to develop a comprehensive wellbore stability study including mud rock interaction, trajectories tortuosity, operational practices reviewing and hole cleaning conditions additionally to the geomechanics analysis.

ACKNOWLEDGEMENTS

The authors would like to acknowledge and thank Ecopetrol S.A. for their permission to publish this work.

REFERENCES

Aadnoy, B. and Looyeh R., 2010. *Petroleum Rock Mechanics, Drilling Operations and Well Design.* Elsevier Inc., USA.

Brett McIntyre and Rachel Dixon, 2009. Wellbore Instability in Forties: Diagnosis of Root Causes for Improved Drilling Performance. Paper SPE 124670. *SPE Offshore Europe Oil & Gas Conference & Exhibition, 8 – 11 September 2009.* Aberdeen, UK.

Daniel Moos, Pavel Peska, Thomas Finkbeiner, Mark Zoback, 2003. Comprehensive wellbore stability analysis utilizing Quantitative Risk Assessment. *Journal of Petroleum Science and Engineering* 38 (2003) 97 – 109.

Fjaer, E.; Holt, R.M.; Horsrud, P.; Raaen, A.M. and Risnes, R., 2008. *Petroleum Related Rock Mechanics,* second edition, Elsevier, Oxford, UK.

Tom M. Gaynor; David C-K Chen; Darren Stuart and Blaine Comeaux, 2001. Tortuosity versus Micro-Tortuosity – Why Little Things Mean a Lot. Paper SPE 67818. *SPE/IADC Drilling Conference, 27 February – 1 March 2001.* Amsterdam, The Netherlands.

Helio Santos and Roberto Perez, 2001. What Have We Been Doing Wrong in Wellbore Stability?. Paper SPE 69493. *SPE Latin American and Caribbean Petroleum Engineering Conference, 25 – 28 March 2001.* Buenos Aires, Argentina.

J.C. Almeida, M. Rangel, G. Rey, M. Pacione, C. Lopez and A. Valdivieso, 2015. Well of the future: A New Approach to Real-Time Wellbore Stability Monitoring in the Colombian Foothills. Paper SPE/IADC 173129-MS. *SPE/IADC Drilling Conference and Exhibition, 17 – 19 March 2015.* London, UK.

N. Last; R. Plumb; R. Harness; P. Charlez; J. Alsen and M. McLean, 1995. An Integrated Approach to Evaluating and Managing Wellbore Stability in The Cusiana Field, Colombia, South America. Paper SPE 30464. *SPE Annual Technical Conference & Exhibition, 22 – 25 October 1995.* Dallas, U.S.A.

Zooback, M., 2007. *Reservoir Geomechanics.* Cambridge. Cambridge University Press.